Computations, Design & Instrumentation for Precision Ion Trap Experiment

Thesis Submitted to AcSIR for the Award of the Degree of
DOCTOR OF PHILOSOPHY
In Physical Sciences

BY

Neha Batra
(Reg. No. : 10PP14A32001)

Under the guidance of

Dr. Subhadeep De

&

Dr. Subhasis Panja

CSIR- NATIONAL PHYSICAL LABORATORY
NEW DELHI-110012, INDIA

Dedicated to

source of all being,
Lord Krishna

Certificate

This is to certify that the work incorporated in this Ph.D. thesis entitled "**Computations, Design & Instrumentation for Precision Ion Trap Experiment**" submitted by **Mrs. Neha Batra** to Academy of Scientific and Innovative Research (AcSIR) in fulfillment of the requirements for the award of the Degree of **Doctor of Philosophy in Physical Sciences**, embodies original research work under my guidance. I further certify that this work has not been submitted to any other University or Institution in part or full for the award of any degree or diploma. Research material obtained from other sources has been duly acknowledged in the thesis. Any text, illustration, table etc., used in the thesis from other sources, have been duly cited and acknowledged.

Neha Batra

CSIR-SRF

Dr Subhadeep De
Supervisor
Scientist
Time & Frequency, Electrical and Electronics Metrology Division,
CSIR-National Physical Laboratory
New Delhi 110012

Dr Subhasis Panja
Co-Supervisor
Sr. Scientist
Time & Frequency, Electrical and Electronics Metrology Division,
CSIR-National Physical Laboratory
New Delhi 110012

Acknowledgement

This Ph.D. thesis carries only my name but many people have contributed in its existence. I have a lot of people that I want to thank and give them due acknowledgement for their contributions and help throughout the five years at NPL. I don't think it would have been possible to complete my journey through Ph.D. without help of these people.

Firstly, I express my deep sense of gratitude to my supervisor Dr. Subhadeep De, for his kind supervision, support and exemplary guidance to complete the work presented in the thesis. I joined him as project assistant in the very beginning of this optical frequency standards project and gained experience in building a new research lab. Later, I got registered as his Ph.D. student in AcSIR. His impeccable knowledge, understanding and to ability to observe minutest of details have always inspired me. He was always present to help and guide even being busy with his other responsibilities. I am very thankful to my co-supervisor Dr. Subhasis Panja whose kind encouragement and calm minded approach to the problems were the key factors for helping me to come the right conclusions. I am specially thankful to Dr. Amitava Sen Gupta who has been one of my greatest inspirations. He was head of Time & Frequency when I joined and was one of my academic course instructor as well. He has always been supportive and ready for discussions despite being so busy. His experience, knowledge of field and peculiar way of teaching make things easy to understand. I am very thankful to my doctoral advisory committee (DAC) member Dr. V N Ojha who is also head of the Time & Frequency, Electrical and Electronics Metrology Division for his expert guidance. I sincerely thank my other DAC members Dr. S. S. Rajput and Dr. Ashish Agarwal for their kind inputs and encouragement throughout the tenure of my thesis. I thank Dr. B. K. Sahoo, PRL Ahmedabad and Dr. Bindiya Arora, GNDU Amritsar for helpful scientific discussions and collaborative work.

I am thankful to Dr. Poonam Arora for her encouragement throughout this journey. I acknowledge valuable inputs of technical staff Mrs. Shuchi Yadav and Mr. Mahavir Olaniya. Mr. Ved Prakash, Mr. Sajjan Singh, Mr. Devinder and Mr. Prem, members of Time and Frequency family deserve special thanks as they have always helped me in administrative processes, procurement/indentation, workshop jobs etc. to expedite my work. I want to thank all the HRD members for their help in paper works for attending conferences and others dealings. I am very thankful to Prof. D. K. Aswal, Director, NPL, for his encouragements and giving me an opportunity to work at one of the best premier laboratories of CSIR, India. I acknowledge CSIR for the grant of senior research fellowship. I extend my gratitude and thanks to my labmates Atish Roy, Lakhi Sharma, Kritika Sharma and Shankar Majhi for scientific discussions and

beyond the bounds help whenever I needed. I am thankful to my beloved friends Komal, Sonia, Naina, Dinesh and Bushra for their love, encouragement, help and counselling to overcome little periods of pessimism and remain lively now and then. I am thankful to all those whose name are not mentioned but helped in realization for my Ph.D. work in one way or other.

I owe this to my parents for their continuous love, moral support, co-operation, patience and sacrifices. My doting elder brothers have always been supportive of my higher education, standing by my side in periods of emotional distress.

And, of course I want to thank my husband Parikshit. He has been my strength, driving force, patience bank and support system throughout. His parents have been loving and very supportive which helped me complete my thesis work. I thank them with my entire heart

Last but not the least I am thankful to my God Krishna for everything I have.

Neha Batra

Abstract

This thesis work is done towards theoretical framework, instrumental development and automation for a precision ion trap experiment. The computations, designs and instrumentation work is being carried for single trapped ion optical clock development out at CSIR-NPL, India in particular.

The thesis work is broadly divided into three parts. First part of the thesis deals with review, comparisons, numerical simulations and computations providing a theoretical framework for the trapped ion optical clock experiment. It introduces various applications of ion traps in science experiments and then further focuses on the use of ion trap for optical clock in the course of this thesis. Thereafter, different ions which have already been demonstrated for optical clocks worldwide and other possible candidates are surveyed before choosing an ionic species for trapping. Further for stable trapping of an ion a suitable trap geometry is identified by numerical simulations and analysis. Dynamics of trapped ion in the potential are also studied for optimizing trap operating parameters. In order to achieve an accuracy of $\sim 10^{-18}$, estimation of major systematic effects and their mitigation techniques have been discussed.

Second part of the thesis describes the design of ion trap assembly which comprises of trap electrodes, its holders, isolators and mounting structure. Constraints behind the design such as zero optical blockage to different laser lights impinged at ion sitting at trap center, precision, symmetry and machinability which can contribute to systematic shifts are also discussed. Thereafter, designs of vacuum chamber and vacuum assembly which are of vital necessity for attaining ultra high vacuum have been discussed. They are designed taking compatible materials, minimum outgassing, volume and different sets of optically accessible ports into consideration.

In the third part, instrumentation work such as optimized design and construction of Helmholtz coils for nullifying stray magnetic field along with indigenously designed digitally controlled stable current sources to drive them has been discussed. Development of an automated control and data acquisition system which runs the experiment remotely and automatically is also discussed.

In the last, a brief summary about the results and observations presented in thesis and future perspectives of the current research work are discussed.

Table of Contents

Abstract
List of Figures
List of Tables
Acknowledgments

1 INTRODUCTION 1

1.1 Frequency Standards 2

1.2 Optical Atomic Clocks 4

1.2.1 Lattice clocks 4

1.2.2 Trapped Ion Optical Clocks 5

1.3 Overview of the thesis 5

2 IDENTIFYING SUITABLE SPECIES FOR TRAPPED ION CLOCK 9

2.1 Singly Charged Ionic Species for Optical Clocks 9

2.1.1 $^{27}Al^{+}$ 11

2.1.2 $^{40,43}Ca^{+}$ 13

2.1.3 $^{88}Sr^{+}$ 14

2.1.4 $^{115}In^{+}$ 14

2.1.5 $^{137,138}Ba^{+}$ 15

2.1.6 $^{171,172}Yb^{+}$ 16

2.1.7 $^{175}Lu^{+}$ 17

2.1.8 $^{199}Hg^{+}$ 17

2.1.9 $^{A}Ra^{+}$ 18

2.2 Systematic Shifts Associated to Ionic Species 19

3 OPTIMIZING TRAP GEOMETRY FOR SUITABLE TRAPPING POTENTIAL 25

3.1 Trapping An Ion 25

3.1.1 Real Trapping Potential: Contributions From Higher Order Poles 34
3.2 Numerical Simulations Of Potential and Validation Of Trap Geometry For Different Parameters 40
3.2.1 Physical Constraints 40
3.2.2 Anharmonicities 42
3.2.3 Ionic Motion 47

4 ESTIMATION OF MAJOR SYSTEMATIC SHIFTS 53
4.1 Electric Quadrupole Shift 53
4.2 Second Order Doppler Shift 58
4.3 DC Stark Shift 62
4.4 Zeeman Shift 64

5 DESIGN OF ION TRAP, UHV CHAMBER AND VACUUM ASSEMBLY 67
5.1 Ion Trap Design 67
5.1.1 Materials Consideration 75
5.2 Vacuum Chamber Design 77
5.3 Vacuum Equipments and Assembly 81

6 HELICAL RESONATOR FOR EFFICIENT DELIVERY OF RF VOLTAGE TO THE ION TRAP 87
6.1 Introduction 87
6.2 Resonator Design 87
6.3 Construction and Measurements 89

7 INSTRUMENTATION FOR MAGNETIC FIELD CANCELLATION AND AXES QUANTIZATION 99
7.1 Helmholtz Coils 99
7.1.1 Construction 102
7.1.2 Digitally Controlled Stable Current Source 103
7.2 Measurements 105

8 AUTOMATED CONTROL AND DATA ACQUISITION SYSTEM 113

8.1 Scheme of Control and Data Acquisition System 113

8.2 Hardware Subsystem 117

8.2.1 Breakout Box 117

8.2.2 Digital Buffer 120

8.3 Controlling Software 125

APPENDICES i

BIBLIOGRAPHY xix

List of Publications xxx

List of Figures:

Figures		Pg. No.
2.1	Energy level diagrams of all atomic-ions that are used for optical clocks: (a) $^{27}Al^{+}$, (b) $^{40}Ca^{+}$, (c) $^{88}Sr^{+}$, (d) $^{115}In^{+}$, (e) $^{137,138}Ba^{+}$, (f) $^{171}Yb^{+}$, (g) $^{175}Lu^{+}$, (h) $^{199}Hg^{+}$, (i) $^{226}Ra^{+}$ ions. Dashed lines correspond to clock transition and the solid lines indicate cooling, repump, shelving.	10
2.2	Electric quadrupole shift $\Delta\nu_Q$ with respect to quadrupole moments of different ion species. The quadrupole moment of $^{175}Lu^{+}$ is taken from [138], however, it is discussed in sec. 2.1.7 that there is a small quadrupole shift	20
3.1	Axial (blue) and radial (green) stability regions plotted simultaneously in $a_z - q_z$ space.	28
3.2	Shows an end cap trap geometry with its different dimensional parameters. Naming conventions: Tip to tip inner electrode separation, $2z_o$; separation between the outer electrodes, $2z_1$; radii of the inner electrodes, $2r_o$; inner and outer radii of the outer electrodes, $2r_1$ and $2r_2$; ;angle of inner and outer electrodes θ_i and θ_o. Trap dimensions used by: (a) NRC, CANADA [74], (b) NPL, UK [49, 162], (c) Universitat Hannover [163].	34
3.3	Composite stability region. Region in black shows region of our interest where non linear resonances due to poles upto 10th order can be avoided.	39
3.4	(a) Angles made by light incident on ion with electrodes' edges. (b) Important geometric parameters of the electrode assembly.	41
3.5	Fractional anharmonicities for different inner and outer electrodes angles at $2r_o$ = 1 mm, $2z_o$ = 0.7 mm.	43
3.6	Potential contours simulated with parameters $2z_o$ = 0.7 mm, $2r_o$ = 1 mm, $\theta_o = 45^o$, $\theta_i = 10^o$ show nearly quadrupole shape of potential	44
3.7	Potential contours simulated with parameters $2z_o$ = 0.7 mm, $2r_o$ = 1 mm, $\theta_o = 45^o$, $\theta_i = 50^o$	44
3.8	Fractional anharmonicities variation with z_o at $2r_o$ = 1 mm, $\theta_i = 10^o$ and $\theta_o = 45^o$.	45

3.9 Fractional anharmonicities variation with z_o at $2r_o$ = 1 mm, θ_i = 11° and θ_o = 45°. 46

3.10 Variation in $|A_m|$; $|A_s|$ and $|A_m/A_s|$ with (a), (c), (f) $2r_o$, for $2z_o$ = 0.6 mm, θ_i = 0°, θ_o = 45°; (b), (d), (e) $2z_o$, for $2r_o$ = 1 mm, θ_i = 11°, θ_o = 45° 47

3.11 Variation in $|A_m|$; $|A_s|$ and $|A_m/A_s|$ with (a), (c), (f) $2z_o$, for $2z_o$ = 1 mm, θ_i = 0°, θ_o = 45°; (b), (d), (e) $2z_o$, for $2r_o$ = 1 mm, θ_i = 0°, θ_o = 45° 48

3.12 Variation in $|A_m|$; $|A_s|$ and $|A_m/A_s|$ with θ_o, at θ_i,=0° (black), 10° (blue), 20° (red), 30° (magenta), 40° (green), 50° (cyan) and 60° (yellow). The distances $2r_o$ = 1 mm, $2z_o$ = 0.6 mm are kept constant for all of them. 49

3.13 Variation in $|A_m|$; $|A_s|$ and $|A_m/A_s|$ with θ_i, at θ_o= 0° (black), 15° (blue), 25° (red), 35° (magneta), 45° (green), 55° (cyan) and 65° (yellow). The distances $2r_o$ = 1 mm, $2z_o$ = 0.6 mm are kept constant for all of them. 50

4.1 Fractional electric quadrupole shifts due to the multipoles up to l = 10 for the (a) E2 and (b) E3 transitions, when the ion is off centered by a distance 0.1 μm (green) and 10 μm (black), respectively. The harmonic potential gives a spatially independent $|\Delta\nu_Q/\nu_o|$. The reported fractional accuracies lie within the grey bands and so far the best accuracies are 1:1 × 10^{-16} [93] and 3 × 10^{-18} [9] for the E2 and E3-transition, respectively. 55

4.2 Fractional electric quadrupole shift for the E2 and E3-clock transitions varying with different geometrical parameters: (a,b) with $2r_o$, $2z_o$ = 0.7 mm, θ_i=10° and θ_o=45°; (c,d) with $2z_o$, $2r_o$ = 1 mm, θ_i=10° and θ_o=45°; and (e, f) with θ_o with $2r_o$= 1 mm, $2z_o$ = 0.7 mm, different colors signify different values of θ_i = 0° (black), 10° (red), 20° (gray), 30° (green), 40° (cyan), 50° (blue) and 60° (purple). The dashed line connects data points for the fixed values of θ_i. 56

4.3 Spatial dependence of the fractional electric quadrupole shifts $\Delta\nu_Q/\nu_o$ for the E2 and E3-clock transitions of $^{171}Yb^+$. The quadrupole trapping potential produces a constant shift (gray).
The spatial dependence in the shift along the radial (red) and axial (blue) directions arise from the anharmonic components $l > 2$ of $\Phi^{(l)}$. 57

4.4	The electric quadrupole shifts from previously reported works and estimated values from this work are shown in (a) for the 6s $^2S_{1/2} \rightarrow 5d^2\ D_{3/2}$ and for the 6s $^2S_{1/2} \rightarrow 4f^{13}6s^2\ ^2F_{7/2}$ clock transitions.	59
4.5	Variation of the second order Doppler shifts with respect to the trap parameters radio-frequency, ω_{rf} (red), ac, V (blue) and dc, U (orange) voltages resulting from (a) temperature of the ion T, (b) patch potential that ion experiences E_p and (c) relative phase difference of rf at two electrodes ϕ_o.	60
4.6	Fractional Second-order Doppler shift $\Delta\nu_{2D}/\nu_o$ with: temperature, T (Red); patch potential generated electric field, E_p (Green); phase difference of rf at endcaps, ϕ_o (Blue).	61
4.7	Variation of the fractional dc Stark shift $\Delta\nu_{dc}/\nu_o$ due to both scalar and tensorial polarizabilities with electric field E_p (red) and the fractional BBR shift $\Delta\nu_{BBR}/\nu_o$ due to scalar polarizability at 300 K (blue). E2 and E3-transitions are distinguished by solid and dashed lines, respectively.	63
5.1	Different designs of the trap assembly (1), (2) and (3) with convention A: trap holder cum stand. B: insulating spacer, C:holder for outer electrodes, D:outer electrodes, E:inner electrodes, F:metallic screws and G:clamping screws. Machined prototypes of (1), (2) and (3) are shown in (1'), (2') and (3') respectively.	69
5.2	Ion trap assembly with its different parts labelled.	71
5.3	Dimensional details the parts A and B of the ion trap. All the dimensions of length are in units of millimeter and the angular dimensions are in units of degree.	72
5.4	Dimensional details the parts C, D and E of the ion trap. All the dimensions of length are in units of millimeter and the angular dimensions are in units of degree.	73
5.5	Dimensional details the parts F and G of the ion trap. All the dimensions of length are in units of millimeter and the angular dimensions are in units of degree.	74
5.6	A cube of arbitrary dimensions with AB as one of its body diagonal aligned along z-axis. Lines CD, EF, GH join the centers of opposite faces.	78

5.7	(a) Initial design of spherical UHV chamber, (b) Final design of UHV with cylindrical symmetry.	83
5.8	Detailed dimensional drawing of UHV chamber assembly. All the dimensions of length are in units of millimeter and the angles are in degree.	84
5.9	Dimensional drawing different parts of UHV chamber assembly. All the dimensions of length are in units of millimeter and the angles are in degree.	85
5.10	(a) Vacuum chamber surrounded by Helmholtz coils. Here, only vacuum chamber is shown as surrounded by coils for clarity. (b) Isometric view of the complete vacuum assembly in 3D.	86
6.1	Schematic representation of a helical resonator with important dimensional parameters.	88
6.2	Picture of the helical resonator fabricated in lab. (a) shows the helical coil inside the shield and (b) shows the primary antenna respectively.	90
6.3	Schematic diagram of the experimental set up for measuring resonant frequency and Q-factor of a helical resonator.	91
6.4	Frequency response of a helical resonator with varying load capacitance (a) C_L = 0, unloaded condition (f_0 = 38.77 MHz), (b) C_L = 4.7 pF (f_0 = 31.33 MHz), (c) C_L = 10 pF (f_0 = 26.25 MHz) and (d) C_L = 20 pF (f_0 = 21.29 MHz).	91
6.5	Variation of f_0 and Q of the resonator for different external load capacitance, C_L.	92
6.6	(a) and (b) showing side and front view of the second resonator.	94
6.7	Variation of f_0 and Q of second resonator with different external load capacitances, C_L.	95
6.8	(a) Resonant frequency f_0 = 26.85 MHz, Q ~583 of second resonator in unloaded condition; (b) when connected with ion trap (as load) resonant frequency, f_0 = 17.915 MHz and Q ~250.	95
6.9	(a) Shows variation of frequency response parameter, δf^2 with load capacitance, C_L and (b) shows variation of $f_0'^2$ with effective capacitance, C' inverse.	96

7.1	(a) Shows standard configuration of Helmholtz coils with circular coils, whereas (b) shows Helmholtz coils with rectangular geometry.	100
7.2	(a) Shows detailed view of side AB of the rectangular coil ABCD shown in above figure, whereas (b) shows isometric view of the coil ABCD along with its distance from point P.	100
7.3	Shows numbering convention of the coils along with their position with respect to the (x, y, z) axes directions and different ports. For clarity, only vacuum chamber is shown as surrounded by the coils not the complete vacuum assembly.	103
7.4	Block diagram depicting working of the current source.	104
7.5	Schematic representation of supply section of the current source circuit.	106
7.6	Schematic representation of current source circuit.	107
7.7	PCB board of current source.	108
7.8	Digitally controlled current source box. (a) Shows front panel of the box which takes input bits, deliver output and has a display; (b) shows inside view of the box with supply, DACM, display and current source sections; (c) shows back panel which mounts MOSFET, heat sinks and has safety fuse.	109
7.9	Shows linear relation of I_{set} vs I_o of a current source. Green markers show the actual experimental values and the green solid line is linearly fitted over the experimental data.	110
7.10	Shows fluctuation at different I_{set}, Black corresponds to just ON situation and Red corresponds to situation after 6 hours of continuous operation. Green line shows the resolution of the D/A converter used in the device. The maximum fluctuation of 12 μA corresponds to a magnetic field of 65 μG at the center of a pair of Helmholtz coils shown by Blue line.	110
7.11	Shows (a) assembly of the magnetic coils put together for mapping magnetic field profile, (b), (c) and (d) profile of magnetic field at the center of coil assembly along z, x and y directions, respectively. Blue line shows simulated field whereas red markers show the experimentally measured values.	111

8.1	Schematic representation of automated control and data acquisition system for our experiment.	114
8.2	Shows (a) connector block SCB-68A for accessing the PCI card installed inside computer, (b) schematic representation of connections inside breakout box and (c) Front panel of a breakout box.	118
8.3	(a) Schematic representation of buffer action for a single digital line and a single bit after travelling 20 m, with (red) and without (black) being buffered at different frequencies, (b) 10 Hz, (c) 10 MHz	121
8.4	Schematic of digital buffer circuit.	122
8.5	Schematic of power supply regulation circuit for digital buffer.	123
8.6	Pictures of a digital buffer box with (a) showing front panel having output channels and XLR connector for supply input; (b) showing inside view of the digital buffer box; (c) showing back panel of the box with output channels and a input channel.	124
8.7	Picture shows algorithm of the GUI developed for CDAQ system.	126
8.8	(a) Shows frequency and amplitude control signals fed into AOM driver, to control its frequency and amplitude. (b) Shows acquired voltage corresponding to the current generated from the current source. It also shows the magnetic field at center of a pair of Helmholtz coils corresponding to the driving current given to them.	128
8.9	Shows a snapshot of front panel of the GUI. Markings (a), (b) and (c) represent the parts for automated operation, manual operation and acquisition whose codes are given in figures ahead.	129
8.10	Part of code for writing a new sequence le for automated control of equipments.	130
8.11	Part of code for loading sequences from existing le and controlling equipments corresponding address, input data and time information.	130

8.12 Part of code for individually controlling equipments. 131

8.13 Part of code for acquiring from different equipments. 131

List of Tables:

Tables		Pg. No.
1.1	List of species that have been demonstrated as an optical frequency standards worldwide are shown with their reported fractional accuracies and frequency standards.	6
2.1	Spectroscopic information of the ions that are demonstrated as frequency standards. Symbols indicate: nuclear spin (I), wavelength (λ), natural linewidth of the transition (Γ), lifetime of the excited state (τ), saturation intensity (I_o), dynamic correction factor (η), Lande-g factor of the ground state (g_g) and excited state (g_e), quadratic Zeeman coefficient (κ_2), differential polarizabilities, scalar ($\Delta\alpha_S$) and tensorial ($\Delta\alpha_T$) and quadrupole moment (Θ) of the excited state associated to the clock transition.	12
3.1	Multipole components of potential ($l \leq 10$)	38
3.2	Limiting angles [degree] with different values of $2r_o$ [mm] and $2z_o$ [mm]	42
3.3	Fractional multipole coefficients and loss factor for different traps used by Schrama *et al.* in [49], Beaty in [167] and [168], Stein in [163] and ion trap in this work.	46
3.4	Trap operation parameters and conditions (along axial direction) for our end cap trap geometry, $2z_o = 0.7$ mm, $2r_o = 1$ mm, $\theta_o = 45^o$, $\theta_i = 10^o$	50
4.1	Calculated values of Θ (bold) along with the values available from other calculations and the experimental results [170].	58
4.2	Fractional shifts due to the systematic effects for the E2 and E3-transitions. The shifts are estimated at the room temperature T = 300 K, rf phase difference $\phi_o = 0.05$, stray electric and magnetic fields $E_p = 20$ mV/mm and $B = 1$ μT. Numerical values of ϕ_o, E_p and B which are used here are typical values that can be achieved with proper minimization techniques.	65

5.1	Electrical, thermal, mechanical and chemical properties of machinable metals: Silver (Ag), Gold (Au), Aluminum (Al), Tantalum (Ta), Titanium (Ti), Tungsten (W), Oxygen free high thermal conductivity (OFHC) Copper, Molybdenum (Mo) and Beryllium-Copper (BeCu) [50].	75
5.2	Selected properties for common materials used for fabricating insulating spacers for the trap structure. These values have been taken from Ref. [189].	77
5.3	Properties of different viewports used along with their respective port numbers.	80
6.1	Peak to peak voltage, V_{PP}, at the trap electrodes for different quality factor, Q and input power, P_{in}. C_1, C_2, and C_3 represent the capacitive load of three different ion traps T_1, T_2 and T_3 respectively.	93
7.1	Optimized values of dimensions and separations of rectangular coils.	102
8.1	Details of DI/O and DG connections inside the breakout box.	119
8.2	Details of internal analog (AI/O) connections inside the breakout box.	119
8.3	Pattern of address and data bits in FRC	120
8.4	Function table for octal buffer SN74HCT541N IC.	121

Chapter 1

Introduction

Various precision experiments investigate charged particles, for that they need to be confined and suspended in a small space. Ion traps have been a great tool for fulfilling this requirement for over half a century for different applications. An ion trap is basically a tool which makes use of electric or magnetic fields to couple with charged particles and capture them. These confined charged particles are further probed for analyzing their masses, manipulating and controlling their quantum states, measuring their atomic transition frequencies to develop atomic clocks, measuring magnetic fields etc. In mass spectrometry, ion traps are used to for sorting ions on basis of their mass-to-charge ratio. The electric and magnetic fields of the trap are used to control the speed of ions and their deflection whose magnitude depends on its mass-to-charge ratio. Ion traps are used in mass separators such as ISOLDE (Isotope mass Separator On-Line facility) at CERN, Geneva is used by various experiments in fields of astrophysics, materials and life sciences etc [1].

One of the most widely researched application of ion traps worldwide is of building quantum computers. Ions confined using electromagnetic traps store qubits in their stable electronic states. Unlike classical computers which encode information in bits, having value of 1 or 0, quantum computers are based on bits which can represent both 0 or 1 at same time known as qubits. Each ion stores a single qubit. If an ion is considered as a magnet with one of its pole aligned UP to represent stored value 0, or DOWN to represent a stored 1, we notice that these magnets can point not only UP or DOWN, but also in other directions such as sideways. This quantization of spin-pointing allows to manipulate the ions as quantum bits and thus allowing the register to store quantum superpositions of 0 and 1. Many groups all over the world from scientific as well as industrial community such as University of Oxford, UK [2], IonQ, Inc. co-founded by C. Monroe. at University of Maryland [3], research group at University of California [4] to name a few are working for not only quenching scientific curiosity but for making "out of the lab" quantum computers.

Many other precision experiments concerning basic physics use trapped ions. For example, measuring atomic parity non-conservation (APNC) due to exchange of a boson between

electrons and nucleons can be measured with a single trapped ion [5]. Such experiments have been carried out with Ba^+ [6] and Ra^+ [7]. Measuring electric dipole moment with atomic and molecular ions, measuring electron-proton mass ratio with molecular ions [8] are some other experiments which make use of ion traps.

Ion traps also find an important application in optical clocks. An ultra narrow transition of a single ion is probed as clock by trapping it and freezing its motion. More recently, single trapped ion optical clock developed with $^{171}Yb^+$ has become the most accurate clock in the world [9]. In the following sections, details of basics of time keeping, frequency standards, optical clocks and their types have been given as the work done towards the development of precision ion trap in the course of this thesis extends its application in developing trapped ion optical frequency standard at CSIR-NPL, India.

1.1. Frequency Standards

One of the great mysteries for mankind has been "Time". Referred as fourth dimension, it has always spurred inquisitive questions in human mind because the other three dimensions which define space can be felt due to their physical nature. Interestingly, as per the popular book by Stephen Hawking, "A Brief History of Time", real time would have begun at a singularity at which the laws of physics would have broken down. Accountability of time was realized by mankind long ago, even the Indus valley civilization has a measure of time. The count of time (or frequency) and time keeping in ancient times were based on the observations of phenomena of the Earths rotation about its axis and around the Sun. Human civilization has come a long way in time and frequency measurements starting from solar, water, pendulum clock up to quartz crystal and atomic clock. Until 1967, time keeping was managed based on Earth's rotation phenomena. Accurate and stable time and frequency measurements contribute vitally to fields of advance technologies such as high speed communication, satellite based navigation, accurate targeting, time synchronization in different sectors. Many of the applied research areas such as mapping of the underground water or natural oil level in the Earth crust use atomic clocks. Weather forecast also relies on accurate time. Other than daily life applications, many advance physics problems [10], such as measuring temporal constancy of the fundamental constants due to an expanding universe like the fine structure constant $7.2973525664(17) \times 10^{-3}$ [11] or electron proton mass ratio [12], detection of the gravitational waves demand clocks with fractional accuracies better than 10^{-18} [10]. Frequency standards produce stable and well known frequencies with a given accuracy and provide references over a huge range of frequencies.

In principle, all time and frequency standards are referenced to a periodic event that repeats at a nearly constant rate. This periodic event is produced by an oscillator with resonant frequency f. The frequency, f, is the reciprocal of the period of oscillation, T; therefore

$f = 1/T$ and vice versa. Thus, a frequency standard needs a stable oscillator and a counter to count the number of oscillations. Stable oscillators can be realized in a number of ways with resonant frequencies depending upon geometries, dimensions and properties of medium etc. For example in oscillators such as quartz crystals, vibrating quartz plate defines the frequency of oscillation [13, 14]. These properties in turn are influenced by environmental parameters as temperature, air pressure, vibrations and gravity. Consequently, the stability of a resonance frequency of a macroscopic oscillator can be kept constant only to that extent to which these parameters can be precisely controlled. For improved stability of frequency standards, resonant transitions in atoms are used as oscillations. An unperturbed atomic transition is identical from atom to atom, so that, unlike a group of quartz oscillators, a group of atomic oscillators generate the same frequency [15]. An atom is a perfect pendulum whose oscillations can be used as a standard of frequency, or counted to measure time interval. Also, the influence of external parameters such as temperature, pressure, vibrations etc on such atomic frequencies is usually very small. An atomic clock can be defined as an oscillator whose frequency is locked to the resonance frequency of an atomic transition [16, 17].

Frequency standards are classified as primary and secondary standards. A primary standard in metrology is a standard that is sufficiently accurate such that it is not calibrated by or subordinate to other standards. Secondary standards are traceable to or derived from primary standards. Cesium atomic clock is a primary frequency standard in which electronic transitions between the two hyperfine ground states of ^{133}Cs atoms are used to control the output frequency. The definition of SI second is based on Cesium atomic frequency standards. Quartz oscillators, rubidium atomic clocks, optical frequency standards are secondary standards which are calibrated against Cesium atomic clocks. Atomic frequency standards are further classified as microwave frequency standards and optical frequency standards depending upon the clock transition frequencies of the atomic systems. In this context, it becomes necessary to mention that the stability of an atomic clock depends upon the ratio of its center frequency ν to the uncertainty in its frequency $\Delta\nu$. For a given value of $\Delta\nu$, the higher the center frequency, the better is the clock in terms of stability. The Allan Deviation (α) which is a measure of the frequency stability of clocks and oscillators is given as:-

$$\alpha = \frac{\Delta\nu}{\nu} \times \frac{1}{\sqrt{N \times \tau}} \tag{1.1}$$

where, α is the Allan deviation factor, N is the number of trapped species (atoms or ions) and τ is the interrogation time or the time interval up to which the trapped species are interrogated by a probe signal.

For microwave clocks such as the cesium atomic clock, the center frequency ν is of the order of 10^{10} Hz whereas visible light has a center frequency of 10^{14} Hz. Thus, the stability of an atomic clock increases by about four orders of magnitude for ultra narrow transitions

in the optical spectrum. From the Allan deviation, it is also clear that larger the number of trapped species and greater the time intervals over which they are interrogated, better is the clock stability. However, large number of trapped species lead to interactions and collisions among them. Likewise, if number of trapped species is too small(as in single ion optical clocks in which case N=1), one gets a poor signal to noise ratio. A microwave frequency standard has so far achieved its best fractional systematic accuracy $\Delta\nu = 1.1\times10^{-16}$ in ^{133}Cs fountain clock [18]. As the Allan Deviation reduces significantly when a frequency standard operates in the optical frequency regime, optical clocks tend to have a much higher accuracy than the microwave clocks and thus could lead to potential applications ranging from improved satellite navigation systems to testing of fundamental theories of physics. In future, these clocks can even lead to the redefinition of 1 second.[17, 19, 20].

1.2. Optical Atomic Clocks

There are two methods for realizing atomic frequency standards with use of optical transitions: Lattice clocks and Trapped ion clocks. Lattice clocks trap neutral atoms where as trapped ion clocks use a single confined ion for clock purpose.

1.2.1 Lattice Clocks

In an optical lattice clock, a large ensemble of laser cooled neutral atoms (typically 10^5) is held in a lattice trap made from two counter- propagating laser beams. The two laser beams interfere giving rise to a periodic intensity pattern which is seen as a periodic potential by the atoms. This potential can be controlled in depth and spacing by varying intensity and angle of laser beams, respectively. As large number of trapped atoms are being interrogated over a long period of time, lattice clocks have a very good signal to noise ratio. To perform a precision measurement, neutral atoms are laser cooled to sub mK temperature while being confined in optical lattices at the "magic-wavelengths". At these wavelengths, atoms are confined at the nodes of a standing wave produced by counter propagating laser beams. In this arrangement the interaction of the laser field with the induced dipole moment of the atoms gives rise to Stark shift of an energy level. However, at the magic-wavelength this shift at both of the energy levels associated to the clock transition cancel each other. As a result of that the absolute clock frequency remain unchanged due to electromagnetic field of the laser lights and that can be probed precisely. The Confinement of the atoms in optical lattices at the magic wavelengths and using them for the frequency standard was proposed by Katori *et al.* in 2003 [21]. Takamoto and Katori experimentally determined [22] the magic wavelength corresponding to the optical lattice clocks using the $^1S_0 - ^3P_0$ transition in ^{87}Sr and within a very short period of time the ^{87}Sr based lattice clocks were demonstrated in several laboratories [23]. So far three atomic species, strontium ^{87,88}Sr [24]-[30], ytterbium ^{171}Yb [31]-[37] and mercury ^{199}Hg [38]-[40] have

been demonstrated as frequency standards trapped in magic wavelength optical lattices.

1.2.2 Trapped Ion Optical Clocks

Optical clocks based on single trapped ions are realized by using coulombic interactions of the ionic charge with the electrodynamic field of the confining potential. A single ion is trapped and then laser-cooled [41]-[46] such that the ion is confined both in the position space as well as in the momentum space making it easier to interrogate over long periods of time. Single ion clocks are free from ion-ion interactions and also there are no frequency shifts via collisions. Ion clocks thus have a long term stability. However, as only one ion would be interrogated, the signal to noise ratio is lesser compared to that of lattice clocks. The ion is localized in a time averaged 3D quadrupole potential well which can be created using several trap geometries, namely, hyperbolic [47], linear [48], ring [43], end-cap [49, 50] traps. In this potential ion posses slow and harmonic secular motion which is temperature dependent and can be reduced by laser cooling. In addition, secular motion is modulated by virtue of rf trapping field. As a result of this the ion undergoes micromotion which is unavoidable, resulting excess energy to the ion and second order Doppler shift. Several other systematics include electric quadrupole shift which is dependent upon trapping potential and residual electric field in vicinity of the ion. These geometries do not only effect the profile of trapping potential but also relevance in terms of access of laser beams to the ions, phase difference among the rf potentials. The materials used for the construction of traps and mounting structure are selected carefully [50], since phenomena like temperature gradients, ohmic heating, patch potentials give rise to systematic effects like black body radiation (BBR), Doppler and Stark shifts, respectively. There are no intra-species collisional shifts as only a single ion is trapped in a quadrupole field providing an unperturbed environment for clock interrogation. As a result of long coherence time, it can be probed for long duration.

Many research groups have developed optical clocks worldwide. Table 1.1 summarizes all reported optical frequency standards based on the neutral atoms and ions. Recent observation of the optical transitions in ^{229}Th nucleus is a step forward for the construction of frequency standard where expected accuracy is $\simeq 10^{-21}$ [80].

1.3. Overview Of The Thesis

Optical atomic clock is an assembly of different building blocks which requires lots of machine design, vacuum technology, lasers and optics, data acquisition and electronics. Developing an atomic clock requires simulations of trap potential along with estimation of uncertainty resulting from different systematic effects. Its experimental setup consists of producing atoms inside ultra high vacuum (UHV) and ionizing them, trapping a single ion, fairly complex laser and optics assembly for photoionization, laser cooling, repump together with their power

Tab. 1.1: List of species that have been demonstrated as an optical frequency standards worldwide are shown with their reported fractional accuracies and frequency standards.

Species (Atom/ion)	Transition $\|g\rangle - \|e\rangle$	Wavelength λ [nm]	Standard Frequency ν_o [Hz]	Fractional Uncertainty [$\times 10^{-17}$]	Lab	Ref
^{24}Mg	$^1S_0$ - $^3P_0$	468.4	655 659 923 839 730(48)	7×10^3	PTB	[51]
			655 058 646 691 000(101000)	154×10^5	NIST	[52]
^{40}Ca	$^1S_0$ - $^3P_0$	657.0	455 986 240 494 144(5.3)	1.2×10^3	PTB	[53]
			455 986 240 494 135.8(3.4)	750	NIST	[54]
^{87}Sr	$^1S_0$ - $^3P_0$	698.4	429 228 004 229 873.65(37)[a]	0.21[b]	JILA	[55][a] [56][b]
			429 228 004 229 873.10(0.17)	31	SYRTE	[57]
			429 228 004 229 873.13(17)	3	PTB	[58]
			429 228 004 229 873.60(0.71)	160	NICT	[59]
			429 228 004 229 872.0(1.6)	370	NMIJ	[60]
			429 228 004 229 873.4(4)[a]	0.72[b]	RIKEN	[61][a] [30][b]
^{88}Sr	$^1S_0$ - $^3P_0$	698.4	429 228 066 418 009(32)	7×10^3	SYRTE	[24]
^{171}Yb	$^1S_0$ - $^3P_0$	578.4	518 295 836 590 865.2(0.7)[a]	0.2[b]	NIST	[62][a] [63][b]
			518 295 836 590 865.2(7)	140	NMIJ	[64]
			518 295 836 590 863.5(8.1)[a]	200[b]	KRISS	[65][a] [66][b]
^{199}Hg	$^1S_0$ - $^3P_0$	265.6	1 128 575 290 808 162.0(6.7)	570	SYRTE	[67]
			1 128 575 290 808 155.4(1.1)	7.2	RIKEN	[40]
^{27}Al$^+$	$^1S_0$ - $^3P_0$	267.4	1 121 015 393 207 857.4(7)[a]	0.86[b]	NIST	[68][a] [98][b]
^{40}Ca$^+$	$^2S_{1/2}$ - $^2D_{5/2}$	729.1	411 042 129 776 393.2(1.0)	240	SYRTE	[69]
			411 042 129 776 393.0(1.6)	390	NIM China	[70]
			411 042 129 776 398.4(1.2)	300	NICT	[71]
			-	7.7	Wuhan Institute of Physics and Mathematics	[72]
^{88}Sr$^+$	$^2S_{1/2}$ - $^2D_{5/2}$	674.0	444 779 044 095 486.71(24)	3	NPL UK	[73]
			444 779 044 095 485.5(9)	2.3	NRC	[74]
^{115}In$^+$	$^1S_0$ - $^3P_0$	236.5	1 267 402 452 900 967(63)	5×10^3	MPIQ	[75]
			1 267 402 452 901 049.9(6.9)	5×10^2	NICT	[76]
^{171}Yb$^+$	$^2S_{1/2}$ - $^2D_{3/2}$	435.5	688 358 979 309 307.82(36)	52	PTB	[77]
			688 358 979 309 308.42(42)	60	NPL UK	[78]
^{171}Yb$^+$	$^2S_{1/2}$ - $^2F_{7/2}$	467.0	642 121 496 772 645.150(1)	0.32	PTB	[9]
			642 121 496 772 644.91(37)	58	NPL UK	[78]
^{199}Hg$^+$	$^2S_{1/2}$ - $^2D_{5/2}$	281.6	1 064 721 609 899 145.30(69)	69	NIST	[79]

and frequency stabilization setups, high resolution imaging for detection of weak fluorescence, sub-Hz linewidth highly stabilized clock laser, controlling and acquiring data for using it as a frequency standard. This thesis discusses computations, design and instrumentation work done towards the development of trapped ($^{171}Yb^{+}$) optical frequency standard. This thesis has been focused on development of a suitable ion trap for performing precision experiment, building its vacuum housing, some of the important mechanical and electronics instrumental development associated to this experiment. Important results obtained during the work of this thesis are listed below:

- Single trapped ion optical clock activity at CSIR-NPL started with identifying the potential ionic species to carry out the experiment. For this several possible ionic species were considered and a feasibility study from both technical and scientific perspective was done.

- An end cap trap geometry is chosen for this experiment. The nature of the trapping potential is dependent on the trap electrode geometry. Numerical calculations for studying effects of geometry dependent trap potential in order to identify a suitable trap geometry is described in this thesis. Further dynamics of trapped ion in the potential are also studied and described.

- An atomic clock experiment is eventually a precision laser spectroscopy. In order to achieve the desired accuracy i.e. on the order of 1 part in 10^{-18}, one of the key steps is detailed estimation of the associated systematics. Some of these systematic effects are induced by the trap itself. Ion trap induced electric quadrupole shift, 2^{nd} order Doppler shift, 2^{nd} order Zeeman shift and Black Body Radiation shift are studied in this thesis work.

- The ion trap assembly which comprises of trap electrodes, its holders, isolators and mounting structure has to be fabricated such that it offers no obstruction to different laser lights impinged at ion sitting at trap center. Precision, symmetry, and machinability are some other important parameters which were optimized. As we are trapping only a single ion, ultra high vacuum (UHV) conditions is a vital necessity. We have designed a vacuum chamber taking into consideration UHV compatible materials, minimum outgassing, volume and different sets of optically accessible ports as required by the experiment.

- Helical resonator with a high quality factor at the desired rf frequency has been designed for delivering this high amplitude rf to the trap electrodes without problems of impedance mismatch and back reflection to the source. Characterization studies of helical resonator was done and trap impedance were calculated.

- Helmholtz coils has been designed to nullify stray magnetic fields in the vicinity of ion which induce 2^{nd} order Zeeman shift. These coils also solve purpose of axis quantization. Computer controlled stable current sources were also designed in house for driving current in these coils.

- An automated control and data acquisition system has been developed using amalgamation of indigenously designed hardware and a prototype version of the graphical user interface (GUI) to identify each of the numerous devices with a particular address, control and manipulate their inputs and acquire output data from them automatically in a predefined sequence.

The above mentioned results are described over different chapters in the following manner. Subsequent chapter 2 discusses various properties of candidate ions used all over the world for the single trapped ion clocks and compares them on the basis of major systematic effects which are directly related to the ion. In the 3rd chapter, trapping an ion within a Paul trap potential and its dynamics is discussed. Further discussion on the trapping potential in ideal and real experimental situations, perturbations of higher orders in analytical forms and their effects is done. Numerical simulations were performed for finding efficient trapping potential. Trapping potentials for different geometries of electrodes and the optimized results yielded by their comparisons are given. Optimized trap geometry was verified on basis of anharmonicities and ion micromotion. In next chapter, major systematic shifts like electric quadrupole, 2nd order Doppler, Zeeman, Stark shift are estimated. These are compared for E2 (at 435.5 nm) and E3 (at 467 nm) clock transitions to find the more accurate choice of the two. The next chapter, *i.e.* chapter 5 describes the constraints for designing ion trap structure, its various designs and finally fabricating ion trap structure with its advantages. It also describes the constraints, considerations and finally design of UHV chamber which houses the ion trap. Chapter 6 discusses need of resonator for efficient delivering rf to the ion trap. It further describes advantages of the helical resonator over traditional quarter wave coaxial resonator. The design, fabrication and results are discussed. Chapter 7 contains the simulation, design and fabrication details of Helmholtz coils built for the stray magnetic field cancellation. It also discusses design and development of computer controlled, low noise, stable current source for driving Helmholtz coils. This precision experiment demands continuous run without manual errors and disturbance. Therefore the plethora of electronics used in the whole experiment needs to be controlled remotely and automatically. An automated control and data acquisition system is developed with indigenous hardware and controlling GUI whose details are discussed in chapter 8. In the concluding chapter, *i.e*, chapter 9 the important observations/developments made in the thesis are summarized.

Chapter 2

Identifying suitable species for trapped ion clock

Optical clocks with trapped ions have already been developed across the world using different species of singly charged ions, with some of them giving best accuracies. Ionic species being trapped are specific for achievable stability and accuracy of the atomic clock experiment because several systematic effects like Electric quadrupole, Zeeman, Stark, Black body radiation effects etc. differ from species to species. So, the first step towards the trapped ion clock experiment is a qualified knowledge about the properties of various candidate ions. There are many ions which can be considered for the trapped ion clock and each of them have advantages and disadvantages if their systematic shifts and technical implementation challenges are considered. The motive behind this comparative study of different ions is not to find an ion with very small systematic shifts but also considering the precision with which these systematics can be determined.

2.1. Singly Charged Ionic Species For Optical Clocks

We review and compare the various ions which are used for establishing optical frequency standards all over the world. The list of ions in the forecoming text is in ascending order of their respective atomic weights. The potential atomic ions are categorized in the periodic table as group 13 elements: $^{11}B^+$,$^{27}Al^+$,$^{115}In^+$; alkaline-earth and their homolog elements: $^{40,43}Ca^+$, $^{88}Sr^+$, $^{137,138}Ba^+$, $^{171,172}Yb^+$, $^{199}Hg^+$, $^{205}Tl^+$ and $^{223-229}Ra^+$. Energy level diagram of all the mentioned ions except $^{205}Tl^+$, relevant to the frequency standard experiment, are shown in Fig. 2.1. Table. 2.1 summarizes some important spectroscopic information of selected ions. $^{205}Tl^+$ was proposed first for single ion optical clock [81, 82] but never got probed. The group 13 elements have $^1S_0$-$^3P_0$ ultra narrow hyperfine induced transitions which are free from linear Zeeman shifts. Also, these states are immune to electric quadrupole shift because of their zero quadrupole moments at both the clock states. Even though strong $^1S_0$-$^1P_1$ electric dipole transitions exist in these species, which are appropriate for laser cooling but in most cases they are in deep UV wavelengths where laser sources are not commercially available. To overcome this, researchers have implemented sympathetic cooling of the desired ions by using

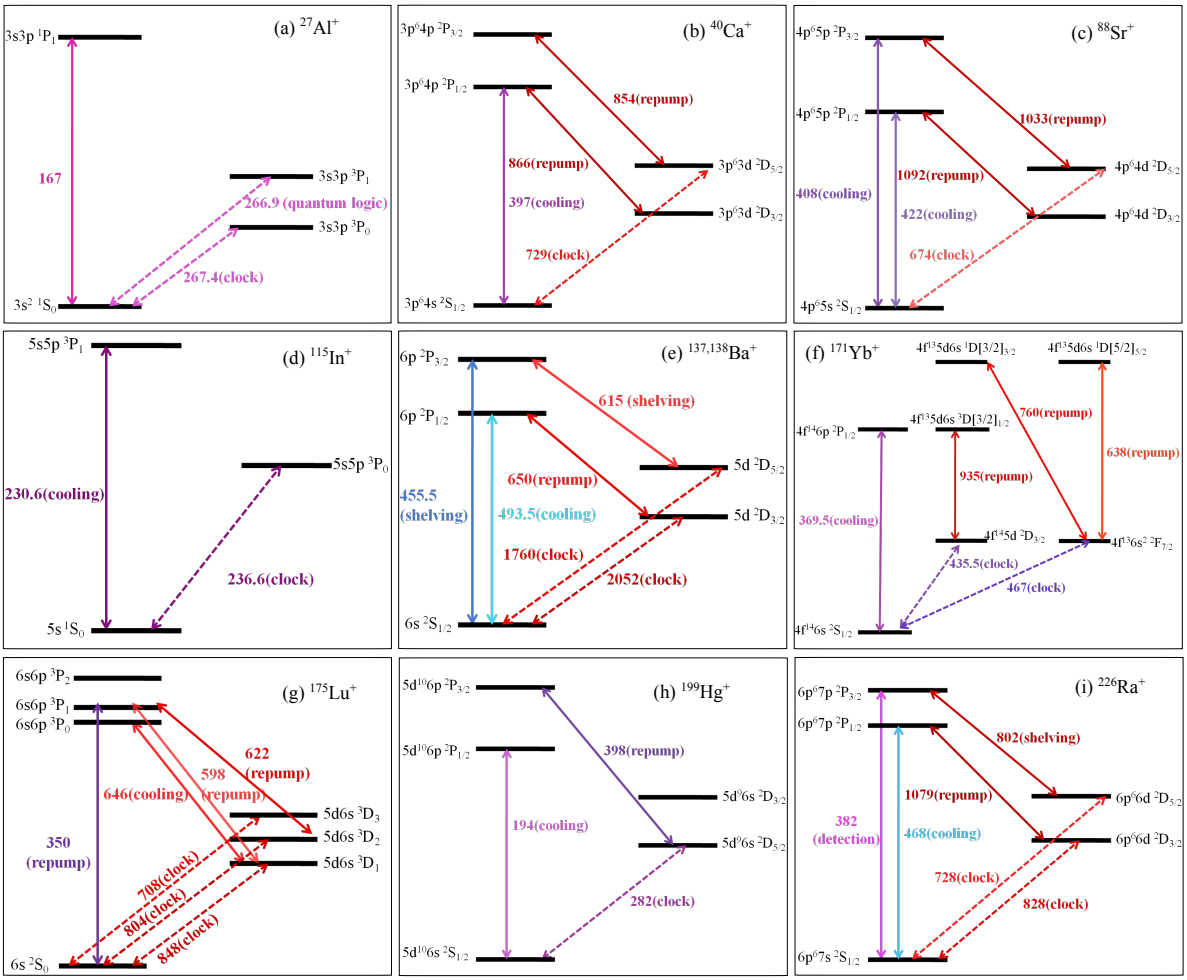

Fig. 2.1: Energy level diagrams of all atomic-ions that are used for optical clocks: (a) $^{27}Al^+$, (b) $^{40}Ca^+$, (c) $^{88}Sr^+$, (d) $^{115}In^+$, (e) $^{137,138}Ba^+$, (f) $^{171}Yb^+$, (g) $^{175}Lu^+$, (h) $^{199}Hg^+$, (i) $^{226}Ra^+$ ions. Dashed lines correspond to clock transition and the solid lines indicate cooling, repump, shelving.

other laser cooled species as a thermal reservoir. Direct florescence detection is also not viable for similar reasons thus quantum logic detection technique is used for them. Trapping of binary species and quantum logic detection altogether makes the experimental setup more complex. Although NIST USA and MPQ Germany have already demonstrated frequency standards with $^{27}Al^+$ and $^{115}In^+$, respectively. The ions in the alkaline-earth and their homolog group have electric quadrupole transitions with $^2S_{1/2}$ as ground state and $^2D_{3/2}$, $^2D_{5/2}$ as excited states. Only $^{171}Yb^+$ has an octupole transition connecting the ground state to a highly forbidden excited $^2F_{7/2}$ state with an ultra narrow linewidth of about 1 nHz. $^{171}Yb^+$ and $^{137}Ba^+$ also offer linear Zeeman free clock transitions whereas others lack in this. $^{171}Yb^+$, $^{88}Sr^+$, $^{40}Ca^+$ are technically easy to work with since all the lasers for photoionization, laser cooling, repumping and the clock transitions are in visible and near infrared wavelengths which are available off the shelves. Radium is radioactive but ^{226}Ra is commercially available since it has very long half life and a tiny amount of Ra is sufficient for single ion experiment.

In the following subsections, we will describe clock transitions, cooling scheme, merits and de-merits of each of the ionic elements as a frequency standards.

2.1.1 $^{27}Al^+$

Aluminium ion, $^{27}Al^+$ is fermionic and stable isotope. The hyperfine induced $3s^2\ ^1S_0|F = 5/2\rangle$-$3s3p\ ^3P_0|F = 5/2\rangle$ ultra narrow transition at wavelength 267 nm with natural linewidth of 8 mHz is one of the most accurate optical clock demonstrated by NIST, USA [98]. Because of spherically symmetric states with zero quadrupole moments, the clock transition is immune to lowest order electric quadrupole shift. Additionally the ion is less sensitive to external electric and magnetic fields except a small quadratic Zeeman shift due to its nuclear magnetic moment. The dominant systematics arise from residual micromotion and remnant secular motion [98, 68]. Despite these advantages, the strong $3s^2\ ^1S_0$-$3s3p\ ^1P_1$ transition suitable for laser cooling of the ion is at wavelength 169 nm which is in the UV regime and practically it is difficult to obtain a laser at this wavelength. Thus, sympathetic cooling technique [99] has been incorporated for cooling this ion. NIST group has devised sympathetic cooling scheme where a different ionic species with similar charge to mass ratio as that of the $^{27}Al^+$ is laser cooled and both of them are trapped together. This results to momentum transfer from $^{27}Al^+$ to the other species due to intra-species binary collisions. Here the cold cloud of other ionic species acts as a reservoir. Due to unavailability of the 267 nm light the fluorescence detection of the ion is also not possible. The reservoir ions, which are sometimes named as logic ion, not only provide sympathetic cooling but are also used for state preparation and detection of $^{27}Al^+$. The logic ions are cooled through conventional laser cooling method and is detected by the popular electron shelving technique. For an efficient energy transfer between spectroscopy ion and the logic ion, their masses must be comparable, hence, $^9Be^+$, $^{25}Mg^+$ and $^{40}Ca^+$ have been used.

Tab. 2.1: Spectroscopic information of the ions that are demonstrated as frequency standards. Symbols indicate: nuclear spin (I), wavelength (λ), natural linewidth of the transition (Γ), lifetime of the excited state (τ), saturation intensity (I_o), dynamic correction factor (η), Lande-g factor of the ground state (g_g) and excited state (g_e), quadratic Zeeman coefficient (κ_2), differential polarizabilities, scalar ($\Delta\alpha_S$) and tensorial ($\Delta\alpha_T$) and quadrupole moment (Θ) of the excited state associated to the clock transition.

Properties	$^{27}Al^+$	$^{40}Ca^+$	$^{88}Sr^+$	$^{115}In^+$	$^{171}Yb^+$	$^{199}Hg^+$
I	5/2	0	0	9/2	1/2	1/2
Clock:						
Transition 1	$3s^2\ ^1S_0$- $3s3p\ ^3P_0$	$4s\ ^2S_{1/2}$- $3d\ ^2D_{5/2}$	$5s\ ^2S_{1/2}$- $4d\ ^2D_{5/2}$	$5s^2\ ^1S_0$- $5s5p\ ^3P_0$	$4f^{14}6s\ ^2S_{1/2}$- $4f^{13}6s\ ^5F_{7/2}$	$5d^{10}6s\ ^2S_{1/2}$- $5d^96s^2\ ^2D_{5/2}$
Type	E1	E2	E2	E1	E3	E2
λ [nm]	267	729	674	236.5	467	282
Γ [Hz]	8×10^{-3}	0.2	0.4	0.82	1×10^{-9}	1.7
τ [s]	20	1.17	0.357	0.2	189216×10^3	90×10^{-3}
Transition 2					$4f^{14}6s\ ^2S_{1/2}$- $4f^{14}6s\ ^5D_{3/2}$	
Type:					E2	
λ [nm]					435.5	
Γ [Hz]					3	
τ [s]					50×10^{-3}	
Cooling:						
Transition	none	$4s\ ^2S_{1/2}$- $6p\ ^2P_{1/2}$	$5s\ ^2S_{1/2}$- $5p\ ^2P_{1/2}$	$5s\ ^1S_0$- $5s5p\ ^3P_1$	$4f^{14}6s\ ^2S_{1/2}$- $4f^{14}6s\ ^2P_{3/2}$	$5d^{10}6s\ ^2S_{1/2}$- $5d^{10}6p\ ^2P_{1/2}$
Type		E1	E1	E2	E1	E1
λ [nm]:		397	422	230.6	369.5	194
Γ [MHz]:		23	21.5	0.36	20	70
I_o [mW/cm^2]:		43.3	37.3	3.83	51	1252
Repump:						
Transition 1	none	$3p^6\ ^2D_{3/2}$- $3p^64p\ ^2P_{1/2}$	$4d\ ^2D_{3/2}$- $5p\ ^2P_{1/2}$	none	$4f^{14}5d\ ^2D_{3/2}$- $4f^{13}5d6s\ ^3D[3/2]_{1/2}$	none
Type		E1	E1		E1	
λ [nm]:		866	1092		935	
Γ [MHz]:		1.69	1.5		4	
Transition 2		$3p^6\ 3d^2D_{5/2}$- $3p^64p\ ^2P_{3/2}$	$4d\ ^2D_{5/2}$- $5p\ ^2P_{3/2}$		$4f^{13}6s^2\ ^2F_{7/2}$- $4f^{13}5d6s\ ^1D[3/2]_{3/2}$	
Type		E1	E1		E2	
λ [nm]:		854	1033		760	
Γ [MHz]:		1.58	1.38		4	
Transition 3					$4f^{13}6s^2\ ^2F_{7/2}$- $4f^{13}5d6s\ ^1D[5/2]_{5/2}$	
Type					E1	
λ [nm]:					638.6	
Systematics:						
g_g	$-0.00079248(14)$[83]	$2.00225664(9)$[84]	2.002[85]	-0.00066647[86]	E3:1.988(2)[87] E2:1.988(2)[87]	$2.0031745(74)$[88]
g_e	$-0.00197686(21)$[83]	$1.2003340(3)$[84]	1.2[85]	$-0.000987(50)$[86]	E3:1.145(2)[87] E2:0.802(2)[87]	$1.1980(7)$[88]
η	$< 10^{-4}$[89]	-	< 0.01[90]	$< 10^{-4}$[89]	E3:- E2:< 0.04[91]	-
$\Delta\alpha_S[10^{-41}\mathrm{Jm^2/V^2}]$	$0.82(8)$[89]	$-73.0(1.0)$[89]	$-47.938(71)$[90, 74, 92]	$3.3(3)$[89]	E3:13(6)[93] E2:$-69(14)$[94]	15[88]
$\Delta\alpha_T[10^{-41}\mathrm{Jm^2/V^2}]$	0	$-24.51(29)$[89]	$-78.6(5)$[90]	0	E3:1.3[93] E2:$-13.6(2.2)$[94]	-3[88]
Magic ω_{rf}[MHz]	-	24.54[72]	14.408[92]	-	≈ 38	
κ_2[MHz/T^2]	-72[95]	-	3.1[95]	-	E3:-1.7×10^3[95] E2:5.2×10^3	-1.9×10^4[95]
Θ[ea$_0^2$]	0.0	$1.83(0.01)$[96]	$2.6(3)$[97]	0.0	E3:$-0.041(5)$[93] E2:$2.08(11)$[94]	$-0.510(18)$[83]

NIST has developed a pair of frequency standards, out of them $^{27}Al^+$ NIST-Al-I [68] which uses $^{9}Be^+$ as logic ion and the other one NIST-Al-II [98] uses $^{25}Mg^+$ as the logic ion. Recently, PTB group has started working with $^{40}Ca^+$ [100] as logic ion. After being sympathetically cooled, $^{27}Al^+$ is excited at its clock transition. The "tick" in the clock operation is detected by "quantum logic" technique, which was originally proposed for quantum information processing and is also implemented here [101]. Quantum jump of $^{27}Al^+$ at clock transition is mapped onto the logic ion through quantum entanglement between the two ions. As a result of that the spin flipping of the logic ion either / or going to a dark state reflects whether or not the $^{27}Al^+$ was excited at the clock transition. To the best of our knowledge, currently PTB Germany and VU, Amsterdam, Netherlands are also engaged in building $^{27}Al^+$ ion clocks.

2.1.2 $^{40,43}Ca^+$

The stable isotope of Calcium, $^{40}Ca^+$, is fermionic in nature with nuclear spin I=0. The Calcium ion is devoid of any hyperfine structure, which provides a simpler closed laser cooling scheme consisting of three lasers. The required lights for laser cooling are in visible and near infrared wavelengths which are easily available from commercial diode and solid state laser systems. It has a quadrupole clock transition $3p^6 4s\ ^2S_{1/2}$-$3p^6 3d\ ^2D_{5/2}$ at wavelength 729 nm having natural linewidth of 0.2 Hz [102]. The laser cooling cycle constitutes, $3p^6 4s\ ^2S_{1/2}$-$3p^6 4p\ ^2P_{1/2}$, strong transition at wavelength 397 nm along with a pair of repumping transitions, $3p^6 3d\ ^2D_{3/2}$-$3p^6 4p\ ^2P_{1/2}$, $3p^6 3d\ ^2D_{5/2}$-$3p^6 4p\ ^2P_{3/2}$ at wavelength 866 nm and 854 nm, respectively. This clock was first demonstrated at University of Innsbruck [69] and then two other groups at the Wuhan Institute of Physics and Mathematics in China [70, 72, 103, 104] and NICT Japan [71] have also reported the clock interrogation of this isotope and all the three results reported are in good agreement. The clock at NICT was improved by two orders of magnitude [71] from its first version [105] by implementing photoionization process which decreased collection of space charge near the ion and also increases ion production efficiency, reducing the stray electric fields by 20 times. Unlike $^{40}Ca^+$, the bosonic isotope $^{43}Ca^+$ has a complex hyperfine structure with a large number of sublevels due to its nuclear spin I=7/2 [106]. This ion provides an electric quadrupole transition $4s\ ^2S_{1/2}|F=4, m_F=0\rangle$-$3d\ ^2D_{5/2}|F=6, m_F=0\rangle$ which has been demonstrated as frequency standards by Champenois group at the University of Florence, France [107]. This transition has a high short term stability as proposed by Kajita *et al.* [108]. But the large number of hyperfine sublevels results in a very complicated laser cooling scheme which is practically very challenging to implement. The performance of the $^{40}Ca^+$ clock is limited by systematic associated to non zero quadrupole moment, linear Zeeman and Doppler shifts. Cancellation of the linear Zeeman shift which arises due to non zero magnetic moments of the clock states is very important for an accurate $^{40}Ca^+$ clock. Hence nullifying of the stray magnetic field at the ion position and averaging of the frequencies measured at a

constant magnetic field between different pairs of hyperfine sublevels of the clock states plays an important role for the accuracy of $^{40}Ca^{+}$-ion clock. Both fermionic and Bosonic $^{40,43}Ca^{+}$ have the advantage of negative scalar differential polarizability [109, 110]. So far, the best reported optical frequency standard of $^{40}Ca^{+}$ is 7.7×10^{-17} by Wuhan Institute of Physics and Mathematics in China[72].

2.1.3 $^{88}Sr^{+}$

Strontium has fermionic $^{88}Sr^{+}$ and a bosonic $^{87}Sr^{+}$ isotopes which are stable in nature. $^{87}Sr^{+}$ has nuclear spin, I=9/2 thus it facilitate a clock transition which is free from linear Zeeman shift. However owing to its complicated hyperfine structure [111], implementation of a closed laser cooling cycle is a major challenge. Also, optical pumping to a desired m_F level associated to the clock transition is not very efficient due to large number of hyperfine sublevels in this isotope. Therefore the current research focuses over the even isotope of the Strontium ion which does not have hyperfine sublevels but lacks of a $m_F = 0$ to $m_F = 0$ linear Zeeman free clock transition. To overcome this drawback the clock transition is being probed in presence of weak magnetic field between each allowed pair of Zeeman sublevels between the clock states and averaged them to obtain the 1^{st} order magnetic field unperturbed transition frequency. In a good experimental condition, when stray magnetic fields are cancelled and there is negligible magnetic field fluctuations from shot-to-shot, the linear Zeeman shift for two opposite pairs of magnetic sublevels cancels each other by this averaging technique. The ion is laser cooled at the strong $^2S_{1/2}$-$^2P_{1/2}$ transition having wavelength 422 nm. The excited state of the cooling transition decays to the $^2D_{1/2}$ and $^2D_{5/2}$ states which are repumped using a pair of lasers at the wavelengths 1092 nm and 1033 nm, respectively. Strontium-ion clocks are developed by NPL UK [112] and NRC Canada [113]. The additional benefit of negative differential scalar polarizability in this transition further facilitates mutual cancellation of scalar Stark effect and second order Doppler effect at trap frequency of about $\simeq$ 14.4MHz [74, 92, 114]. The best frequency standard with this is reported by NRC Canada with a fractional accuracy of 1.2×10^{-17} [92].

2.1.4 $^{115}In^{+}$

Indium $^{115}In^{+}$, is radioactive with a half life of 4.41×10^{15} years and is fermionic in nature with a nuclear spin, I=9/2. It has a hyperfine induced clock transition $5s^2\ ^1S_0|F = 9/2\rangle$-$5s5p\ ^3P_0|F = 9/2\rangle$ at wavelength 236.6 nm which has a natural linewidth of 0.82 Hz. This transition is highly immune to electric quadrupole effect, also, the second order Doppler and Stark effects are at mHz level when the ion is laser cooled [86]. A dominant linear Zeeman shift appears as the g factor deviates due to the admixture of the other excited states to the $^3P_0$ state [115]. Although, many of the systematic effects are reduced in Indium-ion but linewidth of the

laser used for probing the clock transition needs to be produced by quadrupuling of a laser at wavelength 946.4 nm. Laser cooling of $^{115}In^{+}$, at the strong $5s^2\ ^1S_0 - 5s5p\ ^1P_1$ transition at wavelength 159 nm is not possible due to unavailability of the laser light at this wavelength [116]. However the laser cooling was demonstrated at the weak $5s^2\ ^1S_0 - 5s5p\ ^3P_1$ inter-combination transition at wavelength 230.6 nm which provides nearly two level closed cooling cycle [116]. Unlike $^{27}Al^{+}$ the allowed laser cooling using a single light is advantageous in $^{115}In^{+}$. However the cooling light at 230.6 nm needs to be produced by quadrupuling of a laser at wavelength 922.4 nm, which is technically challenging. Production of stable clock and cooling lasers require heroic effort for using them in a frequency standard experiment. Indium ion optical frequency standard has been demonstrated by MPQ Germany [117, 118] and University of Washington, USA, [119]. Currently researchers are working towards achieving a fractional accuracy of 10^{-18} with $^{115}In^{+}$ frequency standards by implementing quantum logic spectroscopy by using a binary mixture of ions. As for example PTB Germany is using $^{172}Yb^{+}$ [120] and NICT, Japan is using $^{40}Ca^{+}$ [121] as logic ions for sympathetic cooling, state preparation and detection of the clock transition. The best accuracy achieved so far with this ion is 5×10^{-15} at NICT Japan [76].

2.1.5 $^{137,138}Ba^{+}$

Barium, $^{137}Ba^{+}$ is a stable bosonic isotope consisting of an electric quadrupole transition $6s\ ^2S_{1/2}|F = 2, m_F = 0\rangle$-$5d\ ^2D_{3/2}|F = 0, m_F = 0\rangle$ at wavelength 2051 nm having a linewidth of 13 mHz. The nuclear spin I=3/2 of this isotope felicitates linear Zeeman free clock transition. This isotope of Barium is also immune to the electric quadrupole shift as the ground state $S^{1/2}|F = 2, m_F = 0\rangle$ acquires zero electric quadrupole moment and the 6j-symbol that appears in the quadrupole shift Hamiltonian [122] becomes zero for the excited state $D_{3/2}|F = 0, m_F = 0\rangle$, even though it has non zero quadrupole moment [119]. Laser cooling of $^{137}Ba^{+}$ occurs on $6s\ ^2S_{1/2}$-$6p\ ^2P_{1/2}$ transition at wavelength 493.5 which is produced by doubling a 986 nm light. The excited state of the cooling transition decays to the long lived $D_{3/2}$ state with lifetime $\approx$ 80 s, therefore, a repumping light at wavelength 650 nm is required to drive $5d\ ^2D_{3/2}$-$6p\ ^2P_{1/2}$ transition. The electron shelving $6s\ ^2S_{1/2}$-$6p\ ^2P_{3/2}$ and de-shelving $5d\ ^2D_{5/2}$-$6p\ ^2P_{3/2}$ transitions at wavelengths 455.5 nm and 615 nm, respectively are driven during clock operation with the trapped and laser cooled ion. University of Washington, USA has been working towards the Barium ion frequency standard with its transition at wavelength 2051 nm [119]. The other isotope of Barium, $^{138}Ba^{+}$ which is fermionic in nature with a nuclear spin $I = 0$ offers a pair of electric quadrupole transition, $6s\ ^2S_{1/2}$-$5d\ ^2D_{5/2}$ and $6s\ ^2S_{1/2}$-$5d\ ^2D_{3/2}$ at wavelength 1760 nm [123, 124, 125] and 2051 nm [126], respectively, which have potential for probing fundamental physics through precision measurements [127, 128]. As for example the 2051 nm transition is suitable for measuring atomic parity non-conservation [5, 6, 129]. This ion also facilitates cancellation of micromotion based scalar Stark shift and second order

doppler shift due to negative differential scalar polarizability [130]. An absolute frequency measurement experiment has also been done relative to Cs primary frequency standard at 24 012 048 319 ± 1 KHz at NRC Canada [131].

2.1.6 $^{171,172}Yb^{+}$

Lanthanide species Ytterbium has fermionic $^{172}Yb^{+}$ and bosonic $^{171}Yb^{+}$ isotopes which are potential for frequency standards. The odd isotope has $I = 1/2$ which facilitates 1^{st} order Zeeman insensitive clock transition which makes this isotope more attractive in particular to the frequency standard. Ytterbium-ion offers three transitions which are suitable for clocks: a pair of narrow quadrupole transitions $4f^{14}6s\ ^2S_{1/2}|F = 0, m_F = 0\rangle$-$4f^{14}5d\ ^2D_{3/2}|F = 2, m_F = 0\rangle$ and $4f^{14}6s\ ^2S_{1/2}|F = 0, m_F = 0\rangle$-$4f^{14}5d\ ^2D_{5/2}|F = 2, m_F = 0\rangle$ at 436 nm and 411 nm, respectively and an ultra narrow octupole transition $4f^{14}6s\ ^2S_{1/2}|F = 0, m_F = 0\rangle$-$4f^{13}6s^2\ ^2F_{7/2}|F = 3, m_F = 0\rangle$ at wavelength 467 nm. The transition at wavelength 411 nm has a natural linewidth of 22 Hz which is very large compared to 3 Hz and 1 nHz for the transitions at wavelengths 436 nm and 467 nm, respectively. Even though the octupole clock transition has ultra-narrow natural linewidth owing to a high quality factor of the frequency standard but in practice the accuracy is limited to linewidth of the probe laser driving this transition. Also, $^2D_{5/2}$ state decays to a lower lying long lived $^2F_{7/2}$ state. Both the transitions at 436 nm and 467 nm are preferred for clock and has been demonstrated as frequency standards by PTB Germany [77] and NPL UK [132]. The transition quadrupole 436 nm also posses an added benefit of negative differential polarizability as measured by PTB group [94] which can be used to cancel quadratic scalar Stark and second order Doppler. The strong electric dipole transition, $4f^{14}6s\ ^2S_{1/2}$-$4f^{14}6p\ ^2P_{1/2}$ at wavelength 369.5 nm is used for laser cooling of the ion. The excited $^2P_{1/2}$ radiatively decays to the metastable $^2D_{3/2}$ state and ion there cascades further to the low-lying $^2F_{7/2}$ state which has a lifetime of years, despite lacking any direct transition. To obtain a closed laser cooling scheme, a pair of repump lasers at wavelength 935 nm and 639 nm or alternatively 935 nm and 760 nm are used to drive the $4f^{14}5d\ ^2D_{3/2}$-$4f^{13}5d6s\ ^3D[3/2]_{1/2}$, $4f^{13}6s^2\ ^2F_{7/2}$-$4f^{13}5d6s\ ^1D[5/2]_{5/2}$ and $4f^{13}6s^2\ ^2F_{7/2}$-$4f^{13}5d6s\ ^1D[3/2]_{3/2}$ transitions. The lasers at different frequencies which are separated by few GHz are required to repump from all the hyperfine sublevels of the ion. As for example the $4f^{14}6s\ ^2S_{1/2}|F = 0\rangle$ ground state gets populated due to the presence of the laser driving the cooling transition at 369.5 nm, which requires a repump laser for driving the $4f^{14}6s\ ^2S_{1/2}|F = 0\rangle$-$4f^{14}6p\ ^2P_{1/2}|F = 1\rangle$ transition and that is 12.7 GHz blue detuned from the cooling light. Similarly, other lasers for repumping atoms from the D and F states are also required at pair of different frequencies. The octupole transition has been probed by NPL UK [132] and PTB Germany [93] that are two pioneering groups in atomic clocks and their reported results are in good agreement. More recently, $^{171}Yb^{+}$ clock based on its octupole transition has reached to a fractional accuracy of 3×10^{-18}

[9] which is about three times better than the alumunium-ion quantum logic clock at NIST USA [98] and almost comparable to the best optical frequency standard reported so far [63].

2.1.7 $^{175}Lu^{+}$

Most recent entry in list of atomic-ion frequency standards is Lutetium, $^{175,176}Lu^{+}$ which is last member in Lanthanide series and has two isotopes with masses 175 and 176. The $^{175}Lu^{+}$ is fermionic in nature with I=7/2, is proposed for frequency standards [133, 134, 135]. This isotope offers three narrow clock transitions $4f^{14}6s\ ^{1}S_0 - 5d6s\ ^{3}D_1$, $4f^{14}6s\ ^{1}S_0 - 5d6s\ ^{3}D_2$ and $4f^{14}6s\ ^{1}S_0 - 5d6s\ ^{3}D_3$ at wavelengths 848 nm, 804 nm and 708 nm, respectively [136]. Out of these, the transition at 848 nm is a highly forbidden magnetic dipole transition having ultra narrow natural linewidth, since the excited state has lifetime of 60 hours approximately [137]. In order to implement laser cooling, $^{175}Lu^{+}$ offers a narrow linewidth cyclic transition $5d6s\ ^{3}D_1 - 6s6p\ ^{3}P_0$ at wavelength 646 nm. Three repump lasers at the wavelengths 350 nm, 622 nm and 598 nm are required to put the ion back into the cooling cycle. The 848 nm clock transition was estimated to be free from electric quadrupole shift owing to zero atomic quadrupole moments for excited $^{3}D_1$ state and $^{1}S_0$ ground state [138] but very recently Barret group at NUS Singapore has reported very small ($\approx$ 1Hz) quadrupole shift measured experimentally [139]. Although, initially differential static polarizability for $^{1}S_0$-$^{3}D_1$ was estimated to be sufficiently small for practical room temperature operation and negative by Kozlov *et. al* as in [138], allowing micro-motion shifts to be eliminated at a trap frequency estimated to be around 23 MHz ("magic rf") [134], But recent studies [135] and measurements [139] done by Barret group doubt this possibility. Reason being currently indeterminate sign of differential static polarizability. Barret group at NUS Singapore is currently performing further measurements using high resolution laser spectroscopy of $^{175}Lu^{+}$ to acquire the required atomic structure information towards developing the first optical frequency standard with its 848 nm transition.

2.1.8 $^{199}Hg^{+}$

The bosonic isotope of the Mercury ion, $^{199}Hg^{+}$ has a nuclear spin of I=1/2 and does not posses any hyperfine structure which makes the energy level structure much simpler as compared to Ytterbium-ion. The $^{199}Hg^{+}$ optical clock has been developed at NIST USA, [140, 141], The ion has an electric quadrupole $5d^{10}6s\ ^{2}S_{1/2}|F = 0, m_F = 0\rangle$-$5d^{9}6s^{2}\ ^{2}D_{5/2}|F = 2, m_F = 0\rangle$ transition at wavelength 282 nm having natural linewidth 1.7 Hz which is suitable for clock. The strong $5d^{10}6s\ ^{2}S_{1/2}$-$5d^{10}6p\ ^{2}P_{1/2}$ transition at wavelength 194 nm is used for laser cooling of the ion and a 6.4 GHz frequency shifted cooling light is used for hyperfine repump. The excited state of the cooling transition decays to the low lying metastable $5d^{9}6s^{2}\ ^{2}D_{5/2}$ state. A laser at wavelength 398 nm is required to depopulate this state and to obtain a closed cooling

cycle. Mercury-ion optical frequency standard is developed at NIST USA within cryogenic environment at liquid Helium temperatures which reduces the systematics due to the Black body effects. Although, incorporating a cryostat to a complex ion trap experiment is nontrivial but it reduces the dominant BBR shift and also it helps to prevent collisional loss of ion from the trap due to ultra high vacuum. The clock transition is free from linear Zeeman effect but suffers from quadratic Zeeman and Stark effects. The remaining shift is the electric quadrupole shift due to D state quadrupole moment. The elimination of this shift by the angular averaging technique, was implemented for the first time in this experiment [88]. Ion micromotion detection and minimization was also proposed [142] for the first time for this ion. So far the best reported frequency standard on this is 1 064 721 609 899 145.30(69) Hz with a fractional accuracy of 6.9×10^{-16} [79].

2.1.9 $^{A}Ra^{+}$

Radium is a radioactive element which has various isotopes. The lighter isotopes $^{209-214}$Ra are highly radioactive and they have half lives of 3 s - 3 min. The heavier isotopes have half lives ranging from few minutes to few thousand years such as, ^{223}Ra: 11.4 d, ^{224}Ra: 3.6 d, ^{225}Ra: 14.9 d, ^{226}Ra: 1600 y, ^{227}Ra: 42.2 min and ^{229}Ra: 4 min. The odd isotopes have half integer nuclear spins such as $^{225}Ra^{+}$ has I=1/2, $^{223,227}Ra^{+}$ has I=3/2, $^{229}Ra^{+}$ has I=5/2 which offers linear Zeeman free clock transitions and the even isotopes have I=0. Smaller systematic effects on the clock transitions make this ion attractive for the frequency standards, which has been estimated by Versolato *et al.* in Ref. [143]. Different spectroscopic experiments and studies for *e.g.* hyperfine structures of Radium isotopes [144], lifetimes of Radium isotopes [145], isotope shifts [146] have been performed for finding suitable Radium isotope in particular to single ion clock. Out of all these isotopes, $^{226}Ra^{+}$ is experimentally more viable for an optical atomic clock since bulk of that is commercially available and does not require elaborate production facility through nuclear reactions. It has a pair of electric quadrupole clocks transitions $7s\ ^2S_{1/2}$-$6d\ ^2D_{5/2}$ and $7s\ ^2S_{1/2}$-$6d\ ^2D_{3/2}$, at the wavelengths 728 nm and 828 nm, respectively which have natural linewidths of 0.53 Hz and 0.25 Hz, respectively. This ion can be laser cooled using the strong electric dipole transition $7s\ ^2S_{1/2}$-$7p\ ^2P_{1/2}$ at the wavelength 468 nm. The excited state decays to the lower lying $6d\ ^2D_{5/2}$ state which requires a repump laser at the wavelength 1079 nm to drive the $6d\ ^2D_{3/2}$ - $7p\ ^2P_{1/2}$ translation. For probing the $7s\ ^2S_{1/2}$ - $6d\ ^2D_{5/2}$ clock transition through electron shelving technique, light at 802 nm is required for de-shelving the ion through $6d\ ^2D_{5/2}$ - $7p\ ^2P_{3/2}$ transition which allows a background free detection of the $7p\ ^2P_{3/2}$-$7s\ ^2S_{1/2}$ fluorescence photons at 382 nm. The laser and optics are technically feasible to setup since all the lasers are available off-the-shelf. It posses negative differential scalar polarizability [130] but the magic wavelength can not be practically implemented ($>$ 3000 GHz). Apart from optical clocks, radium-ion is attractive for probing fundamental sciences, as for example, both of

the clock transitions have high sensitivity towards variation of the fine structure constant [147]. Also atomic parity non conservation (APNC) is strongly enhanced in Ra-ions which is 50 times larger than that in Caesium atoms [7]. Radium makes an excellent candidate for measuring APNC in single trapped ion [148]. Ion clock with Radium species is being developed at KVI, Netherlands [143]. Recently, high resolution spectroscopic measurement have been reported for $^{212-214}Ra^{+}$ with multiple ions trapped in rf trap [149].

2.2. Systematic Shifts Associated To Ionic Species

In this section, we shall discuss major systematic effects which are directly related to the ion and its interaction environment like Electric quadrupole, Doppler, Stark and Zeeman for different ions.

- **Electric quadrupole shift:** which is one of the dominant shifts in trapped ion clocks is caused by interaction of electric field gradient,∇E with the electronic quadrupole moment of the species, $\Theta(\gamma, J)$ of a particular energy state having spectroscopic notation γ and total angular momentum quantum number J, gives rise to energy shift of that state. The reduced form of this interaction hamiltonian can be written as

$$\begin{aligned} \langle \gamma J F m_F | H_Q | \gamma J F m_F \rangle &= \Theta(\gamma, J)\, \mathcal{F}_Q(I, J, F, m_F) \\ &\quad \sum_{q=-2}^{2} \nabla E_q D_{0q}, \end{aligned} \tag{2.1}$$

  where the quadrupole moment operator Θ and electric field gradient ∇E are tensors of rank two, D_{0q} are rotation matrix elements for projecting components of the electric field gradient from the principle axes frame. And $\mathcal{F}_Q$ depend upon 3-j, 6-j coefficients, total angular momentum, F and magnetic quantum number m_F. Details of this shift are given in chapter 4. Quadrupole moment, Θ values for different species are listed in Tab. 2.1 using which we compare the quadrupole shifts for each ion. The comparison is done for a constant electric field gradient 1000 V/cm^2 and is shown in Fig. 2.2. Clearly, this plot shows the maximum shift of ≈ -36 Hz is for $^{226}Ra^{+}$ and zero shift for and $^{27}Al^{+}$,$^{115}In^{+}$, $^{137}Ba^{+}$,$^{175}Lu^{+}$. There are three different ways for elimination of this [88]. Off these, in the popular method, the clock transition frequency is measured when the ion is subjected to quantization axes along three mutually orthogonal directions by using exactly equal magnetic fields. This method has been verified experimentally with $^{88}Sr^{+}$ [112], $^{171}Yb^{+}$ [94] and $^{199}Hg^{+}$ [140, 141].

- **Micromotion shifts: Stark and Doppler** Electric fields influence the clock frequency as they affect the atomic energy levels through the Stark effect. DC or AC electrical fields from quiet a few sources can induce such shifts on the clock transition namely

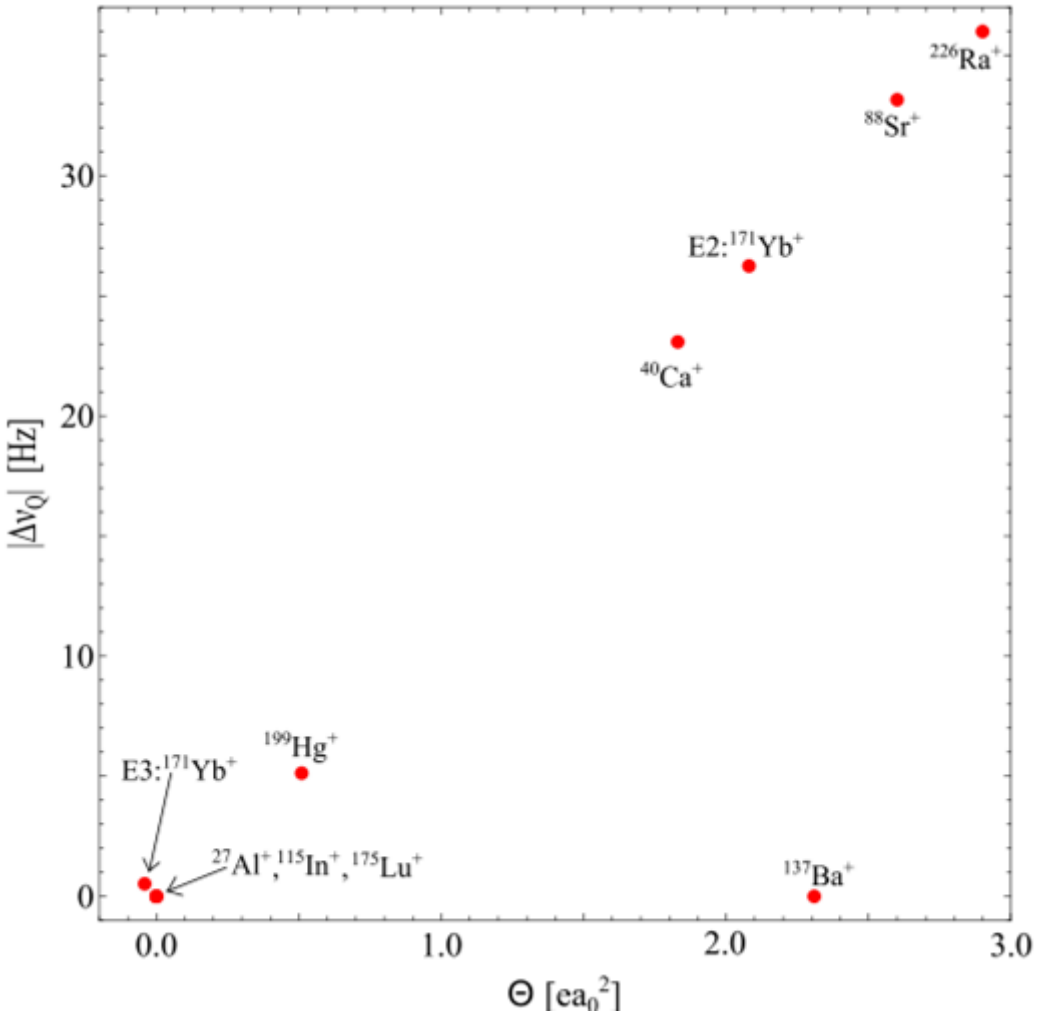

Fig. 2.2: Electric quadrupole shift $\Delta\nu_Q$ with respect to quadrupole moments of different ion species. The quadrupole moment of $^{175}Lu^+$ is taken from [138], however, it is discussed in sec. 2.1.7 that there is a small quadrupole shift.

stray static fields, rf fields for trapping ions, blackbody radiation and electric fields from probe lasers. Due to absence of a permanent electric dipole of ion, the first order Stark effect is zero thus it is generally called quadratic or second order Stark effect. In a transition, energy of both clock levels is shifted thus the transition frequency is shifted by the differential shift. The quadratic Stark shift for a transition is contributed from two terms, one depending upon scalar differential polarizability, $\Delta\alpha_s$ and second term which is dependent upon the tensor differential polarizability, $\Delta\alpha_T$. There also exists a vector component of differential polarizability whose contribution is zero due to use of linearly polarized light in the experiment [91].

$$\frac{\Delta\nu_s}{\nu_o} = -\frac{1}{2h}\left[\Delta\alpha_s + \Delta\alpha_T\right]\langle E^2\rangle \tag{2.2}$$

where, $\langle E^2\rangle$ has different form for different sources. For Stark effect caused by rf fields, $\langle E^2\rangle$ is the time averaged electric field and takes the form

$$\langle E^2\rangle = 2\left(\frac{m\omega_{rf}^2 c}{e\Omega_o}\right)^2 \sum_{x,y,z} R_i \tag{2.3}$$

h is plank's constant, m is mass of the ion, $2\pi\Omega_o{=}\nu_o$ is probe laser frequency, and R_i is the carrier-to-sideband intensity ratio of a Zeeman component.

Electromagnetic radiation from probe laser interacting with the ion causes ac Stark shifts of the clock transition during the probing period. For light induced ac Stark shift $\langle E^2\rangle{=}I/c\epsilon_0$, with I being the intensity of light. Interestingly, the tensor part of quadratic Stark shift which has the same dependence upon m_F^2 and the orientation of principal axis with respect to quantization axis, is cancelled by the averaging method used for cancellation of electric quadrupole shift [74]. This cancellation of tensor component of Stark effect is species independent. The rf field induced Stark shift can be eliminated for few ions belonging to the alkaline earth group on account of their negative differential scalar polarizabilities, $\Delta\alpha_s < 0$. For example ions with $^2S_{1/2}$-$^2D_{5/2}$ transitions $^{40,43}Ca^+$ [109, 110], $^{88}Sr^+$[74, 92], $^{138}Ba^+$[130], and $^{225}Ra^+$[130]. Quadrupole transition, $^2S_{1/2}$-$^2D_{3/2}$ of $^{171}Yb^+$ [94] has also shown this property. With negative $\Delta\alpha_s$, the scalar part of quadratic Stark effect and Second order doppler shifts (micromotion shifts) can be cancelled with each other at a particular trap drive frequency, ω_{rf}. The motion of the ion produces a relativistic Doppler shift in the frequency observed in the laboratory frame. The dominant second order doppler shift is given as

$$\frac{\Delta\nu_{D2}}{\nu_o} = -\frac{\langle v^2\rangle}{2c^2} \tag{2.4}$$

where, $\langle v^2 \rangle$ is the mean squared velocity of the ion. It is contributed by thermal secular motion as well as micromotion. In terms of R_i, fractional shift can be written as

$$\frac{\Delta\nu_{D2}}{\nu_o} = -\left(\frac{\omega_{rf}}{\Omega_o}\right)^2 \sum_{x,y,z} R_i \tag{2.5}$$

If we observe shifts associated to micromotion, i.e., ω_{rf} generated scalar Stark shift and the second order Doppler shift due to micromotion, we observe that they both are originated from same electric field and can written in combination using Eq. 2.2 and 2.5 as $\Delta\nu_{micro}/\nu_o$:

$$\frac{\Delta\nu_{micro}}{\nu_o} = -\left(\frac{\omega_{rf}}{\Omega_o}\right)^2 \left[1 + \frac{2\pi\Delta\alpha_s}{h\Omega_o}\left(\frac{m\omega_{rf}c}{e}\right)^2\right] \sum_{x,y,z} R_i \tag{2.6}$$

The term in square brackets vanish for ions with negative $\Delta\alpha_s$ at a particular driving frequency, fondly called "magic rf", $\omega_{rf} = e/mc\sqrt{-h\Omega_o/2\pi\Delta\alpha_s}$. From this expression, it can clearly be seen that magic ω_{rf} is imaginary for positive values of $\Delta\alpha_s$, but for negative $\Delta\alpha_s$ magic driving frequency possesses a real value.

- **Black body radiation shift:** The temperature of surfaces (both conductors and dielectrics) in the vicinity of the trap get heated due to high rf voltages and emit black body radiation. The electric field of this radiation gives rise to a type of dc Stark shift also known as Black body radiation (BBR) shift. The tensor component is averaged out as mentioned earlier and scalar part of this shift follows form as given in Eq. 2.2. The radiation emitted by a black body at thermal equilibrium follows Planks radiation law and the average electric field is given by

$$< E^2 >= \left(831.9V/m\right)^2 \times (T/300)^4 \tag{2.7}$$

The differential polarizability $\Delta\alpha_s$ is substituted by $\Delta\acute{\alpha}_s = (1+\eta)\Delta\alpha_s$. The coefficient η is dynamic correction coefficient and modifies the value of $\Delta\alpha_s$ for incorporating the frequency distribution of the BBR field. The dynamic correction is usually very small $(10^{-2} - 10^{-4})$ and is listed for few ions in Table 2.1.

- **Zeeman shift:** The ion interacts with external magnetic fields by coupling them through its magnetic moments (both atomic and nuclear) μ. The magnetic field appearing from the BBR, geomagnetic and stray fields result in shift of atomic state energy known as Zeeman shift. The first order shift is proportional to magnetic quantum numbers m_F and lande g-factors of ground and excited states respectively. Whereas the second order

shift is given as

$$\Delta\nu_{\mathrm{QZ}} = -\frac{1}{h}\left(\frac{g_J eB}{4\pi m}\right)^2 \sum_{F'} \frac{|\mathcal{F}_Z(I,J,F,F',m_F)|^2}{\Delta\nu_{HFS}}, \tag{2.8}$$

where $\Delta\nu_{HFS}$ is the hyperfine splitting of the states and the matrix element $< F', m'_F|J_z|F, m_F >$ [150] is given as

$$\begin{aligned} \mathcal{F}_Z &= \sqrt{I(I+1)(2I+1)(2F+1)(2F'+1)} \\ &\begin{pmatrix} F & 1 & F' \\ -m_F & 0 & m_F \end{pmatrix} \begin{Bmatrix} I & F & J \\ F' & I & 1 \end{Bmatrix}. \end{aligned} \tag{2.9}$$

The total shift can therefore be written as

$$\Delta\nu_{\mathrm{Z}} = \kappa_1 B + \kappa_2 B^2 \tag{2.10}$$

For ions like $^{171}\mathrm{Yb}^+$, $^{199}\mathrm{Hg}^+$ whose clock transition states have $m_F = 0$, $\kappa_1 = 0$ and so is the first order shift. The values of $\kappa_1 = (g_e m_{F,e} - g_g m_{F,g})$ can be calculated for different ions by use of lande g-factors given in Table 2.1. First order Zeeman in ions with $m_F \neq 0$, can be cancelled by the same measurement method used for cancellation of electric quadrupole shift. The quadratic Zeeman shift coefficient κ_2 is listed for few ions in the Table 2.1.

All the ions which are studied have some benefits as well as some drawbacks. Among the wide variety of ions, we at CSIR-NPL, have chosen the octupole transition (at 467 nm) Ytterbium ion ($^{171}\mathrm{Yb}^+$) for the development of optical clock. This ion may not have smallest systematic shifts among all but the accuracies with which these shifts can be determined can go really low. Following are the advantages of choosing it for optical clock:

- CIPM has endorsed the $4f^{14}6s\ ^2S_{1/2}(F=0, m_F=0)$-$4f^{13}6s^2\ ^2F_{7/2}(F=3, m_F=0)$ octupole (E3) transition of Yb^+ for the secondary frequency standards [151].
- It has first order Zeeman insensitive clock transitions.
- Lasers at the required wavelengths are available off the shelves.
- Yb^+ chemically reacts with residual H_2 due inelastic collisions and forms $\mathrm{Yb}^+\mathrm{H}$ which is photo-dissociates Yb^+ in presence of cooling laser at 369 nm [152] getting re-trapped.
- The $4f^{13}6s^2\ ^2F_{7/2}$ state in Yb^+ is expected to be five orders of magnitude more sensitive for measuring violation of the local Lorentz symmetry [153] than the current best Ca^+ [154].

- Yb^+ frequency standard (E3 transition) is most sensitive towards variation of fine structure constant α with sensitivity coefficient, A=-5.95 which is much higher than the Hg^+, second in the row with A= -2.94 [155]. Yb^+ E3 transition is 100 times more sensitive compared to Sr atom's clock transition. Inter-comparison of these two clocks could give accurate measurement of the temporal variation of the fine structure constant.

The most accurate clock in the world has been reported with this transition [9], very recently. For above reasons, we choose E3 transition of $^{171}Yb^+$ as our clock transition.

Chapter 3

Optimizing trap geometry for Suitable trapping potential

3.1. Trapping An Ion

Ions confined in ultra high vacuum environment are in isolation from the surroundings which allow to control them as required and felicitate their individual probing. Electromagnetic fields are usually employed to confine ion. But ion traps used in atomic clocks employ electric fields only, as the use of external magnetic field lead to additional systematic Zeeman shift of clock transition frequency. This kind of trap which uses a combination of electrostatic and electrodynamic fields is called Paul trap [156]. In this chapter, basics of the ion trapped in a Paul trap are overviewed, followed by identification of the trap geometry which generates a desired confining potential. The quality of the trap is then examined by analyzing different effects associated to the ion trap geometry for performing a precision experiment with it.

In a Paul trap, the excess charge of ion couples with the trapping electric fields resulting in a Coulomb force on it. This Coulomb pull experienced by the ion increases isotropically as it moves away from the equilibrium position of zero force.

$$\begin{aligned} m\ddot{\mathbf{r}} &= Q\mathbf{E} \\ &= -Q\nabla\Phi(x,y,z) \end{aligned} \tag{3.1}$$

where, m, Q and $\mathbf{r}$ are mass, charge and position vectors of the ion, $\mathbf{E}$ and $\Phi(x,y,z)$ are trapping electric field and potential, respectively. This trapping potential has a quadrupole profile in case of Paul traps. Contributions from higher order poles are discussed later in the following subsections. In cartesian coordinates, the trapping potential can be written as

$$\Phi(x,y,z) = \frac{U}{2}(\alpha x^2 + \beta y^2 + \gamma z^2) + \frac{V_T}{2}(\acute{\alpha} x^2 + \acute{\beta} y^2 + \acute{\gamma} z^2) \tag{3.2}$$

where U is static voltage, V_T is time dependent voltage α, β, γ and $\acute{\alpha}, \acute{\beta}, \acute{\gamma}$ are static and time

dependent geometric coefficients, respectively. In order to satisfy the condition for zero free charge distribution, the trapping potential must satisfy the Laplace equation, $\nabla^2\phi = 0$ at every instant in time. This imposes restrictions on the geometric factors, such that

$$(\alpha + \beta + \gamma) = 0$$
$$(\acute{\alpha} + \acute{\beta} + \acute{\gamma}) = 0$$

If a static potential is considered (i.e. $(\acute{\alpha} = \acute{\beta} = \acute{\gamma} = 0)$), then for 3-dimensional trapping geometric factors would have opposite signs resulting in a saddle point at origin. This saddle point can be thought of as a planar potential confining the ion in x-y plane, but having no confinement along the third, z, direction. So, ion can escape from the trap at any instant of time, due to its motion along the z direction. This implies that confinement of charged particle in three dimensions is not possible using an electrostatic field alone, this is known as Earnshaw's Theorem [157]. However, confinement is possible if a time dependent potential oscillating at a frequency much higher than the motion of the ion is used for trapping. This leads to two choice of geometric factors:

- One choice of geometric factors is for confinement in x-y plane with static potential along z-direction, as the case in linear traps:

$$\begin{aligned} -(\alpha + \beta) &= \gamma > 0 \\ \acute{\alpha} &= -\acute{\beta}, \end{aligned}$$

- Second choice of geometric factors is for 3-dimensional confinement in axisymmetric traps

$$\begin{aligned} \alpha = \beta &= \gamma = 0 \\ \acute{\alpha} + \acute{\beta} &= -\acute{\gamma}, \end{aligned}$$

We are interested in trapping a single ion in a axisymmetric trap, so, here we treat the ion trapping potential, taking second choice of geometric factors. The trapping potential then takes the following form

$$\Phi(x, y, z, t) = \frac{V_T}{2R^2}(2z^2 - x^2 - y^2) \tag{3.3}$$

where $V_T = U + V\cos\omega_{rf}t$. Here, U is the static voltage, V and ω_{rf} are amplitude and frequency of oscillating voltage. Plugging the quadrupole field in Eq. (3.1), the equation of

motion of the trapped ion reduces to,

$$\frac{d^2}{dt^2}\begin{pmatrix} x \\ y \\ z \end{pmatrix} - \frac{Q}{mR^2}[U + V\cos\omega_{rf}t]\begin{pmatrix} x \\ y \\ -2z \end{pmatrix} = 0 \tag{3.4}$$

now to solve the above differential equation, it is transformed in standard Mathieu differential equation [159] by substituting $\omega_{rf}t = 2\tau$ or $\tau = \omega_{rf}t/2$. Using this substitution and

$$\frac{d}{dt} = \frac{d}{d\tau}d\tau dt = \frac{d}{d\tau}\frac{\omega_{rf}}{2} \tag{3.5}$$

we can get differential equation of the form (notation $u_{j=1,2,3} = x, y, z$)

$$\frac{d^2u_1}{d\tau^2} - [\frac{4QU}{m\omega_{rf}^2R^2} + \frac{2QV}{m\omega_{rf}^2R^2}\cos 2\tau]u_1 = 0 \tag{3.6}$$

As the trap is radially symmetric, motion of the ion along u_1=x and u_2=y directions is along radial, r, direction and is symmetric. These notations are used interchangeably in the further analysis. Using the following substitutions

$$a_x = a_y = -\frac{a_z}{2} = -\frac{4QU}{m\omega_{rf}^2R^2};$$
$$q_x = q_y = -\frac{q_z}{2} = \frac{2QV}{m\omega_{rf}^2R^2},$$

The dimensionless parameters a_j and q_j correspond to static and periodic voltages, respectively and are called Mathieu parameters. After these substitutions in Eq. (3.4), standard form of Mathieu differential equation can be given as

$$\frac{d^2u_j}{d\tau^2} + [a_j - 2q_j\cos(2\tau)]u_j = 0 \tag{3.7}$$

For Mathieu equation, stable solution follows from a theory known as Floquet theorem [158, 160].

Floquet theory makes use of two facts:

1. Any solution $y_1(\tau)$ has periodicity of 2π

$$y_1(\tau) = y_1(\tau + 2\pi) \tag{3.8}$$

2. As it is a linear second order differential equation, any of its solution $y(\tau)$ can be written

as linear combination of two independent solutions $y_1(\tau)$ and $y_2(\tau)$.

$$y(\tau) = Ay_1(\tau) + By_2(\tau) \tag{3.9}$$

where A and B are constants determined by initial conditions.

According to Floquet theory there exists at least one solution to Mathieu differential equation of the form $y(\tau) = e^{\mu\tau}\phi(\tau)$

$$y(t) = e^{\mu t}\phi(t) \tag{3.10}$$

with the property $\phi(\tau + 2\pi) = \phi(\tau)$ and μ being a complex constant of the form $\alpha + \imath\beta$. Coefficients α and β as real functions of parameters a and q. Solutions with $\alpha \neq 0$ are exponentially rising as $\tau \to \infty$, thus are unstable. For bounded solutions like ions in a trap $\alpha = 0$ is required. Now, there are two type of solutions, periodic but unstable (when β is integer) and periodic cum stable (when β is rational). Former type of solutions form boundaries referred as characteristic curves on the $a - q$ plane (a_j space plotted against q_j along direction j) between the stable and unstable regions. Latter ones determine motion of ion within the trap [161]. Further, the stability of solutions depends upon values of a and q, i.e. they govern the stability of ion trajectory within the trap whether it remains trapped or gets ejected.

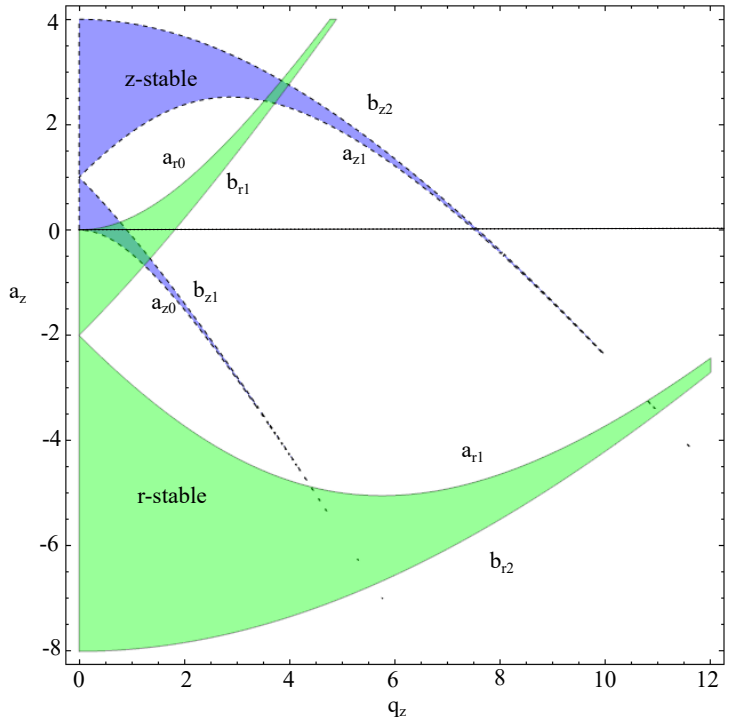

Fig. 3.1: Axial (blue) and radial (green) stability regions plotted simultaneously in a_z-q_z space.

For 3 dimensional confinement, these solutions must be stable in radial, r and axial, z directions simultaneously. And for finding a, q combinations which give simultaneous stable solutions in 3D, recall the relationships between a, q of radial and axial direction from Eq. (3.7). Figure 3.1 shows the stability regions (shaded) in $a - q$ plane along axial and radial directions and the region of overlapping shows the a, q combinations where the solutions are simultaneously stable in both r and z directions. There is a difference of factor of -2 between between a pair for a's, q's of radial directions therefore the composite plot seems to be an overlap of an enlarged upside down image of the other. a_{jn} and b_{jn} are boundaries or characteristic curves along any direction j. The overlapping region near the origin is the lowest intersection region (of curves a_{z0}, b_{z1} and $a_{r0}, b_{r,1}$) and is called the lowest stability region and used routinely. The other overlapping region (intersection of curves a_{z1}, b_{z2} and $a_{r0}, b_{r,1}$) is accessible but not used much because it requires an order or higher values of U.

Rewriting Eq. (3.10), $\phi(\tau) = e^{-\mu\tau}y(\tau)$; $\phi(\tau + 2\pi) = e^{-\mu(\tau+2\pi)}y(\tau + 2\pi) \implies \phi(\tau + 2\pi) = e^{-\mu\tau}y(\tau)$, which implies $\phi(\tau)$ is a periodic function of τ. For sake of simplicity in the discussion of these solutions, subscript j has been removed. Therefore, from the Floquet treatment, the general solution of Eq. (3.7) can be written as

$$
\begin{aligned}
u(\tau) &= \acute{A}e^{\imath\beta\tau}\sum_{n=-\infty}^{n=\infty} C_{2n}e^{\imath 2n\tau} + \acute{B}e^{-\imath\beta\tau}\sum_{n=-\infty}^{n=\infty} C_{2n}e^{-\imath 2n\tau} \qquad (3.11)\\
u(\tau) &= \acute{A}\sum_{n=-\infty}^{n=\infty} C_{2n}e^{\imath(2n+\beta)\tau} + \acute{B}\sum_{n=-\infty}^{n=\infty} C_{2n}e^{-\imath(2n+\beta)\tau}\\
u(\tau) &= \acute{A}\sum_{n=-\infty}^{n=\infty} C_{2n}(\cos(2n+\beta)\tau + \imath\sin(2n+\beta)\tau)\\
&+ \acute{B}\sum_{n=-\infty}^{n=\infty} C_{2n}(\cos(2n+\beta)\tau - \imath\sin(2n+\beta)\tau)
\end{aligned}
$$

$\acute{A}$, $\acute{B}$ are coefficients depending upon initial conditions and C_{2n} are amplitudes of Fourier components in equation of ion motion. Collecting terms with $\cos(2n + \beta)$, $\sin(2n + \beta)$ and substituting coefficients, A=$\acute{A}$+$\acute{B}$, B=$\acute{A}$-$\acute{B}$, solution (3.11) takes form

$$
\begin{aligned}
u(\tau) &= A\sum_{n=-\infty}^{n=\infty} C_{2n}\cos(2n+\beta)\tau \qquad (3.12)\\
&+ \imath B\sum_{n=-\infty}^{n=\infty} C_{2n}\sin(2n+\beta)\tau \qquad (3.13)
\end{aligned}
$$

where coefficients A and B depend upon initial conditions. Solution (3.12)can be plugged back

in to Eq. (3.7) for determining coefficients C_{2n} and β.

$$\begin{aligned}
& A \sum_{n=-\infty}^{n=\infty} C_{2n}(2n+\beta)^2 \cos(2n+\beta)\tau + \imath B \sum_{n=-\infty}^{n=\infty} C_{2n}(2n+\beta)^2 \sin(2n+\beta)\tau \\
= \; & a\left(A \sum_{n=-\infty}^{n=\infty} C_{2n} \cos(2n+\beta)\tau + \imath B \sum_{n=-\infty}^{n=\infty} C_{2n} \sin(2n+\beta)\tau\right) \\
- \; & 2q\cos 2\tau\left(A \sum_{n=-\infty}^{n=\infty} C_{2n} \cos(2n+\beta)\tau + \imath B \sum_{n=-\infty}^{n=\infty} C_{2n} \sin(2n+\beta)\tau\right) \\
\Longrightarrow \; & A \sum_{n=-\infty}^{n=\infty} C_{2n}(2n+\beta)^2 \cos(2n+\beta)\tau + \imath B \sum_{n=-\infty}^{n=\infty} C_{2n}(2n+\beta)^2 \sin(2n+\beta)\tau \\
= \; & a\left(A \sum_{n=-\infty}^{n=\infty} C_{2n} \cos(2n+\beta)\tau + \imath B \sum_{n=-\infty}^{n=\infty} C_{2n} \sin(2n+\beta)\tau\right) \qquad (3.14) \\
- \; & \left(A \sum_{n=-\infty}^{n=\infty} C_{2n} \cos(2n+\beta)\tau \times 2q\cos 2\tau + \imath B \sum_{n=-\infty}^{n=\infty} C_{2n} \sin(2n+\beta)\tau \times 2q\cos 2\tau\right) \qquad (3.15)
\end{aligned}$$

Using relation $2\cos\theta\cos\phi = \cos(\theta+\phi) + \cos(\theta-\phi)$ in Eq. (3.14) and rearranging indices, a recursive relation is obtained by matching the same order cosine terms

$$\begin{aligned}
C_{2n-2} - K_{2n}C_{2n} + C_{2n+2} &= 0, \\
\text{with, } \mathrm{K_{2n}} &= \frac{[\mathrm{a} - (2\mathrm{n}+\beta)^2]}{\mathrm{q}} \\
C_{2n+2} &= \frac{C_{2n}}{K_{2n} - \frac{1}{K_{2n+2} - \frac{1}{\cdots}}} \\
C_{2n} &= \frac{C_{2n-2}}{K_{2n} - \frac{1}{K_{2n-2} - \frac{1}{\cdots}}} \qquad (3.16)
\end{aligned}$$

For n=0 in K_{2n} relation given in Eq. (3.16),

$$k_0 = \frac{a-\beta^2}{q} = \frac{C_2 + C_{-2}}{C_0} \qquad (3.17)$$

using Eq. (3.16), β can be obtained as

$$\beta^2 = a - q\left(\frac{1}{k_0 - \frac{1}{k_2 - \frac{1}{\cdots}}} + \frac{1}{k_0 - \frac{1}{k_{-2} - \frac{1}{\cdots}}}\right) \qquad (3.18)$$

Adiabatic approximation: Further, the ion is subjected to an inhomogeneous high frequency electric field but as the dimension of a trap is usually very small ($\leq$ mm), this inhomogeneity is very small and the amplitude of the field is nearly constant over the oscillation of

the ion. This is also called Adiabatic Approximation. The ion trajectory is approximated to the lowest order, assuming, $\mid a \mid, q^2 \ll 1$. All the coefficients C_n with $n > 2$ are neglected as they fall sharply with increasing values of n. And β can be approximated to:

$$\beta \approx \sqrt{a + \frac{q^2}{2}} \tag{3.19}$$

Further, general form of ion trajectory in any direction (recalling subscript j) can be rewritten by substituting $B = 0$(initial condition) in Eq. (3.14), as

$$u_j(t) \approx 2AC_0 \cos\left(\beta_j \frac{\omega_{rf}}{2} t\right)\left[1 - \frac{q_j}{2}\cos\omega_{rf}t\right] \tag{3.20}$$

Observation of Eq. (3.20) reveals many facts about ionic motion. It exhibits harmonic motion with frequency $\omega_{s,j} = \beta_j/2\omega_{rf}$, called secular frequency. This motion is modulated by a fast motion with frequency ω_{rf} (trap drive frequency) called micromotion. The secular frequency is equal along x and y directions due to radial symmetry of the potential whereas this frequency is different along axial direction.

$$\begin{aligned} \omega_{s,z} &= \frac{\beta_z}{2}\omega_{rf} \\ &= \sqrt{(a_z + \frac{{q_z}^2}{2})}\frac{\omega_{rf}}{2} \qquad (3.21) \\ \omega_{s,r} &= \sqrt{(\frac{{q_r}^2}{8} - 2a_r)}\frac{\omega_{rf}}{2} \qquad (3.22) \end{aligned}$$

Also, the micromotion is opposite in phase to driving frequency and has amplitude smaller than secular motion by a fraction $q_j/2$, but it depends upon the distance of ion from the potential minimum or trap center. If the ion motion center is shifted from center of trapping potential then the micromotion can be so large that it can even exceed secular motion. This undesirable situation can arise from stray static electric field acting upon ion. Ion trap experiments use additional voltage to compensation these static fields and to get the ion back to the trap center.

Ponderomotive potential: As the ion is under influence of an inhomogeneous electric field, the net force experienced by it over a period of oscillation is non-zero. The trapped ion feels an effective potential, U_{eff} which is contributed by potential static voltage, U as well as the oscillating voltage, $V\cos\omega_{rf}t$. The effective force on ion can be written as sum

$$m\ddot{r} = F_U(r) + F_V(r)\cos\omega_{rf}t \tag{3.23}$$

Note that $r \in \{x, y, z\}$ which is position vector of the ion is dependent on time and is sum of

two components: secular motion component, $\kappa(t)$ and micromotion component, $\xi(t)$.

$$r = \kappa(t) + \xi(t) \tag{3.24}$$

As displacement of ion due to micromotion ($\xi \ll$) is very small compared to that due to secular motion, we can write static and oscillating force components of Eq. (3.23) in expanded form as

$$\begin{aligned} F_U(\kappa+\xi) &= F_U(\kappa) + \xi\nabla F_U(\kappa) + \ldots \\ F_V(\kappa+\xi) &= F_V(\kappa) + \xi\nabla F_V(\kappa) + \ldots \end{aligned} \tag{3.25}$$

Substitution of above series expansions in Eq. (3.23) gives

$$m[\ddot{\kappa}(t) + \ddot{\xi}(t)] = [F_U(\kappa) + \xi\nabla F_U(\kappa)] \tag{3.26}$$

$$+ \quad [F_V(\kappa) + \xi\nabla F_V(\kappa)]\cos\omega_{rf}t \tag{3.27}$$

Neglecting terms multiplied with ξ, and separating $\kappa(t)$ and $\xi(t)$ terms, we get

$$m\ddot{\kappa}(t) = F_U(\kappa) \tag{3.28}$$

$$m\ddot{\xi}(t) = F_V(\kappa)\cos\omega_{rf}t \tag{3.29}$$

Integration of Eq. (3.29) twice, gives us the displacement of ion due to micromotion, $\xi(t)$ as

$$\xi(t) = -\frac{F_V}{m{\omega_{rf}}^2}\cos\omega_{rf}t \tag{3.30}$$

Further, substituting $\xi(t)$ in the Eq. (3.26) and averaging this force over a period of oscillation of ion ($2\pi/\omega$) gives

$$\begin{aligned} m\ddot{\kappa}(t) &= F_U(\kappa) + \langle[F_V(\kappa) + \xi\nabla F_V(\kappa)]\cos\omega_{rf}t\rangle \\ &= F_U(\kappa) + \langle F_V(\kappa)\cos\omega_{rf}t\rangle + \langle\xi(t)\nabla F_V(\kappa)\cos\omega_{rf}t\rangle \\ &= F_U(\kappa) - \frac{F_V(\kappa).\nabla F_V(\kappa)}{m{\omega_{rf}}^2}\langle\cos\omega_{rf}t\rangle \\ &= F_U(\kappa) - \frac{F_V(\kappa).\nabla F_V(\kappa)}{2m{\omega_{rf}}^2} \end{aligned} \tag{3.31}$$

as $\langle\cos\omega_{rf}t\rangle$=0 and $\langle\cos^2\omega_{rf}t\rangle$=1/2. Now, using the vector identity $1/2\nabla A.A=\nabla A.A$, above

equation can be written as

$$\begin{aligned} m[\ddot{\kappa}(t)] &= F_U - \frac{\nabla {F_V}^2}{4m{\omega_{rf}}^2} \\ &= -Q\nabla\left(\Phi(U) + \frac{Q\nabla\Phi(V)^2}{4m{\omega_{rf}}^2}\right) \end{aligned} \tag{3.32}$$

So, the time averaged effective potential felt by the ion is a sum contributions from static and oscillating electric fields.

$$U_{eff} = \Phi(U) + \frac{Q\nabla\Phi(V)^2}{4m{\omega_{rf}}^2} \tag{3.33}$$

The potential due to oscillating electric fields, $U_p = Q\nabla\Phi(V)^2/4m{\omega_{rf}}^2$ is called Ponderomotive potential.

Further, under adiabatic approximation the depth of confining potential along axial direction can be written as

$$D_z = \frac{m{z_o}^2{\omega_{rf}}^2{q_z}^2}{16Q} \tag{3.34}$$

where z_o is separation of electrodes along axial direction and r_o is the radius of ring electrodes related to radius of trap volume as $R = \sqrt{\frac{{r_o}^2}{2} + z_o}$. For ${r_o}^2 = 2{z_o}^2$, the depth is given as D_r=$D_z/2$.

Till now equations of an ion trapped in an ideal quadrupole potential produced in a Paul trap were summarized. But in this clock experiment, we opt for an end cap trap geometry because it can provide large obstruction free field of view to its center giving access to the optical and atomic beams. This geometry is modified from the classical design of hyperbolic shape electrodes and yet maintains cylindrical symmetry. It has two counter facing end cap cylindrical electrodes which are cut conical in shape at the front faces. These cylindrical electrodes have a pair of outer cylinders surrounding them with a dielectric material filled in between usually. This geometry can be thought of as that of ring trap with the ring cut into two and pulled back for giving the desired quadrupolar shape to the potential. It produces a nearly quadrupolar potential near center of the trap and have been used by various groups for trapping ions in 3D potential [49, 162, 163, 74]. Some of them are shown in Fig. 3.2 with dimensional details. The following subsection takes into account anharmonic perturbations to the ideal quadrupole potential. Thereafter, Mathieu parameters, trap depth etc. have been modified to account for our trap geometry.

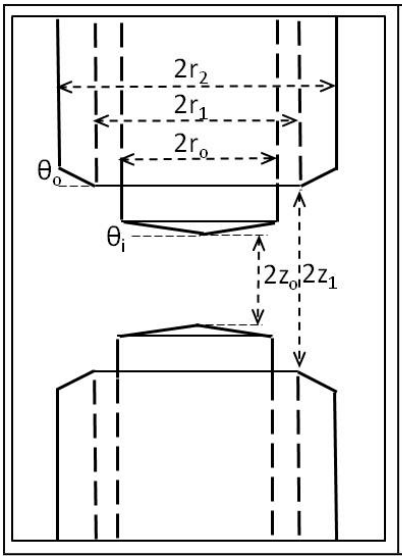

(a) NRC, CANADA	(b) NPL, UK	(c) Universitat Hannover
$2r_o = 0.5$ mm	$2r_o = 0.5$ mm	$2r_o = 0.95$ mm
$2r_1 = 1$ mm	$2r_1 = 1$ mm	$2r_1 = 1.4$ mm
$2r_2 = 2$ mm	$2r_2 = 2$ mm	$2r_2 = 2$ mm
$2z_o = 0.54$ mm	$2z_o = 0.56$ mm	$2z_o = 0.62$ mm
$2z_1 = 1$ mm	$2z_1 = 1$ mm	$2z_1 = 0.9$ mm
$\theta_o = 45^o$	$\theta_o = 45^o$	$\theta_o = 35^o$
$\theta_i = 0^o$	$\theta_i = 0^o$	$\theta_i = 11.83^o$

Fig. 3.2: Shows an end cap trap geometry with its different dimensional parameters. Naming conventions: Tip to tip inner electrode separation, $2z_o$; separation between the outer electrodes, $2z_1$; radii of the inner electrodes, $2r_o$; inner and outer radii of the outer electrodes, $2r_1$ and $2r_2$; angle of inner and outer electrodes θ_i and θ_o. Trap dimensions used by: (a) NRC, CANADA [74], (b) NPL, UK [49, 162], (c) Universitat Hannover [163].

3.1.1 Real Trapping Potential: Contributions From Higher Order Poles

In real life experimental situations, the trapping potential $\Phi(x, y, z, t)$ always contains poles of higher order ($l > 2$) contributing to it with non negligible magnitudes, $\Phi = \Phi_0 + \Phi_1 + \Phi_2 + \Phi_3 + \ldots$. These higher order perturbations owe their existence to electrode length truncation, machining errors or tolerances, asymmetric alignment of the trap assembly etc. Expansion of potential, Φ, in terms of spherical harmonics, looks like [163]

$$\Phi_{lm} = \sum_{m=-l}^{m=l} \sum_{l} a_{lm} \sqrt{\frac{(l-m)!}{(l+m)!}} \left(\frac{r}{z_o}\right)^l exp(\imath m\phi) P_l^m(\cos\theta) \tag{3.35}$$

where l, m are azimuthal and magnetic quantum numbers, respectively, r, θ, ϕ are spherical coordinates, a_{lm} are multipole coefficients and $P_l^m(\cos\theta)$ are associated Legendre polynomials. Alternatively, trap potential equation can also be written in terms of multipoles, A_{lm}, as

$$\Phi = V_T \sum_{l=0}^{\infty} \sum_{m=-l}^{l} a_{lm} A_{lm}(r, \theta, \phi) \tag{3.36}$$

$$where, A_{lm}(r, \theta, \phi) = \sqrt{\frac{4\pi}{2l+1}} \left(\frac{r}{R}\right)^l Y_{lm}(\theta, \phi)$$

$$Y_{lm} = (-1)^m \sqrt{\frac{(l-m)!}{(l+m)!}} \sqrt{\frac{2l+1}{4\pi}} P_{lm}(\cos\theta) e^{im\phi} \tag{3.37}$$

In above expression Y_{lm} correspond to the spherical harmonic terms which can be obtained directly from the standard table of orthonormalized spherical harmonics. Each multipole potential can also be expressed as,

$$\Phi_l = V_T \sum_{m=-l}^{l} a_{lm} A_{lm}(r, \theta, \phi) \tag{3.38}$$

First term in the series, with $(l = 0)$ is just a constant offset and is called monopole. Other higher order terms are dipole, $(l = 1)$; quadrupole, $(l = 2)$; hexapole, $(l = 3)$; octupole, $(l = 4)$; dodecapole, $(l = 6)$; sedecapole, $(l = 8)$ and Icosapole, $(l = 10)$. In the expressions to follow, cartesian system is followed uniformly. Therefore corresponding Y_{lm} values have been converted using the basic spherical-to-cartesian coordinate transformation and Euler's formula as,

$$\begin{aligned} r^2 &= x^2 + y^2 + z^2, \\ \sin\theta &= \frac{\sqrt{x^2+y^2}}{r}, \cos\theta = \frac{z}{r}, \\ \cos\phi &= \frac{x}{\sqrt{x^2+y^2}}, \sin\phi = \frac{y}{\sqrt{x^2+y^2}}, \\ e^{im\phi} &= \cos(m\phi) + i\sin(m\phi) \end{aligned} \tag{3.39}$$

The imaginary part of $e^{im\phi}$, can be neglected because of zero contribution to the potential. The quadrupole potential can be expressed using Eq. (3.38) as,

$$\Phi_2 = V_T(a_{2,0}A_{2,0} + a_{2,1}A_{2,1} + a_{2,-1}A_{2,-1} + a_{2,2}A_{2,2} + a_{2,-2}A_{2,-2}) \tag{3.40}$$

Talking about various symmetries in the trap and their effects, it is found that not every combination of l and m contribute to the corresponding pole of potential. Owing to the mirror symmetry present about the radial plane (perpendicular to the trap axis) in the end cap trap, only multipoles, $A_{l,m}$, with $l + m = even$ are allowed. Inversion symmetry about origin yields $a_{l,m}$=$a_{l,-m}$. Also, these radial plane and inversion symmetry about the origin together result to inversion symmetry about the trap axis. If the trap electrodes are cut into halves along their axis, there is periodicity at every half turn traversed from one end about the trap axis. This symmetry is only met by multipoles with an even m. The symmetry in trap geometry only allows l and m both to be even. Also, if the imaginary part in $Y_{l,m}$'s is neglected, then it can be seen that $Y_{l,m} = (-1)^m Y_{l,-m}$. Hence, multipoles having odd l or odd m simply cancel

out. Hence, equation for quadrupole potential is reduced to,

$$\begin{aligned} \Phi_2 &= V_T(a_{2,0}A_{2,0} + a_{2,2}A_{2,2} + a_{2,-2}A_{2,-2}) \\ \text{or,}\Phi_2 &= V_T\Big[a_{2,0}A_{2,0} + a_{2,2}(A_{2,2} + A_{2,-2})\Big] \end{aligned} \tag{3.41}$$

The values of spherical harmonics $Y_{l,m}$'s, for $l = 2$ are given as,

$$\begin{aligned} Y_{2,0}(\theta,\phi) &= \frac{1}{4}\sqrt{\frac{5}{\pi}}[3\cos^2\theta - 1] \\ Y_{2,-1}(\theta,\phi) &= \frac{1}{2}\sqrt{\frac{15}{2\pi}}\sin\theta\cos\theta\cos(\phi) \\ Y_{2,1}(\theta,\phi) &= \frac{-1}{2}\sqrt{\frac{15}{2\pi}}\sin\theta\cos\theta\cos\phi \end{aligned} \tag{3.42}$$

Note that the imaginary part is neglected in the above expressions. When substituted with these values, Eq. (3.41) can be rewritten as

$$\begin{aligned} \Phi_2 &= V_T\left[\frac{a_{2,0}}{R^2}\frac{(2z^2 - x^2 - r^2)}{2} + \frac{\sqrt{6}a_{2,2}}{4R^2}(2x^2 - 2y^2)\right] \\ \Phi_2 &= V_T\left(\frac{a_{2,0}}{2R^2}\right)[2z^2 - (1-\epsilon_0)x^2 - (1+\epsilon_0)y^2] \end{aligned} \tag{3.43}$$

where the factor $\epsilon_0 = \sqrt{6}a_{2,2}/a_{2,0}$. The terms $Y_{2,1}$, $Y_{2,-1}$, cancel each other and do not contribute in Φ_2 as $Y_{2,1} = (-1)Y_{2,-1}$.

As the trap employed in this experiment is an end cap trap, it does not produce a pure quadrupole potential. The Mathieu parameters obtained from treatment of pure quadrupole potential are multiplied by the fraction of quadrupole component, $a_{2,0}$, present in the trapping potential. As this $a_{2,0}$ depends upon geometry of trap i.e. distances r_o, z_o and angles θ_o, θ_i, thus, Mathieu parameters bear different values for different trap geometries. The relations of Mathieu parameters given in Eq.(3.7) which were for a perfect Paul trap are modified as

$$\begin{aligned} a_x = a_y = -\frac{a_z}{2} = -\frac{4a_{20}QU}{m\omega_{rf}^2 z_o^2}; \\ q_x = q_y = -\frac{q_z}{2} = \frac{2a_{20}QV}{m\omega_{rf}^2 z_o^2} \end{aligned}$$

These parameters given in Eq.(3.7) consisted R as radius of trap volume, but as we have an end cap trap which does not have any ring electrode we replace R with z_o. As per the Adiabatic approximation, the time average effective potential felt by the ion as given in Eq.(3.33) for

quadrupole potential expanded in Eq.(3.43)can be calculated as

$$U_{eff}(2) = Q\Phi_2(U) + \frac{Q^2\Phi_2(V)^2}{4m{\omega_{rf}}^2} \tag{3.44}$$

where static and oscillating parts of $V_T = U + V\cos\omega_{rf}t$ in Φ_2 have been separated.

$$\begin{aligned} U_{eff}{}^{(2)} &= \frac{a_{2,0}}{{z_o}^2}\frac{QU}{2}(2z^2 - (1-\epsilon)x^2 - (1+\epsilon)y^2) \\ &+ \frac{a_{2,0}}{{z_o}^4}\frac{Q^2V^2}{4m{\omega_{rf}}^2}(4z^2 - (1-\epsilon)^2x^2 - (1+\epsilon)^2y^2) \end{aligned} \tag{3.45}$$

Now, solving the above equation further by collecting terms of x^2, y^2 and z^2 together and considering q_x=$(1-\epsilon)q_r$, q_y=$(1+\epsilon)q_r$, a_x=$(1-\epsilon)a_r$ and q_y=$(1+\epsilon)q_r$, we can write Eq. (3.45) as

$$U_{eff}{}^{(2)} = \sum_{u\in\{x,y,z\}}[\frac{m}{16{\omega_{rf}}^2}u^2{q_u}^2 - \frac{m}{8{\omega_{rf}}^2}u^2a_u] \tag{3.46}$$

which represent simple harmonic motion potential along the three directions. Also, under Adiabatic approximation, we observe that the Mathieu parameters along the x, y directions are not symmetric. This lead to different frequencies of motion along x and y directions.

$$\begin{aligned} \omega_{s,x} &= \frac{\omega_{rf}}{2}\sqrt{\frac{(1-\epsilon)^2{q_r}^2}{2} + (1-\epsilon)a_r} \text{ and} \\ \omega_{s,y} &= \frac{\omega_{rf}}{2}\sqrt{\frac{(1+\epsilon)^2{q_r}^2}{2} + (1+\epsilon)a_r} \end{aligned} \tag{3.47}$$

As defined earlier, $\epsilon_0 = \sqrt{6}a_{2,2}/a_{2,0}$ depend upon the ratio of geometry dependent multipole coefficients $a_{2,2}$ and $a_{2,0}$. The depth of confining potential, given in Eq. (3.34) is also multiplied by a_{20} to include the effect of trap geometry as

$$D_z = \frac{a_{20}m{z_o}^2{\omega_{rf}}^2}{16Q} \tag{3.48}$$

Similarly, octupole potential can be expressed using Eq. (3.38) as,

$$\begin{aligned} \Phi_4 &= V_T[(a_{4,0}A_{4,0}) + a_{4,2}(A_{4,2} + A_{4,-2}) + a_{4,4}(A_{4,4} + A_{4,-4})] \\ \Phi_4 &= V_T\left(\frac{a_{4,0}}{8z_o^4}\right)[x^4(3 - \epsilon_1 + \epsilon_2) + y^4(3 + \epsilon_1 + \epsilon_2) + 8z^4 \\ &+ 6x^2y^2(1-\epsilon_2) - 6y^2z^2(4+\epsilon_1) - 6x^2z^2(4-\epsilon_1)] \end{aligned} \tag{3.49}$$

Tab. 3.1: Multipole components of potential (l≤10)

Multipoles, k	$\frac{\Phi_\circ^{(l)}}{V_T}$	$\Gamma^{(l)}$
Quadrupole, 2	$\frac{a_{2,0}}{2z_o^2}$	$2z^2 - r^2$
Octupole, 4	$\frac{a_{4,0}}{8z_o^4}$	$8z^4 + 3r^4 - 24r^2z^2$
Dodecapole, 6	$\frac{a_{6,0}}{16z_o^6}$	$16z^6 - 5r^6 - 120r^2z^4 + 90r^4z^2$
Sedecapole, 8	$\frac{a_{80}}{128z_o^8}$	$128z^8 + 35r^8 - 1792z^6r^2$ $+3360z^4r^4 - 1120z^2r^6$
Icosapole, 10	$\frac{a_{10,0}}{256z_o^{10}}$	$256z^{10} - 63r^{10} - 5760z^8r^2$ $+20160z^6r^4 - 16800z^4r^6 - 3150z^2r^8$

where it is assumed that, $\epsilon_1{=}\sqrt{40}a_{4,2}/a_{4,0}$ and $\epsilon_2 = \sqrt{70}a_{4,4}/a_{4,0}$. The potential $\Phi^{(l)}$ varies with z_o as $1/z_o^l$ so contributions from higher orders keep decreasing. So, in the present analysis we consider poles of order $l \leq 10$ as it is found to suffice for this experiment. The order of pole 10 is chosen on basis of an analysis with electric quadrupole shift (details are discussed in Chapter 4). The potential can be rewritten as

$$\Phi = \sum_l \Phi_{(l)} = \sum_{l=0}^{\infty} \Phi_\circ^{(l)}(U, V, t) \cdot \Gamma^{(l)}(r, z) \tag{3.50}$$

where $r = \sqrt{x^2 + y^2}$ and z are radial and axial directions of the trap, respectively. The coefficient $\Phi_\circ^{(l)} = a_{l,0}/2^l z_o^l \times V_T$ is dependent upon trap operating parameters, V_T and also has different values for different geometry of trap. This is because of presence of factor $c_l = a_{l,0}/2^l z_o^l$. Table 3.1 shows the mathematical form of the higher poles of the trapping potential.

Nonlinear resonances: Efficient trapping of ions require a potential with minimum anharmonicities *i.e.* negligible contributions from $l > 2$. The higher order poles ($l > 2$) makes ion trapping complicated as the force on the ion due to these potentials have nonlinear spatial dependence as listed in Tab. 3.1, which means it increases nonlinearly, as ion goes away from the center. Unlike simple non-coupled ion motion in pure quadrupole potential, higher order poles couple the ion motion along different directions. This leads to serious problems of non linear resonances. Usually, non linear resonances arise when the motion of two or more trapped ions couple on account of their Coulomb interactions. But, in case of single trapped ion these non linearities can be introduced due to deviations of the real potentials from the ideal harmonic ($l = 2$) case. Motion of trapped ions, consist of fundamental secular frequency ω_s and also its higher harmonics but with descending amplitudes. At some discrete values of ac voltage these higher harmonics of ω_s get excited due to the interaction with $l > 2$ multipoles of the non-ideal trapping potential [164]. Hence, even though the trap is operational in the stable a_u-q_u region, these resonance excitations may results to loss of ions from the trap giving

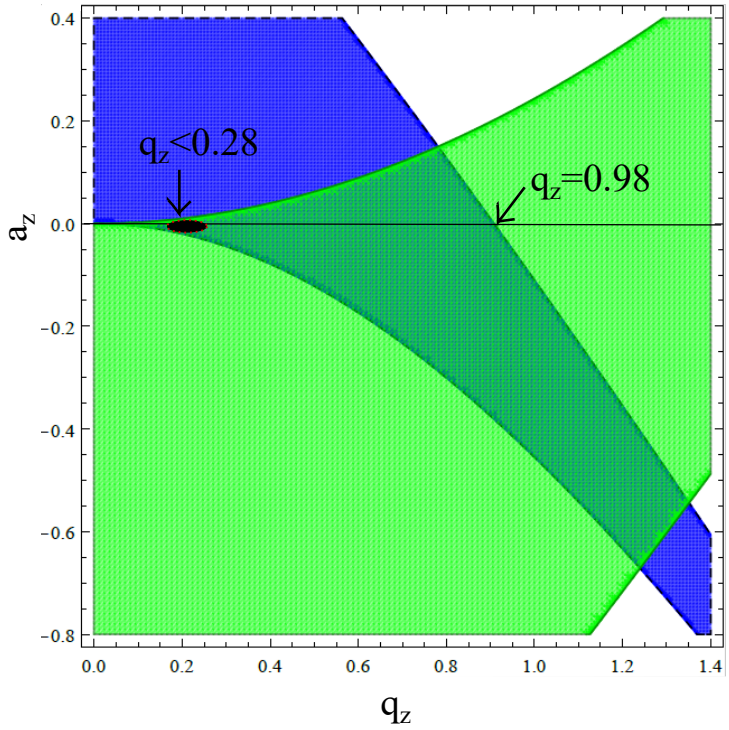

Fig. 3.3: Composite stability region. Region in black shows region of our interest where non linear resonances due to poles upto 10th order can be avoided.

rise to binary possibilities of trapping an ion.

In a rotationally symmetric trap the condition for the nonlinear resonance of ion is given as

$$n_r\omega_{s,r} + n_z\omega_{s,z} = \omega_{rf} \tag{3.51}$$

where n_r and n_z are integers and for l^{th} order multipole they are related as,

$$\mid n_r \mid + \mid n_z \mid = l \tag{3.52}$$

For a nearly pure quadrupole trap, the ion motion close to the trap center is dominated by the quadrupole field and influence of higher order multipoles become significant as the ion goes off centered. At nonlinear resonances, ion starts gaining excess energy from the nonlinear fields as the higher harmonics of the fundamental secular frequencies match with the oscillation frequency produced by the higher order multipole potentials. As a result amplitudes of the ion oscillation increases without any damping and they oscillate over an extended spatial extension which exhibits higher nonlinearity. This leads to escape of ions from the trap when their kinetic

energy exceeds the trap depth [165]. Using relation $|q_z| = |2q_r|$, $|q_z|$ is calculated for different combinations of n_r and n_z which satisfy Eq. (3.52) for upto $l = 10$ order multipole. And it is found that choosing values below $q_z = 0.28$ as shown in Fig. 3.3, can avoid all the possible non linear resonances which can create perturbations to trapping potentials upto and including $l = 10$ order. Although, there are several possible values of q_z above 0.28 which are safe and do not allow transfer of energy between the trapping and the secular frequencies but the adiabatic approximation $q^2 \ll 1$ is also valid in the region so we have sufficiently good q_z.

3.2. Numerical Simulations Of Potential And Validation Of Chosen Trap Geometry

An end cap trap (see Fig. 3.4) is opted for our experiment.The reference geometry in Fig. 3.4(b) shows the distance between the two counter facing inner electrodes, which is referred to as tip to tip separation, $2z_o$; separation between the outer electrodes, $2z_1$; radii of the inner electrodes, $2r_o$; inner and outer radii of the outer electrodes, $2r_1$ and $2r_2$; angle of inner and outer electrodes θ_i and θ_o. These geometric parameters of trap electrodes assembly play a vital role in the shape, depth and trapping efficiency of the potential. We simulated trapping potentials with different trap geometries, varying the geometric parameters. A commercial simulation software, Charged Particle Optics (CPO)[166], is used to solve Green's function for each of the trap geometry using boundary element method. Detailed instructions for using CPO are given in Appendix A. The specified trap geometry is split into a number of small segments to calculate electric field values at different spatial points within the region of interest. Further analysis by numerically fitting these potentials yields the harmonic and anharmonic contents in them. The coefficients of multipole expansion, a_{lm} are then extracted and compared for different geometries.

Selecting the suitable geometry not only takes into consideration efficient trapping potential but also physical constraints like smooth and scatter free optical access to the ion, practical machining etc. This limits various possible choices for trap geometry parameters. In the following subsections, trap geometry parameters which satisfy physical constraints are filtered first. Then the chosen ones are further studied on the basis of anharmonic components present in their corresponding potentials and motion of ion inside them. This way we zero down on the suitable trap geometry to be employed in this experiment.

3.2.1 Physical Constraints

Let us consider the z axis as the axis of trap electrodes and x, y in the perpendicular radial plane with the origin of the axes set at the center of the trap electrodes (see Fig. 3.4). In this clock experiment, three pairs of laser lights coming from three mutually orthogonal directions are required for micromotion detection and quantization purposes. But this cannot be accomplished by these conventional axes as the z axis is blocked by the electrodes. Therefore,

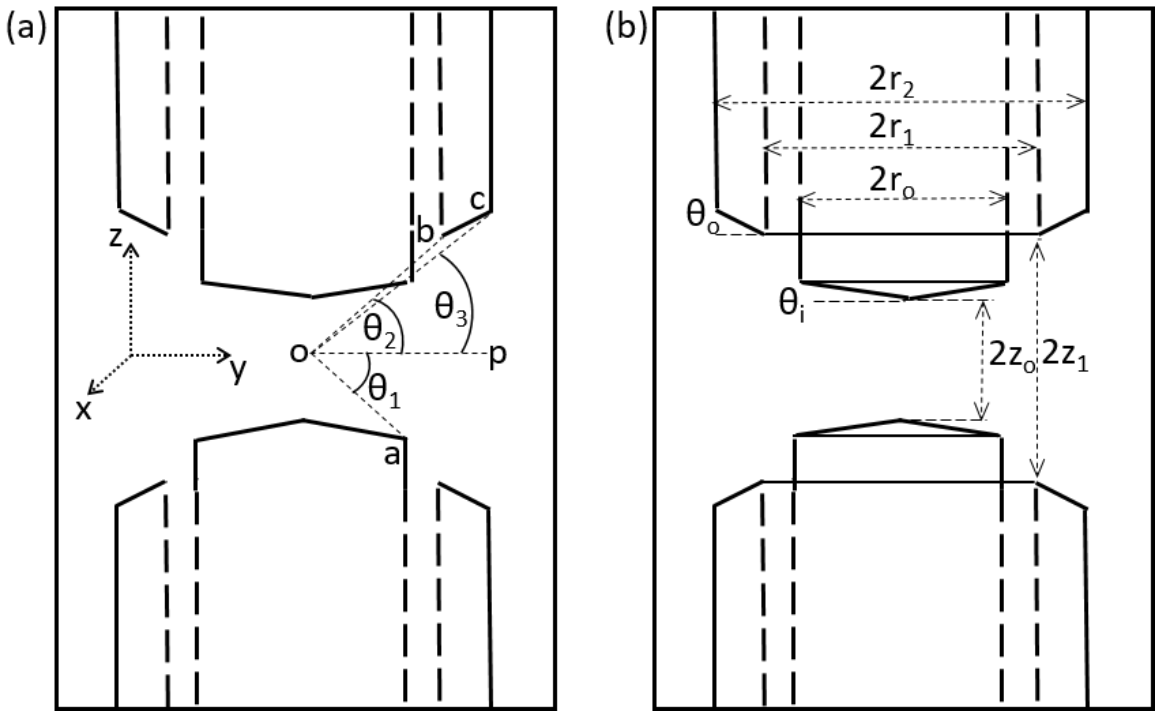

Fig. 3.4: (a) Angles made by light incident on ion with electrodes' edges. (b) Important geometric parameters of the electrode assembly.

another set of three mutually orthogonal axes was used. The axes in this set are such that each of the them makes an angle of 35.27° with the horizontal axis (in x, y). This new set of axes is discussed further in chapter 5. As the light impinges at an angle of 35.27° with the horizontal at the center of the trap, the trap electrodes must not obstruct the light falling upon the ion. Figure 3.4(a) shows the possible limiting edges where the light can scatter if geometry does not give spatial clearance. The angles θ_1, θ_2 and θ_3 must be greater than 35.27° for unobstructive light impingement. Figure 3.4(b) shows the geometric parameters of the electrode assembly affecting the potential profile. The challenge here is to find an optimum geometry so as to get desired potential with minimum higher order perturbations along with enough spatial access to the center. The clearance angle θ_1 clearly depends upon the distances $2r_o$, $2z_o$ and angle θ_i. Similarly, angles θ_2 and θ_3 depend upon $2r_1$, $2z_1$ and $2r_1$, $2r_2$ and θ_o, respectively. We calculated limiting angles for different combinations of trap parameters, some of them are given in Table 3.2. In case of $\theta_i = 0$ meaning flat inner electrodes, with other parameters being constant, $2r_o$ cannot be taken >0.7 mm as the limiting angles do not allow an unobstructed field of view from ion. So, the choices left for $2r_o$ of the inner electrode are 0.5, 0.6 and 0.7 mm which are practically difficult to handle as they bend easily. Further, there is a constraint for the parameter $2z_o$ that the smallest separation which allows angled light unobstructively at the center comes out to be 0.3 mm. With all these physical constraints, we opted for non

Tab. 3.2: Limiting angles [degree] with different values of $2r_o$ [mm] and $2z_o$ [mm]

z_o,	$2r_o$	θ_i	θ_o	θ_1	θ_2	θ_3
0.3	0.5	0	45	50.194	37	39.69
0.3	0.6	0	45	45	37	39.69
0.3	0.7	0	45	40.60	37.00	39.69
0.3	0.8	0	45	36.86	37.00	39.69
0.3	0.9	0	45	33.96	37.00	39.69
0.3	1.0	0	45	30.96	37.00	39.69
0.3	1.0	10	45	31.82	37.00	39.69
0.35	1.0	10	45	41.22	39.65	41.64
0.4	1.0	10	45	44.31	41.98	42.92

zero angles at electrodes faces. Angles cut in the electrodes also effect the shape of potential and can increase harmonic content in it.

3.2.2 Anharmonicities

A series of trap geometries with θ_i ranging from 0° to 60°, θ_o from 0° to 65°, $2r_o$ from 0.5 mm to 1 mm, and $2z_o$ from 0.6 mm to 0.8 mm is simulated and characterized for identifying multipole components in potential. It is found that the diameters of the outer electrode have weak influence on potential which is below the accuracy that is expected from the machining tolerances. So, potentials are obtained for various combinations of θ_i, θ_o, $2r_o$, and $2z_o$ but at the fixed values $2r_1 = 1.4$ mm, $2r_2 = 2$ mm and $2z_1 = 1.16$ mm. The fractional anharmonicities as shown in Fig. 3.5 for the potential simulated with different sets of electrodes angles indicate that the inner electrode's angle θ_i are crucial for shape of potential where as for a given θ_i the potential is negligibly sensitive to outer angle θ_o. As the angle of inner electrode is increased both the harmonic and anharmonic multipole components increase in the net potential. It is desired to increase the harmonic component in the trapping potential but it can be done at the expense of presence of anharmonic components to some extent. This tradeoff is bearable till the anharmonic part do not perturb the potential strongly in a manner that the loss factor, L of the ion trap is not very high. As defined in Ref. [49], L is used to characterize a trap which is a measure of reduction in quadrupole content of the potential from an ideal one for which, L=1.

In order to understand the effect of electrode angles on potential, consider an end cap trap, in which both the inner electrodes are supplied with same oscillating voltage $V \cos \omega_{rf} t$ with respect to outer electrodes. At any time t, either both the electrodes are positive or are at negative potential with respect to the outer electrodes. Consider this situation as of two

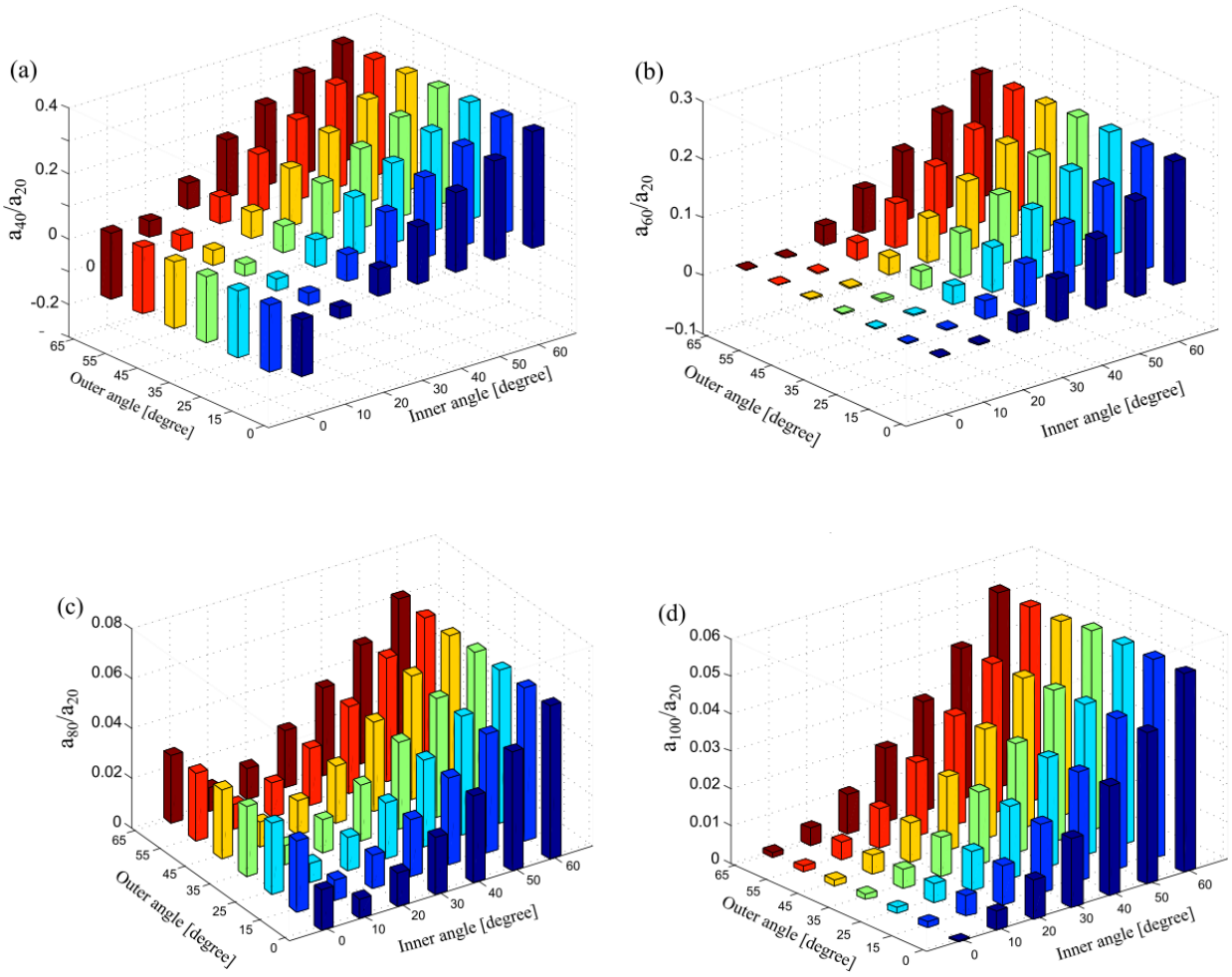

Fig. 3.5: Fractional anharmonicities for different inner and outer electrodes angles at $2r_o = 1$ mm, $2z_o = 0.7$ mm.

positive charges placed close to each other. The electric field lines start perpendicularly from the surface of higher potential towards the lower potential. Thus the field lines start from the inner electrodes towards the outer ones with their intensity decreasing in their direction of progression. If we join the heads of these field lines what we get are the contours of constant potential as shown in Fig. 3.6. Clearly, the shape of these potential contours depend upon the shape of electrode. If the angle of the inner electrode is increased the shape of the contours become more steep. And the distance between tip of inner and outer electrodes increase due to increased angle resulting in distorted shape of potential. Thus the potential profile now has a dependence $\propto R^l, l > 2$. Potential from an electrode assembly with $\theta_i = 50°$ is shown in the Fig. 3.7

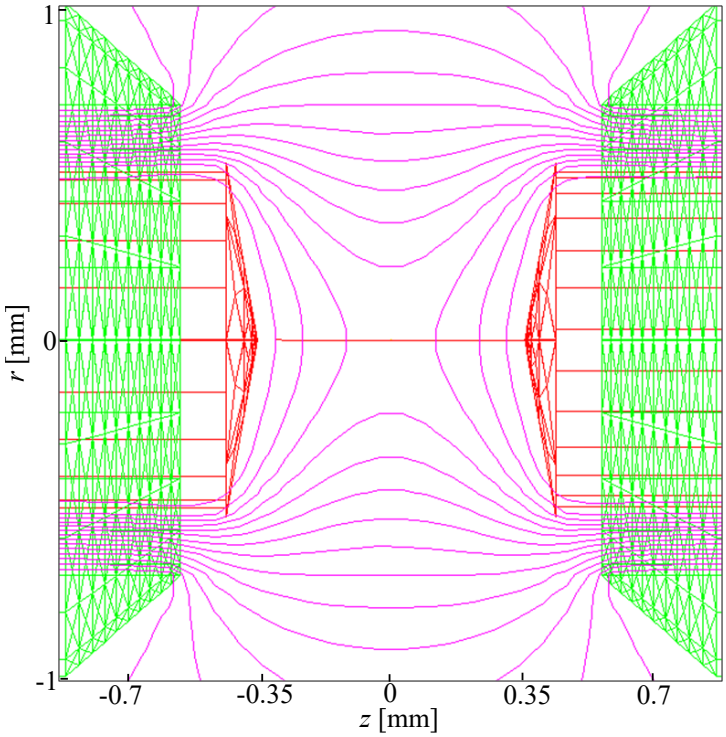

Fig. 3.6: Potential contours simulated with parameters $2z_o = 0.7$ mm, $2r_o = 1$ mm, $\theta_o = 45°$, $\theta_i = 10°$ show nearly quadrupolar shape of potential.

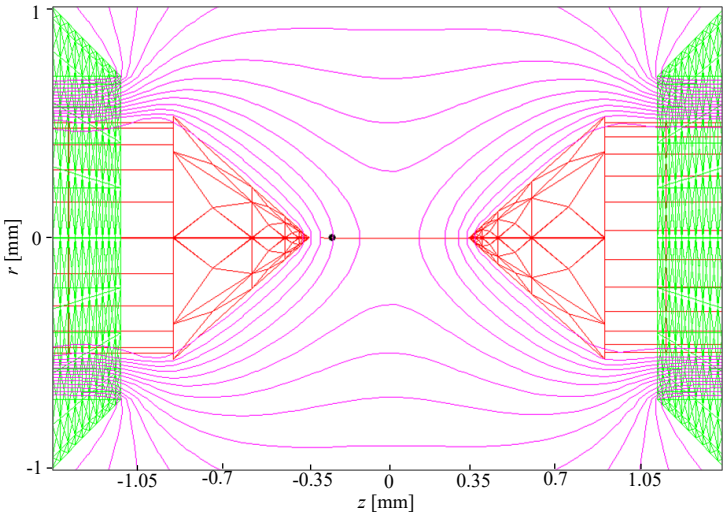

Fig. 3.7: Potential contours simulated with parameters $2z_o = 0.7$ mm, $2r_o = 1$ mm, $\theta_o = 45°$, $\theta_i = 50°$.

There are very few choices for $2r_o$, and $2z_o$ as placing electrodes very close to each other or having larger diameters introduce optical blockage as discussed in subsec. 3.2.1. We found two set of θ_i and θ_o: (1) 10°,45°; (2) 11°, 45° at $2r_o = 1$ mm, with very low contribution from higher order poles. Fractional anharmonicities corresponding to these two geometries are compared

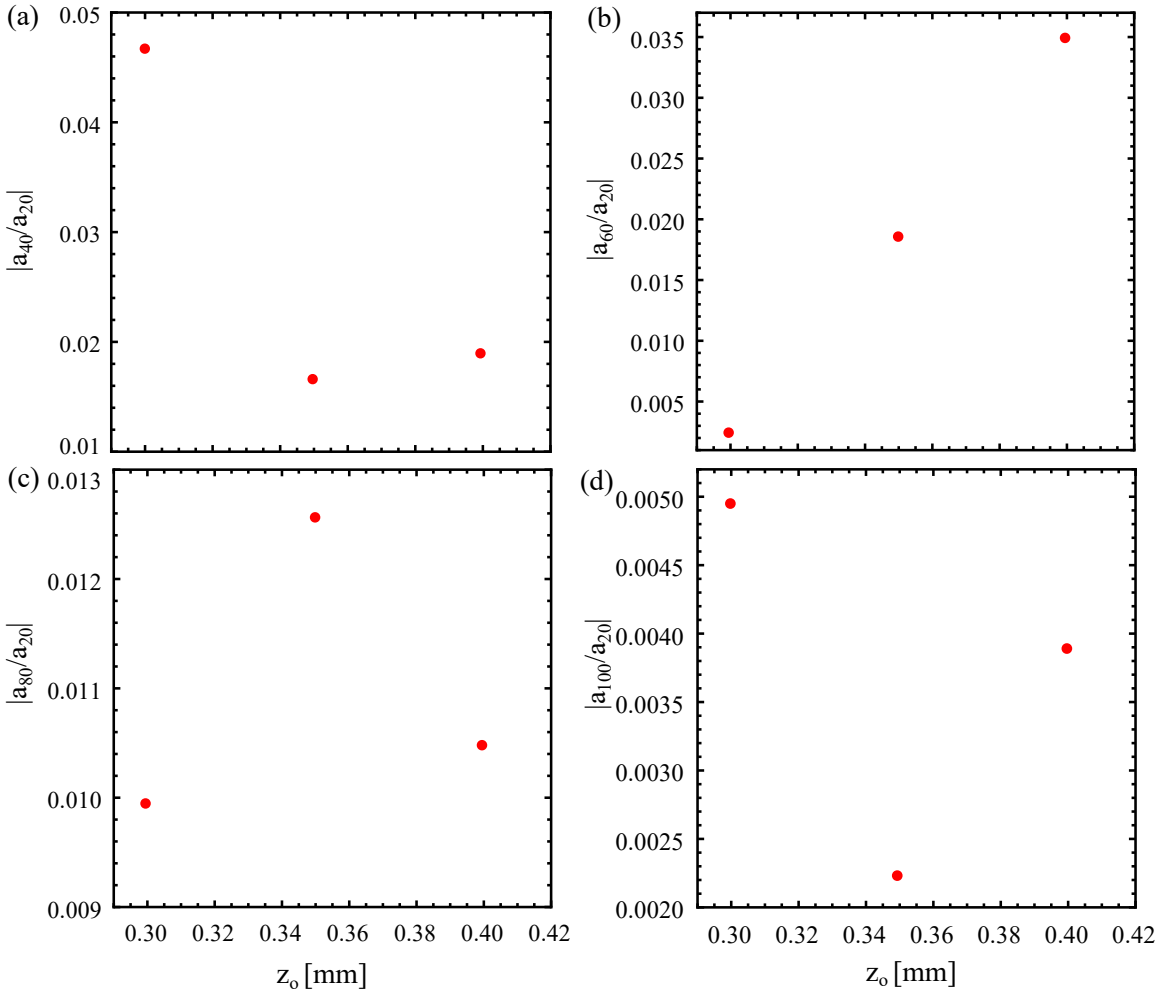

Fig. 3.8: Fractional anharmonicities variation with z_o at $2r_o = 1$ mm, θ_i=10° and θ_o=45°.

while varying the separation z_o as in Fig. 3.8 and 3.9. It shows that both the geometries offer good trapping potentials at tip to tip separation of $2z_o$=0.7 mm. Particularly, the octupole component which dominantly contributes in the potential, is pretty low for this separation of inner electrodes.

Both the trap geometries, (1) $\theta_i = 10°$, $\theta_o = 45°$, $2z_o = 0.7$ mm with $2r_o = 1$ mm, (2) $\theta_i = 11°$, $\theta_o = 45°$, $2z_o = 0.7$ mm with $2r_o = 1$ mm give a balanced admixture of harmonic and anharmonic components in the trapping potential. We chose geometry (1) for our ion trap. A comparison of the fractional anharmonicities and loss factor L corresponding to our trap and of prior traps has been given in Tab. 3.3. Octupole component which is one of the dominating contributors in trapping potential has a lower value in the potential created by this trap than that of Stein's. Also, Dodecapole which is contributing majorally in Schrama's trap

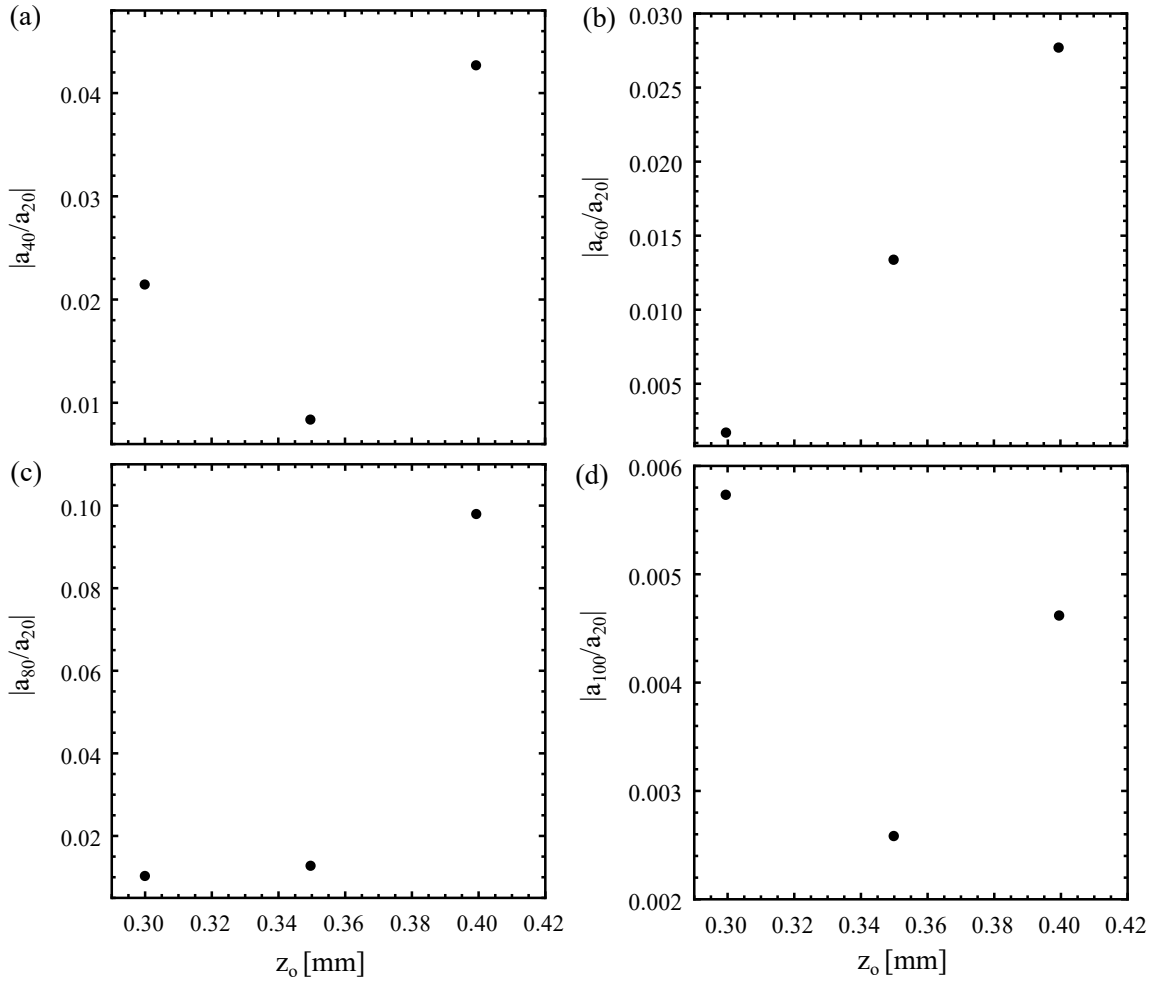

Fig. 3.9: Fractional anharmonicities variation with z_o at $2r_o = 1$ mm, θ_i=11° and θ_o=45°.

Tab. 3.3: Fractional multipole coefficients and loss factor for different traps used by Schrama *et al.* in [49], Beaty in [167] and [168], Stein in [163] and ion trap in this work.

	Schrama	Beaty1	Beaty2	Stein	This work (geometry (1))
$\mid a_{40}/a_{20} \mid$	0.004975	0.00232	0.003152	0.01365	0.00826
$\mid a_{60}/a_{20} \mid$	0.088382	0.00014	0.000816	0.00505	0.01319
$\mid a_{80}/a_{20} \mid$	0.006546	0.013859	0.00132	0	0.0126
$\mid a_{100}/a_{20} \mid$	-	-	-	-	0.00639
L	1.7	1.1	1.1	2.5	2.2

potential has a lower value for this trap. Comparing the various anharmonic components of different traps along with the loss factor, it is found that the anharmonicities in this trap are

comparable to that of other traps. In all, this trap balances between less anharmonicities and high harmonic component (less loss factor L).

3.2.3 Ionic Motion

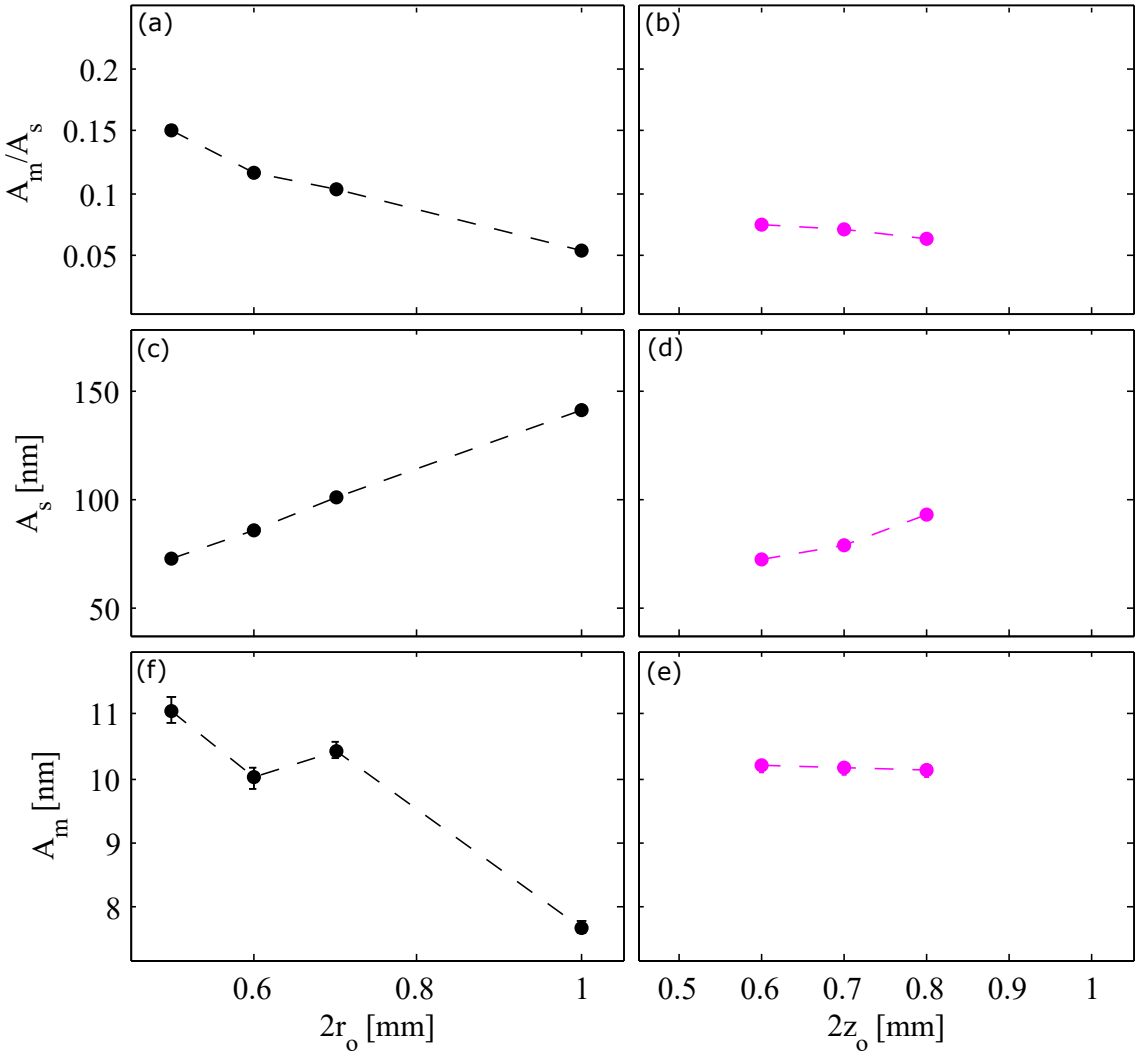

Fig. 3.10: Variation in $\mid A_m \mid$; $\mid A_s \mid$ and $\mid A_m/A_s \mid$ with (a), (c), (f) $2r_o$, for $2z_o = 0.6$ mm, $\theta_i = 0°$ and $\theta_o = 45°$; (b), (d), (e) $2z_o$, for $2r_o = 1$mm, θ_i=11° and θ_o=45°.

In this subsection, different trap geometries are further analyzed on the basis of ionic motion inside the trap. The trajectory of ion motion as given in Eq. 3.20, shows its two components: secular motion ($\beta_j \omega_{rf}/2$), which confines the ion within a boundary as well as micromotion (ω_{rf}), which makes ion move around that boundary. The amplitudes of both these motions

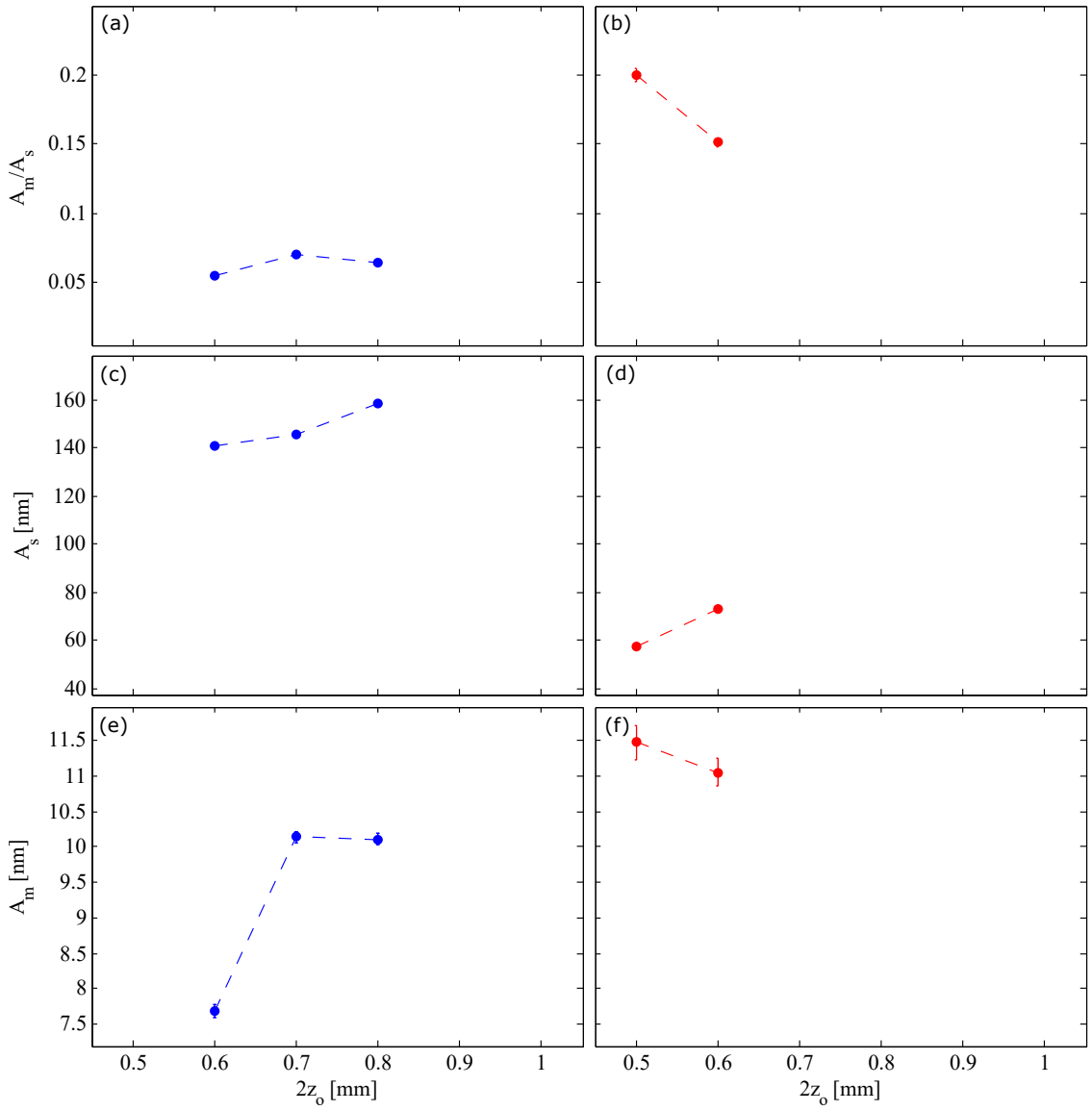

Fig. 3.11: Variation in | A_m |; | A_s | and | A_m/A_s | with: (a), (c), (f) $2z_o$ for $2r_o = 1$ mm, $\theta_i = 0°$ and $\theta_o = 45°$;(b), (d), (e) $2z_o$ for $2r_o = 0.5$ mm, $\theta_i = 0°$ and $\theta_o = 45°$.

depend upon Mathieu parameters a_j and q_j which in turn depend upon the trap geometry as well as operating parameters (see Eq. (3.44)). The equation of motion for trapped Yb^+ ion (mass = 171 a.m.u) is solved for the following trap operating parameters: $U = 0$ V, $V = 500$ V, $\omega_{rf} = 15$ MHz. As amplitude of ion motion have dependence on the trap geometry parameters (for given trap operating parameters), we compare the amplitudes of micromotoion | A_m |; secular motion, | A_s | as well as their ratio | A_m/A_s | for different trap geometries simulated. Figure 3.10 shows a comparison of amplitudes of motion for various $2r_o$ and $2z_o$, keeping other

parameters constant. Larger inner electrode diameter, $2r_o$, is resulting in less micromotion amplitudes. It is expected because of less steep potential for given angles of electrodes θ_i, θ_o. Also, Fig. 3.10 shows that the micromotion amplitudes do not change much over different $2z_o$ values, for $2z_o$ = 1mm, θ_i=11° and θ_o=45° which proved to be a good choice for trap geometry in terms of anharmonicities. This forgiving feature of this geometry is a good for possible inaccuracies and tolerances in distances while assembling. In Fig. 3.11, we try to explore the other sets of geometries with flat inner electrode with increasing the $2z_o$. The effect of angles on amplitudes of motion can be seen in Fig. 3.12 and 3.13. The secular motion amplitudes clearly depend steeply on inner electrode angles with a change of ≈ 80 nm over the range of inner angles from 0° to 60° where as it is hardly changing with ∼ 10 nm over the range of outer angles from 0° to 65°.

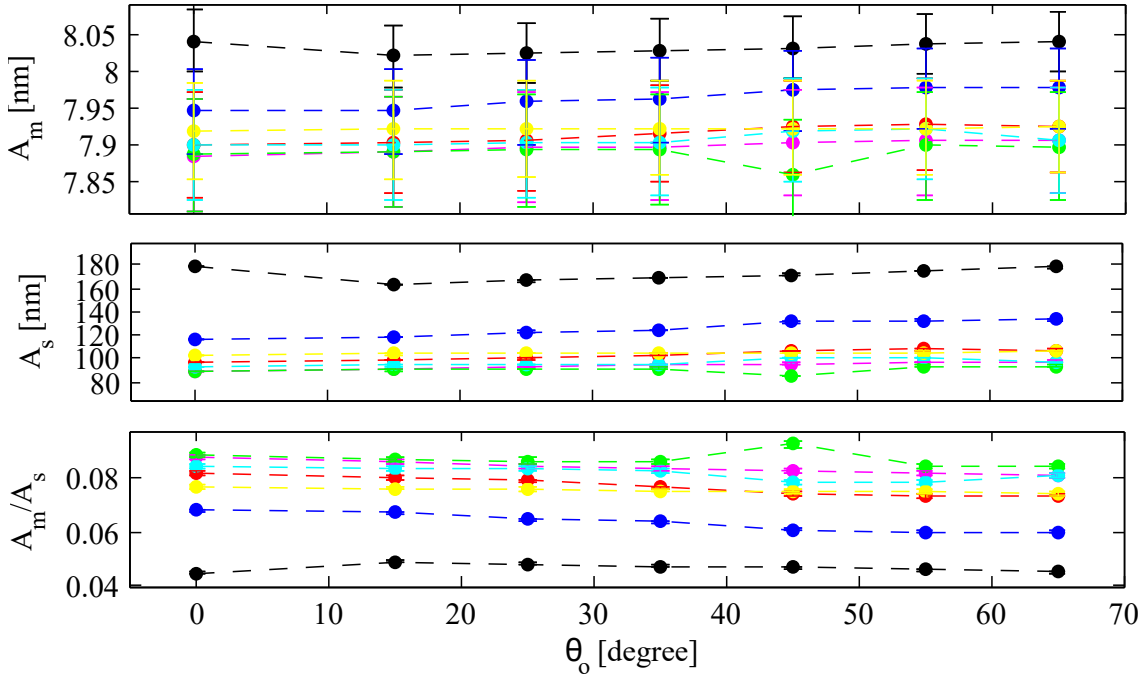

Fig. 3.12: Variation in | A_m |; | A_s | and | A_m/A_s | with θ_o, at $\theta_i = 0°$ (black), 10° (blue), 20° (red), 30° (magenta), 40° (green), 50° (cyan) and 60° (yellow). The distances $2r_o$ = 1 mm, $2z_o$ = 0.6 mm are kept constant for all of them.

Studies of different electrode geometries from perspective of different constraints like obstruction to light, reduced anharmonicities, magnitude of harmonic component and ionic motion agree upon the chosen geometry with parameters $2r_o$ = 1 mm, $2z_o$ = 0.7 mm, θ_i = 10°, and θ_o = 45°. The value of coefficient c_2 (as defined earlier, $c_l = a_{l,0}/2^l z_o^l$) obtained for this geometry is $0.932/mm^2$. From the definition of c_2, the multipole coefficient is calculated to

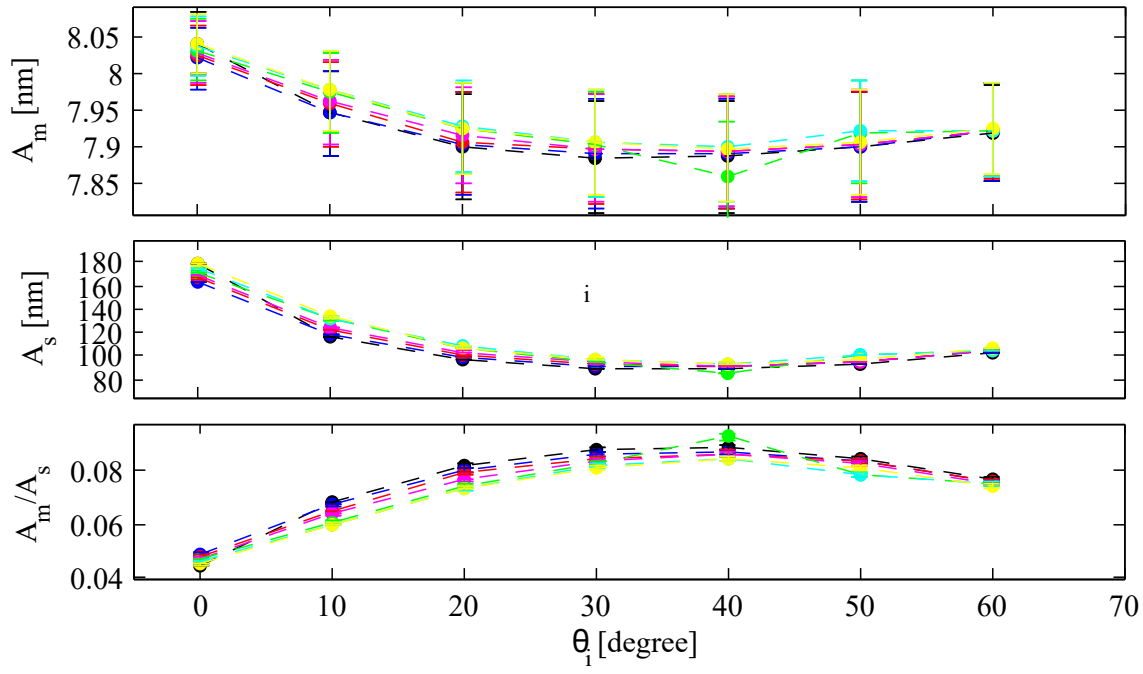

Fig. 3.13: Variation in $\mid A_m \mid$; $\mid A_s \mid$ and $\mid A_m/A_s \mid$ with θ_i, at $\theta_o = 0°$ (black), 15° (blue), 25° (red), 35° (magenta), 45° (green), 55° (cyan) and 65° (yellow). The distances $2r_o = 1$ mm, $2z_o = 0.6$ mm are kept constant for all of them.

be $a_{2,0} = 0.44$. Further, in earlier discussion it was found that taking $q_z \leq 0.28$ can avoid non-linear resonances caused by potential multipoles of $l \leq 10$. If we take $q_z = 0.28$ and apply zero static voltage i.e. $a_z = 0$, then for a fixed value of trap drive frequency we can find the amplitude of trap drive voltage from Eq. (3.44). Let us take $\omega_{rf} = 15$ MHz then for our geometry i.e. $2z_o$=0.7 mm, $2r_o$=1 mm, $\theta_o = 45°$, $\theta_i = 10°$ which correspond to $a_{20} = 0.44$, it is found that V comes out to be ≈ 660 V. Depth of the trapping potential can be calculated for these operating parameters with Eq. (3.48). This gives an axial potential depth of $D_z \approx 9$ eV. As potential depth can be defined in terms of temperatures the maximum temperature of the trapped ion inside trapping potential without being laser cooled is $\approx 10^5$ K, for $D_z \approx 9$

Tab. 3.4: Trap operation parameters and conditions (along axial direction) for our end cap trap geometry, $2z_o$=0.7 mm, $2r_o$=1 mm, $\theta_o = 45°$, $\theta_i = 10°$

Trap Operation	
$a_{2,0}$=0.44	q_z=0.28
U=0	ω_{rf}=0.28
V ≈660 V	D_z=9 eV
a_z=0	$\omega_{s,z}$=1.4 MHz

eV this temperature. The frequency of secular motion along axial direction is calculated to be $\omega_{s,z} \approx 1.4$ MHz for this set of operating parameters. There can be other choices of trap operating parameters but the Mathieu parameters must lie in stability region as shown in Fig. 3.3.

Chapter 4

Estimation of major systematic shifts

The ion trapped in potential is affected by its surrounding rf electric fields, uncompensated stray dc potentials, raised temperature etc and translate these external influences to shift of the observed transition frequency. These are inherent to the system unlike random experimental errors and hence are named systematic shifts. As an optimized geometry is chosen for efficient trapping potential in the last chapter, here the reduced quadrupole shift is calculated for the chosen geometry. This chapter also gives calculated tolerances or restrictions imposed on ion trap structure for targeted accuracy on account of Doppler effect. An estimation of dc Stark, 2nd order Zeeman shifts for our Yb^+ clock is done. Another goal of these shift estimations was to compare the two clock transitions, quadrupole $6s\ ^2S_{1/2}(F=0, m_F=0) \rightarrow 5d\ ^2D_{3/2}(F=2, m_F=0)$ transition at 435.5 nm and octupole $6s\ ^2S_{1/2}(F=0, m_F=0) \rightarrow 4f^{13}6s^2\ ^2F_{7/2}(F=3, m_F=0)$ transition at 467 nm for more accurate clock transition.

4.1. Electric Quadrupole Shift

As already introduced in chapter 2, electric quadrupole shift $\Delta\nu_Q$ to an atomic state with angular momentum F arises due to the interaction of the quadrupole moment $\Theta(\gamma, F)$ with an applied external electric field gradient ∇E, where γ represents for the other quantum numbers of the state. A non-zero atomic angular momentum results in a non-spherical charge distribution, thus atom acquires higher order moments. Thus, the S ground state owing to its spherical charge distribution does not contribute to quadrupole shift in our system. However, the excited states of the $6s\ ^2S_{1/2}(F=0, m_F=0) \rightarrow 5d\ ^2D_{3/2}(F=2, m_F=0)$ and $6s\ ^2S_{1/2}(F=0, m_F=0) \rightarrow 4f^{13}6s^2\ ^2F_{7/2}(F=3, m_F=0)$ clock transitions have $J=3/2; F=2$ and $J=7/2; F=3$ resulting in nonzero quadrupole moments and thus finite quadrupole shifts. These shifts can be estimated by calculating the expectation value of the Hamiltonian given by [122]

$$H_Q = \boldsymbol{\nabla} E \cdot \boldsymbol{\Theta}(\gamma, F) = \sum_{q=-2}^{2} (-1)^q \nabla E_q \Theta_{-q}, \tag{4.1}$$

where ranks of the $\boldsymbol{\nabla} E$ and $\boldsymbol{\Theta}$ tensors are two and their components are indicated by subscript q. The expectation value of H_Q in reduced form can be expressed as [88]

$$\begin{aligned}\langle \gamma J F m_F | H_Q | \gamma J F m_F \rangle &= \Theta(\gamma, J)\, \mathcal{F}_Q(I, J, F, m_F) \\ &\quad \times \sum_{q=-2}^{2} \nabla E_q D_{0q}, \end{aligned} \tag{4.2}$$

where m_F is the magnetic quantum number, D_{0q} are the rotation matrix elements of the projecting components of ∇E in the principal axis frame that are used to convert from the trap axes to the lab frame [169], $\Theta(\gamma, J)$ is the quadrupole moment of the atomic state with angular momentum J and

$$\begin{aligned}\mathcal{F}_Q = (-1)^{I+J+F}(2F+1) &\begin{pmatrix} F & 2 & F \\ -m_F & 0 & m_F \end{pmatrix} \\ \times &\begin{pmatrix} J & 2 & J \\ -J & 0 & J \end{pmatrix}^{-1} \begin{Bmatrix} J & 2 & J \\ F & I & F \end{Bmatrix}. \end{aligned} \tag{4.3}$$

Here the quantities within ( ) and { } represent the $3j$ and $6j$-coefficients, respectively. Both the excited states of the above mentioned clock transitions acquire $\mathcal{F}_Q = 1$. Due to axial symmetry of the trap, the frequency shift contributions from $D_{0\pm1}$ cancel with each other, thus finite contributions comes only from the $D_{00} = (3\cos^2\theta - 1)/2$ and $D_{0\pm2} = \sqrt{3/8}\sin^2\theta(\cos 2\phi \mp i \sin 2\phi)$ components, for the Euler's angles θ and ϕ. For estimation of this shift, we required values of quadrupole moments for which we collaborated with Dr. B. K. Sahoo who calculated Θ values for the $5d^2D_{3/2}(F = 2)$ and $4f^{13}6s^2\ {}^2F_{7/2}(F = 3)$ states to be 2.079(8) and -0.224(10) respectively. The method used for these calculations was Coupled cluster single-double $CCSD_{ex}$ with experimental values of ΔE_v, the attachment energy of the electron in the valence orbital v and ΔE_a, the ionization potential of the electron in the orbital a, details of these can be found in [170]. We used these values to find out the optimum electrode geometries that can produce nearly-ideal quadrupole confining potentials with reduced anharmonicities.

In order to estimate quality of the trap potentials, we consider l up to 10 since amplitudes of $\Phi^{(l)}$ fall drastically at higher k. The quadrupole shift due to the l^{th} order multipole depends on amplitude of the potential which falls steeply as R^{-l}. For $l > 2$ the shift vanishes at the trap center and increases nonlinearly, as the ion goes away from the center. The fractional quadrupole shift $\Delta\nu_Q/\nu_0$ at each l is estimated from Eq. (4.2). The variation of $\Delta\nu_Q/\nu_0$ for all multipole potentials up to $l = 10$ at two different distances from the trap center are estimated for the E2 and E3-clock transitions, which are shown in Fig. 4.1(a-b). The reported experimental values of the quadrupole shifts for these two transitions are also depicted in the same figure for the comparison. The dominating perturbation of $\Phi^{(2)}$ arises from the octupole

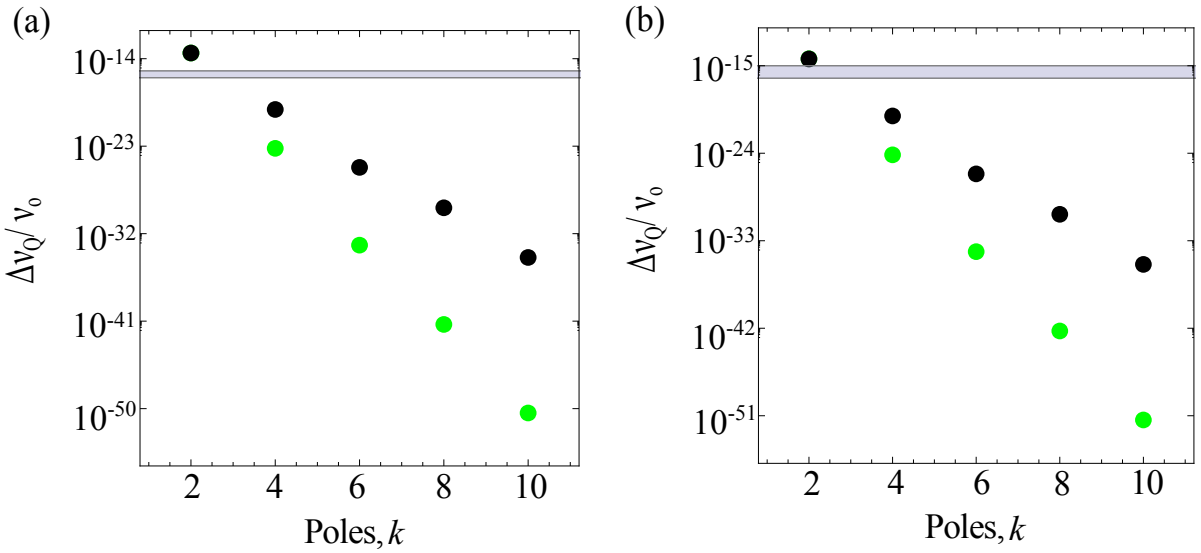

Fig. 4.1: Fractional electric quadrupole shifts due to the multipoles up to $l = 10$ for the (a) E2 and (b) E3 transitions, when the ion is off centered by a distance 0.1 μm (green) and 10 μm (black), respectively. The harmonic potential gives a spatially independent $|\Delta\nu_Q/\nu_o|$. The reported fractional accuracies lie within the grey bands and so far the best accuracies are 1.1×10^{-16} [93] and 3×10^{-18} [9] for the E2 and E3-transition, respectively.

term $\Phi^{(4)}$ which may largely affect the quadrupole shift of the trapped ion frequency standards due to wrong choice of the electrode geometry. Therefore, we simplify the analysis considering $\Phi(x, y, z) \simeq \Phi^{(2)} + \Phi^{(4)}$ since other higher orders are less significant for the quadrupole shift. The first order quadrupole shift from the ac voltage $V\cos(\omega_{rf}t)$ component averages to zero [94] and its second order is proportional to m_F, so it is also zero in our case. We estimate the shift considering dc component of the voltage only with $U = 10$ V. The quadrupole shift as given by $\sum_q \nabla E_q D_{0q}$ results to $2V_T c_2[D_{00} - D_{02}/\sqrt{6}]$ due to the harmonic part of the potential and it is constant within the trapping volume. The spatial dependency comes from the higher orders, for example $\Phi^{(4)}$ results to a quadrupole shift of $12V_T c_4[4z^2(D_{00} - D_{02}/\sqrt{6}) - r^2(2D_{00} - \sqrt{3/2}D_{02})]$. Figure 4.2(a-d), shows variation of the quadrupole shift at the center of the trap with diameter and tip-to-tip separation of the inner electrode keeping θ_i and θ_o values fixed. As analyzed in last chapter, the optimized values of radii and separations came out to be $2r_o = 1$ mm and $2z_o = 0.7$ mm for which $\Delta\nu_Q$ is reduced but not minimized. Further attempt to minimize the quadrupole shift causes increase in anharmonicity and micromotions. Dependence of the quadrupole shift on θ_i and θ_o are shown in Figs. 4.2 (e-f). These clearly show that the quadrupole shift increases at large θ_i but it has relatively weak influence on θ_o. A pair of inner electrodes with flat surfaces introduces minimum shift. However, as discussed earlier $\theta_i = 0$ gives optical blockage at our optimized $2z_o = 0.7$ mm. To avoid the optical blockage we have optimized the values of θ_i and θ_o at 10° and 45°, respectively. These would produce insignificant

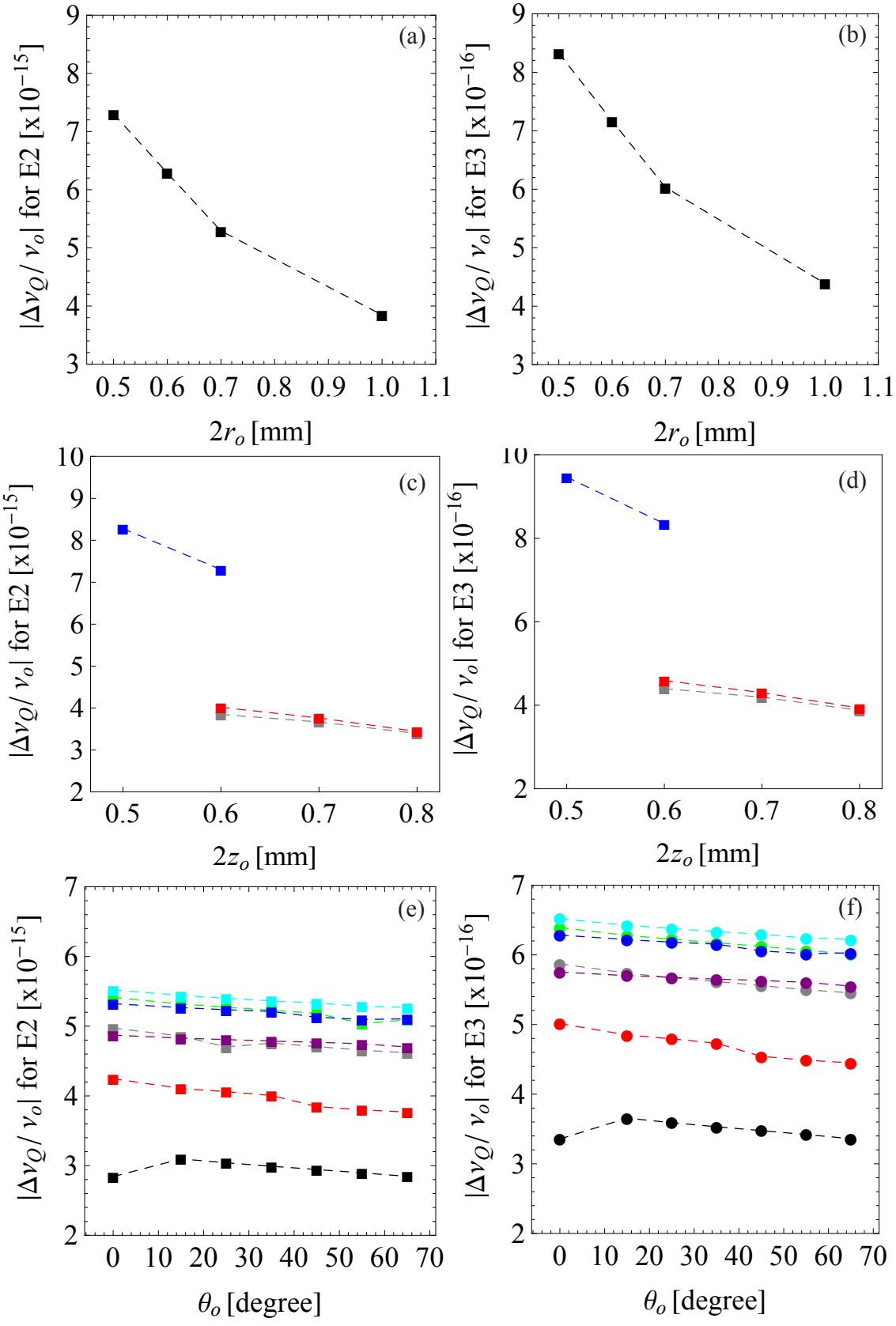

Fig. 4.2: Fractional electric quadrupole shift for the E2 and E3-clock transitions varying with different geometrical parameters: (a, b) with $2r_o$, $2z_o = 0.7$ mm, $\theta_i = 10°$ and $\theta_o = 45°$; (c, d) with $2z_o$ $2r_o = 1$ mm, $\theta_i = 10°$ and $\theta_o = 45°$; and (e, f) with θ_o, $2r_o = 1$ mm and $2z_o = 0.7$ mm, different colors signify different values of θ_i: 0° (black), 10° (red), 20° (gray), 30° (green), 40° (cyan), 50° (blue) and 60° (purple). The dashed line connects data points for the fixed values of θ_i.

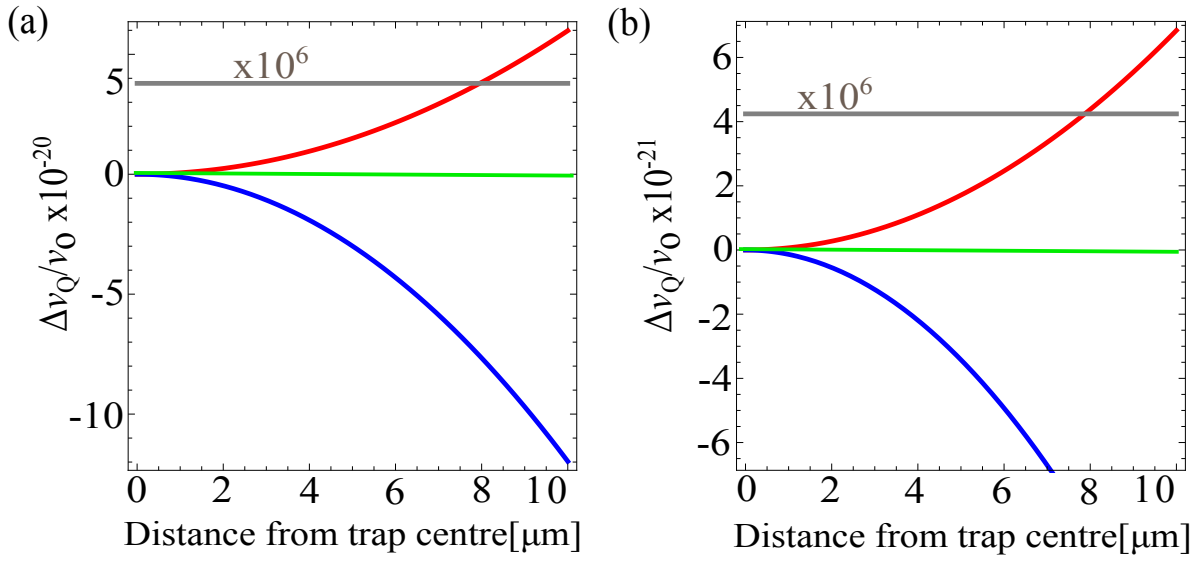

Fig. 4.3: Spatial dependence of the fractional electric quadrupole shifts $\Delta\nu_Q/\nu_o$ for the E2 and E3-clock transitions of $^{171}Yb^+$. The quadrupole trapping potential produces a constant shift (gray). The spatial dependence in the shift along the radial (red) and axial (blue) directions arise from the anharmonic components $l > 2$ of $\Phi^{(l)}$.

number of scattered photons from the tails of Gaussian laser beams which will propagate along the three mutually orthogonal directions. For our trap geometry the coefficients c_2 and c_4 are 0.93 and 0.11, respectively.

The ion still undergoes a residual thermal motion after being laser cooled, making it unlikely to probe the clock transition while it being sitting at the center of the trap. Also there is a possibility of shift in mean position of the ion from the trap center due to imperfect stray field compensation. This results to a spatially dependent $\Delta\nu_Q$ in a non-ideal ion trap. Figure 4.3 shows spatial variation of $\Delta\nu_Q/\nu_0$ due to $\Phi^{(4)}$ and compares that with shift resulting from $\Phi^{(2)}$. Figures 4.1 and 4.3 clearly show that the quadrupole shift due to the dominating anharmonic potential is insignificant for a frequency standard of accuracy $\sim 10^{-18}$, when the ion is positioned in the vicinity of the trap center within sub-micron precision and at a tight confinement. The quadrupole shift due to $\Phi^{(2)}$ can be eliminated by measuring the clock frequency along the three mutually orthogonal orientations in the lab frame and averaging them while quantizing the ion using the magnetic fields of equal amplitudes [88, 142]. Such angular averaging also eliminates the quadrupole shift due to $\Phi^{(4)}$ provided the trap is perfectly axially symmetric, as shown in Fig. 4.3. In practice the trap can deviate from such an ideal situation which could lead to inaccuracy in eliminating the quadrupole shift by angular averaging. In such a non ideal trap the inaccuracies of eliminating the quadrupole shift are generally induced by $\Phi^{(4)}$ but it is below the accuracy of frequency standard that is aimed. The present analysis helps us in building a suitable trap electrode where the effect of $\Phi^{(2)}$ in the quadrupole shift is

Tab. 4.1: Calculated values of Θ (bold) along with the values available from other calculations and the experimental results [170].

Method	$4f^{14}5d\,^5\mathrm{D}_{3/2}$	$4f^{13}6s^2\,^2\mathrm{F}_{7/2}$
$\mathbf{CCSD_{ex}}$	**2.079(8)**	**− 0.224(10)**
Others	2.174[172]	−0.22[171]
	2.157[174]	−0.20[173]
	2.068(12)[175]	−0.216(20)[175]
Experiment	2.08(11)[94]	−0.041(5)[93]

reduced.

To get a figure of merit of our design, we have estimated the quadrupole shifts along with their uncertainties in our optimized setup and compared the result with the previously available values. The formula for quadrupole shift given above can be simplified and can be written in terms of multipole coefficient dependence as

$$\Delta\nu_Q = \frac{c_2 U}{R^2} \times \mathcal{F}_Q \times \Theta. \tag{4.4}$$

Substituting values of Θs from Table 4.1, we estimate these shifts for a constant $c_2U/R^2 = 932$ V/cm^2 which is expected in our trap geometry at $U = 10$ V. All the resultant quadrupole shifts for the E2 and E3-clock transitions are shown in Figs. 4.4 (a) and (b), respectively. This shows that in our trap the quadrupole moment of the $5d\,^2D_{3/2}(F = 2)$ state can be measured to an accuracy of 1 part in 10^3. This uncertainty will be one order of magnitude better than the previous measurement [94]. Similarly, the quadrupole moment of the $4f^{13}6s^2\,^2F_{7/2}(F = 3)$ state was previously measured with 12% accuracy. The accuracy of this quantity is also expected to be improved using our proposed ion trap. This will help to verify the reported discrepancies among the experimental and theoretical results.

4.2. Second Order Doppler Shift

The relative motion between the laboratory and the ionic frames of reference introduces a shift in the observed frequency. The absorbed or emitted radiation $E_o \cos(\omega_o t)$ at frequency $\omega_o = 2\pi\nu_o$ (wavelength λ_o) experiences a phase modulation $\eta \sin\omega_s t$ due to secular motion of the trapped ion at frequency ω_s. The modulation depth $\eta = \Delta\omega_o/\omega_s$ depends on the Doppler shift $\Delta\omega_o = 2\pi v/\lambda_o$ due to ion's velocity $v = \omega_s r$. A modulated spectrum $E_o \cos(\omega_o t) \pm \eta E_o \cos(\omega_o \pm \omega_s)t$ is expected when the ion is confined within $r < \lambda_o$ [176], which has been observed in an absorption spectroscopy for a narrow transition [177]. This allows accurate determination of the first order Doppler unshifted ν_o for a laser cooled ion. However the second order Doppler

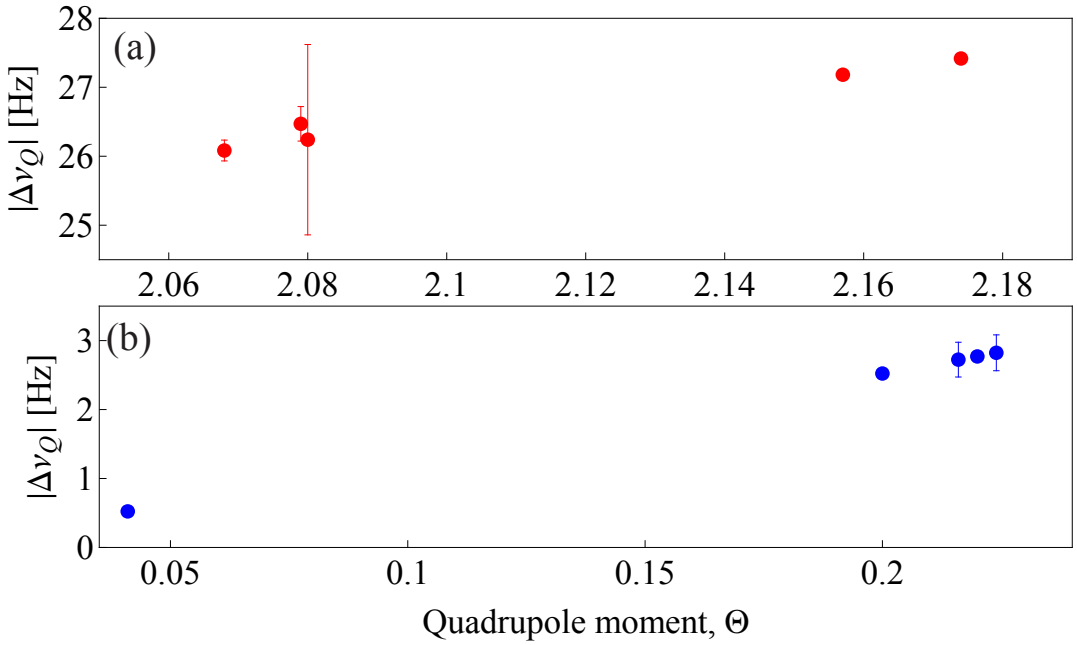

Fig. 4.4: The electric quadrupole shifts from previously reported works and estimated values from this work are shown in (a) for the $6s\ ^2S_{1/2} \rightarrow 5d\ ^2D_{3/2}$ and (b) for the $6s\ ^2S_{1/2} \rightarrow 4f^{13}6s^2\ ^2F_{7/2}$ clock transitions.

effect introduces a frequency shift, which is

$$\frac{\Delta\nu_{D2}}{\nu_o} = -\frac{v^2}{2c^2} = \frac{2\varepsilon_k}{mc^2} \tag{4.5}$$

for kinetic energy ε_k of the ion; c is speed of light.

Velocity of the trapped ion can be calculated from its trajectory, which gets deviated from Eq. (3.20) due to slowly varying stray electric fields. These electric fields may result from the patches of unwanted atoms on the electrode surface or relative phase differences of the rf delivered to them. Over the time, Tantalum electrodes get coated with ^{171}Yb atoms coming out of the oven. The differential work-function of Ytterbium and the Tantalum results to an electric field E_p, which varies slowly with the deposition of atoms. As a result of an extra force, QE_p, the minimum of the confining potential shifts. And this results in a shift in ion trajectory (see Eq. (3.20)) by an amount $\acute{C_0} = QE_p \cdot \hat{u}/(m\omega_s^2)$ resulting in a increase of micromotion [142].

Another cause of stray electric field is difference in path lengths and non-identical dimensions of the electrodes. Due to this difference in path lengths, there arises a phase difference ϕ_o between the rf and result in voltages $V\cos(\omega_{rf}t \pm \phi_o/2)$ on either of the electrodes. This means there exists a short duration of time when the two inner electrodes does not have same polarity. As the diameter of inner electrodes is small and so is the θ_i, therefore the counterfacing surfaces

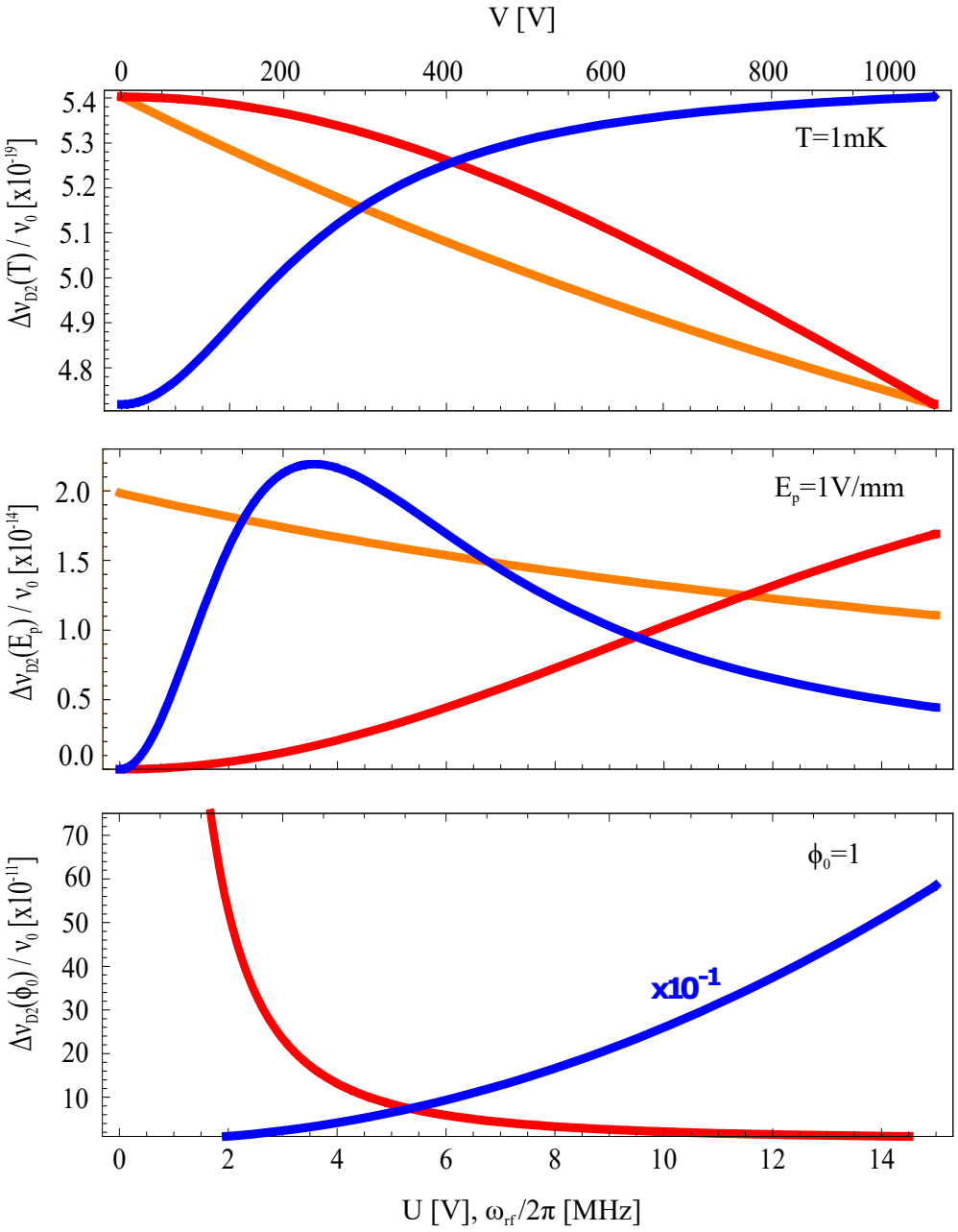

Fig. 4.5: Variation of the second order Doppler shifts with respect to the trap parameters radio-frequency, ω_{rf} (red); ac, V (blue) and dc, U (orange) voltages resulting from (a) temperature of the ion T, (b) patch potential that ion experiences E_p and (c) relative phase difference of rf at two electrodes ϕ_o.

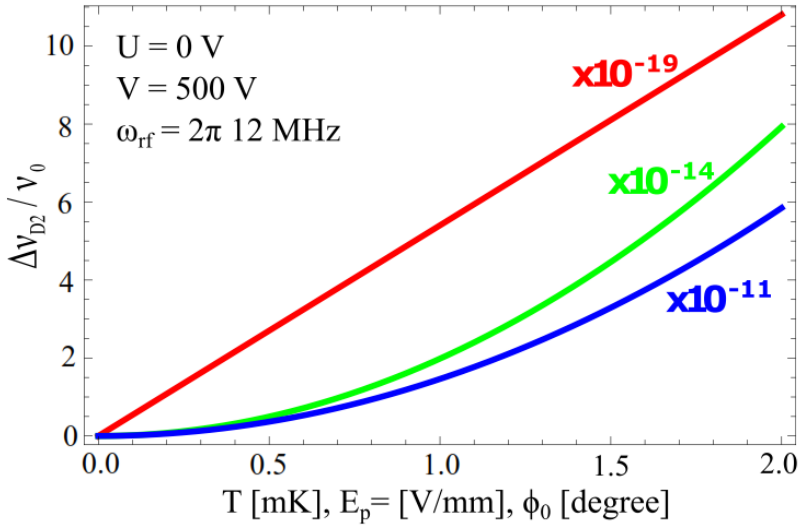

Fig. 4.6: Fractional Second-order Doppler shift $\Delta\nu_{2D}/\nu_o$ with: temperature, T (red); patch potential generated electric field, E_p (green); phase difference of rf at endcaps, ϕ_o (blue).

can be approximated to flat plates. And the electrodes' assembly can be approximated to a parallel plate capacitor. Separation between them is given by $2z_o/\alpha$ where the geometric factor $\alpha \approx 0.8$ for trap geometries satisfying ${r_o}^2 = 2{z_o}^2$ [178, 168]. Expanding the rf on one of the electrode at a given time, we get:

$$V\cos(\omega_{rf}t - \frac{\phi_o}{2}) = V(\cos\omega_{rf}t\cos\frac{\phi_o}{2} + \sin\omega_{rf}t\sin\frac{\phi_o}{2}) \tag{4.6}$$

For $\phi_o \ll 1$,

$$\cos\frac{\phi_o}{2} \approx 1; \tag{4.7}$$

$$\sin\frac{\phi_o}{2} \approx \frac{\phi_o}{2} \tag{4.8}$$

So, the total rf voltage at the electrode is given as

$$= \quad V\cos\omega_{rf}t + V\frac{\phi_o}{2}\sin\omega_{rf}t \tag{4.9}$$

and the extra potential on the electrodes due to phase difference ϕ_o is $\pm V\frac{\phi_o}{2}\sin\omega_{rf}t$. This results in an alternating stray electric field $E_{\phi_0} = \alpha V\phi_o\sin\omega_{rf}t/2z_o\hat{z}$ across the parallel plates of the capacitor which increases micromotion along the axial direction. If C_e be the capacitance of the parallel plate capacitor and Q_e be the charge stored then electric field can be written as $E_{\phi_0} = \alpha Q_e/2C_e z_o$. The numerical values of capacitance C_e and charge Q_e can be simulated for trap assemblies.

The above mentioned stray electric fields subject ion to excess force hence the ion trajectory

gets modified as

$$\begin{aligned} u(t) &\cong [\acute{C_0} + C_0\cos(\omega_{rf}t)]\Big[1 + \frac{q_u}{2}\cos(\omega_{rf}t)\Big] \\ &- \frac{1}{4}q_u z_o \alpha\phi_0 \sin(\omega_{rf}t)\delta_{u,z}. \end{aligned} \tag{4.10}$$

as described in Ref. [142], which gives excess kinetic energy to the ion. The average kinetic energy is

$$\begin{aligned} \varepsilon_{k,u} &= \frac{1}{4}mC_0^2\Big[\omega_s^2 + \frac{1}{8}q_u^2{\omega_{rf}}^2\Big] + \frac{4}{m}\Big[\frac{Qq_uE_p\cdot\hat{u}}{(2a_u+q_u^2)\omega_{rf}}\Big]^2 \\ &+ \Big[\frac{m(q_uz_o\alpha\phi_o\omega_{rf})^2}{64}\Big]\delta_{u,z} \end{aligned} \tag{4.11}$$

where the first term contributes from the confining potential and remaining two terms are due to the E_p and ϕ_o, respectively. The fractional frequency shift which is independent of ν_o can be calculated using Eq. (4.5). Each component of $\Delta\nu_{D2}/\nu_o$ depends on the trap parameters ω_{rf}, V and U as shown in Fig. 4.5. Figure 4.6 shows $\Delta\nu_{2D}/\nu_o$ due to the patch potentials and ac phase difference at the two counteracting electrodes can produce orders of magnitude larger frequency shift than any other systematic effects. These are also discussed by Berkeland et. al. in Ref. [142] and by P. Gill in Ref. [179]. This concludes, for building a frequency standards of fractional accuracy 10^{-17}, one has to control at a level $\phi_o < 0.05$ degree and E_p < 20 mV/mm respectively. We will employ two additional pairs of compensation electrodes in the radial plane for cancelling stray potentials that ion experiences and the accurate machining will be essential for maintaining nearly zero path difference of the applied rf to the electrodes.

4.3. DC Stark Shift

Interaction of electric dipole moment (EDM) of an atom with an electric field results in Stark shift [180, 88] of the atomic energy levels. The interaction energy is given as

$$H_I = -\vec{E}\cdot\vec{d}, \tag{4.12}$$

where $\vec{E}$ is the electric field and $\vec{d}$ is the electric-dipole. In an experiment the patch potentials lead to a dc Stark shift. The electro-magnetic (EM) radiations at the non-zero temperature of the apparatus also introduces dc Stark shift which is known as black body radiation (BBR) shift. For $^{171}Yb^+$ the first order Stark shift is zero because ion acquires a zero permanent EDM. The coupling of the $^2S_{1/2}$, $^2D_{3/2}$ and $^2F_{7/2}$ states in $^{171}Yb^+$ to all the other states via electric dipole interaction results to a non-zero second-order Stark shift which is not negligible. An induced EDM produce second order Stark shift [180], which can be expressed using Wigner-

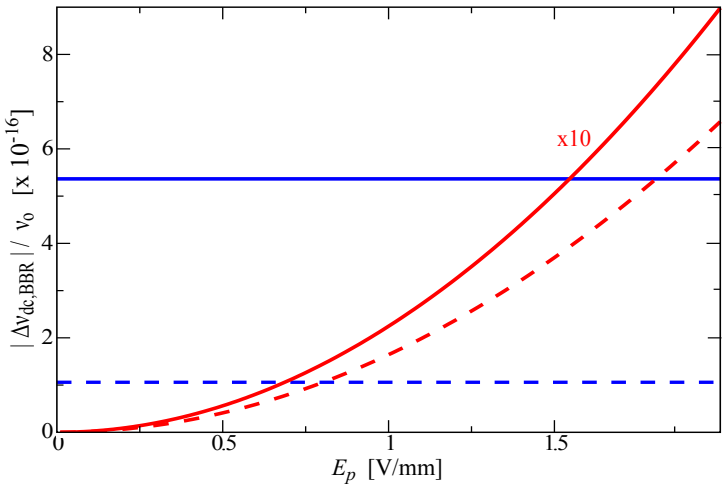

Fig. 4.7: Variation of the fractional dc Stark shift $\Delta\nu_{dc}/\nu_o$ due to both scalar and tensorial polarizabilities with electric field E_p (red) and the fractional BBR shift $\Delta\nu_{BBR}/\nu_o$ due to scalar polarizability at 300 K (blue). E2 and E3-transitions are distinguished by solid and dashed lines, respectively.

Eckart theorem as

$$\Delta\nu_{dc} = -\frac{1}{2h}\alpha E_p^2, \tag{4.13}$$

where h is the Plank constant, α is polarizability having both scalar (α_s) and tensor (α_T) contributions. The effective $\Delta\nu_{dc}$ is calculated as the difference between the shifts of the states involved in the clock transition [88, 181] as

$$\Delta\nu_{dc} = \frac{1}{4h}\left[2\Delta\alpha_s + \Delta\alpha_T(3\cos^2\theta - 1)\right] E_p^2, \tag{4.14}$$

where θ is the angle between electric field and the quantization axis, $\Delta\alpha_s$ and $\Delta\alpha_T$ are the polarizability differences of the states associated to the clock transition. The Stark shift becomes independent of $\Delta\alpha_T$ at $\theta = 54.73^o$ but in our experiment $\theta \approx 0^o$ fixed by geometry of the apparatus. Here we estimate the second order Stark shifts resulting from dc electric field and EM-radiation.

The Stark shift due to the $\Delta\alpha_T$ vanishes at the ground state because of its symmetric nature but is non zero for the $^2D_{3/2}$ and $^2F_{7/2}$ states. Using the measured polarizibilities of $^2S_{1/2}$, $^2D_{3/2}$ states [94] and $^2F_{7/2}$ state [93] variation of $\Delta\nu_{dc}$ for the E2 and E3-transitions are shown in Fig. 4.7. The electric field associated to the EM-radiation at finite temperature of the apparatus gives rise to BBR shift, which is one of the dominating systematic uncertainty in frequency standards. The spectral energy density is given by the Planck's law [182] as

$$E^2(\omega)d\omega = B^2(\omega)d\omega = \frac{8\alpha^3}{\pi}\frac{\omega^3 d\omega}{\exp(\frac{\omega}{k_B T}) - 1}, \tag{4.15}$$

where B is magnetic field, α is emissivity of the material and ω is frequency of EM-radiation. The wavelength corresponding to the maximum of the spectral energy density at 300 K is 9.7 μm [183], which is large compared to the longest transition wavelength ≈ 2.4 μm in $^{171}Yb^{+}$. To a good approximation the BBR generated RMS amplitude of E and B fields are $< E^2 >= E_o^2 \times (T/300)^4$ V/m and $< B^2 >= B_o^2 \times (T/300)^4$ T, where $E_o = 831.9$ V/m and $B_o = 2.775 \times 10^{-6}$ T, respectively [184]. The magnetic field contributes to a Zeeman shift, which will be discussed in the section 4.4. The contribution due to α_T can be neglected for an isotropic EM-radiation and the effective BBR shift can be written as

$$\Delta\nu_{BBR} = -\frac{1}{2h}\Delta\alpha_s\, E_o^2 \left(\frac{T}{300}\right)^4. \tag{4.16}$$

At room temperature a shift of about 0.36 Hz and 0.068 Hz is estimated for E2 and E3-transitions, respectively. The fractional uncertainty due to this shift was calculated to be 5.23×10^{-16} and 1.06×10^{-16} for E2 and E3-transitions, respectively.

4.4. Zeeman Shift

As already discussed in chapter 2, Zeeman shift arises due to the interaction of atomic and nuclear magnetic moments μ_J and μ_I with a magnetic field. In an experiment, magnetic field appears from the BBR, geomagnetic and stray fields. The E2 and E3-clock transitions are insensitive to the linear Zeeman effect since both the ground and excited states associated to them are with $m_F = 0$. Neglecting the nuclear part of the shift, since the g-factor for the electrons g_J are much larger than it is for the nucleus g_I, the second order Zeeman shift [185] of the sublevels can be determined as

$$\Delta\nu_{\mathrm{QZ}} = -\frac{1}{h}\left(\frac{g_J e B}{4\pi m}\right)^2 \sum_{F'} \frac{|\mathcal{F}_Z(I,J,F,F',m_F)|^2}{\Delta\nu_{HFS}}, \tag{4.17}$$

where $\Delta\nu_{HFS}$ is the hyperfine splitting of the states and the matrix element $< F', m'_F|J_z|F, m_F >$ [150] is given as

$$\begin{aligned} \mathcal{F}_Z &= \sqrt{I(I+1)(2I+1)(2F+1)(2F'+1)} \\ &\quad \begin{pmatrix} F & 1 & F' \\ -m_F & 0 & m_F \end{pmatrix} \begin{Bmatrix} I & F & J \\ F' & I & 1 \end{Bmatrix}. \end{aligned} \tag{4.18}$$

The calculated $|\mathcal{F}_Z|^2 = 1/4$ for the $^2S_{1/2}$, $^2D_{3/2}$ and $^2F_{7/2}$ states in $^{171}Yb^{+}$, using their $g_J = 1.998, 0.8021, 1.1429$ and $\Delta\nu_{HFS} = 12.643, 0.86, 3.62$ GHz, respectively [186]. The geomagnetic field in New Delhi, India is approximately 50 μT which produces $\Delta\nu_{\mathrm{QZ}}$ of 38.75

Hz, 91.15 Hz, and 44.19 Hz at the $^2S_{1/2}$, $^2D_{3/2}$ and $^2F_{7/2}$ states, respectively. This results to a net second order Zeeman shift of 52.40 Hz and 5.44 Hz for the E2 and E3-clock transitions, respectively. These are much larger than the effect of the magnetic field due to BBR at the room temperature whose values are 0.16 Hz and 0.017 Hz for E2 and E3 clock transitions, respectively.

Tab. 4.2: Fractional shifts due to the systematic effects for the E2 and E3-transitions. The shifts are estimated at the room temperature $T = 300$ K, rf phase difference $\phi_o = 0.05°$, stray electric and magnetic fields $E_p = 20$ mV/mm and $B = 1$ μT. Numerical values of ϕ_o, E_p and B which are used here are typical values that can be achieved with proper minimization techniques.

Systematic effect	E2-transition $[\times 10^{-17}]$	E3-transition $[\times 10^{-18}]$
Electric quadrupole	3813.3	−789.1
Second order Doppler	−1	−10
dc Stark	−0.09	−0.07
BBR	−52.3	−106
Second order Zeeman	−7.55	−3.39

The systematic shifts from different source which have been estimated for the E2 and E3-transitions are summarized in Tab. 4.2. Even though the electric quadrupole shift is the largest, averaging the measured frequency along three orthogonal directions effectively cancels $\Delta\nu_Q$. Three pairs of mutually orthogonal Helmholtz coils has been designed and installed for defining the quantization axes (discussed in chapter 7). These coils will be used to cancel the Earth's and static stray magnetic fields as well, for minimizing the quadratic Zeeman shift. The thermal part of $\Delta\nu_{D2}(T)$ is an order of magnitude smaller compared to the frequency standard that we aim for. Careful wiring for supplying rf and accurate machining of the electrodes is very important for making $\phi_o \approx 0°$. Two pairs of electrodes will be installed in the radial plane for compensating the local electric fields that a trapped ion feels, which is required for minimizing $\Delta\nu_{D2}(E_p)$ and $\Delta\nu_{dc}$. Temperature at the position of ion needs to be measured accurately for estimating the shifts produced by BBR, for which we plan to place temperature sensors inside UHV (see chapter 5). Apart from the $\Delta\nu_Q$ our estimation concludes that the E3-transition can provide factor of five accurate frequency standard than the E2-transition of $^{171}Yb^+$.

Chapter 5

Design of ion trap, UHV chamber and vacuum assembly

After identification of suitable trap electrodes geometry (discussed in chapter 3), in this chapter the design of ion trap structure inside the ultra high vacuum (UHV) chamber has been discussed. Many systematics as well as lifetime of ion inside trapping potential also depends upon various factors such as choice of materials for machining electrodes, design and materials of structure which holds them inside UHV, type of electrical connections etc. Additionally, for an accurate clock thoughtful design of UHV chamber which houses the ion trap structure, atomic oven, collection lens etc. are very important. Besides structural constraints, the design also needs to fulfil constraints arising due to experimental conditions and physics requirements. This chapter describes constraints, requirements and the design process of the ion trap structure along with UHV chamber starting from the thought process to the fabricated and assembled products. It also discusses the design of complete ultra high vacuum assembly. Details of complete lab set up with its layout has also been discussed.

5.1. Ion Trap Design

A trapped ion is affected by its surroundings in the ultra high vacuum through heat exchange mainly from dielectric insulators. Different parts of the trap when not in good thermal contact, do not support proper heat flow and develop temperature gradients across them. These design flaws lead to Black body radiation (BBR) effect. As different surfaces of the trap are made of different materials like metals and dielectrics which come in direct line of sight of ion have different temperatures and emissivities, estimating temperature in the vicinity of ion accurately is quite difficult. The inner electrode which is nearest to the ion covers a large portion of solid angle made by ion needs to be protected from heat transfers from dielectrics and stray potentials. A carefully designed trap can do that. Delivery of out of phase radio frequencies across two electrodes subject ion to additional electric field and thus give rise to second order Doppler. Some major constraints out of many constraints which need to be considered while

designing a trap are listed below (in no particular order):

- No obstruction to incident light beams impinging on the ion
- Ideally, there must not be any path difference between electrodes carrying rf. Considering machining tolerances in real cases, path difference must be minimum
- Insulation between rf and dc voltages, i.e. between inner and outer electrodes
- Concentricity of inner-outer electrodes among themselves as well as their counter facing sub-assembly
- Minimal use of dielectrics as they contribute in increased trap capacitance
- Avoiding direct contact of inner electrodes with insulating dielectric material which result in heat exchange.
- Proper ventilation from nook and corners for pumping out gas molecules
- Precise machinability
- Stable assembly of all the parts and firm mounting mechanism of the trap to avoid time dependent changes.

As discussed in chapter 3, an end cap trap geometry is opted for this clock experiment. The end cap trap has two counter facing end cap cylindrical electrodes which are cut conical in shape at the front faces. These cylindrical electrodes have a pair of outer cylinders surrounding them. The inner electrodes are supplied with an oscillating voltage and the outer electrodes are kept either at ground or at a dc voltage. These two sets of electrodes need to be aligned in such a way that they are concentric to the other set as well as within themselves. Many versions of end cap trap have been designed and prototyped, following the above mentioned constraints as design guidelines. Few of them are described here with their flaws and advantages.

Figure 5.1 show three versions of trap designs. The first design of trap, named 1, is shown in Fig. 5.1(1). It has a metallic holder-cum-stand, part A, as the main support structure which has a C-shaped section and a mounting arm. The C-shaped section of part A holds inner electrodes at its two cantilever arms through push fit mechanism and is used for applying identical rf voltage to the inner electrodes as it is mounted on an electrical feedthrough. This design provides identical path lengths up to the electrodes which ensure negligible phase difference between rf voltages applied to the electrodes. The outer electrodes are push fitted into a separate L shaped holder, part C, to place them coaxial with the inner electrodes. Part C is attached to part A via an L-shaped insulating spacer, part B. Both the inner and outer holders are used for electrical connections of rf and dc voltages being separated by the L shaped insulating spacer. Part A can be machined out of a single block in which a through hole assures

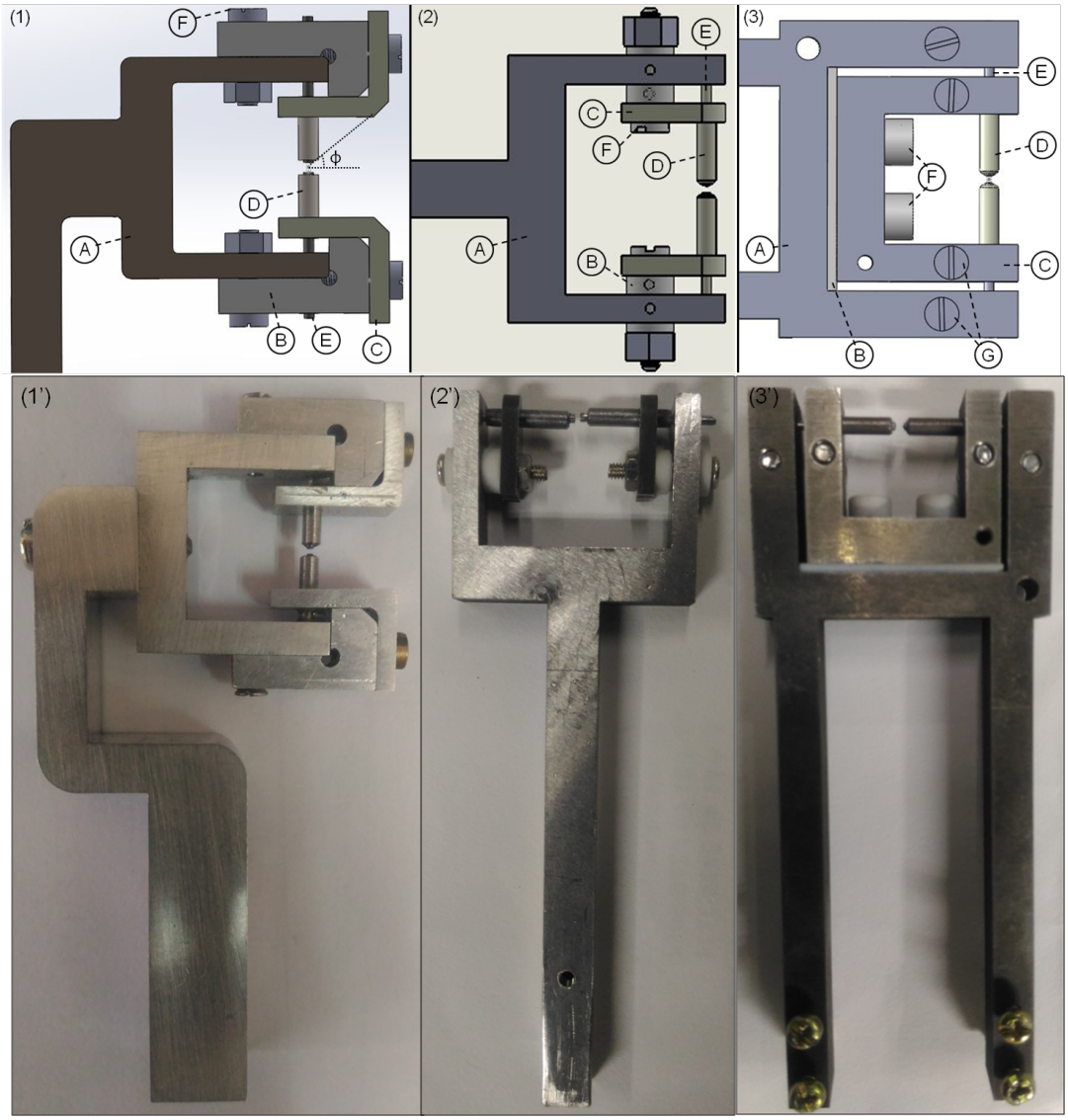

Fig. 5.1: Different designs of the trap assembly (1), (2) and (3) with convention A: trap holder cum stand. B:insulating spacer, C:holder for outer electrodes, D:outer electrodes, E:inner electrodes, F:metallic screws and G:clamping screws. Machined prototypes of (1), (2) and (3) are shown in (1'), (2') and (3') respectively.

common axis for the counter facing inner electrodes, reducing assembly inaccuracies. This trap has mounting arm parallel to the z-axis or electrode axis. Despite its symmetry, machinability and simple structure some important design flaws were identified. Due to thickness of part B, the distance between the electrode axis and the outer edge of the trap assembly is about 7.5 mm. This means, trap structure limits the maximum incident angle of the laser beams with the y-axis to $\phi = 38.8^\circ$ (ϕ shown in Fig. 5.1(1)). A Gaussian laser beam propagating at this angle, having waist $\sim 10\mu$m at the trap center ($\sim 120\mu$m at the vertex of part B) is obstructed

at the vertex of part B. This issue could be fixed by decreasing thickness of part B but it turned out that the minimum machinable thickness of part B which was sturdy enough to hold the fastening screw could only allow light an additional degree i.e. $\sim \phi = 39.8°$. Another flaw in this design was that part B forms a direct thermal contact with the inner electrode, part E, as it is push fitted in part A upto part B, this may result in heat transfer to the inner electrode which covers a large fraction of field of view of ion. Apart from these, the parts A-B-C are assembled with help of single screw. It thus gives a lot of freedom to B and C for moving around the axis of the screw resulting in non concentric electrodes and asymmetrical trap. Also, push fitting the outer electrodes was inconvenient with its holders already being in place. The only way to push fit was by pushing the angled end of the electrodes from the outer face of the part A by striking the flat end of the electrodes slowly while making its way down. But this method of push fitting could damage the angled as well as other surfaces of the electrodes. A fabricated prototype of this design is shown in Fig. 5.1(1'). This design therefore failed to align with the main considerations and was reconsidered for fixing these flaws.

Second version of the trap structure as shown in Fig. 5.1(2) eradicates one of the major problems of light obstruction. Lets call it trap design 2. An I-shaped metallic holder, part C, is designed for holding the outer electrodes in place. The insulator i.e. part B is replaced with a new cylindrical spacer design. This decreased the distance between electrodes' axis and vertex to 2 mm and allowed light to fall at maximum angle $\phi = 41.4°$ with the horizontal. Note that the angle ϕ in this design clears the constraint of limiting angle, $\theta_0 = 41.2°$ (for chosen electrode geometry) as discussed in section 3 of last chapter. The dielectric insulators, part B, are not directly touching the inner electrodes and are also far from direct line of sight from ion. Fig. 5.1(2') shows the manufactured prototype of this design. The trial pieces were made in non-magnetic stainless steel 316LN to check the design loopholes.

The problem of difficult push-fit electrode assembly was solved by detachable arms of the C-section of part A. This resulted in A being split into a T-piece and two detachable cantilever arms which could be assembled individually and then with the T-piece (details are shown in Ref. [50]). But it was figured out that the part A is better made from a single block rather with detachable arms despite its advantage of easy electrode assembly because despite having steps and groves for avoiding rotational misalignments, precise positioning is difficult. Also, the detachable arms did not make good thermal contacts with the t-piece which would hamper heat conductance and caused temperature gradients in the structure. A good trap would conduct and dispose heat outside via feedthrough. Another concern of steps and groves in the common arm is increase in the outgassing surfaces added to the drawbacks. In both the above discussed trap designs 1 and 2, there are two pieces of part B and there are machining differences between these two pieces in the real world. This created additional misalignments between the two counter facing electrode sub-assemblies. Clearly, as seen in (Fig. 5.1(2')) the electrode are not concentric. The design is machinable but the short connection is a result of mismatched

machining of the outer electrode holders. The problem of push fitting the electrodes while holders already in place remained unsolved. Although the light obstruction issue was fixed but the problems of push fitting electrodes and single-screw held trap assembly remained unsolved. The assembly of parts A and C holding inner and outer electrodes respectively still have rotational freedom around the axis of the screw. Both the designs (1 and 2) have single arm mounting facility i.e. they are mounted on a single pin of electrical feedthrough giving the freedom of slight position or orientation tweaking. But along with this freedom comes the question of stable mounting. The single feedthrough pin may slowly bend by the weight of the trap assembly structure.

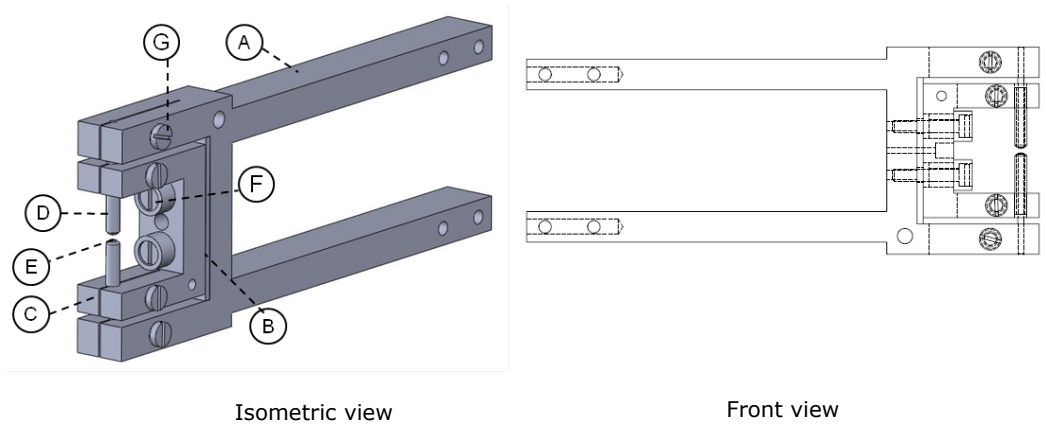

Fig. 5.2: Ion trap assembly with its different parts labelled.

The final design as shown in Fig. 5.1(3) removes these drawbacks. In design 3, the part A has two mounting arms unlike the previous ones. Both the part A and C are made of metal with a flat plate part B working as insulation between them. The part A and C are designed such that the through holes are machined aligning the pieces together, reducing possibilities of misalignments. In designs 1 and 2, it was inconvenient assembling electrodes when holders are already in place, this issue is solved by slit and clamp mechanism used in both parts A and C. This slit and clamp design ensures pumping out of trapped air molecules in the screws. Insulating dielectric is neither in direct touch with inner electrodes nor it is in ion's field of view hence ion is protected to a extent from dielectric heat. The screwed flat surfaces of the parts C and A, make good thermal contacts avoiding temperature gradients across the trap. This design reduces the rotational freedom of the parts as they are fastened using two screws instead of one. The central hole in between the fastening screws is for placing temperature sensor. Figure 5.1(3') shows the machined trap and Fig. 5.2, 5.3 and 5.4 give the detailed drawing dimensions. As the trap is directly mounted to feedthrough pins, properties of feedthrough materials play important role. The rf carrying pins can heat up themselves transferring this heat to the trap body. The feedthrough avoids this, as its pins are made of copper and are

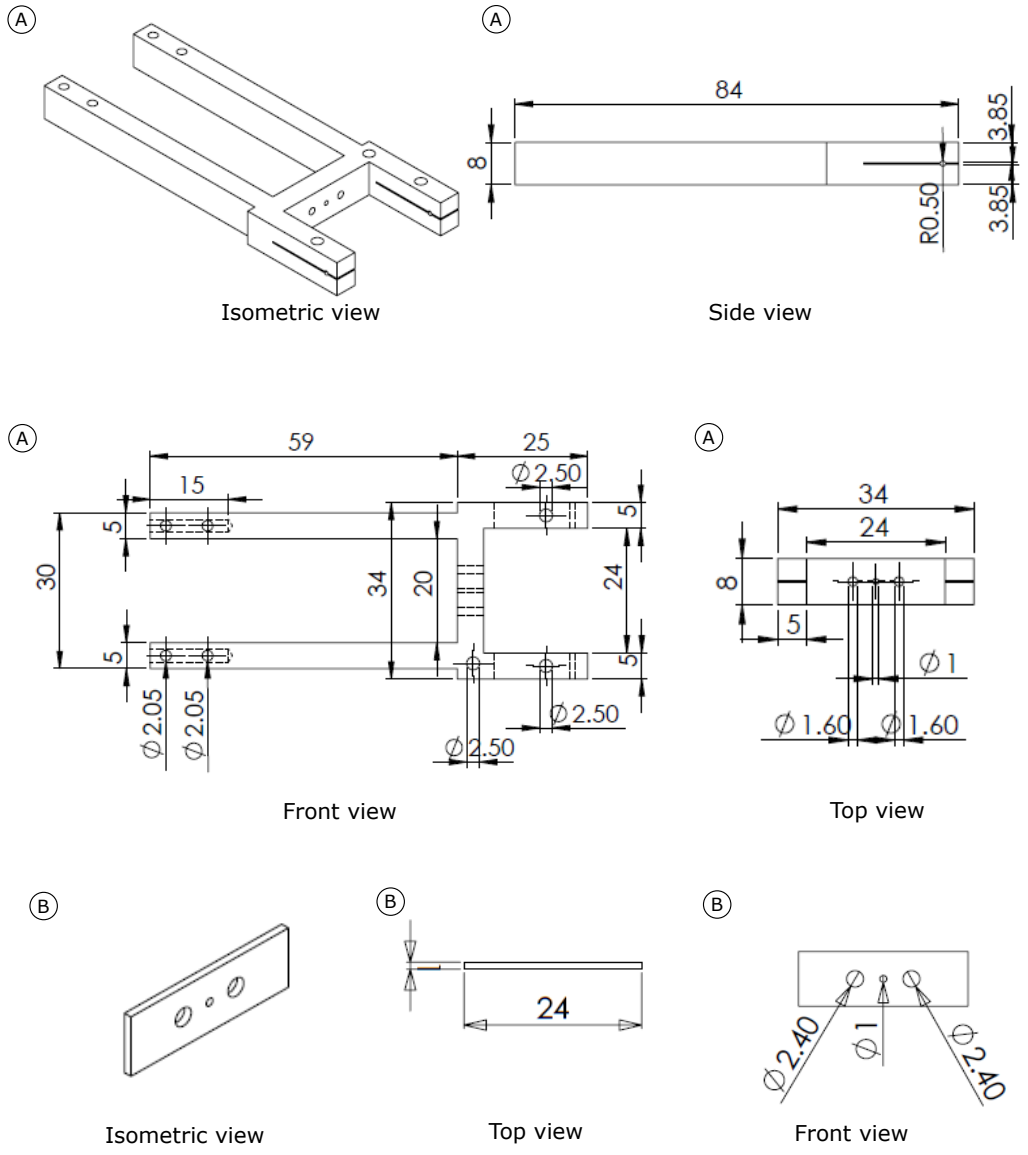

Fig. 5.3: Dimensional details the parts A and B of the ion trap. All the dimensions of length are in units of millimeter and the angular dimensions are in units of degree.

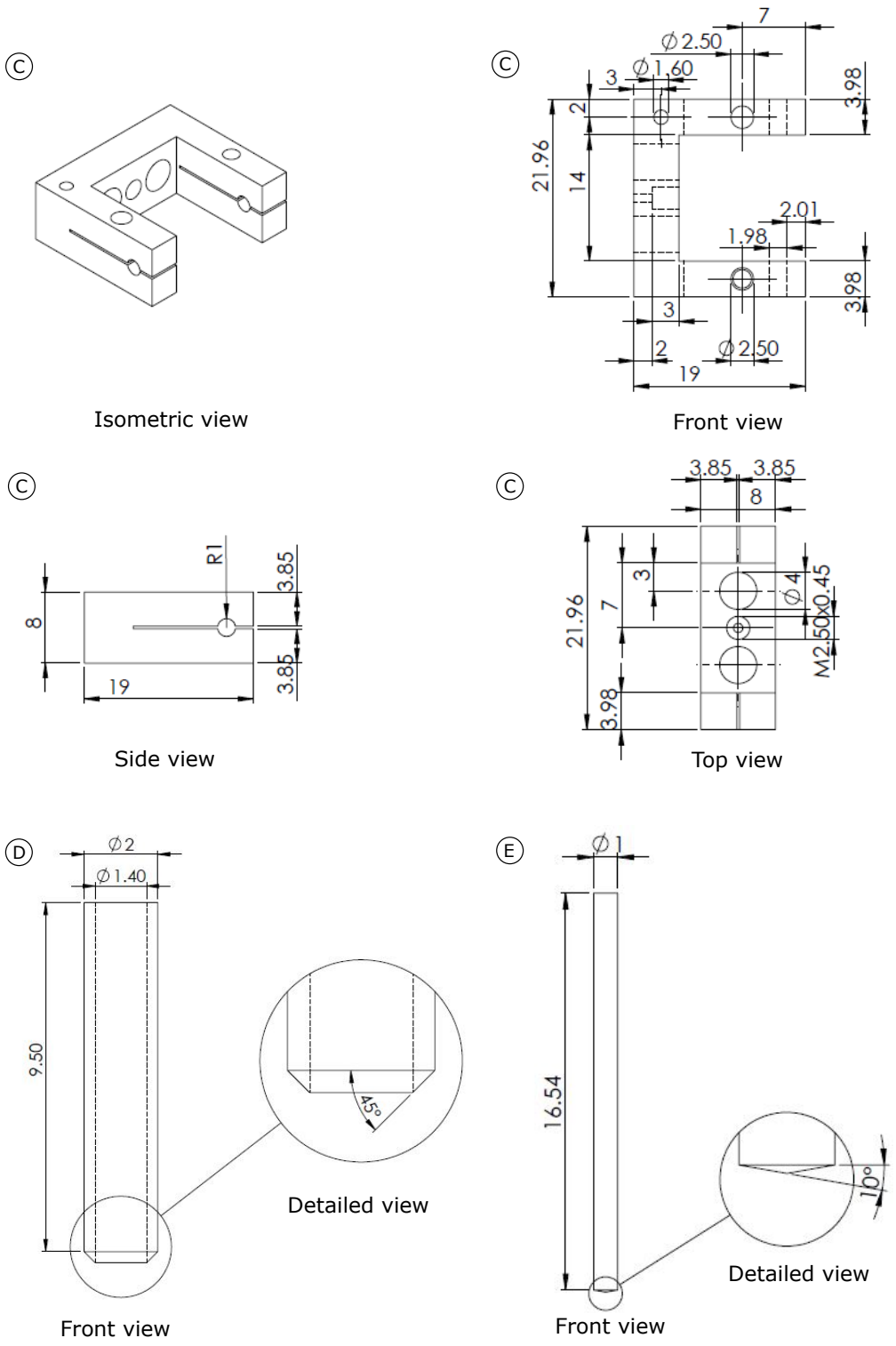

Fig. 5.4: Dimensional details the parts C, D and E of the ion trap. All the dimensions of length are in units of millimeter and the angular dimensions are in units of degree.

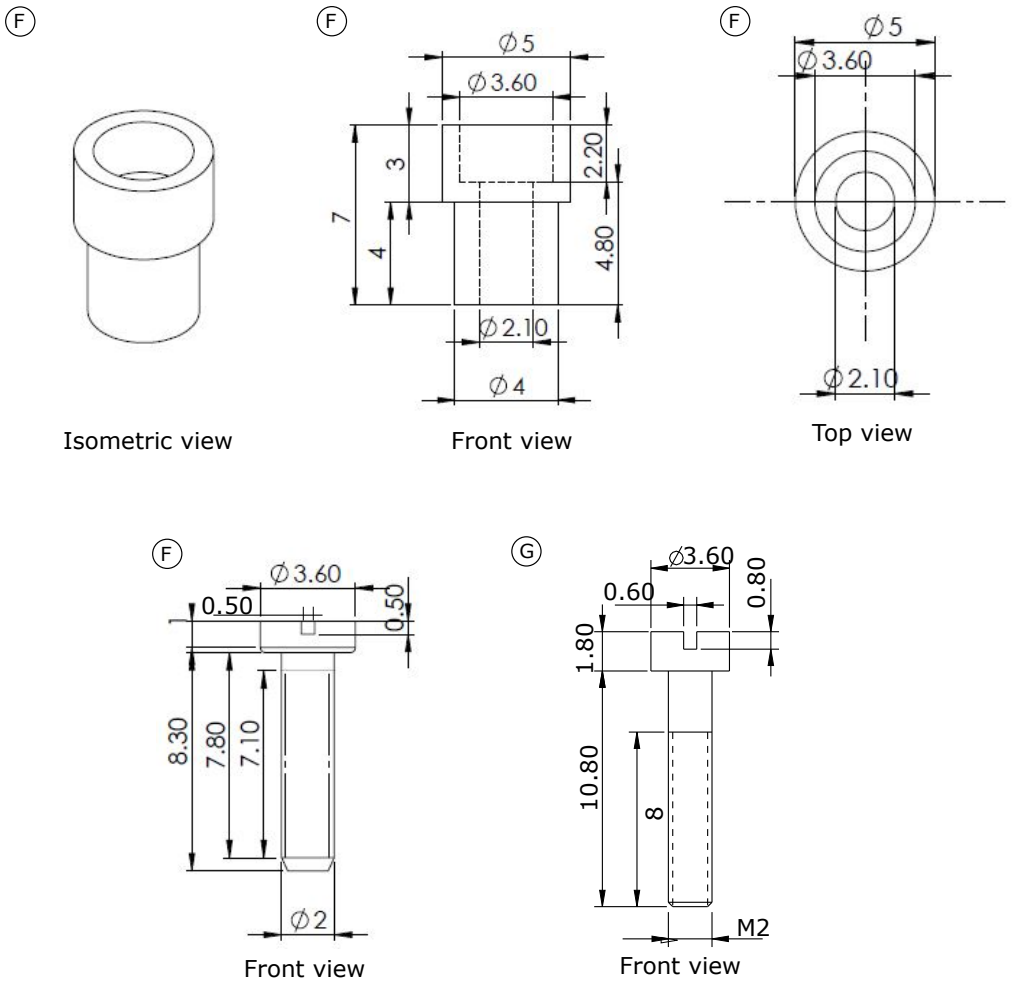

Fig. 5.5: Dimensional details the parts F and G of the ion trap. All the dimensions of length are in units of millimeter and the angular dimensions are in units of degree.

solid as per recommendations given in Ref. [189]. Tiny temperature sensors (1.6 mm × 5 mm), PT100 (Allectra:343-PT100-C2-1M) are to be used for temperature measurement in the vicinity of trap inside the ultra high vacuum chamber. These are UHV compatible Platinum resistors working in the temperature range −200°C to 750°C. The wires used for electrical connections inside vacuum, are low resistance multi-strand silver plated copper wires (Allectra: 311-KAPM-025) which are UHV compatible and can withstand high temperatures ∼ 1000°C.

Now, as the design is finalized and a prototype is machined for the checking design loopholes and precision check, the question of appropriate materials for real trap arises. The single ion clock experiment requires UHV surroundings, this compels use of materials which are compatible to such low pressures.

5.1.1 Materials Consideration

Tab. 5.1: Electrical, thermal, mechanical and chemical properties of machinable metals: Silver (Ag), Gold (Au), Aluminum (Al), Tantalum (Ta), Titanium (Ti), Tungsten (W), Oxygen free high thermal conductivity (OFHC) Copper, Molybdenum (Mo) and Beryllium-Copper (BeCu) [50].

Properties,	Ag	Au	Al	Ta	Ti	W	OFHC	Mo	BeCu
Electrical conductivity[$\times 10^6$S/m] (@20° C)	63	41	35	7.6	2.4	18.5	60	18.7	12.2
Thermal expansion coefficient[μmm^{-1}K^{-1}] (@25°C)	18.9	14.2	23.1	6.3	6.6	4.5	19.4	4.8	17.8
Young's modulus [GPa]	83	79	70	186	116	411	125	329	124
Thermal emissivity	0.02 −0.3	0.37 −0.83	0.04 −0.06	0.14 −0.30	0.19	0.04	0.02 −0.6	0.05 −0.18	0.03
Chemical nature	Inert	Inert	Reactive	Inert	Reactive	Inert	Inert	Inert	Toxic

Choice of materials which can be used for constructing different parts of the trap structure such as electrodes, their holders, insulators, screws etc. depends on their properties such as electrical, thermal, mechanical and chemical. Together with these, compatibility to a base pressure of 10^{-10} Pa and below is a must. Various UHV compatible and machinable metals with their properties have been listed in Tab. 5.1. Let us discuss about the choice of metals for electrodes first. Metals like silver, gold and aluminium are excellent conductors but are soft, have lower mechanical strengths and relatively higher thermal expansion coefficients. This means heat due high voltages could expand the structure unevenly and result in unwanted electrode misalignments. Metals like tantalum and titanium are good electrical conductors besides having high elastic strengths. Additionally, they have lower thermal expansion coefficients than gold and aluminum. However, titanium, aluminium and silver have strong tendencies to

form oxides and nitrides on their surfaces. Oxygen free high conductivity (OFHC) copper has excellent electrical conductivity, high mechanical strength, and is chemically inert but it has a high thermal expansion coefficient which again may lead to misalignment of the electrodes in case of slight temperature change. Tungsten is also a suitable choice for electrodes in terms of conductivity, mechanical strength, inertness and thermal expansion but it has inherent porosity and its outgassing rate limits the achievable vacuum [187]. In an ion trap, the voltage sources are connected to the electrodes in open circuits. The nature of the confining potentials depends on the machining accuracy and precise alignment of the electrodes. Thus, low and relatively similar thermal expansion coefficients for all the parts composing the trap assembly are preferable than high conductivity. With these considerations tantalum and molybdenum are most suitable materials for fabricating the electrodes. Their low thermal emissivity scales down radiated power at a given temperature, which decreases the systematic shift due to the BBR. It is very important for electrodes' materials to have similar composition throughout the surfaces. Surface composition variation can result from oxide formations or deposition of other particles over them. In our experiment, a resistive heated effusive atomic oven is used for producing Yb atoms in gaseous state for photoionizing them. While spraying atoms from oven pointing towards the center of the trap, the electrode surface gets contaminated as the atoms coat them. The diffusion of adsorbate atoms causes a change in the local work function thereby giving rise to unwanted inhomogeneous electric fields. This is known as the patch effect [188], which is primarily a surface phenomenon. This can give rise to unwanted heating of the trapped ions as these stray fields in turn contribute to excess micromotion to the ions giving rise due to second order Doppler and dc Stark effects. Due to the inert nature of molybdenum and tantalum, formation of their oxide layers is unlikely, hence, the patch effect is dominated by deposited ytterbium. We choose tantalum since ytterbium-tantalum differential work-function is less compared to that of ytterbium-molybdenum.

The structure holding the trap has to provide a rugged and sturdy support together with the desired electrical and thermal properties. Molybdenum and beryllium-copper are both suitable for this purpose. The relative thermal expansion of the electrode holder and the electrodes themselves may result in misalignment. We estimate the approximate change of the tip-to-tip separation between the two inner electrodes as $\ell \times (\alpha_1 - \alpha_2)$ per K, where ℓ is twice the length of the inner electrode, and α_1 and α_2 are the thermal expansion coefficients of the trap holder and electrode materials, respectively. The differential thermal expansion coefficient of tantalum and beryllium-copper is higher than that of tantalum and molybdenum, also beryllium-copper releases toxic fumes while machining. So, Molybdenum is chosen in for trap structure instead of beryllium-copper.

Common choices for materials which are used for fabrication of insulating spacer are alumina ceramic, macor and fused silica. Few selected properties of these materials as given in Tab. 5.2 are compared for an informed choice. The relative permittivity of insulator piece is desired to be

Tab. 5.2: Selected properties for common materials used for fabricating insulating spacers for the trap structure. These values have been taken from Ref. [189]

Properties,	Macor	Alumina ceramic	Fused Silica
Electrical Conductivity [S m^{-1}]	$< 1 \times 10^{-14}$	$< 1 \times 10^{-12}$	$< 1 \times 10^{-18}$
Thermal Conductivity [W $m^{-1}K^{-1}$]	1.46	4-35	1.35
Relative Permittivity	5.67	9.5	3.82
Dielectric loss tangent [$\times 10^{-4}$]	11;20	2	0.15

less as higher value lead to higher capacitance of the trap resulting in heat generation. Alumina ceramic has higher relative permittivity compared to macor and fused silica. When compared on basis of electrical insulation, fused silica is the best choice among the three while alumina scores low on this property. For the trap in the discussion, macor is chosen for fabricating insulating spacer (part B) which separate holders of the inner and outer electrodes. Among other properties, it is stable up to 1000° C and is also easily machinable. Also, the bush (part F) used for separation of screws and part C is made of macor. After studying properties of different materials for fabricating different parts of trap, Molybdenum is chosen for trap structure and screws (parts A, C, F and G), Macor is chosen for insulator piece (part B and F) and Tantalum is chosen for inner and outer electrodes (parts D and E).

5.2. Vacuum Chamber Design

For achieving trapping life time of the ions, collisions with background gases need to be minimized thus we aim for vacuum of the order of 10^{-12} mbar. In this section the design of UHV chamber that will house the ion trap, atomic oven, compensation electrodes and fluorescence collection lens is described. Let a coordinate system $x - y - z$ such that the trap center lies at the origin of this coordinate system and trap electrode axis is coaxial with the z axis. Some of the main considerations for design of UHV chamber to be kept in mind are as follows:

- The chamber must be made of UHV compatible material to support low pressures.
- The geometric center of the UHV chamber must coincide with that of the trap and thus the origin of the $x - y - z$ coordinate system. View ports along $x - y - z$ axes for ease of access to the trap center.
- The trapped ion is required to be probed along three mutually orthogonal directions for micromotion detection and quantization purposes (as discussed in chapter 4). But the z axis does not give access to the trap center, due to blockage from electrodes another orthogonal set of axes other than the conventional $x - y - z$ is required. This axes system

must be such that the light impinged along these axes, upon the ion at center is not obstructed.

- Sufficient number of ports for various impinging laser lights, collecting light for imaging, mounting trap, compensation electrodes and atomic oven.
- Closest possible mounting of florescence collection lens inside the chamber without obstructing the laser lights.
- Minimum possible volume with space for ion trap structure, atomic oven, compensation electrodes and collection lens.

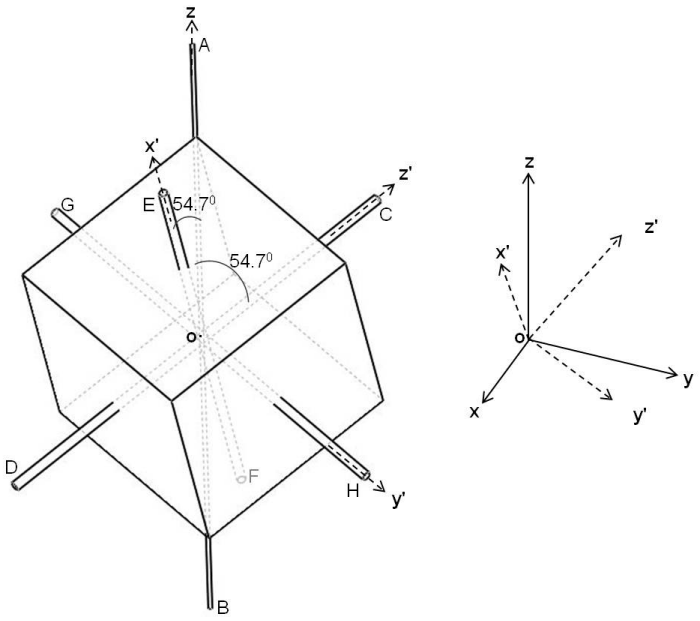

Fig. 5.6: A cube of arbitrary dimensions with AB as one of its body diagonal aligned along z-axis. Lines CD, EF, GH join the centers of opposite faces.

As discussed in chapter 4, electric quadrupole and micromotion generated systematic effects are major causes of shifts in the clock experiment. Their mitigation require quantization of axes as well as impinging lights along them. To find out the another set of orthogonal axes other than the conventional $x-y-z$ set of axes, let us exercise a thought experiment. Consider a cube of arbitrary dimensions, see Fig. 5.6 for reference. Take any of the body diagonal of the cube, say AB. Consider it as the vertical z axis and along with other perpendicular directions it forms the $x-y-z$ axes set. Now, join the opposite faces of the cube at their respective centers forming three mutually perpendicular lines CD, EF and GH. These form $\acute{x}-\acute{y}-\acute{z}$ axes set. The angle made by the vertical z axis and the $\acute{z}$ axis is 54.7°. This way two orthogonal set of axes

are identified for making optical ports along them. As the trap center needs to be optically accessible for photoionizing, cooling, repumping and clock lasers, fluorescence imaging together with the possibility of attaching the trap, atomic oven and pumping system a minimum of 10 number of ports are required. With all the angled ports, lens holder and trap, optimizing for minimal volume was another challenge. Two designs of UHV chamber as shown in Fig. 5.7, were drafted and compared. In one of the designs, a sphere and an arbitrary axis was considered such that the z axis of the cube shown in Fig. 5.6 is coaxial to this axis. The other design is based on a cylinder such that its vertical axis is coaxial to z axis of the cube. The details of the designs are described in the following paragraphs.

The first version of chamber design as shown in Fig. 5.7a was based on spherical ball shaped chamber with ports at vertices of two set of orthogonal axes. The outer radius of the solid sphere was 90 mm, this is the minimum dimension with which the angled ports were possible which was huge. The ports along $x - y - z$ axes had CF-35 flanges and angled ports were having CF-16 half nipples for accessing center. To reduce the volume of the chamber the opposite faces along x and z axes with CF-35 were cut flat. The main drawback of this design was its machinability. It is very challenging to mill out of a solid sphere, as the machining tools does not have accessibility to inner volume of a small size sphere. Also, the free space volume inside the chamber would depend upon the machinability but we require space for atomic oven, lens holder etc. This was not feasible with machining facilities available therefore another design for vacuum chamber was thought of.

Second version of chamber design was cylindrically symmetric as shown in Fig. 5.7b unlike the first one and can be easily machined starting from a hollow cylinder of outer diameter 120 mm and inner diameter of 64 mm. The center is accessible from 12 ports in total. Standard ConFlat (CF) components for ports are chosen as their stainless steel knife edges compress the copper gasket to provide a good vacuum seal. Because of all metal construction they can be baked to high temperatures. The ports in the conventional $x - y$ directions are argon welded with CF-35 flanges on half nipples and are numbered in the Fig. 5.8. Two of the CF-35 flanges on diagonally opposite faces are rotatable (Flange 1 and 3 as shown in Fig. 5.8) and the other two are fixed (Flange 2 and 4). The rotatable flanges facilitate freedom for orientation adjustments, which is needed in trap mounting. For successful scatter-free light beams falling at the trap center, the trap can only be mounted from the rotatable CF-35 port 3 which is at a fixed azimuthal angle with respect to these angled ports as shown in Fig. 5.8. The directions $\acute{x} - \acute{y} - \acute{z}$ have six half nipples welded along them, angled at 54.7° from the vertical z axis. These have ports of CF-16 size. These ports thus facilitate a mutually orthogonal set of axes to impinge cooling lights at the ion. One of these CF-16 ports is used to mount atomic oven for spraying Yb atoms. As fluorescence light at 369.5 nm, from the single ion is very weak, it can be easily lost after multiple reflections from the glass windows. Also, if the cooling and detection light (369.5 nm) which is impinged from CF-16 ports is reflected at the optical viewports, it

will not be transferred optimally to the UHV. It may also falsely exaggerate fluorescence light signal leading to wrong imaging results. The fluorescence light must also reflect back into the UHV chamber at port used for imaging (port 1). For this reason, the viewports chosen for the CF-16 ports and port 1 have special antireflection coatings transmitting upto 99% light at wavelength 369.5 nm. These optical viewports are commercially procured from Torr Scientific Ltd. and the details are given in Tab. 5.3. The ports along z axis are of CF-75 size. The port

Tab. 5.3: Properties of different viewports used along with their respective port numbers.

Port	Viewport properties
1	size: CF-35 substrate:Sapphire flange material: SS316LN coating: double side VAR @ 369.5nm (0° incident angle) reflectance:0.5% per face surface quality:60/40 scratch dig flatness: $< 8\lambda$
2	size: CF-35 substrate:Sapphire, flange material: SS316LN reflectance:0.5% per face surface quality:60/40 scratch dig flatness: $< 8\lambda$
4	size: CF-35 substrate:Sapphire, flange material: SS316LN reflectance:0.5% per face surface quality:60/40 scratch dig flatness: $< 8\lambda$
all CF-16 ports	size: CF-16 substrate:Sapphire, flange material: SS316LN coating: double side VAR @ 369.5nm (0° incident angle) reflectance:0.5% per face surface quality:60/40 scratch dig flatness: $< 8\lambda$
Top port (CF-75)	size: CF-75 substrate:Sapphire, flange material: SS316LN reflectance:0.5% per face surface quality:60/40 scratch dig flatness: $< 8\lambda$

at top uses CF-75 blank flange and is used to access inner volume for trap or oven adjustments

by hand. The bottom port has a CF-75 to CF-35 reducer flange with CF-35 side facing inside the chamber. The compensation electrodes which are used to shift the position of the ion are planned to be mounted on this flange. The bottom reducer flange also has provision to mount a lens holder as shown in Fig. 5.9. The lens holder can be mounted on the bottom flange at four positions in the $x - y$ plane such that it is parallel to any of the CF-35 port. The distance of the lens holder is optimized such that it does not obstructs incident angled light beams and hold an aspheric florescence collection lens at a distance of ∼28.3 mm from the trap center. The outer side (opposite to that of knife edged side) of the reducer flange has four M6 size mounting holes on the CF-75 side for stable setup on the optics table. The inner surface of chamber is electropolished for reduced roughness and porosity. The total volume of the chamber is estimated to be ∼1 Litre. The outer wall of the chamber has four tiny M2 holes in the $x - y$ plane in between the CF-35 ports, machined for placing temperature sensors. Fig. 5.8 and 5.9 show detailed 2D drawing of the chamber marked with important dimensions. The chamber is fabricated with non magnetic stainless steel, SS316LN. For ease of mounting optics and impinging lights through the viewports, optical cage system will be used. For this reason, indigenously designed circular plates are used to screw optical cage system to the flanges. These circular plates are made with non-magnetic SS316LN in sizes compatible to CF-35 and CF-16 flanges. Optical cage system is made using standard 16 mm and 30 mm cage plates and cage rods(Thorlabs) as shown in Fig. 5.10(a) in next section.

The ion trap and the vacuum chamber have been fabricated and tested dimensionally. The trap when housed inside the UHV chamber can easily be adjusted such that they both have a common geometric center. An elaborate optical set up was fabricated with the help of lenses and folding mirrors to check the validity of the assembly for unobstructed lights. No obstruction to the light impinged from angled ports at the center of the trap with lens holder in place was found.

5.3. Vacuum Equipments And Assembly

A precision experiment like this requires very low pressures $\leq 10^{-11}$ mbar, so as to avoid collisions of the stored ion with background gas. Still a lot ($\sim 10^5$) gas molecules per cubic centimeter at room temperature exist in this pressure range, leading to about 1 collision every minute but the usual trapping depth of few eV does not allow any harm to the trapped ion system. For reaching and maintaining this ultra-high vacuum (UHV) environment it requires careful assembly, strict cleaning and baking procedures among other common practices to avoid leaks and contaminations. A vacuum assembly has been designed and set up but not pumped to low pressures as atomic oven characterization is in final stage. The design of vacuum assembly is discussed in this section.

Before details of the vacuum assembly, refer detailed layout of lab enclosure discussed in

Appendix B. The vacuum assembly is mounted on optics table 2 (see Appendix B) and is surrounded by three pairs of magnetic coils mounted in Helmholtz configuration. Details of these magnetic coils are given in chapter 7. For clarity the vacuum assembly is shown in two parts in Fig. 5.10. Figure 5.10(a) shows a vacuum chamber assembly with three pairs of magnetic field coils mounted around it in Helmholtz configuration. Figure 5.10(b) shows a detailed isometric view of vacuum assembly. The UHV chamber is connected to a standard CF-35 I-piece through port 1 with the other end of the I-piece connected to a CF-35 size T-piece. In the T-piece, the port along the axis of port 1 is utilized for imaging. The perpendicular end of the T-piece is connected to a turbomolecular pump (Agilent HiCube classic 80) through a bellow via an right angled all metal valve. A gate valve separates this part of the assembly from rest of the assembly which has specialized vacuum pumps. The segregation allows to first pump the pressure down from the turbo before starting speciality pumps. A quadrupole gas analyzer (Stanford Research Systems 200 amu RGA) is used in the assembly for detection of any leaks and determination of impurities. An ion pump (Agilent Vaclon plus 55, Starcell) having maximum pumping speed of 55 L/s is connected in the vacuum system. Ion pump functions on magnetron motion of electrons pulled by applying high voltages to anodes surrounded by strong magnets. These spinning electron clouds collide and ionize gas molecules, which when attracted to Titanium or tantalum cathodes form compounds and settle there. A Ti-sublimation pump (Agilent) is used in conjunction to the ion pump. This pump consists of titanium coated filament which is heated to sublimate and coat the surrounding chamber walls. Active gases like O_2, CO, and water vapors in the chamber react chemically with Titanium to form oxides, hydroxides etc and get buried onto the vacuum chamber walls.

An ion trap is designed that satisfies constraints of no light obstruction, minimal dielectric use, equal rf path lengths etc. The materials used for ion trap machining are carefully selected by considering their electrical, mechanical, thermal, chemical and machinability properties. Designed vacuum chamber is compatible to UHV and has ports for mounting ion trap, atomic oven, compensation electrodes and imaging. It is provisioned with ports in a special configuration required for micromotion detection and quadrupole shift's cancellation. Apart from that practical issues like ease of access and freedom for adjustment to achieve alignments have also been considered. The ion trap and UHV chamber have been tested successfully together to test their geometric compatibility and zero hindrance to optical path.

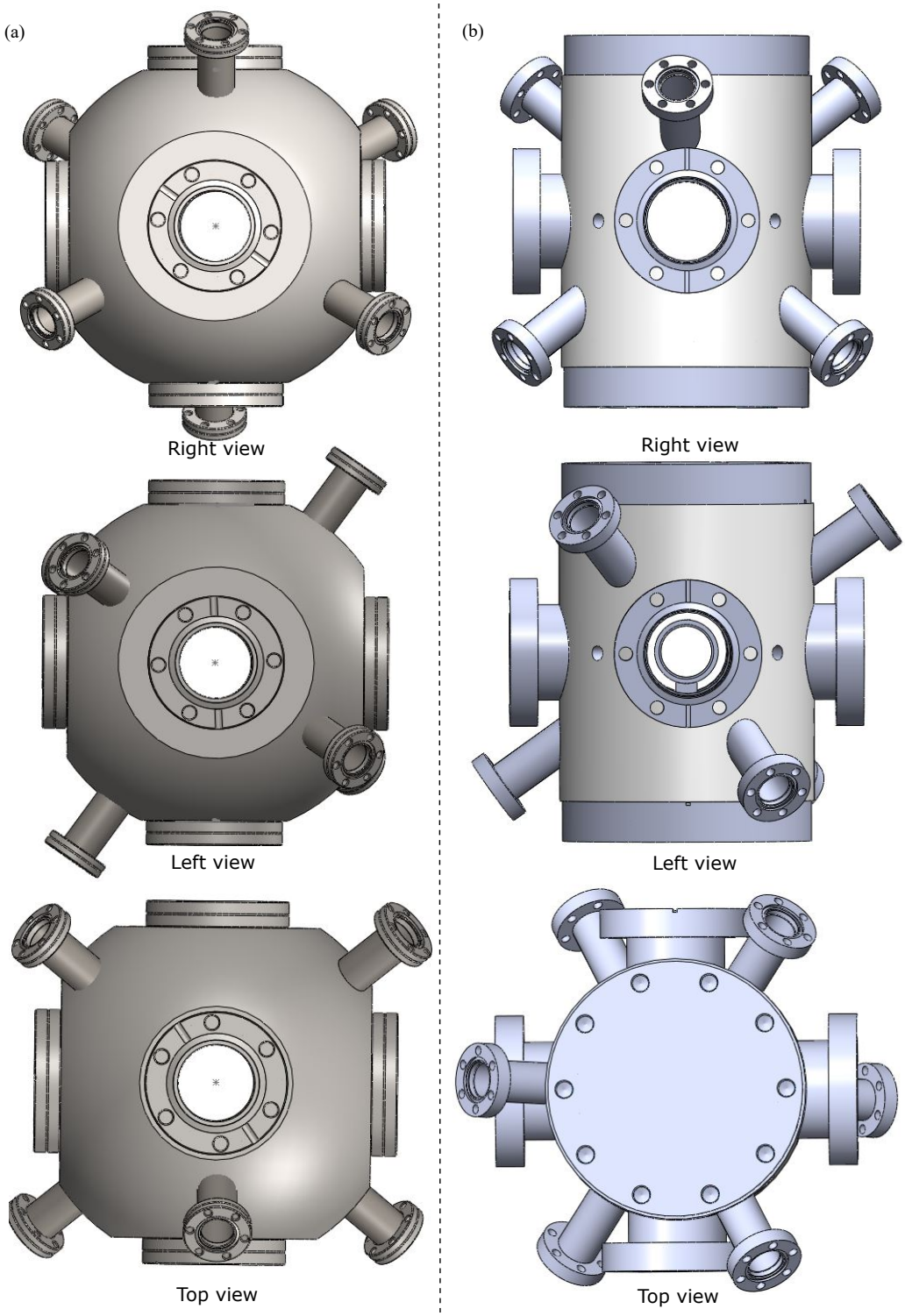

Fig. 5.7: (a) Initial design of spherical UHV chamber, (b) Final design of UHV with cylindrical symmetry.

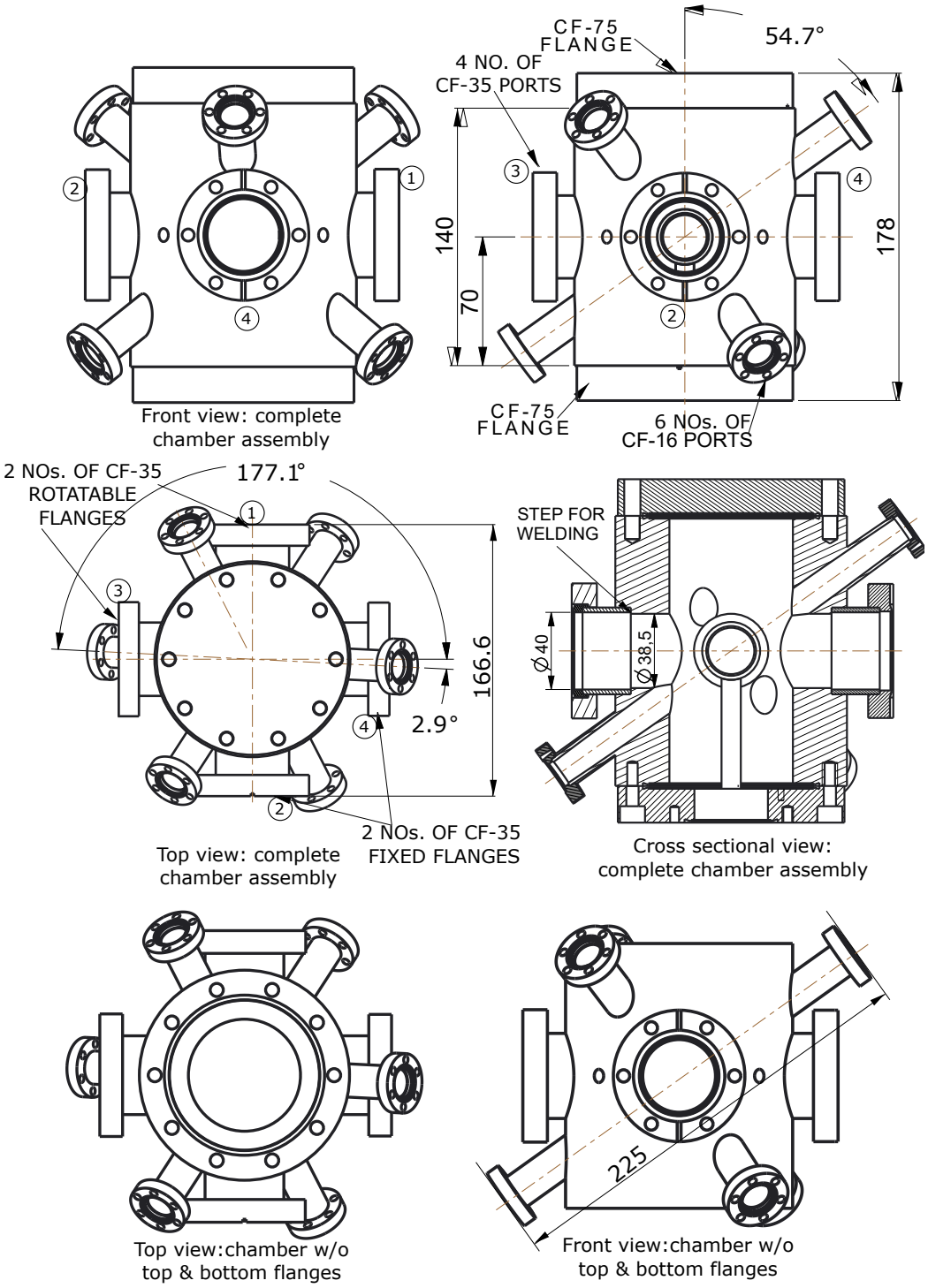

Fig. 5.8: Detailed dimensional drawing of UHV chamber assembly. All the dimensions of length are in units of millimeter and the angles are in degree.

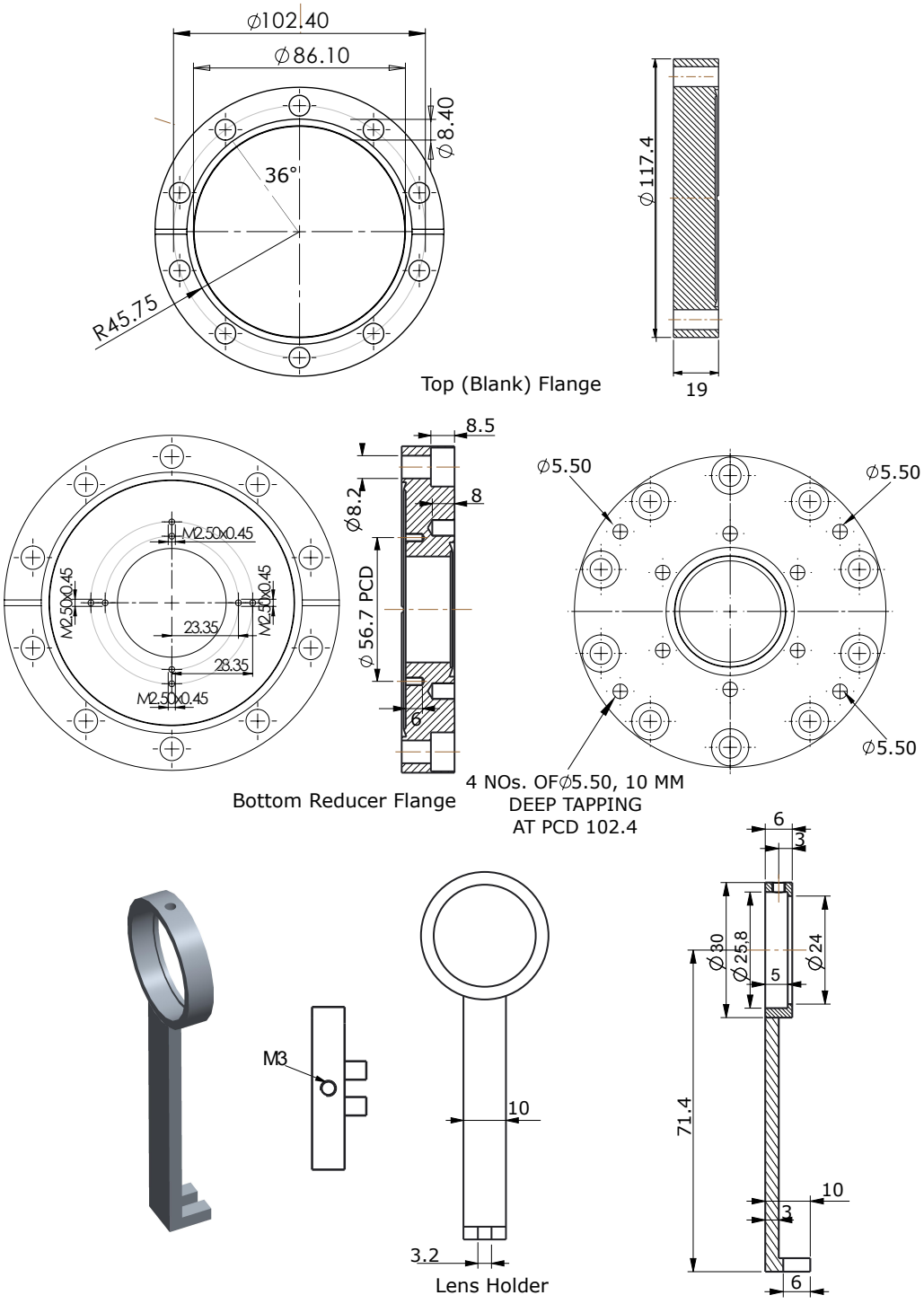

Fig. 5.9: Dimensional drawing different parts of UHV chamber assembly. All the dimensions of length are in units of millimeter and the angles are in degree.

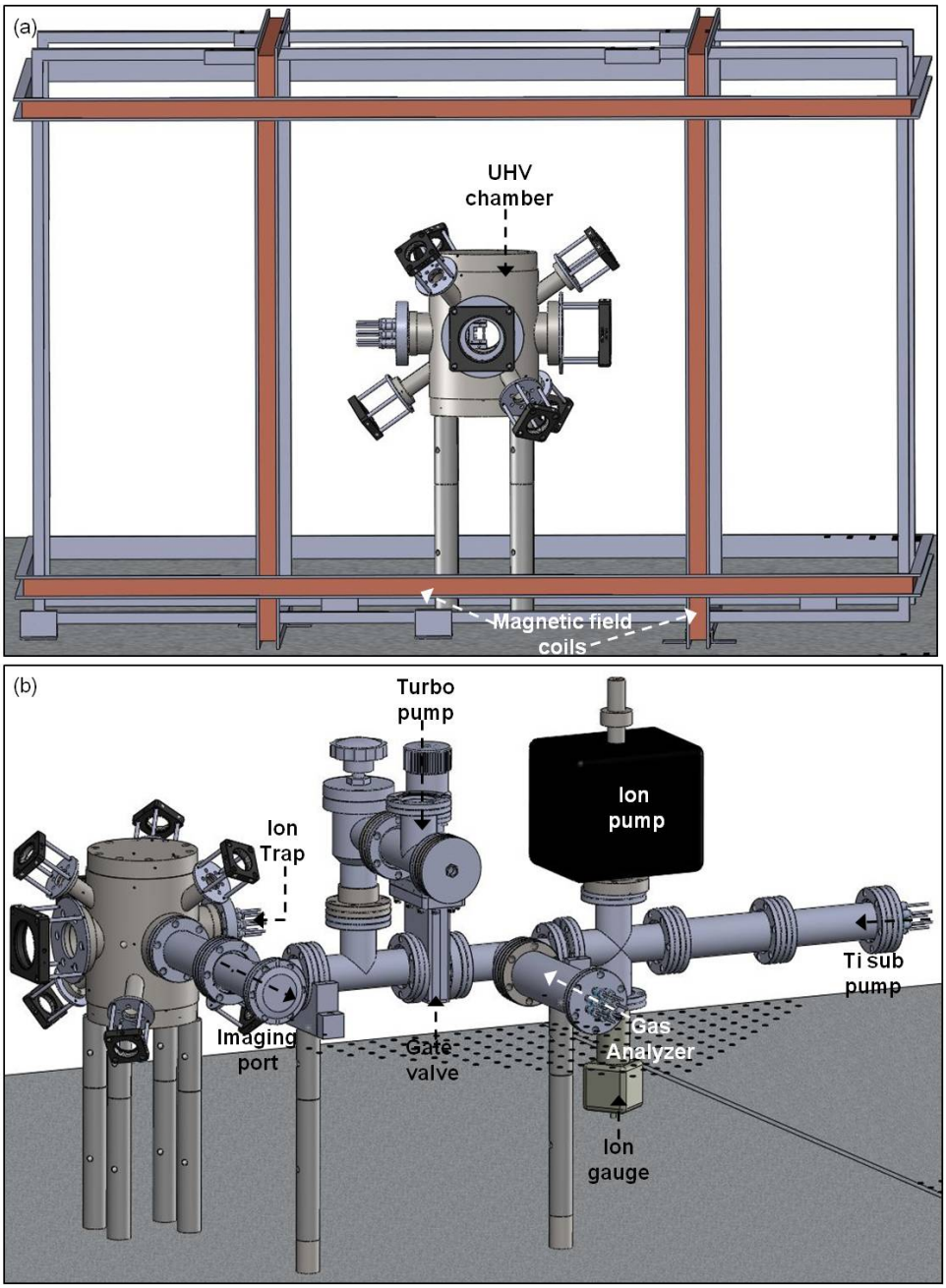

Fig. 5.10: (a) Vacuum chamber surrounded by Helmholtz coils. Here, only vacuum chamber is shown as surrounded by coils for clarity.(b)Isometric view of the complete vacuum assembly in 3D.

Chapter 6

Helical resonator for efficient delivery of RF voltage to the ion trap

6.1. Introduction

The depth of the trapping potential within an rf trap depends upon the rf voltage applied at the trap electrodes. In order to achieve deeper trapping potential, a high voltage rf is applied across the trap electrodes. Signal from rf generators when amplified can generate high rf power and have usually high resistive component impedance whereas the trap electrodes offer almost a purely capacitive load. Therefore, the rf source and the trap should be impedance matched in order to transfer maximum power from the source to the trap. For this a resonator with high quality factor, Q is used to match the impedance between rf source and the ion trap. Rf voltages applied through a high Q resonator also act as filters, reducing the power of unwanted frequencies and thus reduces their contribution to motional heating of ions. However, the traditional coaxial resonators have dimensions of quarter of the wavelength to be transferred. Therefore, an rf signal in operating range $\sim$ 15-30 MHz would require impractical resonator dimension of about 2 meters. Considering the limitation of the linear quarter wave resonator, helical resonator are commonly being used for rf ion trap. In this chapter, the design and construction of helical resonator for delivering high rf voltage to the ion trap in our experiment is described.

6.2. Resonator Design

The concept of helical Resonator, which was first proposed by Macalpine and Schildknecht [190] is very similar to a coaxial quarter-wavelength resonator [191] but the main difference is that the central conductor is wound as a single layer helix. Key advantage of using helical resonators include its relatively small size compared to coaxial quarter wave resonator without compromising its Q. Schematic diagram of the helical resonator is shown in Fig. 6.1. It consists of a helical coil surrounded by a cylindrical copper shield and closed with two caps at each

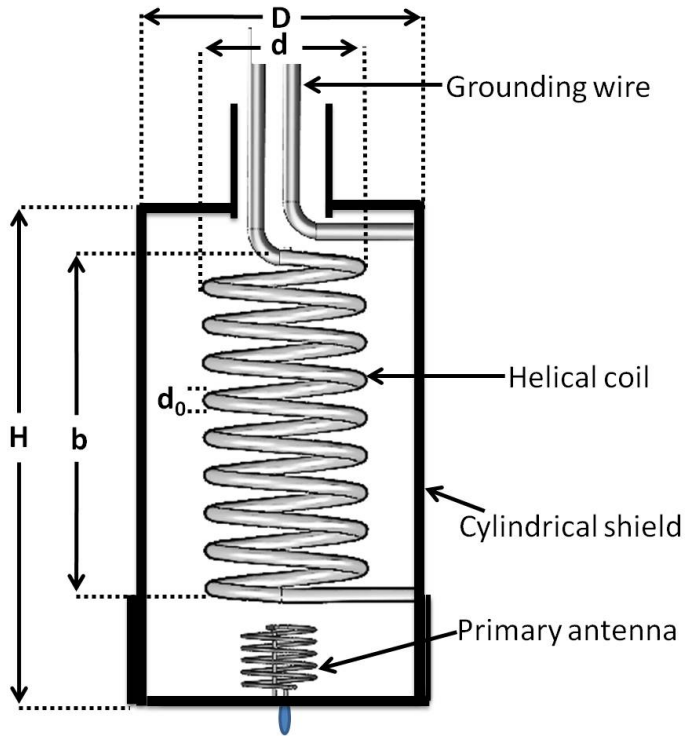

Fig. 6.1: Schematic representation of a helical resonator with important dimensional parameters.

end. A small antenna is connected to one of the end cap which couples input rf signal to the resonator. One end of the helical coil is connected to a conducting metallic shield surrounding it and the other end is open for connecting load. The rf signal applied to the small (primary) antenna coil is inductively coupled to helical (secondary) coil at its shield-connected end. In order to match the impedance of the resonator to the rf voltage source, physical parameters of the primary antenna coil can be adjusted. The primary antenna coil acts as a inductor and couples with secondary coil through mutual inductance. Also, the performance i.e. Q-factor and coupling at resonant frequency f_0 depends on the diameter of shield, D; its height, H; diameter of the helical coil, d, height of the coil, b, diameter of the copper tube of the coil, d_0; the number of turns in the helical coil, N and the winding pitch of the coil, τ as shown in Fig. 6.1. The resonant frequency, f_0 and Q of the resonator at unloaded condition can be estimated from a set of empirical relations as given in Ref. [190, 192]

$$f_0 = \frac{\omega_0}{2\pi} \approx \frac{48260}{ND} \tag{6.1}$$

$$Q \propto D{f_0}^{1/2} \tag{6.2}$$

where f_0 and D are in units of MHz and centimeters, respectively. Relations given above can estimate valid values of f_0 and Q only if they follow few limiting conditions such as coil height

b must be greater than coil diameter d and their ratio should be within $1 < b/d < 4$. Another one being obvious, coil diameter d must be smaller than shield diameter D but with their ratio within $0.45 < d/D < 0.6$. The diameter of the pipe used for making helical coil d_0 must be smaller than the pitch of the helix τ_0 such that $0.4 < d_0/\tau < 0.6$, at $b/d = 1.5$ and the pitch being much smaller than diameter of the coil $\tau < d/2$.

The above empirical relations serve as boundary conditions for constructing helical resonator of desired frequency and performances. Along with these few points need to be considered for fabricating different parts of the resonator such as:

- The coils as well as the shield should be made of highly conducting material.
- Both the primary antenna coil as well as secondary coil should be made such that the windings are uniform in pitch and shape.
- For ensuring mechanical stability the wire/tube used should be thick enough. Also, as the current flows through the surface a thicker tube is preferred because of its higher conductivity.
- Connections must be made such that they offer low resistance.
- The antenna coil should be placed centrally along the axis of secondary coil.
- There should be room to play the distance between the two coils so as to achieve maximum coupling condition.

6.3. Construction and Measurements

Initially, we designed a resonator using above conditions as guidelines for expected resonant frequency f_0=50 MHz at unloaded conditions with $Q \approx$1500. However, when an ion trap is connected the f_0, Q and the output voltage V_{rms} of the resonator changes due to its capacitive impedance. The physical dimensions of the resonator are: helical coil of diameter (d) 60 mm was made with a copper tube of diameter (d_0) 6 mm, which was wound around a solid tube of diameter 54 mm. Notches were made into that solid tube to ensure the winding pitch and diameters of the coils remain unchanged over its length (95 mm). The copper tube was heated up by a blow torch in order to increase its flexibility. The shield of the resonator is made with a 160 mm long (H) copper cylinder of diameter (D) 120 mm and the helical coil with 8.5 helical turns N is placed exactly at the centre of it for achieving minimum capacitance. The helical coil is welded at one end with the shield, whereas the grounding wire is welded on the other end of the shield. The free end of the helical coil and the grounding wire exit the shield parallel to each other. Figure 6.2 shows actual picture of the resonator fabricated at our lab. The primary antenna coil, which is used for feeding rf signal from the source to the resonator

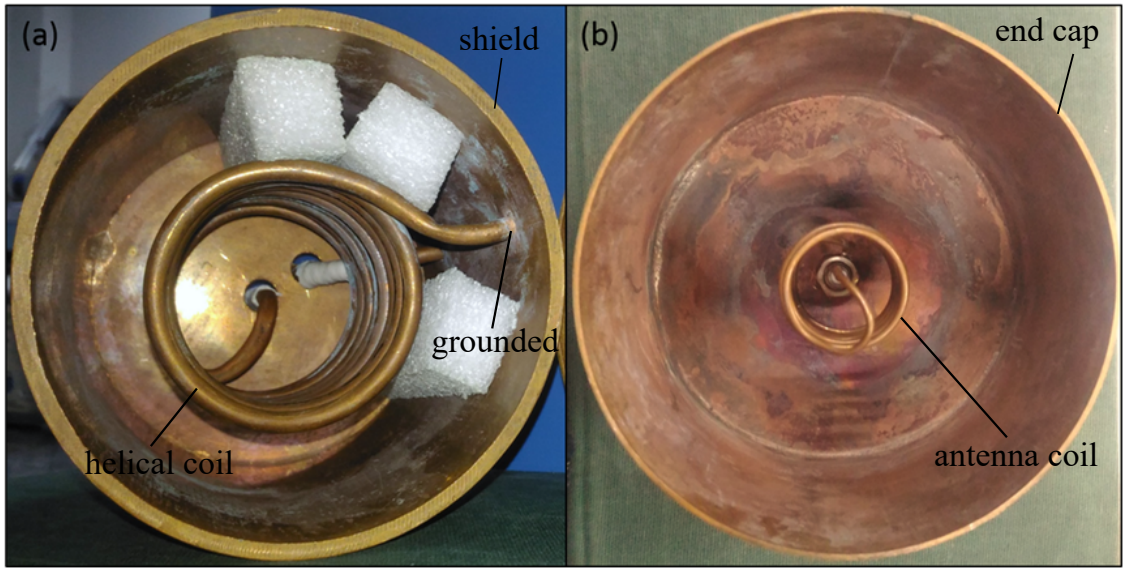

Fig. 6.2: Picture of the helical resonator fabricated in lab. (a) shows the helical coil inside the shield and (b) shows the primary antenna respectively.

is also made with a 2 mm diameter copper wire and it has 6 turns of diameter 35 mm and the overall height is 37 mm.

For measuring f_0 and Q of the helical resonator a unidirectional coupler ($ZFDC-20-3-S+$, Mini circuits) is connected between the rf source and the primary antenna coil. The coupler isolates the reflected part of the rf signal and sends to a signal analyzer ($N9020A$, Agilent Technology). Intensity of the reflected signal is lower at the resonant frequency and if the rf signal is off resonant, most of it is reflected back from the resonator. So by monitoring the reflected signal from the resonator both f_0 and Q of the resonator can be measured. This phenomenon is used for tuning the resonator's mechanical parameters to set it at the desired frequency. The schematic of this experimental setup is shown in Fig. 6.3. Q of the resonator is measured by ratio of f_0 and the full width at half maxima, δf_0 of power rejection. δf_0 can be found by the difference of frequencies on the either side of f_0 at which the power is reduced to half of the maximum value. Figure 6.4(a) depicts the frequency response of the resonator at unloaded condition. The measured resonant frequency at unloaded condition is $f_0 = 38.75 \pm 0.5$ MHz with $Q = 600 \pm 20$. Calculated ($\sim$ 50 MHz) and Q ($\sim$ 1500) of our resonator following the empirical formulas, as given in Eq. (6.1), are quite different compared to the measured values. The empirical formulas consider isolated operation of the resonator, where the resonant frequency arises due to the coil inductance and shield capacitance only. For establishing connection to an ion trap, the free end of the helical coil along with a grounding wire of similar diameter protrude out of the resonator's shield. This additional copper wire definitely adds some capacitive load in the system. Secondly, these two wires are welded to the

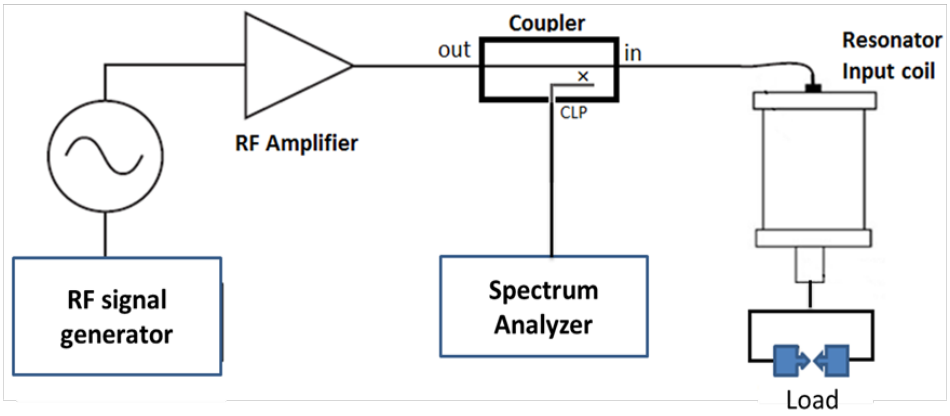

Fig. 6.3: Schematic diagram of the experimental set up for measuring resonant frequency and Q-factor of a helical resonator.

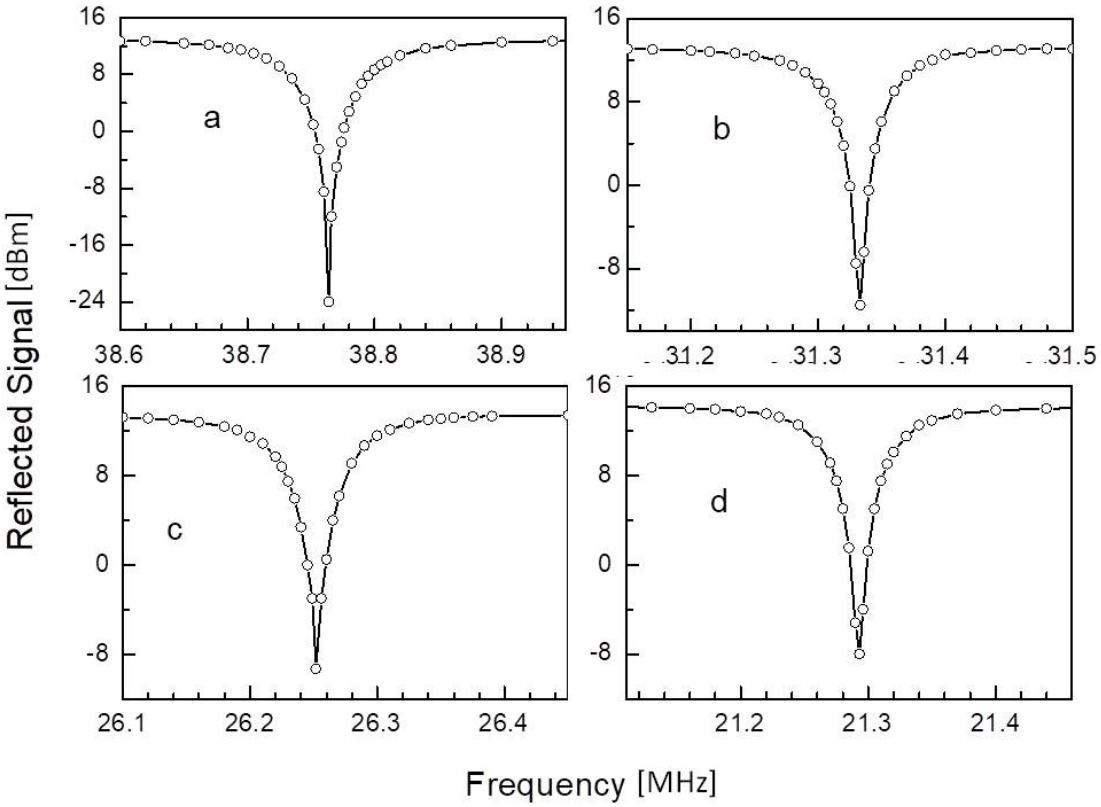

Fig. 6.4: Frequency response of a helical resonator with varying load capacitance (a) $C_L = 0$, unloaded condition ($f_0 = 38.77$ MHz), (b) $C_L = 4.7$ pF ($f_0 = 31.33$ MHz), (c) $C_L = 10$ pF ($f_0 = 26.25$ MHz) and (d) $C_L = 20$ pF ($f_0 = 21.29$ MHz).

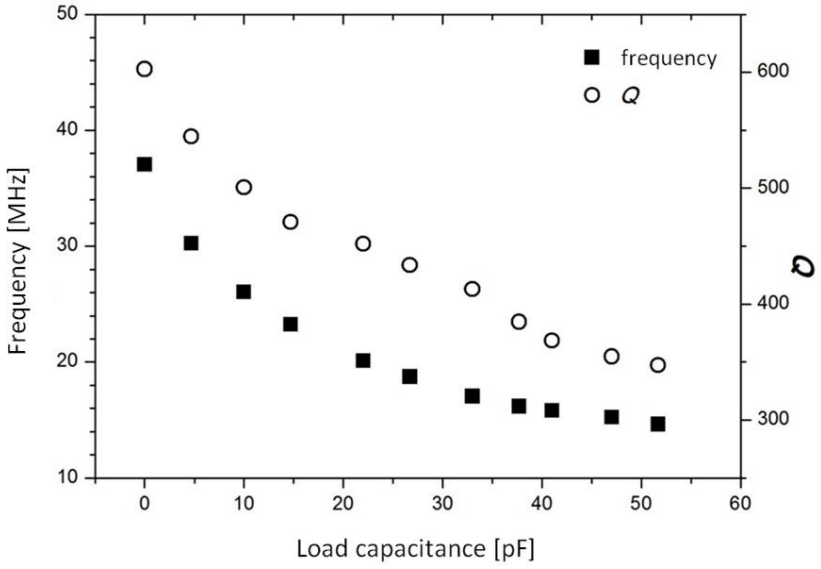

Fig. 6.5: Variation of f_0 and Q of the resonator for different external load capacitance, C_L

shielding tube, adding some more capacitance to the resonator. So, the deviation of f_0 and Q from the calculated value must be because of these additional load capacitances.

As the capacitance of resonator cannot be measured directly, we used a simple technique for estimating equivalent capacitance and inductance of the helical resonator [193]. The resonator was characterized by doing a systematic study on the variation of its f_0 and Q for different capacitive loads. As both f_0 and Q of a resonator depends on its inductance (L) and capacitance (C) following the relations: $f_0 = 1/2\pi\sqrt{LC}$ and $Q = 1/R\sqrt{L/C}$, where C is the total capacitance i.e., the sum of C_0, self-capacitance of resonator and C_L, load capacitance across the resonator. Fig. 6.5 shows the variation of the f_0 and Q of the helical resonator as a function of load capacitance. If f_0 and f_0' are the resonant frequencies of the resonator at unloaded condition and with a load capacitance (C_L), they should follow the relationship

$$f_0 = \frac{1}{2\pi}\sqrt{\frac{1}{LC}} \tag{6.3}$$

$$f_0' = \frac{1}{2\pi}\sqrt{\frac{1}{L(C+C_L)}}$$

$$f_0' = \sqrt{\frac{C}{(C+C_L)}}f_0 \tag{6.4}$$

simplifying the above equations, one can get

$$C = \frac{C_L}{[(\frac{f_0}{f_0'})^2 - 1]} = \left(\frac{C_L}{\delta f^2}\right) \tag{6.5}$$

Tab. 6.1: Peak to peak voltage, V_{PP}, at the trap electrodes for different quality factor, Q and input power, P_{in}. C_1, C_2, and C_3 represent the capacitive load of three different ion traps T_1, T_2 and T_3 respectively.

Q	V_{pp}[V] (@P=5W)			V_{pp}[V] (@P=3W)		
	C_1 = 10 pF	C_1=15 pF	C_1 = 20 pF	C_1 = 10 pF	C_1 = 15 pF	C_1 = 10 pF
200	801.25	755.23	719.98	620.64	584.9	557.70
240	877.72	827.31	788.71	679.88	640.83	610.93
280	948.05	893.60	851.90	734.35	692.18	659.88
320	1013.5	955.30	910.72	785.06	739.97	705.44
360	1074.99	1013.24	965.96	832.68	784.85	748.23
400	1133.14	1068.06	1018.21	877.72	827.31	788.70

Where δf^2=$[(f_0/f_0')^2 - 1]$ is the frequency response parameter. By measuring f_0' for different C_L and finding δf^2, the equivalent capacitance (C) of the resonator can be calculated. Once the equivalent capacitance of the resonator is known, the inductance of the resonator can also be estimated in similar way. The resonant frequency, (f_0') varies with the load capacitance and can be expressed as

$$f_0'^2 = \frac{1}{4\pi^2 L(C + C_L)} = \frac{1}{4\pi^2 LC'} \tag{6.6}$$

Where $C' = C + C_L$, is the effective capacitance at loaded condition.
Now studying the variation of $f_0'^2$ with C_L, the inductance (L) of the helical resonator can be calculated. Considering C and L, one can calculate the resonant frequencies of the resonator for a wide range of external load capacitance and check for its agreement with the experimentally measured values. Both f_0 and Q decrease with the increase of capacitive load. Variation of the frequency response of the resonator for three load capacitances have been presented in Fig. 6.4, which shows that both f_0 and Q decrease with increasing load capacitance. The effective Q of the helical resonator has been optimized by adjusting the position of the primary antenna with respect to the helical coil i.e., altering the mutual inductance between the two coils [193]. The load capacitance of any ion trap can be estimated from this calibration by connecting the ion trap with the resonator and measuring its loaded resonant frequency.

The prime objective of constructing a helical resonator with higher Q is to maximize its frequency filtering efficiency for avoiding multiple and complex oscillations of the trapped ions and also to deliver high voltage rf to the ion trap. The rms voltage across the trap electrode depends on the input power P and Q of the resonator [194] and can be expressed as

$$V_{rms} = \zeta\sqrt{PQ} \tag{6.7}$$

where, $\zeta = (L/C)^{1/4}$, is the trap parameter. Considering C and L of the helical resonator

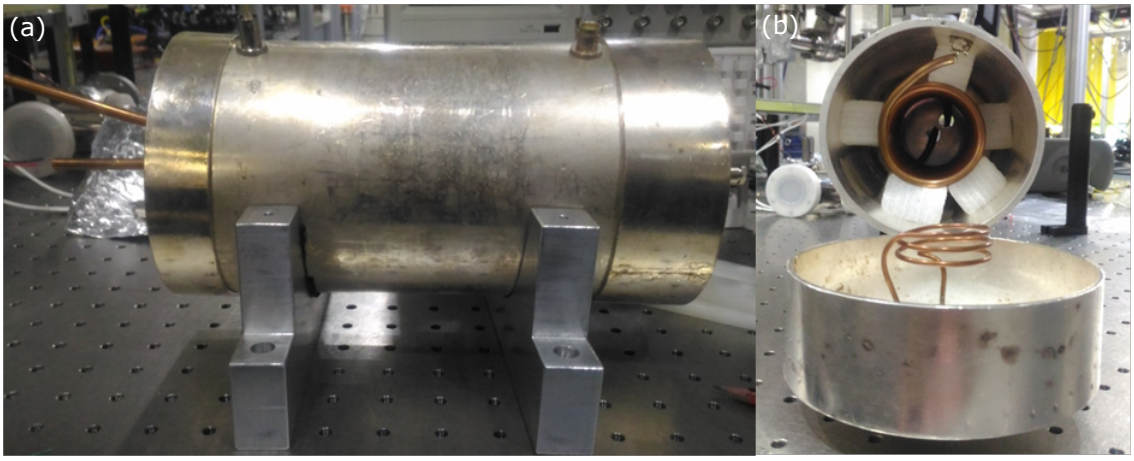

Fig. 6.6: Shows (a) side and (b) front view of the second resonator.

as 8.73 pF and 1.93 μH [193] respectively, dependencies of peak to peak voltage delivered by the helical resonator have been estimated as given in Tab. 6.1 for different Q of the resonator and also for three different ion trap with capacitive load of 10 pF, 15 pF and 20 pF. Helical resonators with higher Q have better efficiency of converting its input power into high voltage output with minimum current *i.e.*, higher Q of a resonator provides higher output voltages per input power.

The ion trap is planned to be driven at frequency range of 12-20 MHz. The resonant frequency of a helical resonator loaded with trap is usually around half its value at unloaded condition. So, another resonator for a lower resonant frequency of f_0 ~30 MHz in unloaded condition designed and constructed. The design parameters were chosen as per the relations given in Eq. (6.1), and are given as: $d = 62$ mm, $d_0 = 6$ mm, $b = 135$ mm, $D = 120$ mm, $H = 210$ mm, $N = 13.5$, $\tau = 0.7$ mm. The primary antenna coil in this case is made with a 2 mm diameter hollow copper wire and it has 3 turns of diameter 35 mm. Its height from end cap surface is 46 mm. The distance between the two coils can be optimized for maximum coupling condition.

At lower frequencies, Q also tend to decrease therefore few design techniques have been improve, for achieving better Q. As described earlier, the helical coil was welded to the copper shielding tube resulting in high impedance. So, in this resonator we connected the shielding tube and the helical coil through a BNC connector (see 6.6(a)). The helical coil is soldered (with low impedance soldering material) to the BNC which is screwed to the shielding tube. Since, the cylindrical shield of resonator is made of copper which gets oxidized easily causing decrease in Q, it was decided to coat the copper cylinder. We decided to coat it with a metal having better conductivity, as it will increase current flow (through the surface) leading to better Q. So, copper shield was plated with 20μm thick layer of silver. It is important that

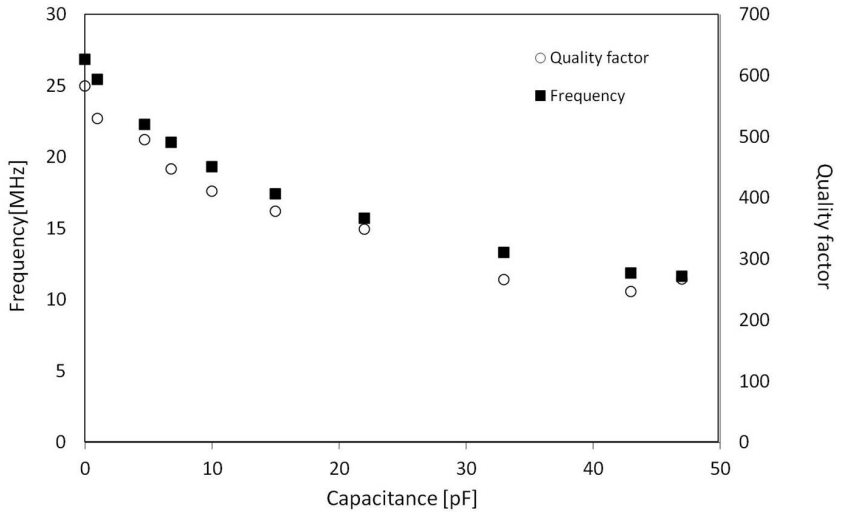

Fig. 6.7: Variation of f_0 and Q of second resonator with different load capacitances, C_L

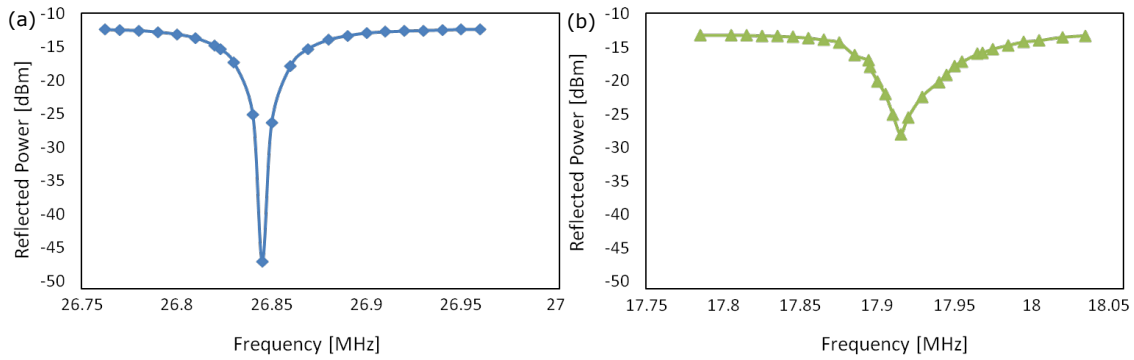

Fig. 6.8: (a) Resonant frequency $f_0 = 26.85$ MHz of second resonator in unloaded condition, $Q \sim 583$; (b) when connected with ion trap (as load) resonant frequency, $f_0 = 17.915$ MHz and $Q \sim 250$

the plating should be smooth and free of microscopic irregularities which may even result in dropping the Q. The coils can also be silver plated for further reduction in impedance. Figure 6.6 shows the actual picture of the second resonator. The measured resonant frequency at unloaded condition is $f_0 = 26.845$ MHz with $Q = 583$. This resonator is also calibrated for different load capacitances as shown in Fig. 6.7 with the same setup as shown in Fig. 6.3. The equivalent capacitance C and inductance L of this resonator is calculated using equations (6.5) and (6.6). Figure 6.9(a) shows the linear dependence of δf^2 with C_L. Capacitance C of the resonator can be calculated from inverse of the slope. The capacitance is calculated to be $C \approx 10.7$ pF. The variation of $f_0'^2$ with the inverse of total effective capacitance, C' of the resonator is shown in Fig. 6.9(b) and the inductance of the resonator is calculated to be $L = 3.3$ μH from its slope.

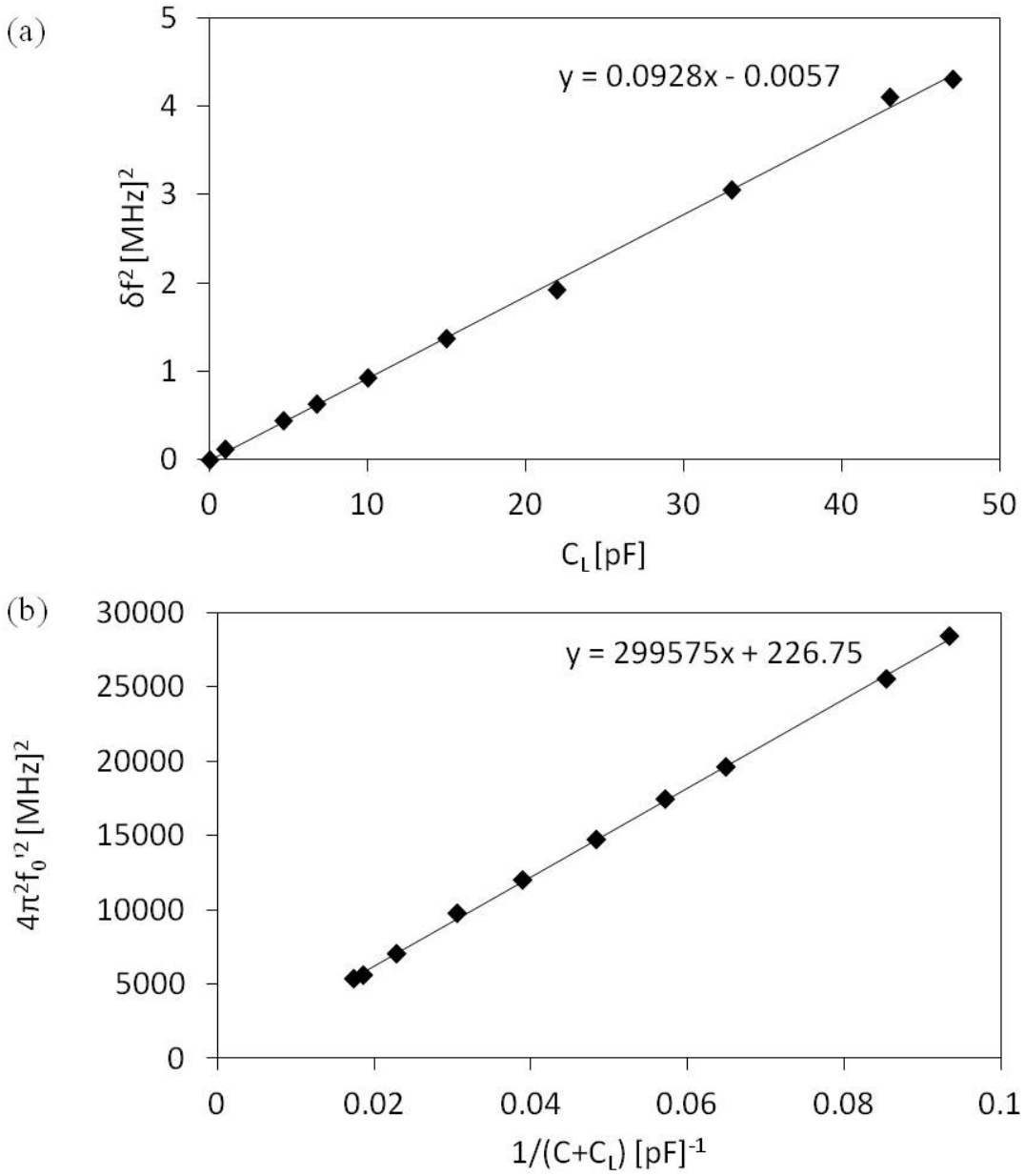

Fig. 6.9: (a) Shows variation of frequency response parameter, δf^2 with load capacitance, C_L and (b) shows variation of $f_0'^2$ with effective capacitance, C' inverse.

The resonator was connected to the ion trap and due to the capacitive impedance of the trap resonant frequency is shifted. Figure 6.8(a) shows the resonant freq in unloaded condition and (b) shows with ion trap connected as load. As the resonant frequency is shifted to $f_0 =$ 17.915 MHz, the trap capacitance is estimated to be $\sim$ 10 pF from the calibrated data. The Q achieved for maximum power transferred to the trap is $\approx$ 250. The trap is not directly

connected to the resonator output, it has an electrical feedthrough and copper connecter in between. These junctions in the connections along with the capacitance offered by the connector and feedthrough causes Q to decrease from the expected value of $Q = 400$. An estimated value of V_{pp} is 744 V at 2 W input power with this $Q = 250$ using Eq. 6.7. The output voltage V_{pp} can be tweaked to desired value either by changing input power or by adjusting the coupling between the primary and secondary antenna coils carefully which changes Q. For shifting the frequency of the resonator to lower side, one can introduce additional capacitive load but that will also cause lowering of resonator Q. So, The helical resonator within desired frequency range (loaded f_0=17.915 MHz) and Q$\simeq$ 250 has been designed and built for efficient delivery of rf to the trap.

Chapter 7

Instrumentation for magnetic field cancellation and axes quantization

The accuracy of optical clock depends upon the determination and mitigation of systematic effects. As discussed in chapter 4, the common systematic effects like Zeeman and electric quadrupole shifts can be determined and eliminated using averaging methods. This chapter discusses simulation, design, fabrication and test results of Helmholtz coils and its driver current source which are used for compensating the stray magnetic fields around the trapping region. The averaging method used for elimination of electric quadrupole shift and micromotion detection techniques also require quantization of axes which is achieved by applying small magnetic field along the directions of spectroscopy laser beam.

7.1. Helmholtz Coils

Helmholtz coils are a pair of conducting circular coils (solenoids) of radius R each with N number of turns and carrying current I in same direction. The coils are separated by a distance s which is equal to the radius, R of the circular loop as shown in Fig. 7.1(a). At this separation, they produce a region of homogeneous magnetic field B in the middle-plane between the two circular coils. The strength of magnetic field produced by the Helmholtz coils, at point, P, at the center the two coils is derived from Biot Savart's law and is given as

$$B = \frac{8\mu_o NI}{\sqrt{125}R} \tag{7.1}$$

The strength of the magnetic field is dependent upon the current, I, the number of turns, N, and the radius a of the coil.

As already discussed in chapter 4, the value of geomagnetic field at New Delhi, India is approximately 50 μT or 0.5G which produces a net second order Zeeman shift of 5.44 Hz in E3-clock transition. This field needs to be compensated by equal and opposite uniform magnetic field with very low gradient at trapping center. Also, in this experiment as the laser light beams

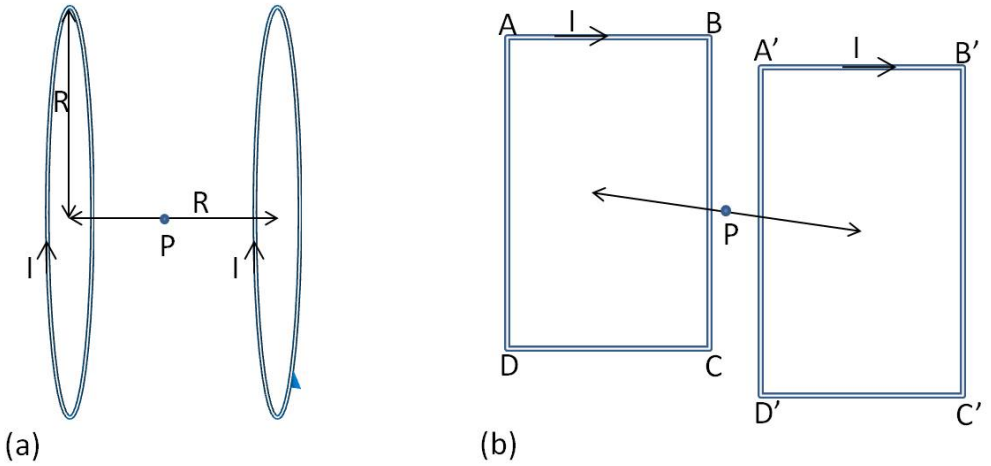

Fig. 7.1: (a) Shows standard configuration of Helmholtz coils with circular coils, whereas (b) shows Helmholtz coils with rectangular geometry.

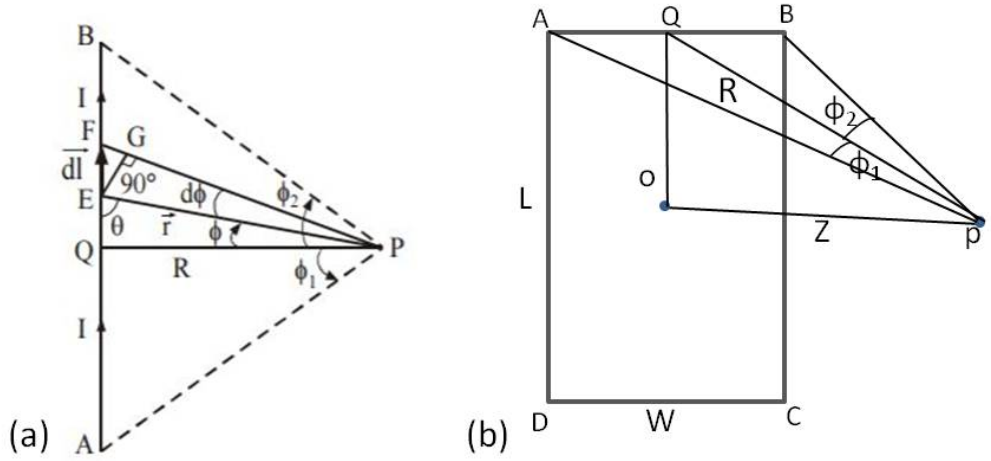

Fig. 7.2: (a) Shows detailed view of side AB of the rectangular coil ABCD shown in above figure, whereas (b) shows isometric view of the coil ABCD along with its distance from point P.

(369.5 nm) are impinged from the CF-16 ports along the *x́-ý-ź* axes (as discussed in chapter 5), 3 pairs of magnetic coils are required to quantize these axes. The experiment also requires a field with a high gradient at the trapping center which is done by antihelmholtz coils but separation in this case is not critical therefore the optimization is achieved for the Helmholtz case only. Considering spatial constraints of elaborate vacuum assembly and ease of mounting, it was decided to use coils of rectangular geometry. Consider a pair of similar rectangular coils, ABCD and ÁB́ĆD́ as shown in Fig. 7.1(b). Each of the coils have dimensions L×W, number ofturns, N and current I flowing through them along same direction. So, the magnetic field at point P is a vector sum of field contributions from coil ABCD, B_{ABCD} and coil ÁB́ĆD́,

$B_{\acute{A}\acute{B}\acute{C}\acute{D}}$. Further, field due to each coil is sum of fields due to each side of the rectangular coil, for e.g. $B_{ABCD} = B_{AB} + B_{BC} + B_{CD} + B_{DA}$. Consider section AB of the coil ABCD as shown in Fig. 7.2(a) with dl being a small length element and r being the distance of this element from point P. Magnetic field at point P due to dl can be written as

$$dB = \frac{\mu_o}{4\pi}\frac{Idl \times r}{r^3} \tag{7.2}$$

where the number of turns N is considered to be 1. As the angle between dl and r is $(180^\circ - \theta)$, the above equation can be rewritten as

$$\begin{aligned} dB &= \frac{\mu_o}{4\pi}\frac{Idl\sin(180^\circ - \theta)}{r^2}, \\ dB &= \frac{\mu_o}{4\pi}\frac{Idl\sin\theta}{r^2} \end{aligned} \tag{7.3}$$

Further, EG=EFsin θ= $dl \sin\theta$,
also, EG=EPsin $d\phi$=$rd\phi$ (as $d\phi \ll$). Therefore, $dl \sin\theta$=$rd\phi$ and Eq. (7.4) can be written as

$$dB = \frac{\mu_o}{4\pi}\frac{Id\phi}{r} \tag{7.4}$$

Also, from ΔEQP, $r = R/\cos\phi$, so,

$$dB = \frac{\mu_o}{4\pi}\frac{I\cos\phi d\phi}{R} \tag{7.5}$$

Integrating above equation for line section AB,

$$\begin{aligned} B_{AB} &= \frac{\mu_o}{4\pi}\int_{-\phi_1}^{\phi_2}\frac{I\cos\phi d\phi}{R} \\ B_{AB} &= \frac{\mu_o}{4\pi}\frac{I}{R}(\sin\phi_1 + \sin\phi_2) \end{aligned} \tag{7.6}$$

From Fig. 7.2(b), we can find ϕ_1 and ϕ_2 and simplify further to achieve

$$B_{AB} = \frac{\mu_o}{4\pi}\frac{I}{\sqrt{(\frac{L}{2})^2 + Z^2}}\frac{W}{2\sqrt{(\frac{W}{2})^2 + (\frac{L}{2})^2 + Z^2}} \tag{7.7}$$

Similarly, for smaller side BC of the rectangular coil

$$B_{BC} = \frac{\mu_o}{4\pi}\frac{I}{\sqrt{(\frac{W}{2})^2 + Z^2}}\frac{L}{2\sqrt{(\frac{W}{2})^2 + (\frac{L}{2})^2 + Z^2}} \tag{7.8}$$

Tab. 7.1: Optimized values of dimensions and separations of rectangular coils.

Coil frames	1, 2	3, 4	5, 6
Inside length [mm]	903	943	976
Outside length[mm]	921	961	994
Inside breadth [mm]	643	637	930
Outside breadth[mm]	661	613	954
Separation [mm]	397	390	500
Turns	24	24	24

The magnetic field at point P due to single turn of coil ABCD is

$$B_{ABCD} = \frac{\mu_o ILW}{4\pi\sqrt{(\frac{W}{2})^2 + (\frac{L}{2})^2 + Z^2}}\left[\frac{1}{\sqrt{(\frac{L}{2})^2 + Z^2}} + \frac{1}{\sqrt{(\frac{W}{2})^2 + Z^2}}\right] \tag{7.9}$$

Expression for $B_{\acute{A}\acute{B}\acute{C}\acute{D}}$ is obtained in a similar manner. The effective magnetic field is vector sum of B_{ABCD} and $B_{\acute{A}\acute{B}\acute{C}\acute{D}}$. The region of uniform magnetic field is optimized by varying the parameters, Z (separation between coils) and L×W (dimensions of coils). For this optimization the coil assembly was simulated in Mathematica software. The dimensions and separation values of the coils were constrained by the height of the shelf above the optics table (see Appendix B) as well as the vacuum assembly. The detailed Mathematica code is given in Appendix C. For easy mounting and convention all the six coils are numbered as 1,2,..6 and paired such that the two coils in a pair have identical dimensions. The pairs namely, $\{1, 2\}$, $\{3, 4\}$ and $\{5, 6\}$ are for three perpendicular directions (x, y, z) around the vacuum chamber as shown in Fig. 7.3. The figure shows position of the coils with respect to different ports which have already been discussed in chapter 5. Table 7.1 lists the dimensions of different coils along with their optimized separations.

7.1.1 Construction

For the construction of the coils, varnish coated 18 SWG (diameter = 1.829 mm) solid copper wire having a maximum current capacity of 3.7 A was used. For each of the coils, this wire was wound tightly by hand on an aluminum frame held by a lathe. The aluminum frames are of rectangular shape as given in Tab. 7.1. For achieving both Helmholtz and antihelmholtz configurations with same set of coils, the windings in each of the coils were done in two sets with teflon insulation between them. Each coil was first wound with a double layer winding set and then finished with outgoing leads at the ends for connections. Although the copper wire is enamelled but a teflon insulation is still inserted between coils before starting the winding of set two. The second set of winding contains a single layer and has outgoing leads at ends. Each winding layer accommodates 12 windings. The first set that is the double layer winding is used in Helmholtz configuration whereas the second set with single layer winding is used

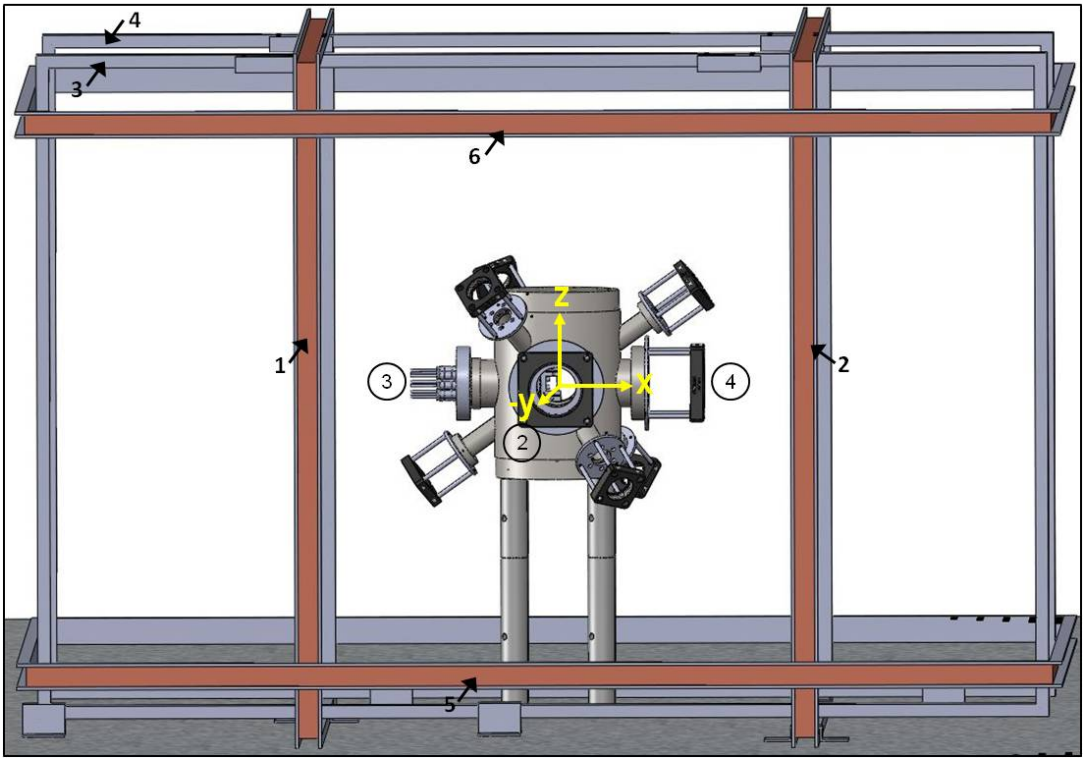

Fig. 7.3: Shows numbering convention of the coils along with their position with respect to the (x, y, z) axes directions and different ports. For clarity, only vacuum chamber is shown as surrounded by the coils not the complete vacuum assembly.

in antihelmholtz configuration. For rigidity and insulation, the final winding is covered with teflon along the whole coil frame. This also help the coils to lie flat against the mounting surface. Aluminium mounts were designed and fabricated to hold the coil frames in place as shown in Fig. 7.3. Current sources used for driving the coils are also designed indigenously and are described in following subsection.

7.1.2 Digitally Controlled Stable Current Source

The current source has been designed for driving solenoids discussed in last section. The circuit uses digital-to-analog converter (DAC), a precision op amp, and MOSFET transistor. The current source circuit is used in conjunction with digitally operated addressing and control module (DACM) which helps in its digital selection and output control through DAQ card installed in computer (NI PCIe6353 in our case). The digital control system can control number of equipments in the lab and is based on 16-bit data and 6-bit address. The bits are generated by the PCIe DAQ card and travel over flat ribbon cables throught out the lab. Chapter 8 discusses this system in detail. DACM takes 16-bit data and selects equipment on basis of 6-bit address. It latches the data bits and transfers them to the equipment with desired

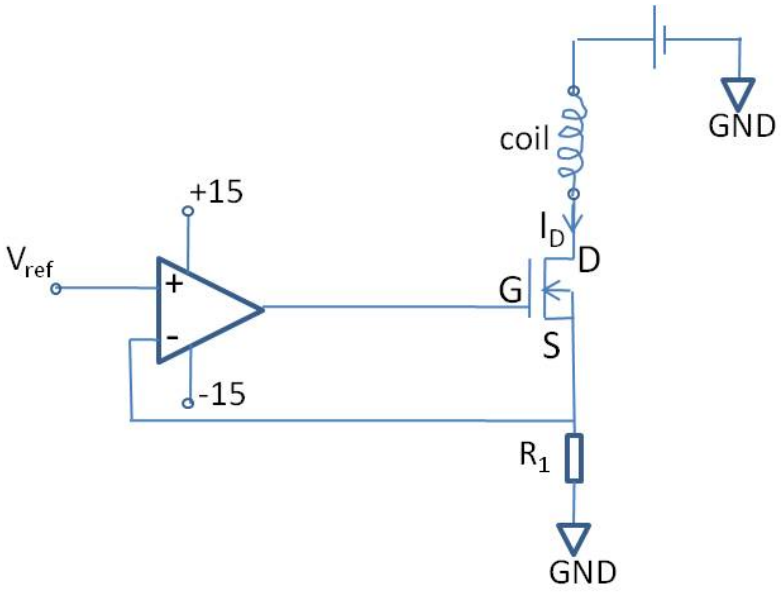

Fig. 7.4: Block diagram depicting working of the current source.

address as described in Ref. [198, 195].

Circuit Description: The current source circuit is composed of two stages. The first stage which is the input stage is composed of the 16-bit DAC (DAC-712P) and a precision op amp (OP07). The second stage is an N-channel MOSFET (BUZ15/BUZ45) transistor output stage, which supplies the current in response to the digital bits sent to the circuit. The DAC at the input stage takes 16-bit input data from the DACM module and converts it into an analog voltage. This analog voltage, V_{ref}, is fed at non inverting terminal of op amp. The MOSFET in conjunction with the op amp makes a high current output follower circuit. The op amp is fed with a negative feedback from the source pin of the transistor to regulate the value of the current through the R_1 resistor. When the MOSFET is biased a drain current I_D flows through the load (coils in this case) which is controlled by gate source voltage, V_{GS}. The circuit uses regulated +5 V supply for the DAC and ±15 V supplies for the op amp. It also uses a dc supply of 20V/6A for biasing drain of the MOSFET. Figure 7.5 shows the supply section and the Fig. 7.6 shows the current source circuit. As shown in Fig. 7.6, there is an option for using DIP or smd package op amp which can be chosen with the help of jumpers provided. The circuit was initially tested with precision op amp LT1677 (smd package) but it was found that LT1677 did not stabilize the current as desired. Thus it was replaced by the OP07 op amp. Also, the 20V/6A supply regulation is not included in the printed circuit board because of the high current which is rectified through a commercially available rectifier board. Figure 7.7 shows the printed circuit board (pcb) design of the current source. This pcb is multilayer and 6cm×8cm in size. The current source pcb, DACM and other components

are installed in a standard 19' rack-mount, 3U size box as shown in Fig. 7.8. The peripheral accessories on the front panel include of a pair of standard male-female DB-25 connectors for taking input bits, standard banana receptacles for taking output, a toggle switch for ON/OFF action and a standard 7-segment display. The back panel has MOSFET BUZ15 mounted on a heat sink, high wattage (50 watt) resistor R1=1.7 ohms and a 6 A safety fuse.

Characteristics: Three modules of the digitally controlled current source were built to drive 3 pairs of magnetic coils. Their characteristics and fidelity of operation were tested by connecting their output to a coil in series with a 6 and 1/2 digit precision multimeter from Fluke (model 8846a). The output of each current source was first tested for linearity. Input data bits corresponding to desired value of current, I_{set} were given to the current source from a LabVIEW based graphical user interface (GUI) (details are discussed in chapter 8). Multiple readings (20 in number) of output current I_o were recorded at intervals of 10 s for a fixed value of I_{set} over range of 1A to 5A. Figure 7.9 shows linear operation of one such current source. The linear fit model to the experimental readings give an intercept of 0.0165 and a slope of 0.9535. The stability of the current source is tested by comparing the current values at just ON situation and after 6 hours of continuous operation at each I_{set} as shown in Fig. 7.10. The maximum fluctuation in current is found to be 12μA which is well within the resolution of DAC used in the circuit. This results in the a magnetic field error of $\pm$65 μG at the center of a pair of Helmholtz coils. The current sources produce linear and stable current values. After successful testing of all three current source modules for their characteristics, they were used to drive the Helmholtz coils for magnetic field mapping.

7.2. Measurements

The coil frames are required to be mounted on the optics table with trap center as the center of coils assembly but for obstruction free mapping of magnetic field at regular spatial intervals the coils were assembled with empty space (no vacuum assembly) inside them with exactly same separations and orientations, they are supposed to be in. Tin wires were tightly tied through the center of the frames along the axis of the coils to mark the center and also to guide the measurement probe of Gauss meter. The gauss meter used is Lutron precision milli-gauss meter, model:GU-3001. It is an AC/DC milligauss magnetometer with resolution of 0.1 milligauss. Stickers with millimeter markings on them were attached along the length of tin wires so as to move the probe at consistent spatial intervals. This set up was used for mapping the profile of magnetic field along the three directions. A DC current of 1 A was passed through each pair of opposite coils which make a series connection ensuring equal current flowing in same direction. The maximum error in the experimental readings due to measuring instrument (gaussmeter) is $\pm$2% of the measured value. This was the dominant limiting factor in determining the characteristics of the constructed coils. An error of $\pm$ 65

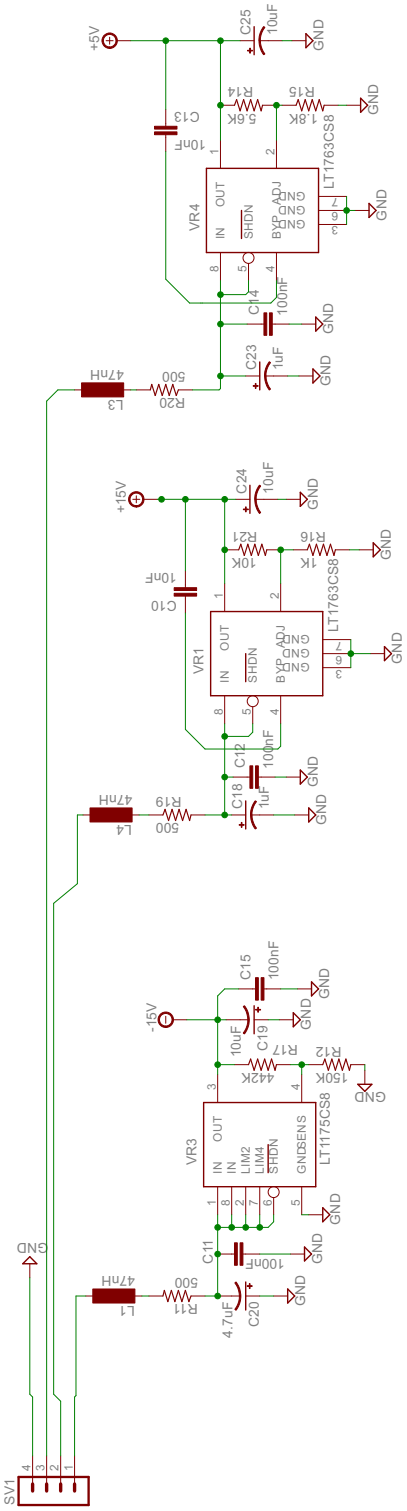

Fig. 7.5: Schematic representation of supply section of the current source circuit.

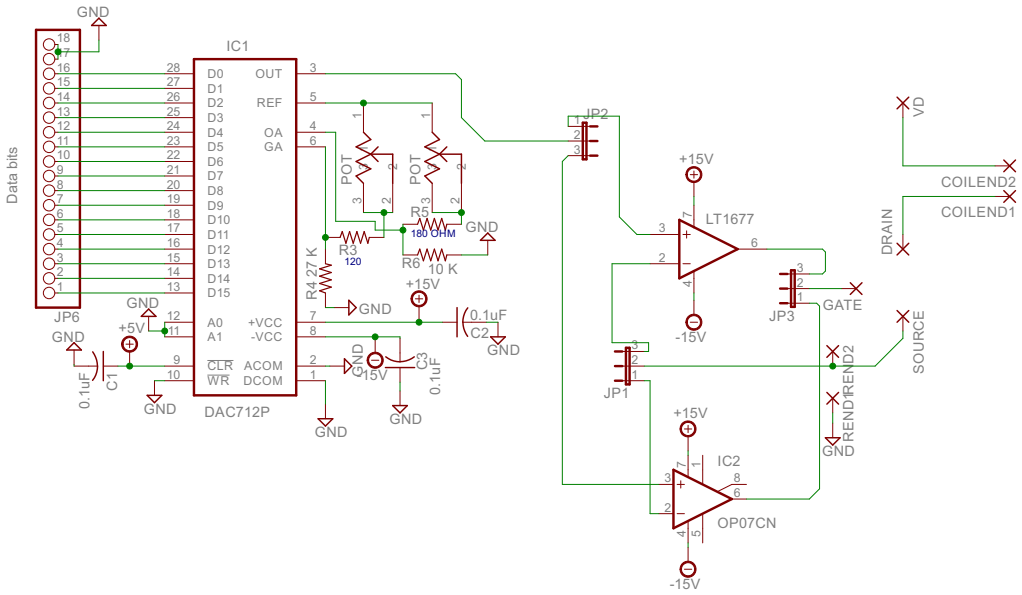

Fig. 7.6: Schematic representation of current source circuit.

μG was also contributed from the fluctuation in current I as discussed in previous subsection. Also, the error in spatial positioning of the probe along the span of the measurements is taken to be $\pm$0.3cm. The plots shown in Fig. 7.11 give the profile of magnetic field along the x, y and z directions, respectively. The Red colored markers represent experimentally measured data where as the blue colored line represent the simulated magnetic field profile for 1 A driving current. The uniform magnetic field region has a very low curvature on the order of $\sim 10^{-11}$ G/cm over the central trapping region of $\pm$0.2cm. The value of magnetic field can be altered to suit the requirement by altering driving current.

Helmholtz coils have been optimally designed and assembled to neutralize stray magnetic fields in the vicinity of ion which induce 2^{nd} order Zeeman shift. These coils also solve purpose of axis quantization. Digitally controlled stable current sources were also designed in house for driving current in these coils.

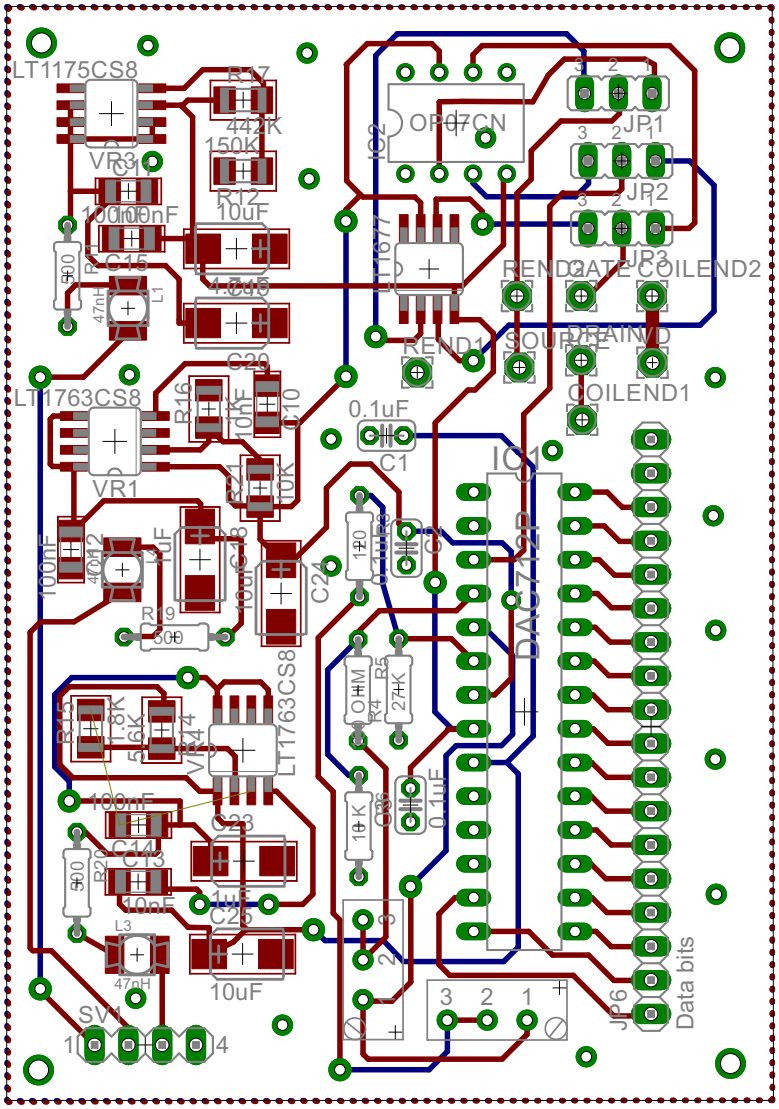

Fig. 7.7: PCB board of current source.

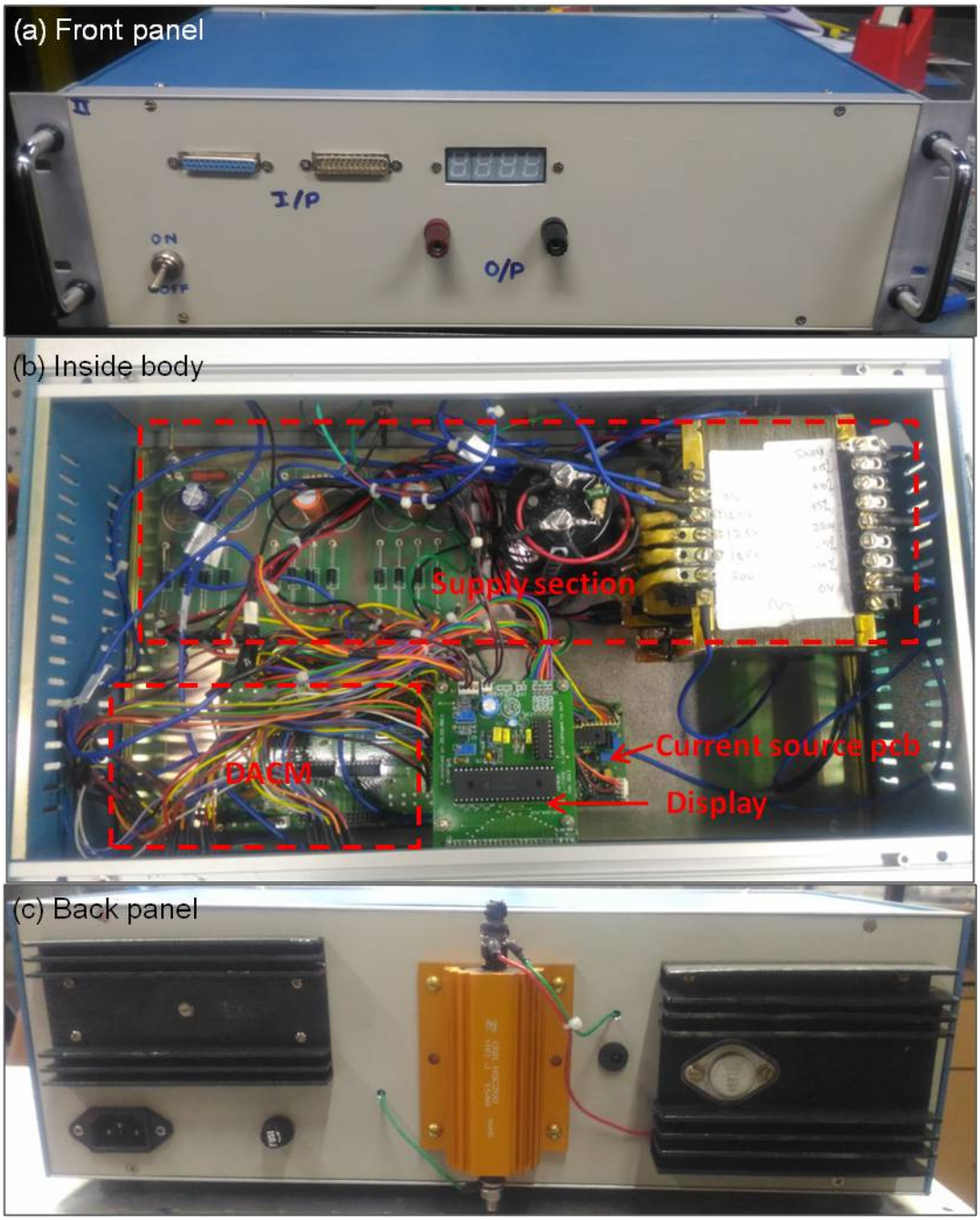

Fig. 7.8: Digitally controlled current source box. (a) Shows front panel of the box which takes input bits, deliver output and has a display; (b) shows inside view of the box with supply, DACM, display and current source sections; (c) shows back panel which mounts MOSFET, heat sinks and has safety fuse.

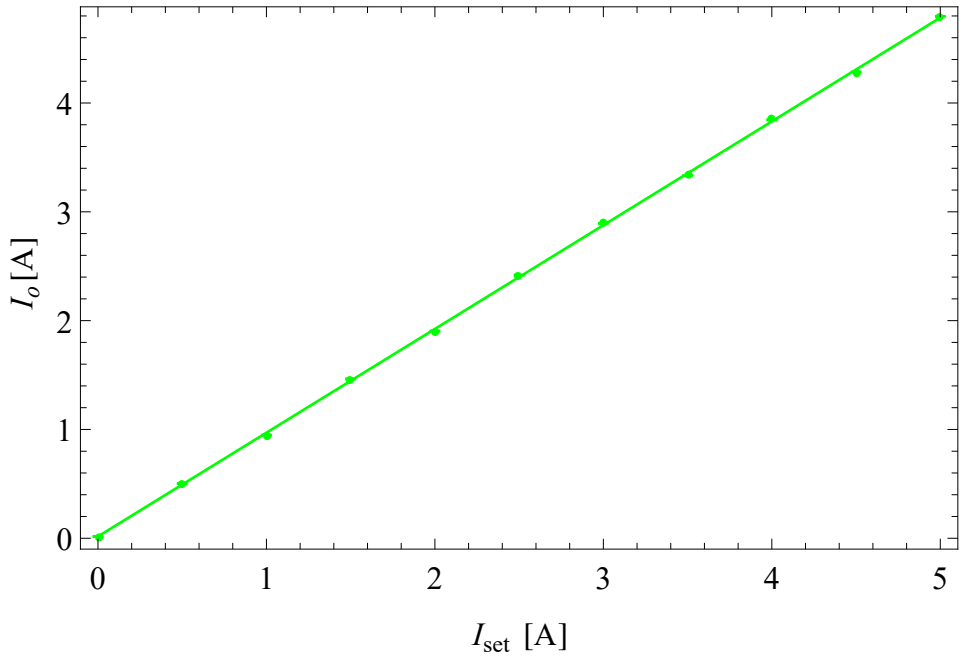

Fig. 7.9: Shows linear relation of I_{set} vs I_o of a current source. Green markers show the actual experimental values and the green solid line is linearly fitted over the experimental data.

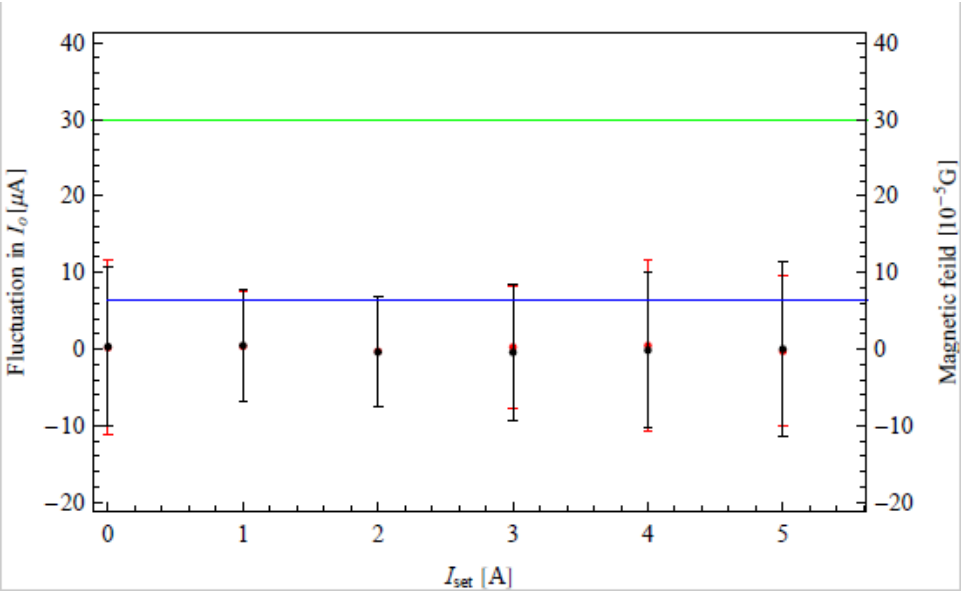

Fig. 7.10: Shows fluctuation at different I_{set}, Black corresponds to just ON situation and Red corresponds to situation after 6 hours of continuous operation. Green line shows the resolution of the D/A converter used in the device. The maximum fluctuation of 12μA corresponds to a magnetic field of 65 μG at the center of a pair of Helmholtz coils shown by Blue line.

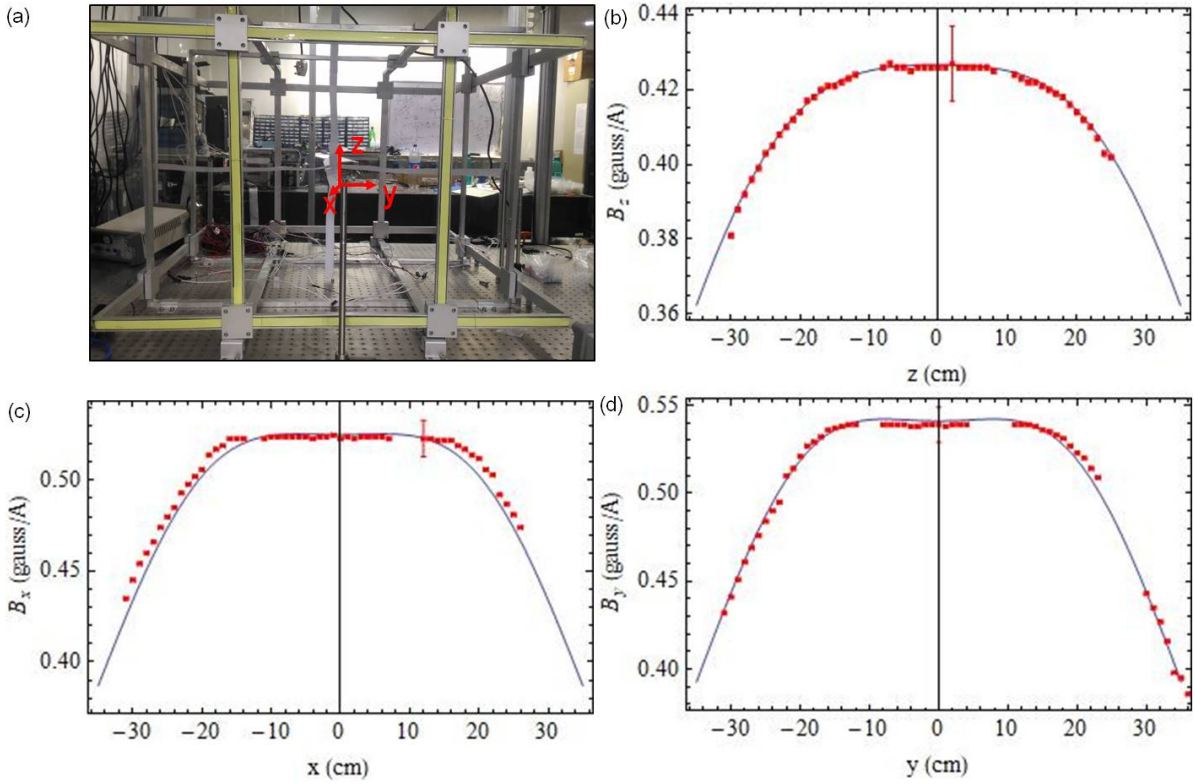

Fig. 7.11: Shows (a) assembly of the magnetic coils put together for mapping magnetic field profile, (b), (c) and (d) profile of magnetic field at the center of coil assembly along z, x and y directions, respectively. Blue line shows simulated field whereas red markers show the experimentally measured values.

Chapter 8

Automated Control and Data Acquisition System

Any experiment consists of several different steps to be carried in a particular order following a protocol called an experimental cycle. The steps of an experimental cycle which are often required to be repeated can be broadly divided in input generation, controlling of equipment, sample preparation, probing the desired objective, acquiring data and analysis. This can get really complicated in a precision experiment as large number of equipments need to be operated and checked at short intervals of time for data collection simultaneously. Hence, most of such state-of-the-art experiments rely on automation of the entire operation to avoid any human errors or delays. The Yb^+ clock experimental protocol involves production of ytterbium atomic beam, photoionization of the atoms, trapping, laser cooling, interrogation of the clock transition and high resolution imaging of the single ion. Each of these processes involve custom designed, indigenously developed modules which include computer controlled dc power supply [195] used to deliver dc volatage to the ion trap, Acousto-optic modulator (AOM) drivers for shifting frequency of laser lights, constant current sources for driving Helmholtz coils, shutter drivers [196] for blocking/unblocking light at desired rates etc. And the task of controlling, monitoring and acquiring a range of parameters from this plethora of instruments reliably is to be done continuously and precisely for days.

8.1. Scheme of Control and Data Acquisition System

An automated control and data acquisition (CDAQ) system is developed for running the clock experiment efficiently and remotely. This indigenously developed system is a combination of controlling software and supporting hardware subsystems. The CDAQ system is composed of hardware modules, connectors and software listed below:

- High performance computer (workstation)
- National Instruments Peripheral Component Interconnect (PCI) card (NI PCIe 6353), its accessories: connector block (NI SCB-68A), NI standard VHDCI accessory cable

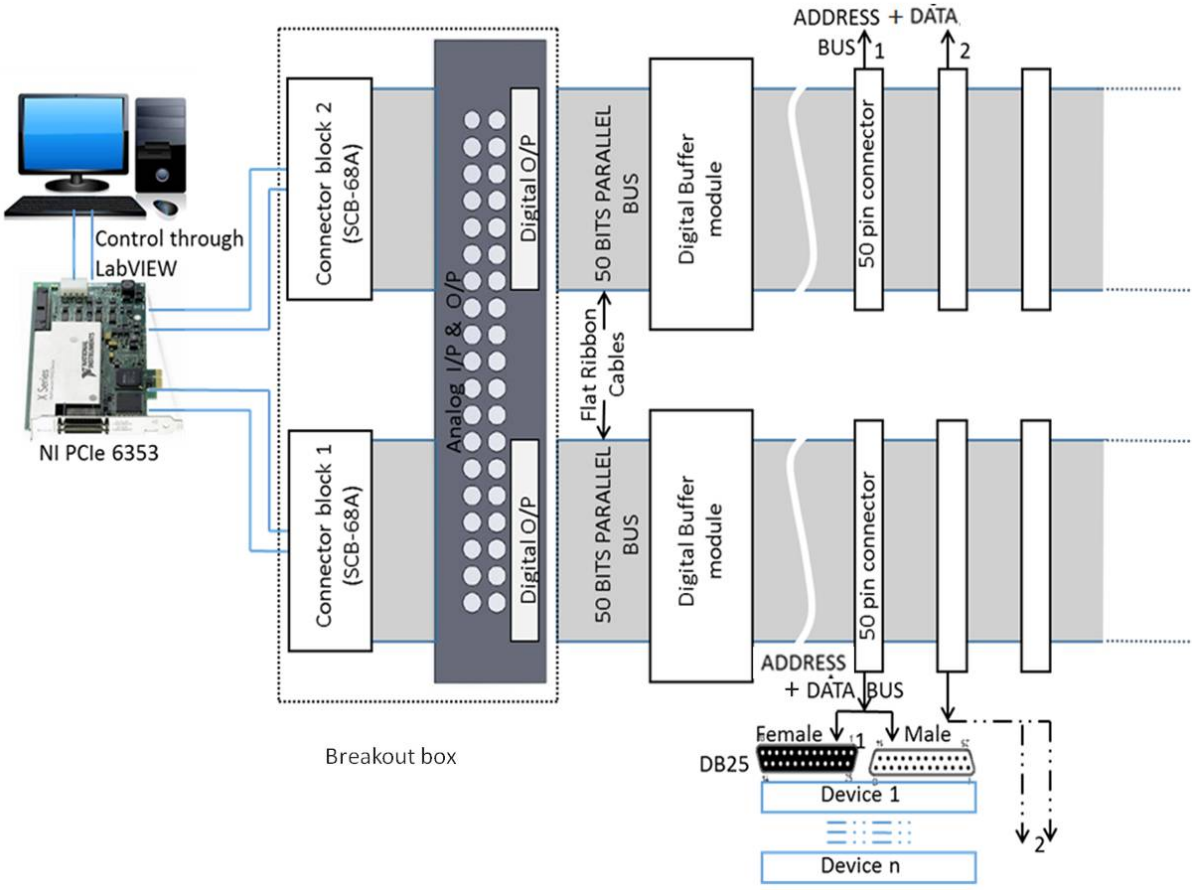

Fig. 8.1: Schematic representation of automated control and data acquisition system for our experiment.

- 50-line Flat Ribbon Cables (FRCs)
- 50-pin FRC IDC type connectors, both male and female
- Breakout box (components required: connector blocks, subminiature male crimps, standard BNC receptacles, coaxial cables (RG174), 50-line FRC and connectors, a 19' rack-mount, 3U size box)
- Digital buffer module (components required: SN74HCT541N/ MH74HCT541B1R, 1PS70SB14/ BAT54SWT1G, 4116R-1-RC, LT1963, XLR connector, 50-line FRC and connectors, a 19' rack-mount, 3U size box)
- Digitally operated addressing and control module (DACM) [198, 195]
- Laboratory Virtual Instrument Engineering Workbench (NI LabVIEW)

A schematic representation of CDAQ is shown in Fig. 8.1. The PCI card used has 48 digital output/input (DO/DI), 24 digital grounds (DG), 32 single ended (or 16 differential) analog input (AI), 4 single ended analog output (AO) channels and 16 analog grounds (AG) with maximum multichannel sample rate of 1 MHz/s [197]. The PCI card is mounted inside a high performance CPU of a computer (workstation) which is dedicatedly used for CDAQ system. The equipments used in the experiment are controlled from the workstation through a graphical user interface (GUI) programmed in LabVIEW. The access ports of the PCI card are extended out through a pair of connector blocks. These connector blocks are installed in a standard 19' rack-mount, 3U size box for easy to use universal conventions of the I/Os. This box has been named as breakout box. All the DI/DO's, AI/AO's along with there respective grounds are connected inside this breakout box so that the end-user does not need to use screw terminals of the connecting blocks for connections. Since most of the equipment used in this experiment, such as AOM drivers, constant current sources, dc power supplies, shutter driver etc. are positioned outside the dust free optics friendly enclosure (as shown in Appendix A), therefore, the equipment are being controlled from a distance of about 10-20 m. A pair of 50-line FRCs is used for carrying DO/DI+DG and standard 50-ohm BNC's to carry AO/AI+AG from breakout box to the experiment or vice-versa. The digital BUS travelling over FRCs comprise of address and data which is broadcasted to all the equipments connected. All these equipments are provided with a unique address with the help of a DACM which is attached to each of the equipment, as described in Ref. [198, 195]. This DACM selects a specific equipment and then the data is latched in them by using DOs from the PCI card. The data BUS is available to all the equipment but only used by the equipment which is addressed/ selected. As a large number of equipment access 6-bit address cum 16-bit data BUS from the PCI card, altogether drawing few hundred mA current. However, any PCI card has a maximum value of current per channel, which restricts the number of equipment which can be controlled. This problem is

solved by using an indigenously designed digital buffer module increasing the current capacity of each channel. Another problem observed is that the digital bits acquire arbitrary delays among them after travelling through a long cable, even though they are identical at the initial point. As a result the bit pattern becomes time dependent which effects both selection and control. To overcome this problem, an additional pulse is used in the address BUS. This pulse triggers the selection only after all the other digital bits reach their desired states. The PCI card used in CDAQ can generate a trigger pulse as fast as 1 MHz. The trigger pulse is timed with a delay > 0.4 μs for a 30 m long FRC to eliminate the possibilities of reading incorrect bits by the equipment.

Conventions: The CDAQ is configured to work with a 6-bit address for equipment identification. Thus, there can be 2^6=64 unique combinations of binary bits '0' and '1', so, with 6-bit addressing, one PCI card can identify and control up to 64 different devices. The CDAQ system can easily be augmented to suit the requirements for more complex experiments with any number of equipment by simply adding PCI card and hardware subsystems to it. The signal BUS travelling over 50-line FRCs is split into two 25-line FRC at the device end. Each of these carrying DO and DG alternately at the odd and even lines of the BUS, respectively. We use a pair of DB25 connectors at end of each equipment to establish connections with the two 25-lines FRC used for selection and data control. The bit-ordering in the first 25-line FRC is such that it carries trigger pulse in first (red colored) wire, followed by 6-bit address of the equipment and then 1st 6-bits of data information along with the alternate DGs in between. The convention followed through out the CDAQ is in a manner that the bit pattern starts from most significant bit (MSB) and ends at least significant bit (LSB). This can been defined other way around as it depends upon configuring the channels programmatically. The trigger pulse along with the 6-bit address bits are used for selection of equipment using its DACM module. The bit-ordering in the second 25-line FRC is in a way that the 7th bit of the data (starting from MSB) is carried in first wire followed by other bits till the 16th bit (LSB) of the data with alternate DGs in between. The selected equipment then latches 16-bit data, spread over two 25-line FRCs. The other details of bit-ordering and conventions are discussed in subsection 8.2.1 ahead. Each of these 25-line FRCs are crimped to a pair of 25-way male-female DSUB (DB25) connectors. The bit pattern starts at first 25-line split FRC which is crimped on a male DB25 connecter and the second part of 25-line FRC is crimped on a female DB25 connecter. The DB25 connecter counterparts are panel mounted at the equipment to take the input from the FRCs. To avoid possibilities of bit order mismatch due to swapping of DB25 connectors at device end, the pair of male-and-female DB25 at the end equipment are mounted upside-down (as shown in schematic 8.1). Analog signals are transported using BNC mounted RG174 cables. Apart from 23 DOs for addressing and controlling the equipment, we often require DOs for triggering other devices such as mechanical shutters [196] used for blocking and unblocking laser beams, CCD camera and PMT, which are carried by second 25-line BUS. All these analog

and digital signals are brought in the vicinity of the equipment from the breakout box through 38 BNC cables and two 50-line FRCs in total. In the following sections we discuss the hardware and software requirements of this data acquisition system.

8.2. Hardware Subsystems

The automated CDAQ system has numerous devices which are connected to a single PCI card and controlled by a GUI. To be able to drive so many equipment from a single PCI card, dedicated hardware subsystems were developed indigenously as described in following subsections

8.2.1 Breakout Box

The digital, DI/DO's and analog, AI/AO's channels carry the information to-fro between the PCI card and the equipment cannot be accessed directly at the PCI card as it is installed inside workstation. The access to them is through a NI standard VHDCI accessory cable which has 68-Position Cable Connector Plug (Male) on the PCI card end and 68-pin 0.050 SCSI D-Type Connector Male on the accessory (connector block, SCB-68A) end. For the PCI card used in CDAQ system, i.e. NI PCIe 6353, two connector blocks were required to access all its 48 DI/DO and 36 AI/AO channels. Each connector block as shown in Fig. 8.2(a) has screw terminals for connections. Each of these screw terminals corresponding to a channel is named uniquely. In the CDAQ system, there are numerous equipments to be controlled and it is not possible to connect each of them to the connector blocks directly to broadcast the address cum data BUS to them. To avoid all these cumbersome connections for end user and for a universal convention throughout the CDAQ system a breakout box is developed. Figure 8.2(b) shows schematic representation of connections inside the breakout box.

Connections and bit-order Conventions: The CDAQ naming convention is set such that the two connector blocks mounted inside the breakout box are named PART A and PART B. Each of these PARTS has 24 DI/O, 24 DG; 2 AOs, 16 single ended AI and 10 corresponding AGs. So, one breakout box consists of 48 DI/Os, 48 DGs, 4 AOs and 32 AIs as shown in Fig. 8.2(c). The connections inside the breakout box are made using subminiature male crimps, crimped on each line of the 50-line FRC. These are screwed to different screw terminals corresponding to digital channels. At the other end of this 50-line FRC, there is a 50-pin FRC IDC type male connector mounted on the front panel of a standard 19' 3U aluminium box. There are two 50-pin FRC IDC type male connectors on either side i.e. for PART A and PART B. As described earlier, FRC based CDAQ BUS carry DI/Os and DGs alternatively, with first pin being a DI/O. The pattern of bits according to this convention is given in Tab. 8.3. Line no. 47 of FRC is left open and so is the pin no. 48 due to the fact that there are only 24 DI/Os+ 24 DGs in each PART unlike the 50-lines of FRC. The orientation of the FRC cable

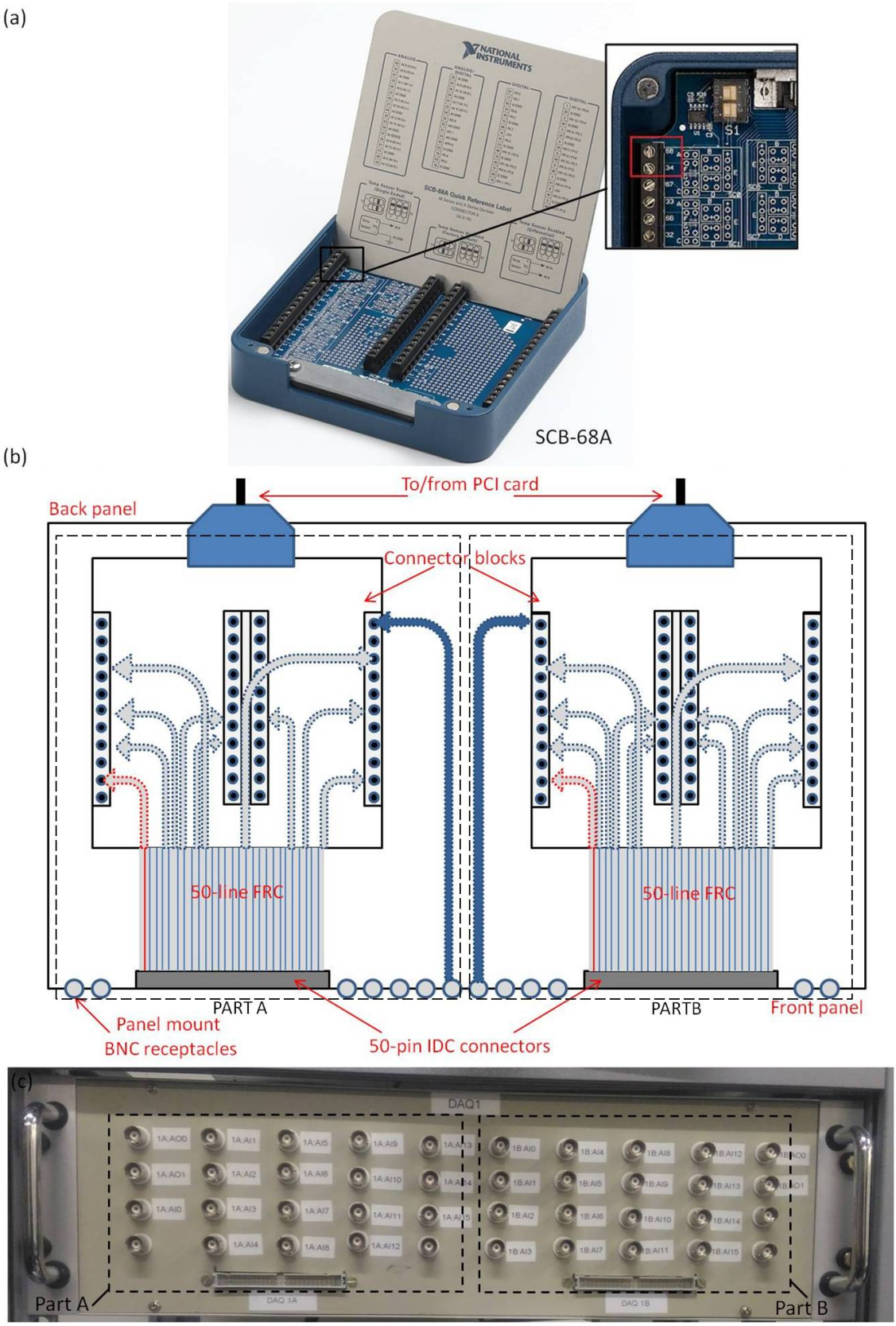

Fig. 8.2: Shows (a) Connector block SCB-68A for accessing the PCI card installed inside computer. The zoomed in view shows screw terminal connections. (b) Schematic representation of connections inside breakout box. (c) Front panel of a breakout box.

Tab. 8.1: Details of DI/O and DG connections inside the breakout box.

Digital line (connector block)	Breakout box (Part A)	Digital line (connector block)	Breakout box (Part B)	Digital Ground (connector block)	Breakout box (Part A/B)
0.0	1DO:0	0.8	1DO:24	18	1DG:0
0.1	1DO:1	0.9	1DO:25	50	1DG:1
0.2	1DO:2	0.10	1DO:26	15	1DG:2
0.3	1DO:3	0.11	1DO:27	13	1DG:3
0.4	1DO:4	0.12	1DO:28	53	1DG:4
0.5	1DO:5	0.13	1DO:29	18	1DG:5
0.6	1DO:6	0.14	1DO:30	50	1DG:6
0.7	1DO:7	0.15	1DO:31	15	1DG:7
1.0	1DO:8	0.16	1DO:32	44	1DG:8
1.1	1DO:9	0.17	1DO:33	44	1DG:9
1.2	1DO:10	0.18	1DO:34	9	1DG:10
1.3	1DO:11	0.19	1DO:35	9	1DG:11
1.4	1DO:12	0.20	1DO:36	7	1DG:12
1.5	1DO:13	0.21	1DO:37	7	1DG:13
1.6	1DO:14	0.22	1DO:38	4	1DG:14
1.7	1DO:15	0.23	1DO:39	4	1DG:15
2.0	1DO:16	0.24	1DO:40	36	1DG:16
2.1	1DO:17	0.25	1DO:41	36	1DG:17
2.2	1DO:18	0.26	1DO:42	36	1DG:18
2.3	1DO:19	0.27	1DO:43	12	1DG:19
2.4	1DO:20	0.28	1DO:44	12	1DG:20
2.5	1DO:21	0.29	1DO:45	35	1DG:21
2.6	1DO:22	0.30	1DO:46	7	1DG:22
2.7	1DO:23	0.31	1DO:47	35	1DG:23

Tab. 8.2: Details of internal analog (AI/O) connections inside the breakout box.

Analog line (connector block)	Breakout box (Part A)	Analog line (connector block)	Breakout box (Part B)
AI15	A:AI0	AI16	B:AI0
AI7	A:AI1	AI24	B:AI1
AI14	A:AI2	AI17	B:AI2
AI6	A:AI3	AI25	B:AI3
AI13	A:AI4	AI18	B:AI4
AI5	A:AI5	AI26	B:AI5
AI12	A:AI6	AI19	B:AI6
AI4	A:AI7	AI27	B:AI7
AI11	A:AI8	AI20	B:AI8
AI3	A:AI9	AI28	B:AI9
AI10	A:AI10	AI21	B:AI10
AI2	A:AI11	AI29	B:AI11
AI9	A:AI12	AI22	B:AI12
AI1	A:AI13	AI30	B:AI13
AI8	A:AI14	AI23	B:AI14
AI0	A:AI15	AI31	B:AI15

Tab. 8.3: Pattern of address and data bits in FRC.

FRC line	Bits reserved for
1	Trigger
2, 4, 6...46 (even number)	DG
3,5,7,9,11,13	Address
15,17,19,21,23,25,27,29 31,33,35,39,41,43,45	Data

when crimped to the 50-pin FRC IDC male connector is with notch of the connector facing upwards and the 1st line of the FRC which is red in color starting in left side. The FRC used to take output from the breakout box is crimped with a female 50-pin FRC IDC connector crimped following the same convention. The chances of bit order mismatch while taking output from the breakout box is zero as panel mount connectors will socket its counterpart only if the two notches on either side face each other. Table 8.1 lists the details of digital connections of each PART inside the breakout box. The connector block column gives the NI standard names and the breakout box column lists the names given to each line of FRC. Although the end user does not see digital channel connections inside the breakout box and only use the easy to plug in 50-pin FRC connector but one can easily use this table for reproducing a breakout box.

Analog channels from both the PARTS A and B can be accessed through standard BNC receptacle connectors mounted on the from panel as shown in the Fig. 8.2(c). Inside the breakout box, these BNC receptacles are connected to RG174 cables which on the other end are again crimped with subminiature male crimps and screwed to screw terminals corresponding to different analog channels. The AI/O channels have both AI/O+ and AI/O- connections, which when used single ended double up the number of analog channels. Note that the analog voltage acquired by AI channels is limited by 0 to $\pm$10 V or -5 V to +5 V. Also, the analog output produced by AO channels is limited by same values. The analog connections are given in table 8.2 where again the connector block column gives the NI standard names and the breakout box column lists the names given to each analog channel on the breakout box.

8.2.2 Digital Buffer

In CDAQ system, a single PCI card can read and control a total of 64-devices. Theoretically, this can be implemented without any problem but in practical we need to consider the maximum output current limit of 24mA/ digital channel of our PCI card [197]. The address as well as data bits are used by DACM of every equipment to select and latch data for correct address, respectively. The number of equipments controlled by one PCI card are hence limited by output drive current capacity. To increase the output current capacity we need a buffer for

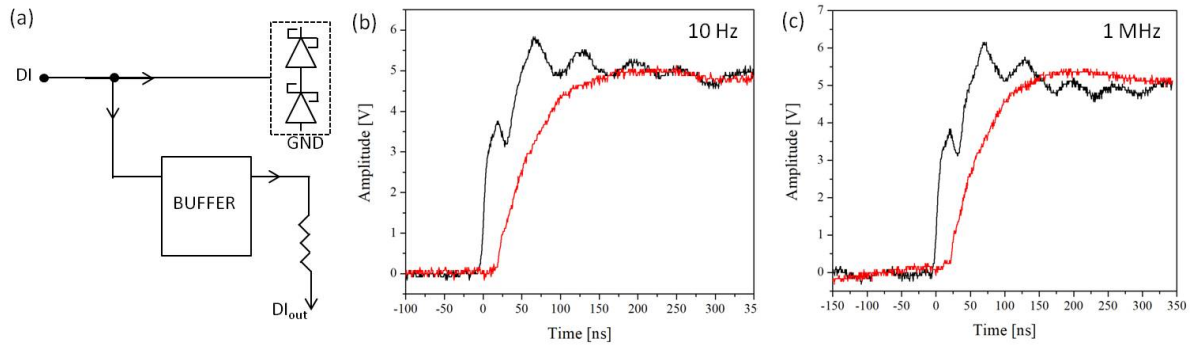

Fig. 8.3: (a)Schematic representation of buffer action for a single digital line and a single bit after travelling 20 m, with (red) and without (black) being buffered at different frequencies, (b) 10 Hz, (c) 10 MHz

Tab. 8.4: Function table for octal buffer SN74HCT541N IC.

Inputs			Outputs
$\bar{OE}1$	$\bar{OE}2$	A	Y
L	L	L	L
L	L	H	H
H	×	×	Z
×	H	×	Z

each digital channel. Another problem to be addressed in practical implementation is that the digital signals travel all through the lab across a distance of about 20 m over the FRCs. The signal is attenuated after travelling across the lab and received in a much lower strength at device end. This can lead to ambiguous and mis-read signals, as the system works on TTL logic where 0-0.8 V and 2-5 V are considered logic low and high level, respectively. We have built a digital buffer box indigenously for solving the above mentioned issues. Functioning in multiple ways, it can be used as buffer for increasing output drive current capacity or just as a signal refresher.

The buffer circuit uses a tri-state octal buffer SN74HCT541N/ MH74HCT541B1R, which is an 8 bit buffer IC, it has good output drive current capacity of ±6mA. As this octal buffer has a tri state action it has a high impedance, Z, output apart from the low, L and high, H. It has two output-enable (OE1, OE2) controls. Table 8.4 gives the function table of this buffer IC. If any one of the OE1 and OE2 input is high, all eight outputs are in the high-impedance state which disconnects the output from rest of the circuit. The buffer acts as a transparent latch only if both OE1 and OE2 are low. Therefore, in the buffer circuit we have connected both OE1 and OE2 to ground for desired action. We use resistor array of 1 k, 4116R-1-RC instead of

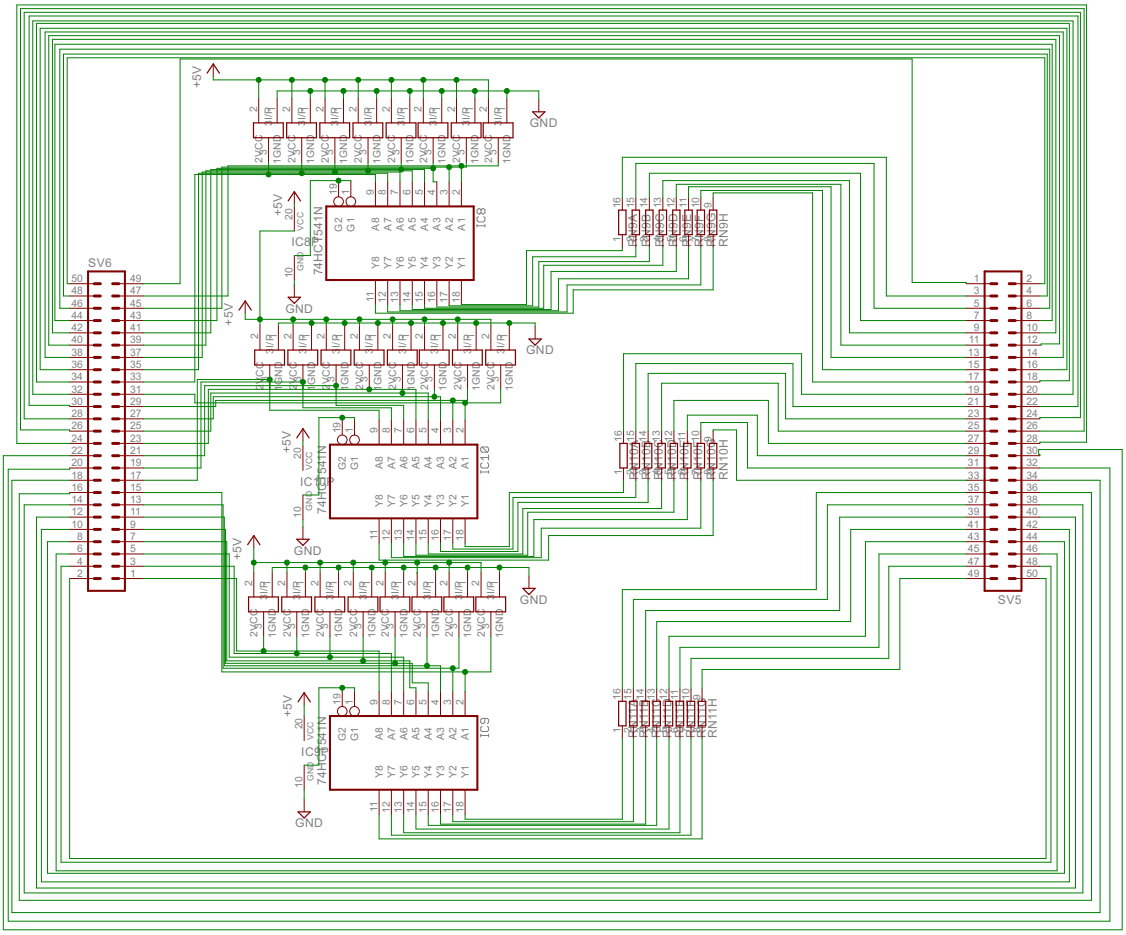

Fig. 8.4: Schematic of digital buffer circuit.

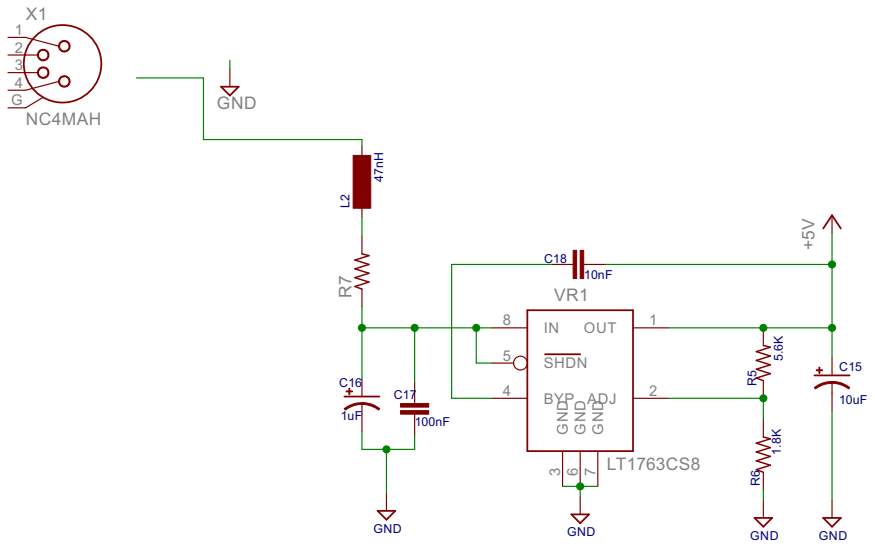

Fig. 8.5: Schematic of power supply regulation circuit for digital buffer.

common axial lead resistors for saving space in the circuit board. Schottky diodes 1PS70SB14/ BAT54SWT1G are used for protection purposes in the circuit. If the data line has a voltage surge $\sim$ 5.5 V, the diode towards 5 V becomes conducting and dissipates the energy in the overshooting pulse. If the voltage on the data line goes below $\sim$ - 0.5 V, the diode towards ground becomes conducting. The schematic shown in Fig. 8.3(a) shows buffer action for a single bit. Figure 8.3(b) and (c) shows conditioned digital clock signal of frequencies 10 Hz and 1 MHz, respectively. This clock signal is recorded after travelling a distance of about 20 m in lab over the FRC without being buffered (black) and after passed through buffer circuit (red). Clearly, after being passed through the digital buffer, signal is smoothened but it acquires a delay of $\sim$ 25 ns. This small delay is introduced due to the propagation delay of octal buffer IC used (maximum $\sim$ 25 ns). It is studied for a range of input signal frequencies from 10 Hz to 1 MHz and is found to be constant. As this delay is irrespective of the frequency of the input signal and thus can be can be taken into account through programming.

Each of the digital buffer boxes consists of twelve buffer circuits where each buffer circuit has 48 bits DI/O. Each buffer circuit uses three octal buffer ICs so as to cover all 1 trigger + 6 address + 16 data digital bits as shown Fig. 8.4. The DGs are connected without buffering. Each digital bit is passed through Schottky diodes so as to avoid back reflection of any excess voltage. For this reason each circuit uses 1PS70SB14/ BAT54SWT1G diode for each input line. The supply section of the circuit is shown separately in Fig. 8.5. There is a single common input to all the 12 buffer circuits in the box through a 50-line FRC provisioned at the back

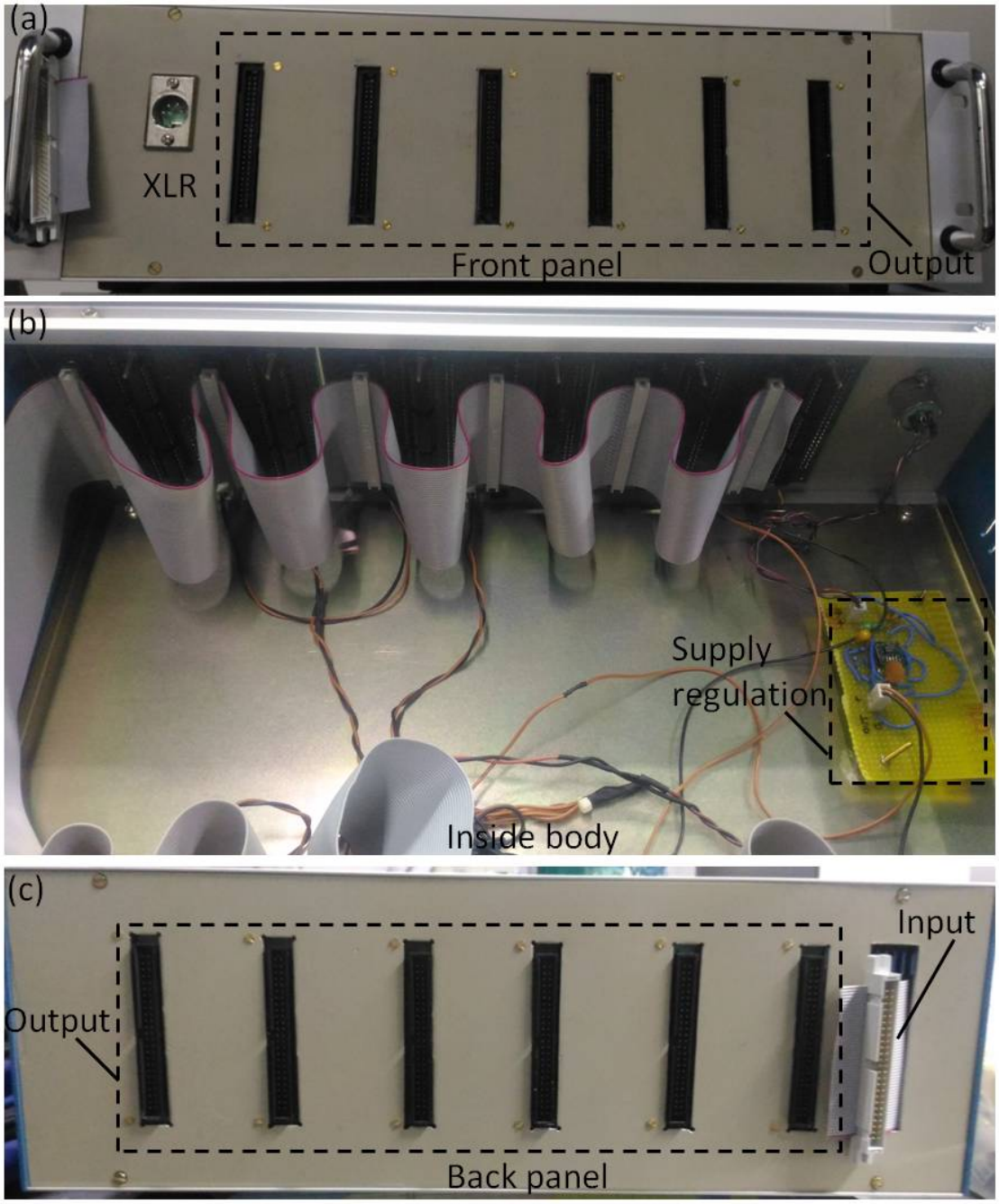

Fig. 8.6: Pictures of a digital buffer box with (a) showing front panel having output channels and XLR connector for supply input; (b) showing inside view of the digital buffer box; (c) showing back panel of the box with output channels and a input channel.

panel of the box as shown in Fig. 8.6. The buffered outputs can be taken from the front panel as well as the back panel of the box, from 12 channels in total. Also, there is an XLR connector at the front panel for the + 5 V input supply. Reason behind use of XLR connector for power input is compatibility to available fixed DC power supplies in the lab. The supply voltage taken is then regulated using LT1963. LT1763 can also be used for regulation but in this case higher output current is required so as to drive 12 buffer circuits in the box. The printed circuit board (PCB) is designed such that it has two independent buffer circuits. Each buffer circuit can drive upto four devices and there are 12 such buffer circuits in a digital buffer box therefore each box can be connected to upto 48 devices without loading the PCI card. Four such digital buffer boxes have been developed for the CDAQ system.

8.3. Controlling Software

The CDAQ system is required to be operated remotely from the workstation. For that a graphical user interface (GUI) is developed in Laboratory Virtual Instrument Engineering Workbench (LabVIEW) development environment which uses a graphical programming language "G" unlike text based programming languages. For efficient of control and acquisition simultaneously from many equipments, few considerations are required to be taken into account while coding the GUI. Configuration of generation/ acquisition channel (through DAQ assistant) with proper sampling rate is very important. It must be at least twice the highest frequency component present in the signal (Nyquist theorem) for avoiding signal reading errors or generating smooth signals. This experiment requires many equipments to be operated in a sequence to run the cycle of events for short periods of time ($\leq$ few μs). For instance, applying desired voltage to trap electrodes, shifting the frequencies of laser lights using AOM drivers, block-unblock laser lights using mechanical shutters etc. So, the user must be able to define and save a sequence of events, specifying equipment address, desired output value and time for run or operate the equipments according to a previously written such sequence for automated control. It also requires configuring same digital channels (output generation) for different equipments in compliance to FRC convention (1 bit trigger + 6 bit address + 16 bit data), as described in above section. The simultaneous delivery of address and data signals is another important requirement. Lead or lag of address bits to the data bits by even few ns leads to wrong equipment selection and control. For example, the dc power supply built indigenously [195] and another homebuild equipment, a constant current source both are operated from the GUI. The dc power supply can reach up to 100 V where as the constant current source can deliver a maximum of 6 A current. If in a cycle of events these equipments are operated sequentially and there is a delay between address and data bits then it may result in undesired output values or sequence of operation. Apart from controlling, acquiring and logging data from equipments is another requirement. A GUI has been developed and tested for control

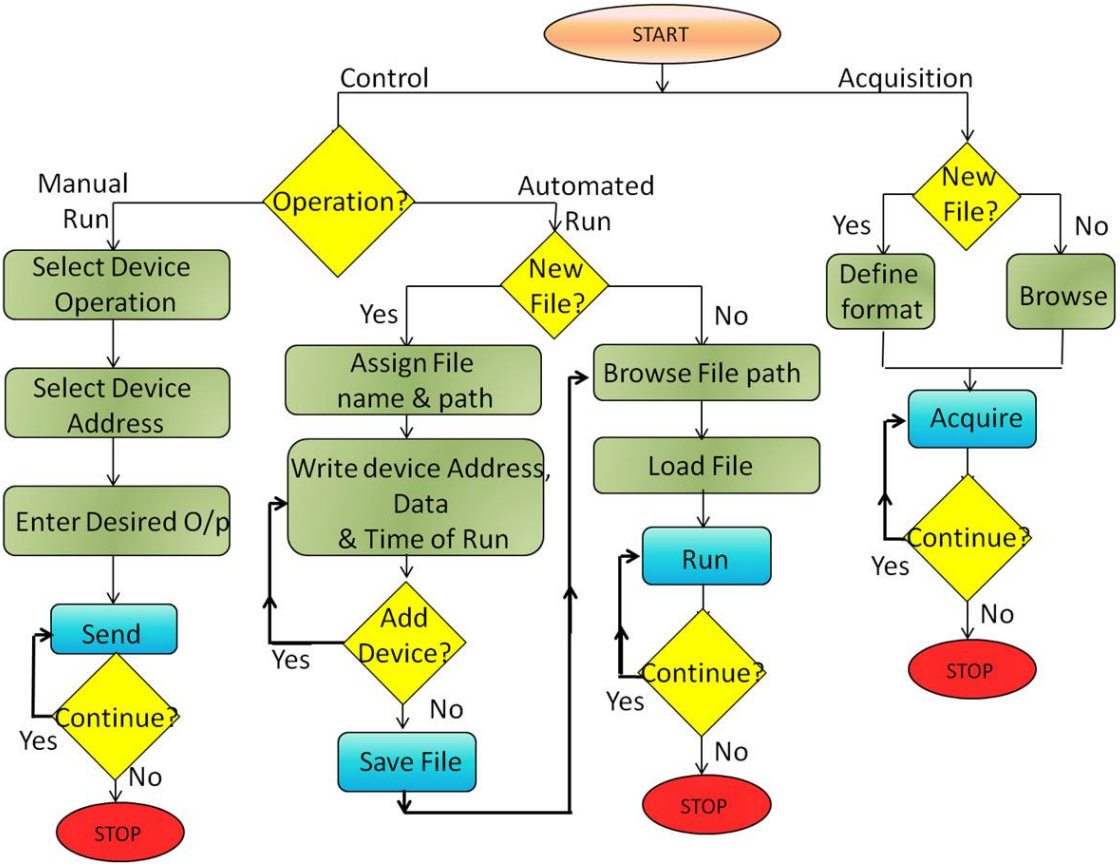

Fig. 8.7: Picture shows algorithm of the GUI developed for CDAQ system.

and data acquisition from different equipments. Algorithm given in Fig. 8.7 shows the flow of steps for GUI program. There are many instances where the user may not need to sequential operation of equipment, for development and testing purposes. The GUI offers options for manual as well as automated control of equipments. The GUI offers to control equipments such that the desired output can be a single value or a function. For example, it is possible to drive the voltage output from the dc power supply as a function of sin or sawtooth profile with specified frequency, range and step size.

Test and Measurements: The CDAQ system controls and acquires from many equipments across the lab making the whole experiment run smoothly. For example, laser lights used in the experiment (e.g. cooling light at 369.5 nm and repump light at 760 and 935 nm) are required to be frequency shifted to match up with the different transition frequencies. The homebuild AOM driver used for this purpose takes 16-bit input/control signals from the CDAQ system for generating sinusoidal signal, f. The control signals specify the frequency and amplitude of f. This signal f is fed as input to the AOM and the incident laser light, say F, on AOM is diffracted to produce lights of 0th order F, 1st order F+f, and so on. The frequency and amplitude of signal f are controlled through the GUI as shown in Fig. 8.8(a). In an another instance, a current source which drives the Helmholtz coils producing magnetic field for shielding and axis quantization purposes is controlled. The homebuild current source takes 16-bit data input from the CDAQ system and drives the coils. The PCI card cannot acquire and measure current directly. The output current is acquired by connecting a suitable resistance in series to it. Which means that the voltage corresponding to the produced current is acquired. Figure 8.8(b) shows, the magnetic field produced at the center of Helmholtz coil pair due to the applied current. The acquired data is logged and saved in an easy to work ".tdms" file format. The format of data logging file is customizable and can be changed to ".txt" or a binary file as per requirement. The time stamps on the data logged are customizable in the sense that there is a choice for real or absolute time stamps. The rate at which the data points are saved is also customizable and can go to a minimum of 10 ms, which means saving data points which are 10 ms apart in time. Figure 8.9 shows a snapshot of GUI. As the code for this GUI is very big, markings a, b and c shown in Fig. 8.9 have been used for different parts of the code, helping simple understanding. The GUI Codes allows to control the equipments in two ways, automated and manual. The equipments can be operated in a sequence specified by user. The sequence is a list of events where one event is considered as sending control signal to an equipment once. Each event is defined by the address of the equipment, input/ control data value and time for its run. User saves a list of events in a sequence file or it is allowed to load a pre-existing sequence file. Equipments are run in a sequence automatically according to the information loaded form the sequence file. On the contrary, a user can control an equipment individually which is highly desired for testing purposes. This is called manual operation. The user can acquire and log data into a data file from multiple channels irrespective of choosing

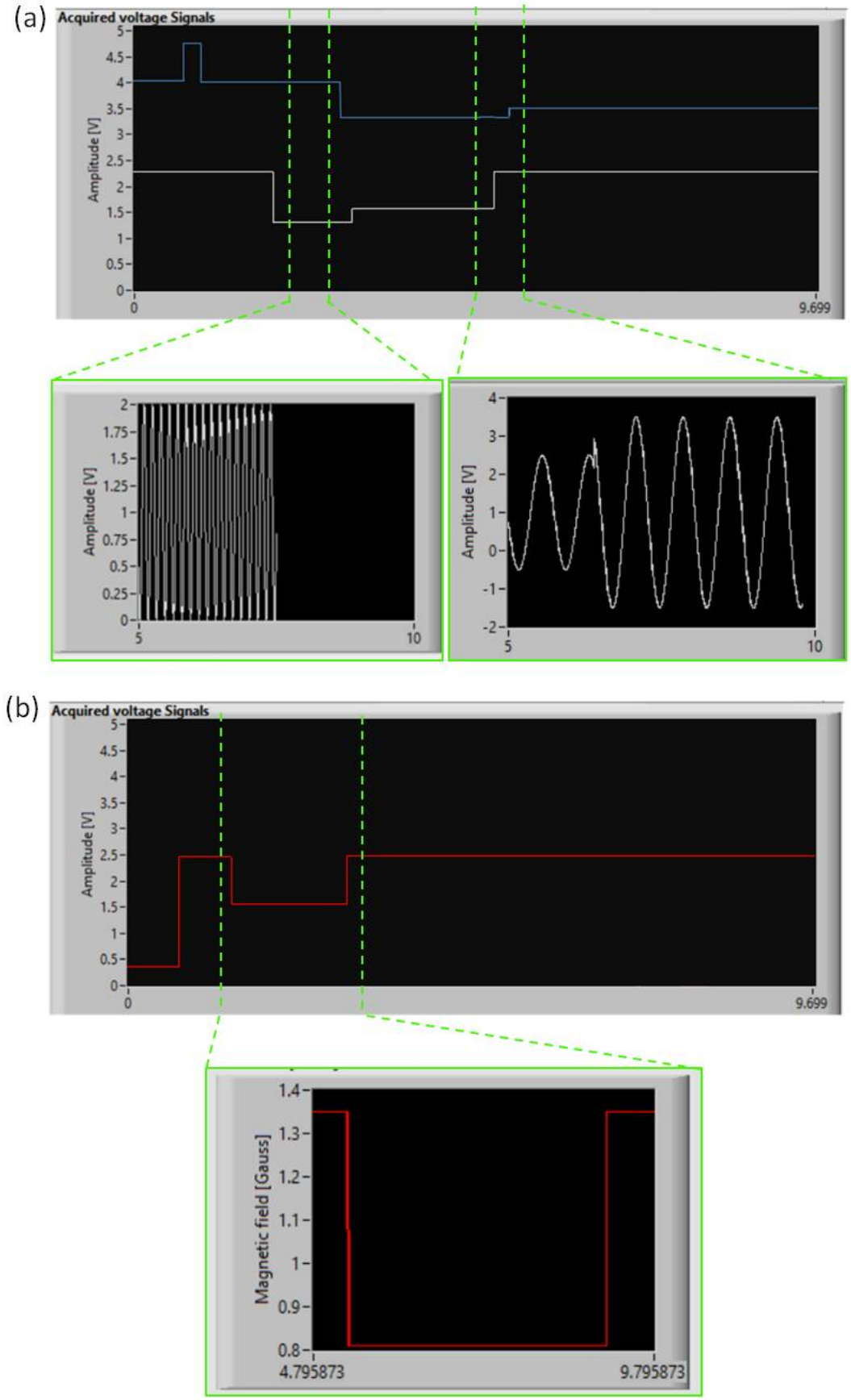

Fig. 8.8: (a) Shows frequency and amplitude control signals fed into AOM driver, to control its frequency and amplitude. (b) Shows acquired voltage corresponding to the current generated from the current source. It also shows the magnetic field at center of a pair of Helmholtz coils corresponding to the driving current given to them.

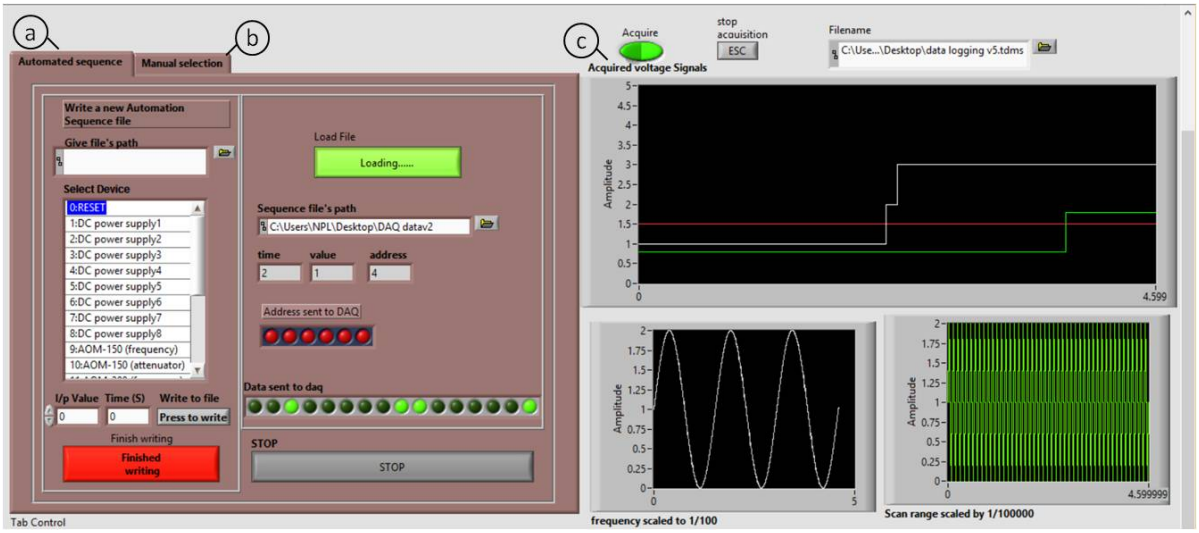

Fig. 8.9: Shows a snapshot of front panel of the GUI. Markings as a, b and c represent the parts for automated operation, manual operation and acquisition whose codes are given in figures ahead.

automated/ manual operation. Codes for these parts are given in Fig. 8.10, 8.11; Fig. 8.12; and Fig. 8.13, respectively.

The CDAQ system developed successfully automates the job of equipment control and data acquisition using amalgamation of indigenously designed hardware and a graphical user interface (GUI). The digital nature of the system makes it easy to be advanced as per the requirements identified during operation of experiment.

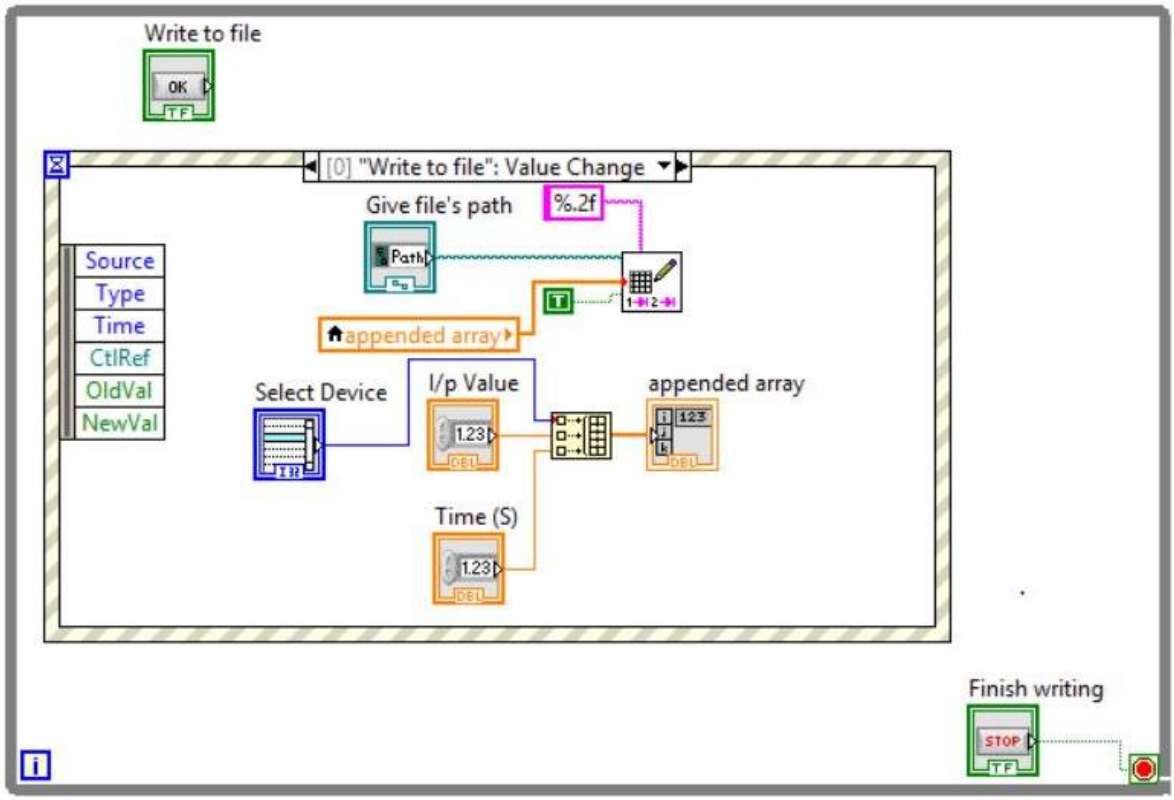

Fig. 8.10: Part of code for writing a new sequence file for automated control of equipments.

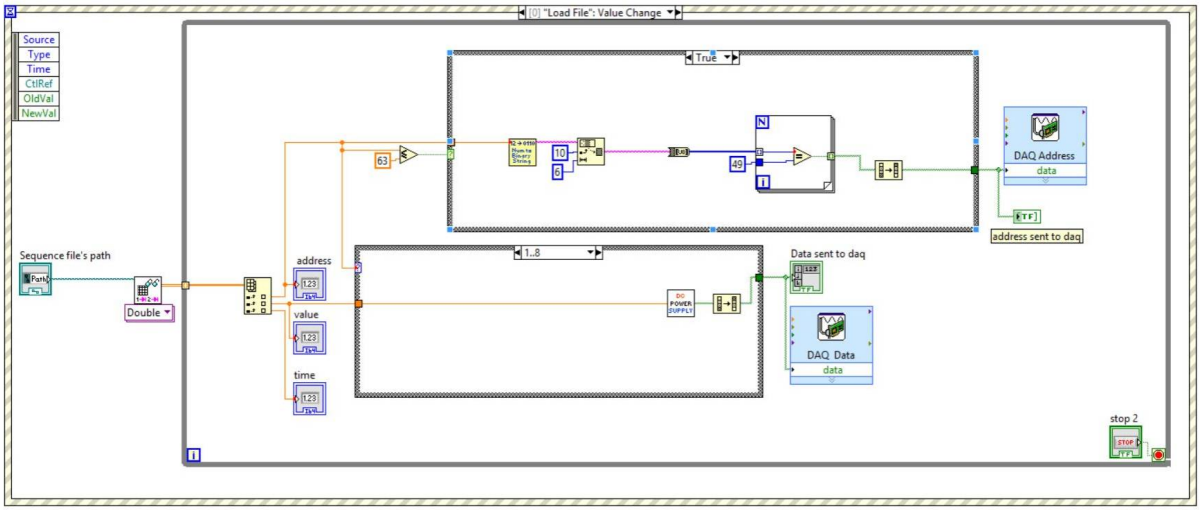

Fig. 8.11: Part of code for loading sequences from existing file and controlling equipments corresponding address, input data and time information.

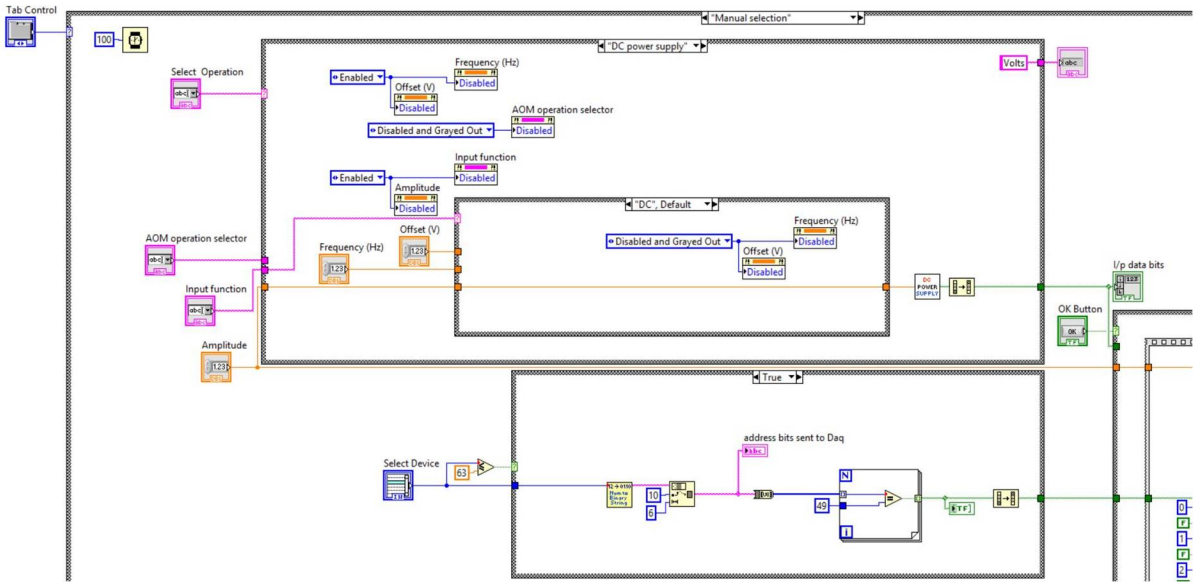

Fig. 8.12: Part of code for individually controlling equipments .

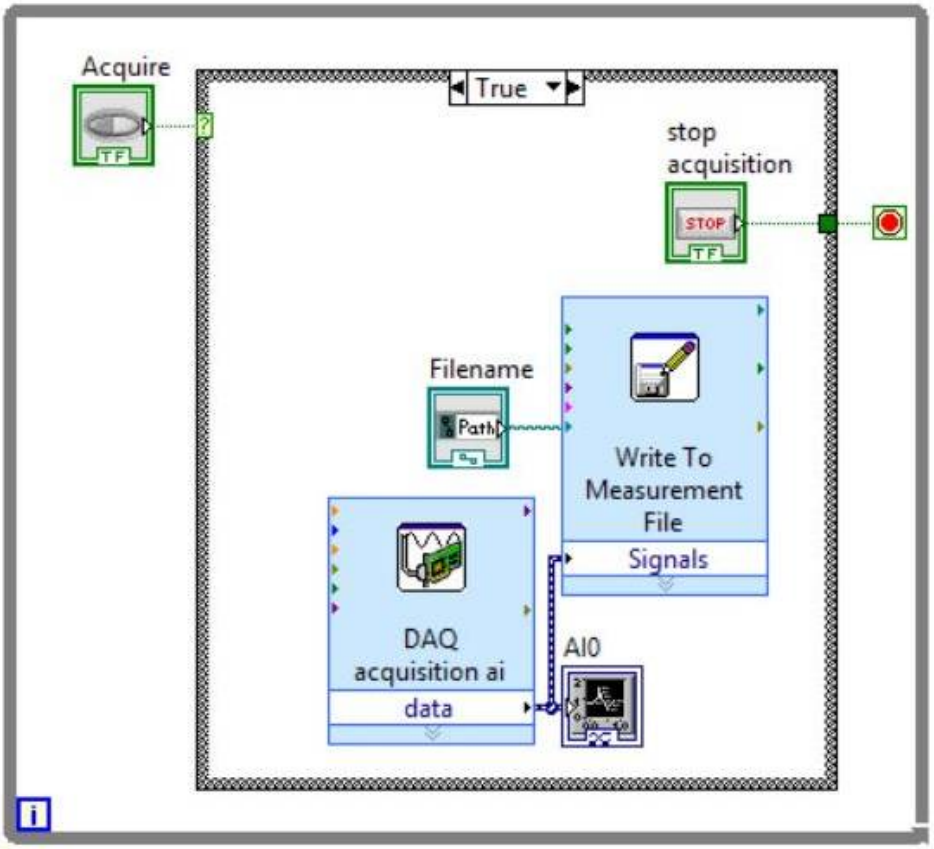

Fig. 8.13: Part of code for acquiring from different equipments.

Chapter 9

Conclusion and Outlook

In this thesis key components for building a precision ion trap experiment have been developed. These are particularly used towards development of single trapped ion optical clock at CSIR NPL, India. The preliminary requisite for this optical clock experiment is choice of suitable ion. A detailed theoretical review of several candidate ions used worldwide is done and $^{171}Yb^{+}$, which is one of the CIPM recommended ions for secondary definition of SI second is chosen. Advantageous properties of $^{171}Yb^{+}$ such as first order Zeeman effect free narrow clock transitions, off the shelve available lasers and higher sensitivity of clock transition states towards measuring local Lorentz symmetry violation and fine structure constant, α have been discussed.

The nature of the trapping potential is dependent on the ion trap electrodes geometry, so in the next step a suitable electrodes geometry for producing an efficient trapping potential was identified. Many trap electrode geometries were simulated numerically and were analyzed on the basis of physical constraints, anharmonicity and micromotion. The analysis lead to a suitable electrodes' geometry (inner electrodes' radii $2r_o = 1$ mm; inter electrode separation, $2z_o = 0.7$ mm; inner electrode angle, $\theta_i = 10^\circ$ and outer electrode angle, $\theta_o = 45^\circ$) which produces a trapping potential with a balanced trade-off between desired harmonic and unwanted anharmonic components as compared to prior traps. Studies of non linear resonances and trap stability region resulted in identification of a range of trap operating parameters like rf trapping frequency and voltage for stable trapping. In order to achieve the desired accuracy *i.e.* on the order of 1 part in 10^{-18}, one of the key steps is detailed estimation of the associated systematics. Major systematic shifts namely electric quadrupole, 2^{nd} order Doppler, 2^{nd} order Zeeman, BBR and dc Stark were estimated for both quadrupole (E2, 435.5 nm) and octupole (E3, 467 nm) clock transition choices. Comparison of E2 and E3 on basis of systematic shifts revealed that E3 as clock transition can give about 5 times more accurate clock than E2 as clock transition. The electric quadrupole shift depends upon trap geometry and calculations show that quadrupole moment values for clock transition states of $^{171}Yb^{+}$ can be measured with more accuracy in our ion trap set up as compared to other published values. Some of these

systematic shifts' are induced by trap itself therefore these studies also provided tolerances and considerations for trap structure design.

The ion trap assembly which comprises of trap electrodes, its holders, isolators and mounting structure is designed and fabricated such that it offers no obstruction to different laser lights impinged at ion sitting at trap center. Design flaws, precision, symmetry, and machinability are some other important parameters which were optimized to avoid contribution to systematic shifts. As the experiment involves only a single ion, ultra high vacuum (UHV) conditions is a vital necessity. A vacuum chamber is designed considering UHV compatible materials, minimum outgassing, volume and unobstructive laser light impingement at ion trap center from different sets of optically accessible ports as required by the experiment. Complete vacuum assembly set up has been planned and put together. An atomic oven for producing Yb atoms inside the UHV chamber which is currently being characterized by a colleague in the lab is awaited for starting the vacuum and pumping pressure down.

In order to deliver rf voltage efficiently to the trap, a helical resonator has been designed which delivered rf at resonant frequency, $f_0 = 17.915$ MHz to the ion trap with a quality factor, $Q \approx 250$. Characterization studies of helical resonator was done and trap impedance were capacitance was also estimated to be ~ 10 pF. For cancellation of Zeeman and electric quadrupole shifts and detection of micromotion 3 pairs of Helmholtz coils along with digitally controlled stable current sources to drive them have been designed and instrumented indigenously. An automated control and data acquisition system for remote address and control of equipments has been developed. The basic scheme can be used for any precision experiment in general with changes and augmentation as per requirements. As the thesis work was started with establishing a new lab, a dust free enclosure (class 100,000) was indigenously designed and constructed as a teamwork in the lab.

All these computations, design and instrumentation make basic building blocks required for developing the trapped ion clock experiment. Further, other important components of the experiment like optics setup for cooling (369.5 nm) and repump (760, 935 nm) lasers, laser stabilization and high resolution imaging setup are currently being pursued by researchers in our group. Trapping ions in UHV environment and and detecting them is the subsequent step in this experiment. Exciting and innovative developments in the clock experiment are to be expected in the next few years. An ion trap is a basic tool for many atomic physics experiments related to storing and manipulating qubits for quantum computations or measuring local Lorentz symmetry violations etc. Together with lucrative properties of $^{171}Yb^{+}$ this setup offers excellent possibilities for basic physics precision experiments.

APPENDICES

A. CHARGED PARTICLE OPTICS

Charge particle optics is a simulation software which uses boundary element method for calculation of potential or electric field for a geometry of electrodes specified by user with a given voltage. The software setup comes with a USB dongle and can only be used in a system with this USB. Insert the USB and click open CPO2D to start the software. Following are the steps to build an electrode geometry and simulate potential.

I Start the software package and open an example data file. To edit it click **File** $\longrightarrow$ **Open for running and databuilding** (refer Fig. A.1. Select a sample file from the list and save the file you've opened under a new name by clicking **File** $\longrightarrow$ **Save As**(data builder file) and choosing a new name for your project in **".DAT"** extension. In the new saved file, you can draw desired electrodes by deleting or editing previously drawn electrodes.

II In **Databuilder** $\longrightarrow$ **File names**, you can specify name of the output file in which the output will be written. This output file has to be in same directory as **CPO2D.exe**. This file is cumulative i.e for each run data keeps on copying beneath the previous. The name of the output file should be given along with path. There is another file which is a hidden file written as : processed data file name. It contains information about the electrodes etc. In this window there is also an option to write comments. Some files with extensions **".yyy", ".yzz", ".yxx"** etc are also created which need to be deleted to avoid overloading the computer memory (refer Fig. A.2 and A.3).

III In our case, for simulating a trap structure we need to draw appropriate electrodes with all the distances correctly specified. Start this by clicking **Databuilder** $\longrightarrow$ **Electrodes** (refer Fig. A.4), so that the Edit electrodes window appears. Here you can edit or delete the previous electrodes and can also insert new ones. These are numbered as electrodes 1; 2; 3; 4 and so on. In the subsequent dialog box, choose the type, shape of the electrode (e.g. for the end cap ion trap, we have selected one cylindrical surface). It is important to note that this takes into account the surfaces, not the shapes in whole. The resulting window, allows us to enter in the parameters for this electrode. You can define the geometry of the electrodes using coordinates of its center, radius etc. Let us take the dimensions of the electrode in our case as an example. For the cylinder we have, Radius: 0.25, Center of 1st end: 0.71, -2.3, 0; Center of 2nd end: 0.71, 2.3, 0; where the three numbers separated by commas refer to the coordinates x, y, z. This means a cylinder with radius 0.25 mm is

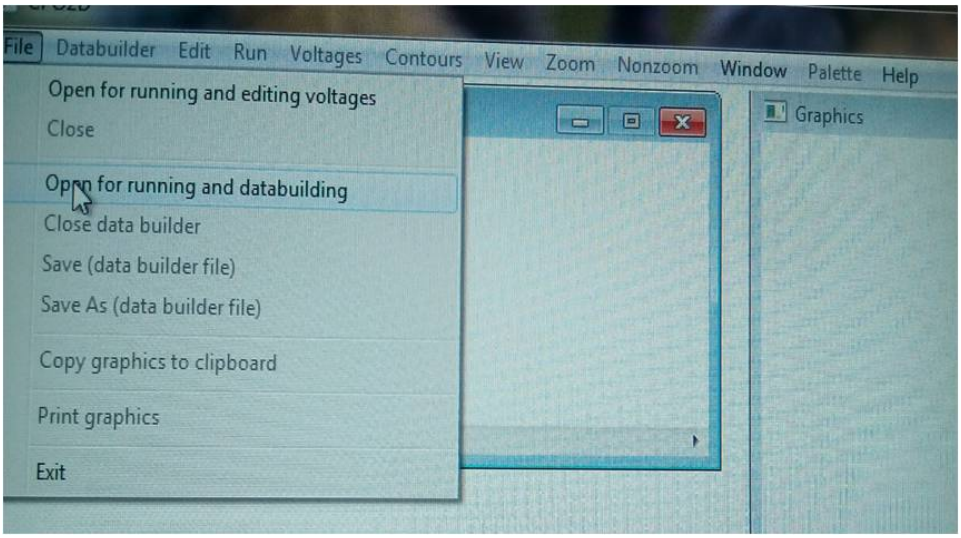

Fig. A.1: Shows how to open a databuilder file.

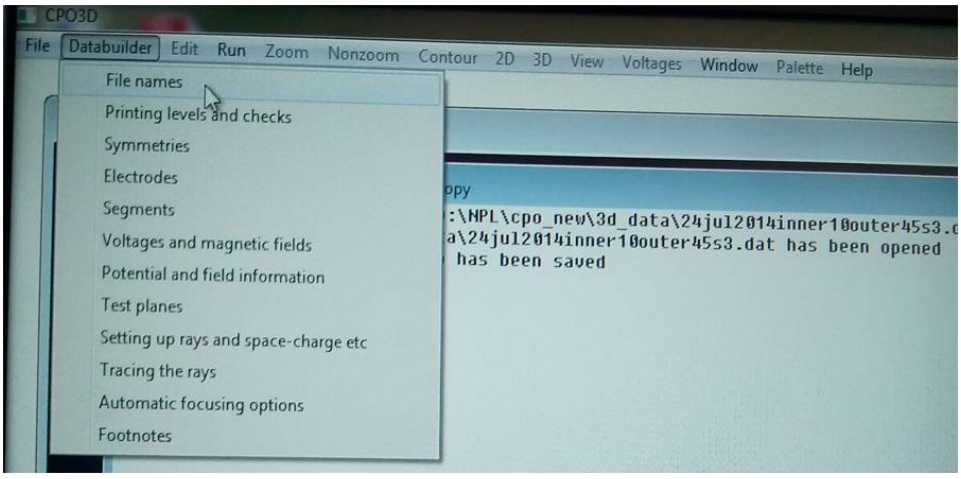

Fig. A.2: Shows how to specify an output file.

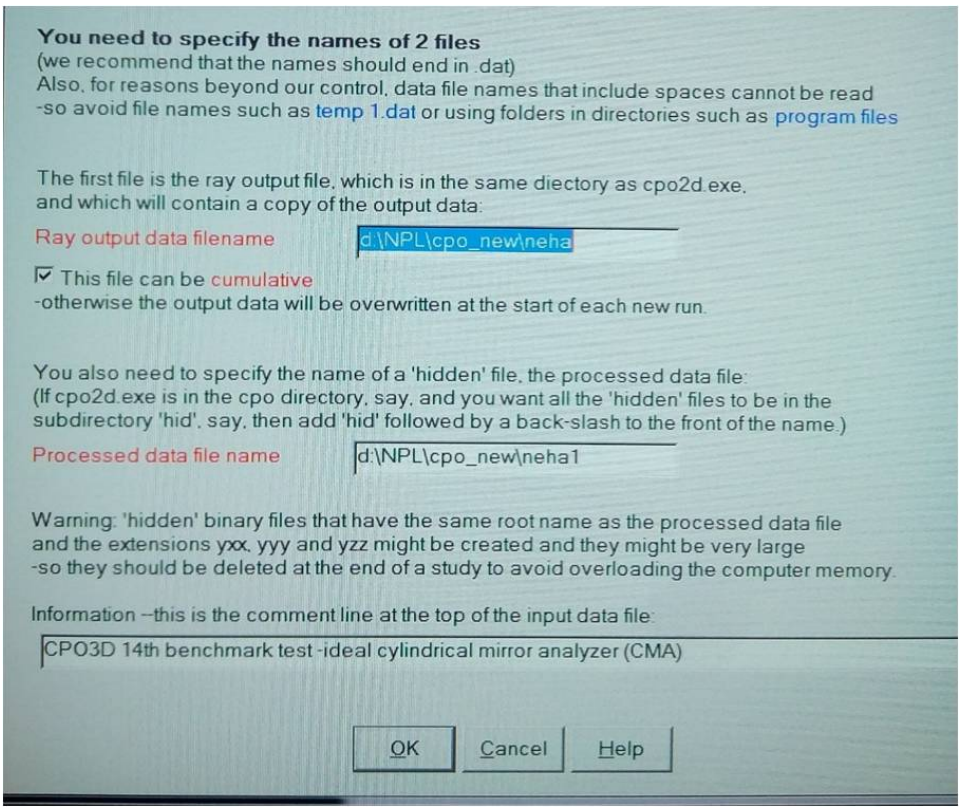

Fig. A.3: Showing window for saving an output file.

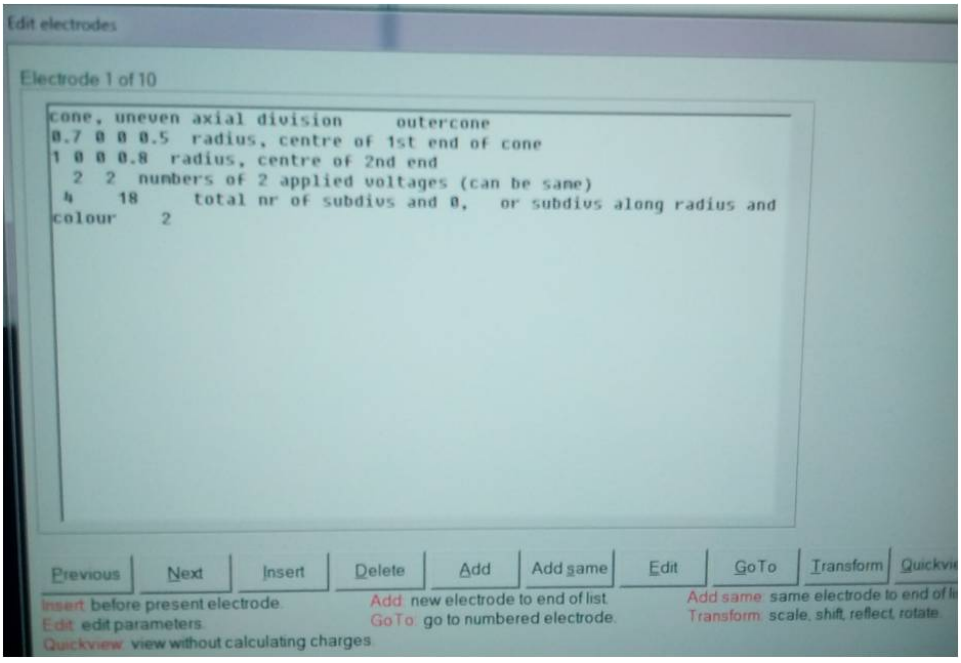

Fig. A.4: Showing window for editing electrodes information such as shape, coordinates etc.

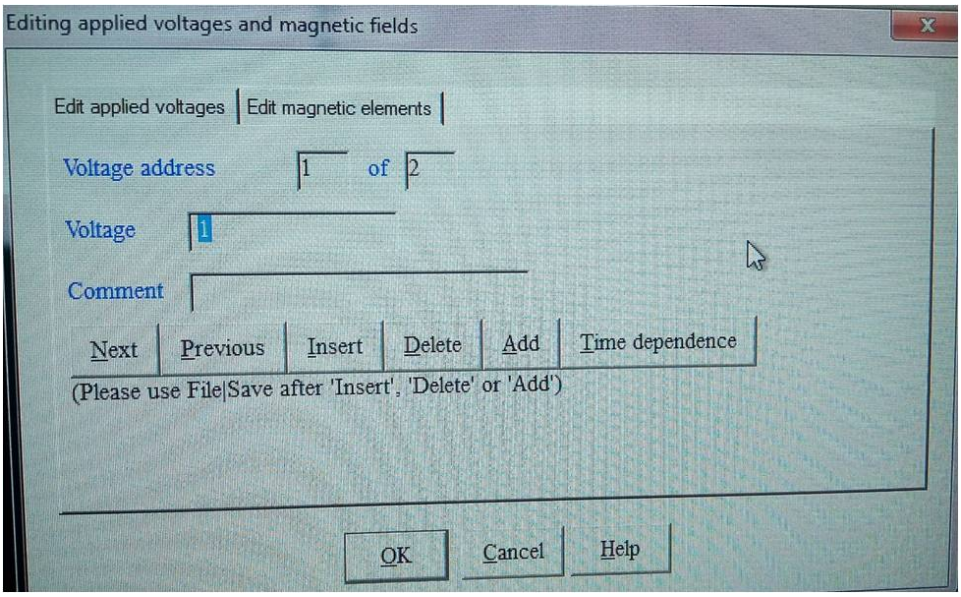

Fig. A.5: Applying voltages and magnetic fields to the electrodes.

drawn with center of its first end at coordinates 0.71, -2.3, 0 and the center of second end at 0.71, 2.3, 0. Also, in the first box, Commentline: give the electrode a descriptive name (e.g. inner cone 1). Choose the address of the voltages to be applied to this electrode, addresses of two voltages that will be applied: 1, 2. Input of two separate addresses allows us to create a voltage gradient across the electrode. However, in the our case we do not have a voltage gradient so these two addresses were kept same (e.g. 2, 2). Note that this entry is a voltage address, not the actual voltage being applied. Now, ensure that electrodes that will require different voltages are assigned to separate voltage addresses. One also needs to choose how to segment the electrode. In general, the larger the number of segments, the more precise the simulation will be with longer computation time.

IV Click in **Databuilder** $\longrightarrow$ **Editing applied voltages and magnetic fields**, so that the window where applied voltage can be altered appears. Here, in present case we keep on changing the voltages between 0 and 1 for different electrodes (different electrodes are assigned different voltage addresses) after each run (refer Fiig. A.5).

V After this, click **Run** and you get four options: **ZY view, XY view, ZX view**. All three views, when any of the view is selected the electrode designed is shown on screen with that view. This helps one check whether the electrode defined is same as the electrode desired or not. However, one cannot see the dimensions mentioned but the gross shape and geometry, distance and orientation of the electrodes with respect to each other etc. can be seen by this.

VI In the next step, **Contour** $\longrightarrow$ **Potential** $\longrightarrow$ **grid** (refer Fig. A.7), the no. of grid points

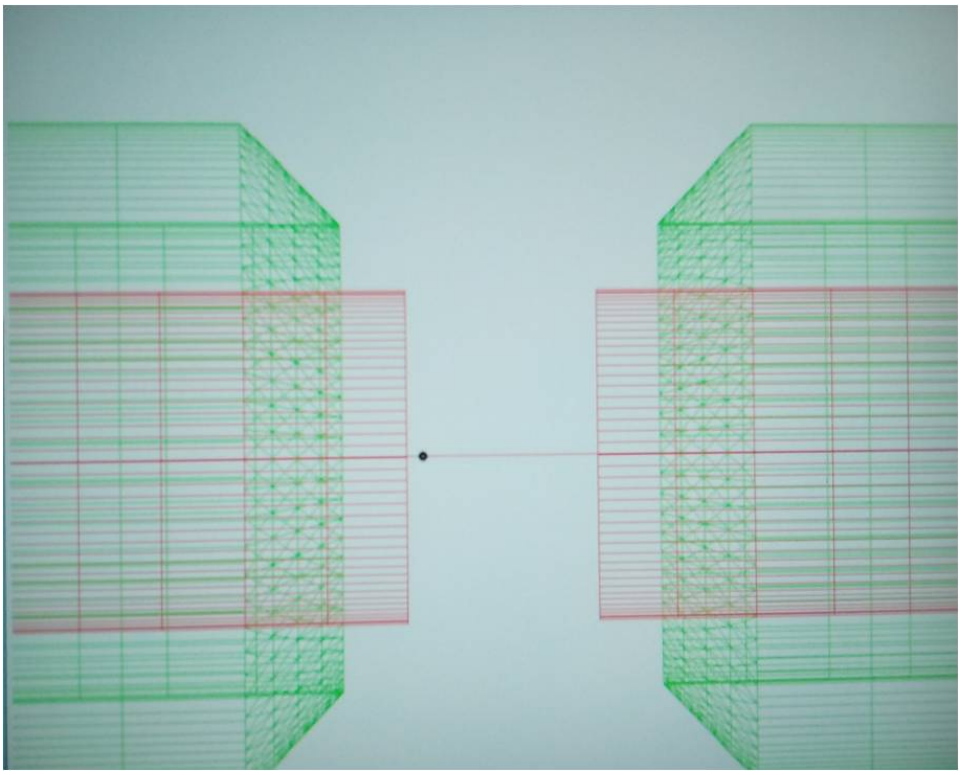

Fig. A.6: Showing XZ view of an example trap electrodes assembly.

are set up. If you had earlier chosen XZ view in the **Run**, (which means Y=0) then in this window value of constant coordinate in Y direction 0 will be shown and there are options for entering the minimum and maximum values for X and Z directions which are nothing but coordinates for region of interest in the XZ plane). In present case, we have kept grid values for both X and Z as 50. This then gives the output in the output file defined before. All the views can be run similarly.

VII Now, if you want to take data along a direction not a plane, then you can set the other direction as 0 in this window. For e.g. In the XY plane, Z direction zero and if you set the grid points along Y direction equal to 0, the output is along X direction but in that case set the grid points for X direction to be 1000. If one wants to get the data for electric field instead of potential, one needs to repeat same steps in **Contour** $\longrightarrow$ **Electric field** $\longrightarrow$ **grid** window (refer Fig. A.8).

This way one can get the potential and electric field data from CPO. The output ".DAT" file saves the potential profile in the desired region of interest and with precision according to the no. of divisions chosen.

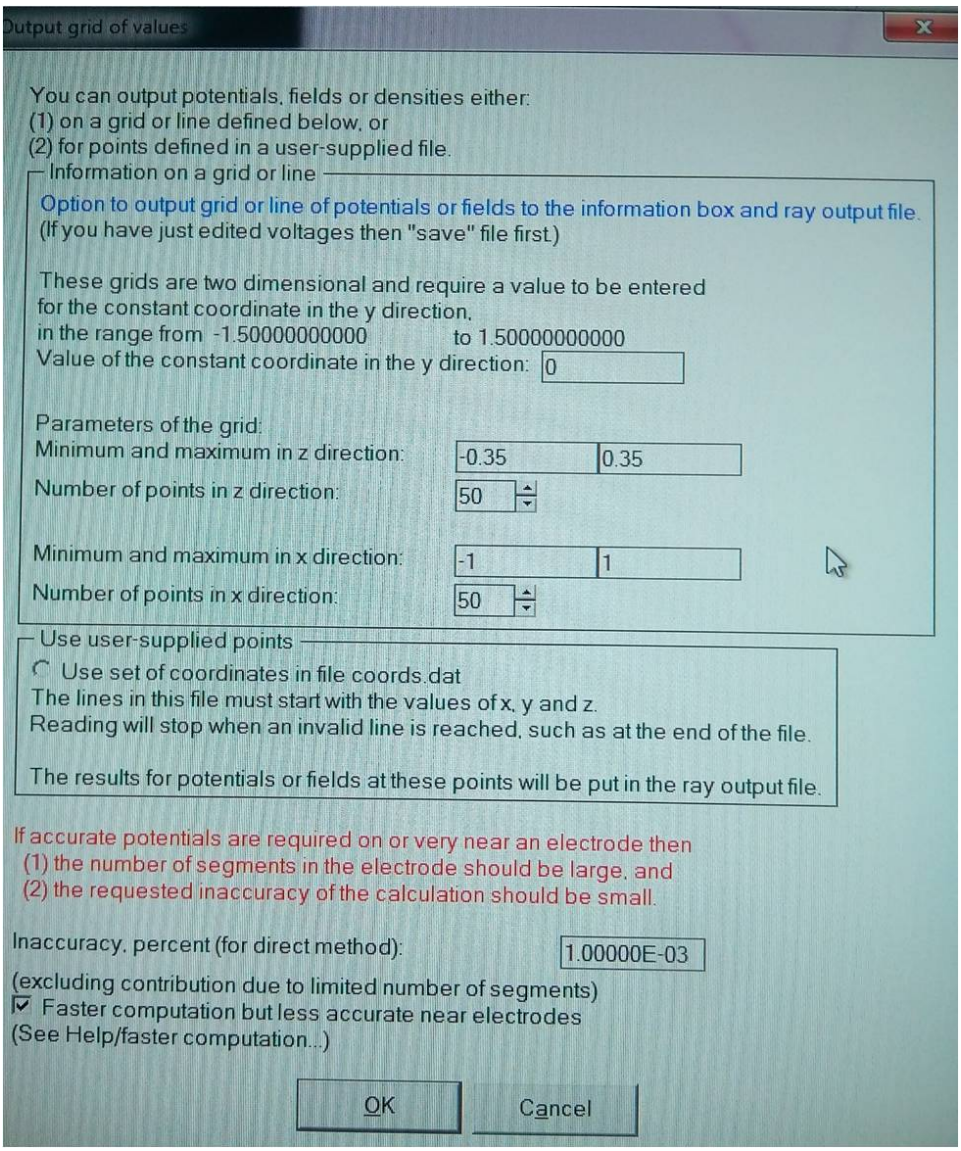

Fig. A.7: Showing window for specifying region of interest and no. of grid points for potential calculation.

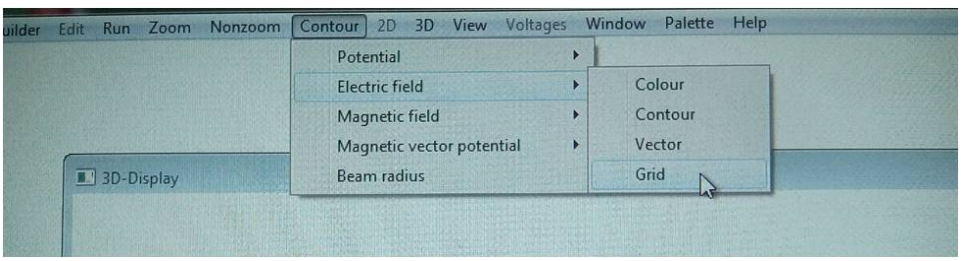

Fig. A.8: Showing window for specifying region of interest and no. of grid points for electric field calculation.

B. LAB SPACE LAYOUT

Single trapped ion optical frequency (STIOS) lab is built in apex metrology building space which is a newly built facility at CSIR-NPL. The lab has 6.2×12.6 m^2 area and is mainly divided into two regions: a dust free enclosure for main experiment and the general usage area which is outside the dust free enclosure. The main experiment area i.e. the enclosure covers 4×6 m^2 area and has 2.4 m high ceiling from ground level as shown in Fig. B.9. This structure is indigenously designed and built using standard 40-80 and 30-30 aluminium extrusions as shown in Fig. B.11. The extrusions were joined together to form the enclosure room using indigenously designed parts like die cast brackets, joint bars and connecting plates as shown in Fig. B.12, B.13, B.14 and B.15 respecively. The enclosure is class 100,000 clean room installed with four High Efficiency Particulate Air (HEPA) filters (TM-RSC, AAF India Pvt. ltd.) at its ceiling. The clean room houses two non magnetic optical tables: table 1 which is 1.2×3 m^2 (Newport M-RPR-N-410-12) and table two which is 1.2×3 m^2 (M-RPR-N510-12) in dimensions. Both tables are 12 inch thick and are placed adjacent to each other making an L-shape. The tables rest over eight 23.5" tall non-magnetic vibration isolators with automatic re-leveling (Newport S-2000), as shown in Fig. B.9 and B.10. The lasers and optics setup is on optics table 1, whereas the optics table 2 places vacuum assembly and the imaging system. Clean room is provisioned with shelves over the L shaped table arrangement, for placing opto-electronics and other equipments. Overhead cable trays keep cables and optical fibres clear of the experiment area. The outside area is used for data acquisition computer systems and R&D. Almost all the electronic equipments have been installed outside the clean room to avoid disturbance to the main experiment area. Indigenous design and fabrication of clean room gave cost effective customized solution.

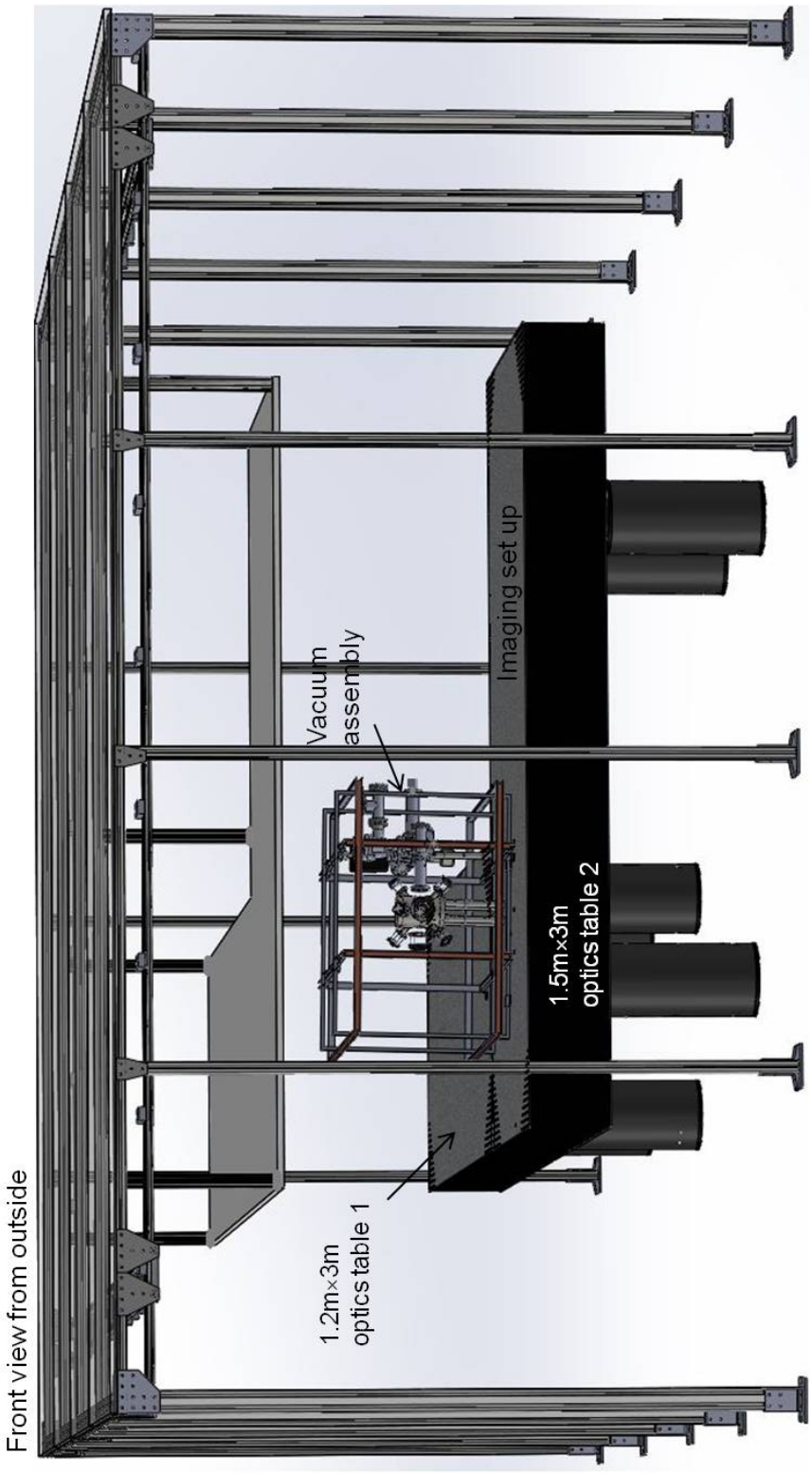

Fig. B.9: Shows 3D model of the dust free enclosure, viewing from front.

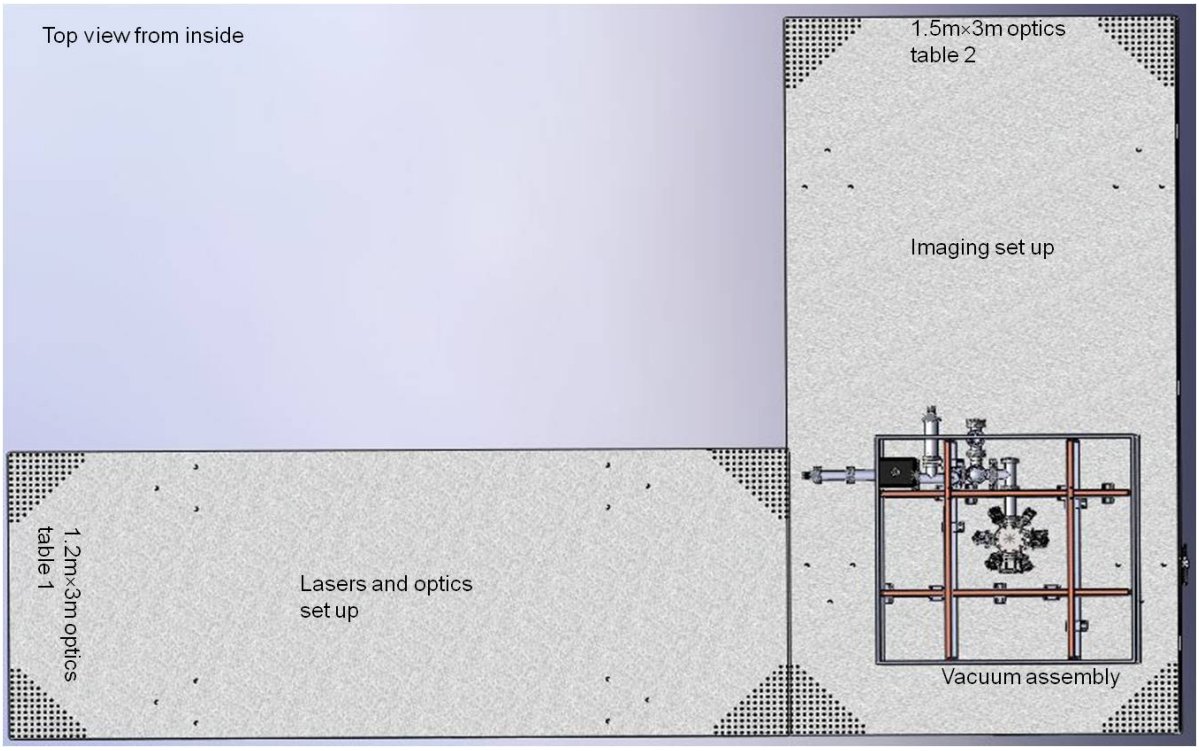

Fig. B.10: Shows 3D model of the dust free enclosure viewing from top.

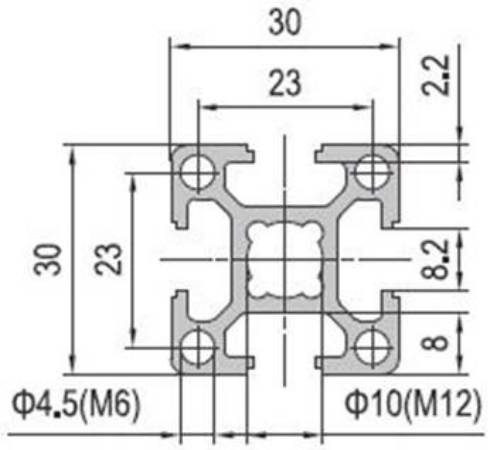

30-30 cross section view

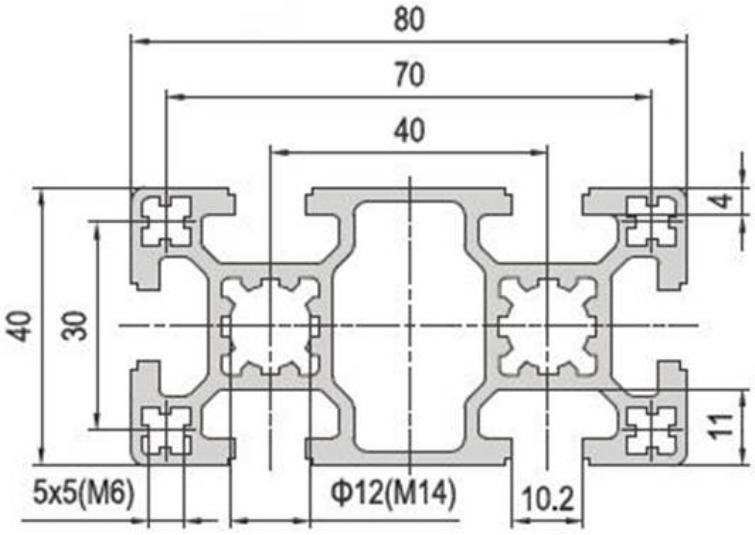

40-80 cross section view

Fig. B.11: Shows dimensions of (a) standard 30-30 and (b) standard 40-80 aluminium extrusions.

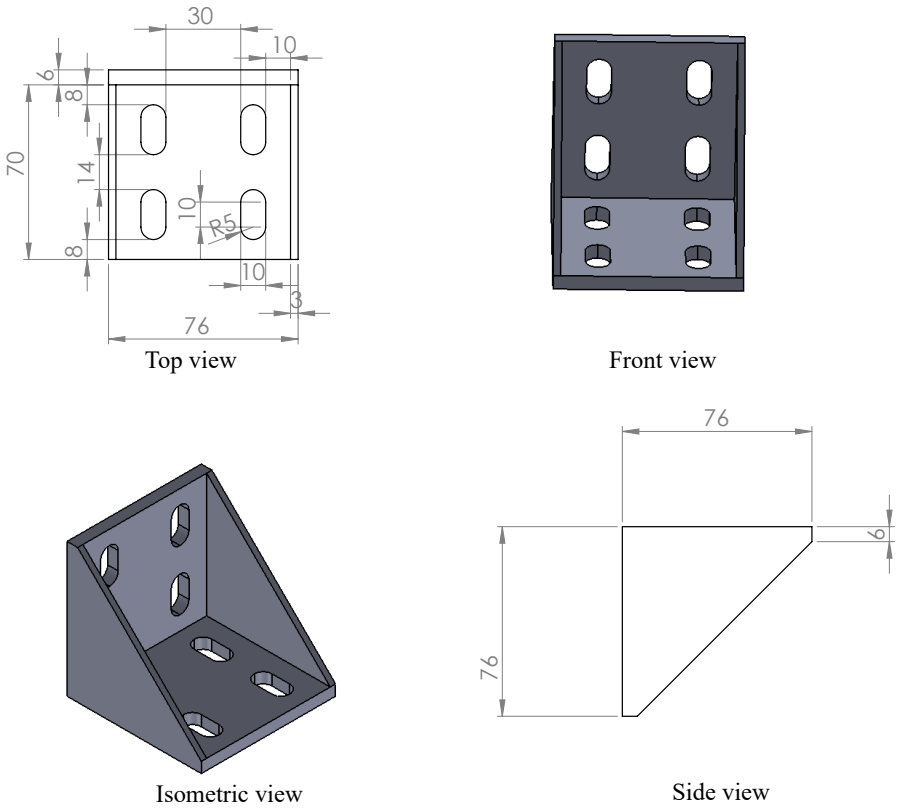

Fig. B.12: Shows indigenous design of die cast bracket used for connecting 40-80 together at right angles. All dimensions are in millimeter.

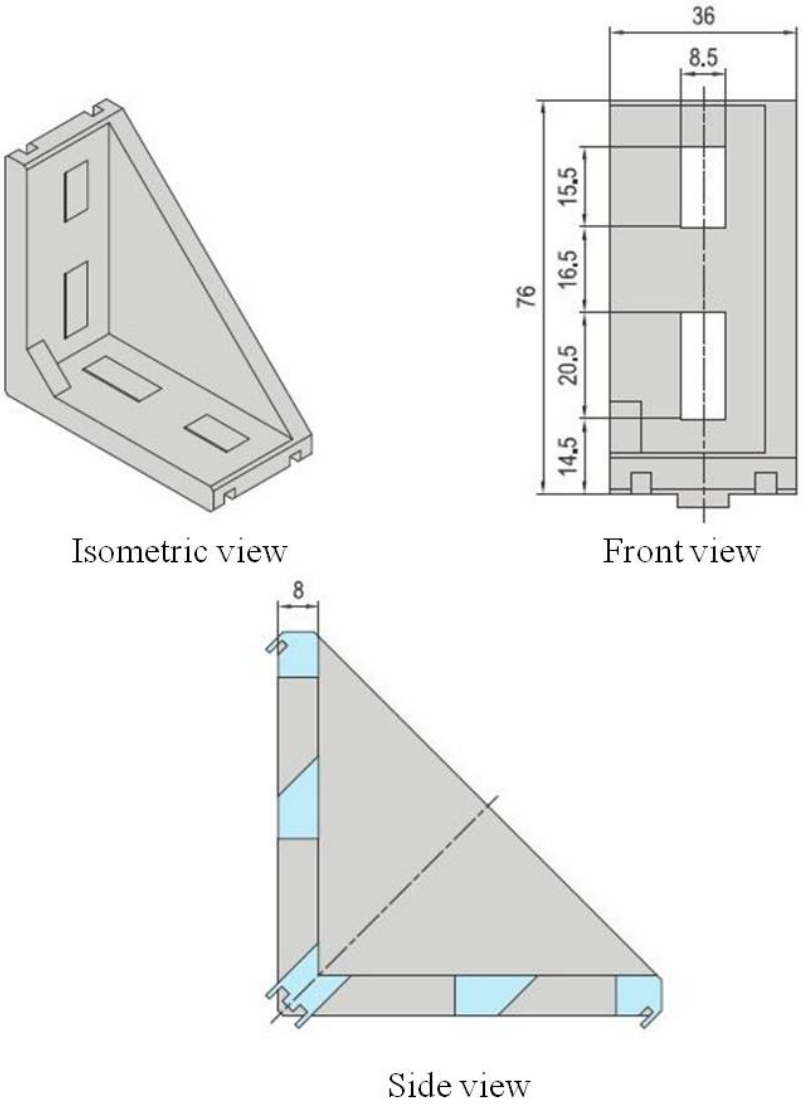

Fig. B.13: Shows indigenous design of die cast half bracket used for connecting 30-30 together at right angles. All dimensions are in millimeter.

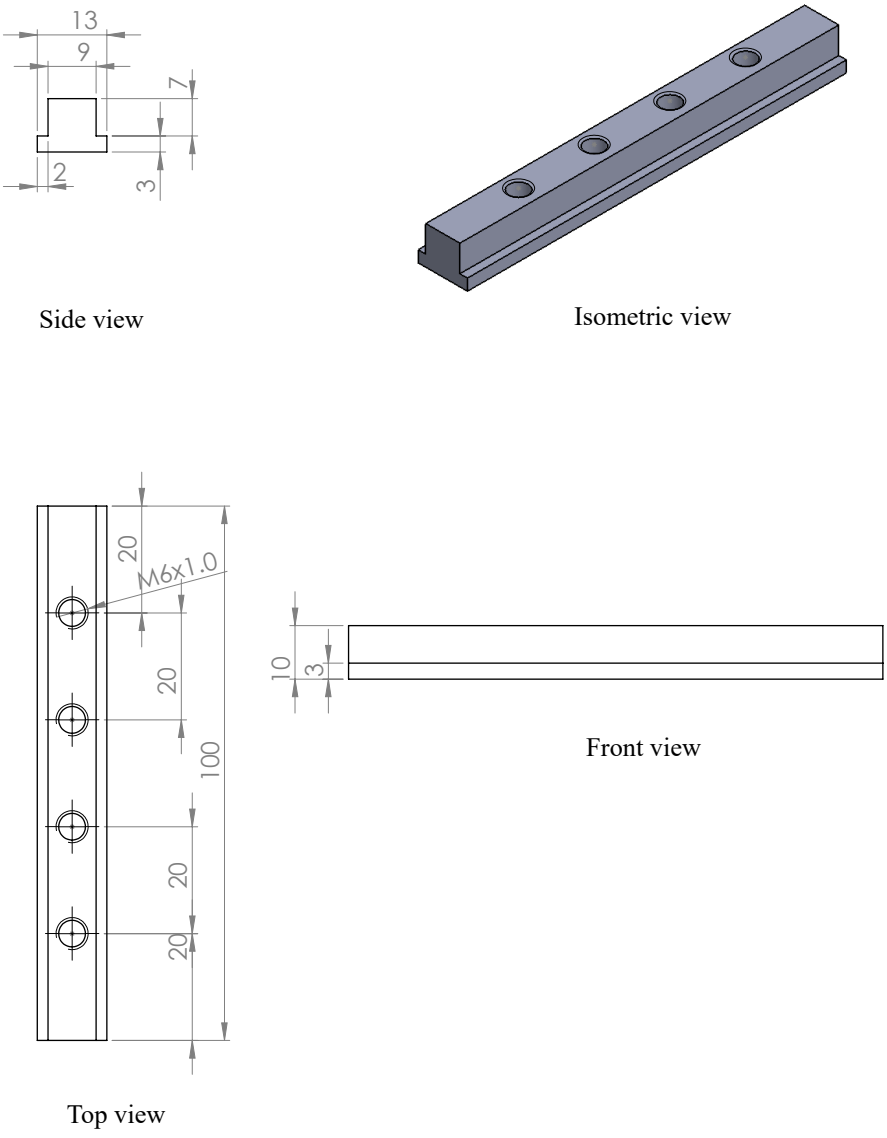

Fig. B.14: Shows indigenous design of a t-shaped joint bar used for connecting 40-80 and 30-30 together along their lengths. All dimensions are in millimeter.

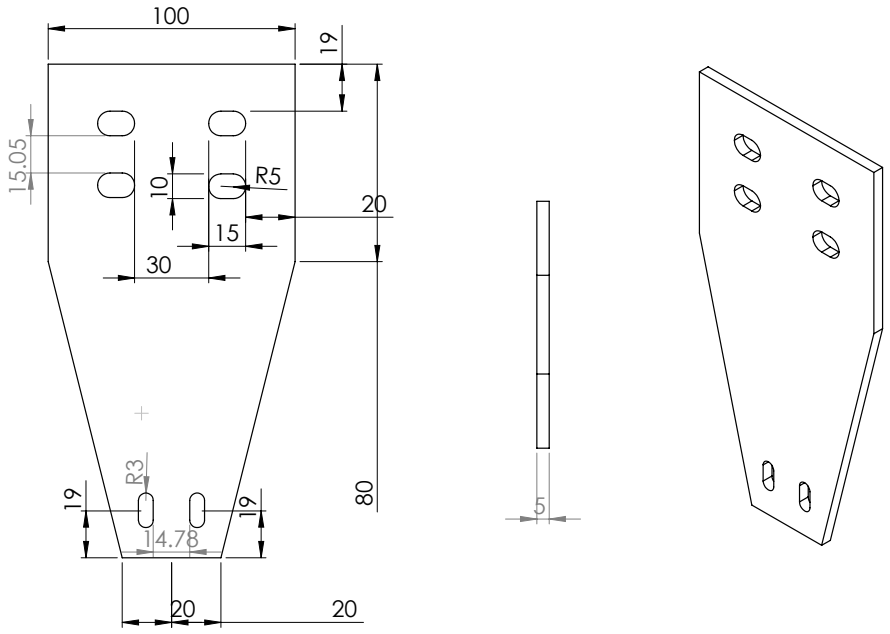

Fig. B.15: Shows indigenous design of connecting plates used in putting up cable trays together. All dimensions are in millimeter.

C. HELMHOLTZ COILS OPTIMIZATION CODE

A code written in Mathematica for finding magnetic field at the center of coils placed in Helmholtz configuration is given here. The analytical treatment in chapter 7 derives the uniform magnetic field at the center of the coils' assembly considering infinitesimally small widths and depths of the coils but in practical situations the contributions are non negligible. Consider a pair of rectangular coils separated by a distance h as shown in Fig. 7.1. Each coil is considered to have inner, l_1 and outer, l_2 lengths. Consider w_1 and w_2 as inner and outer breadths. The coil thickness is considered to be uniform through out *i.e.* $l_1 - l_2 = w_1 - w_2$. If d is the depth of the coil then the number of turns in the coil depends upon d, $l_1 - l_2$ and diameter, s of the wire used to wound the coil. As with each turn, the distance between the center point and the coil turn changes function L, W and H have been defined. The uniform magnetic field field at the center of coils can be optimized by changing separation and dimensions of the coils.

```
(*MATHEMATICA CODE*)

ClearAll[l1, l2, w1, w2, L, W, H, r, h, x, y, z, p, q, i]
μ0 = 4 Pi 10^-7; (* permeability of free space *)
l1 = 920 × 10^-3(* outer length of coil in meters,
 for e.g. if it is 50 cm, input 0.5 *);
l2 = 900 × 10^-3; (*inner length of coil in meters*)
(*We are considering a coordinate system such that origin is at the centre
  between two coils and on the axis of coils. Axis of the coils are along Z-
 axis and coils are in the X-Y plane sitting at some +
 Z and -Z points along the Z-axis*)
(* Keeping (l1-l2) = (w1-w2)*)
w1 = 720 × 10^-3; (* outer breadth 1 in meters*)
w2 = 700 × 10^-3; (* inner breadth 2 in meters*)
d = 20 × 10^-3; (*depth in meters*)
s = 2 × 10^-3; (*radius of wire in meters*)
h = 200 × 10^-3; (*separation between coils in meters*)
i = 1 * 10^-6; (*current in Amperes*)
(*define turns and distance parameters*)
pmax = Floor[ d / (2 s) ](* Segments along axial direction *)
qmax = Floor[ (l1 - l2) / (2 s) ](* Segments along radial direction *)
(*We can take another paramerter rmax= Floor[ (w1-w2) / (2 s) ],
for the third axis but in general we take frames
```

```
such that l1-l2=w1-w2, i.e. of uniform thickeness along length and breadth,
so qmax is used as rmax in defining W parameter below*)
Turns = pmax × qmax
(* Define L, W and H functions as distances are changing with every turn *)
L[q_] := (l2 / 2 + (l1 - l2) / (2 * (qmax + 1)) + q * (l1 - l2) / (qmax + 1));
W[q_] := (w2 / 2 + (w1 - w2) / (2 * (qmax + 1)) + q * (w1 - w2) / (qmax + 1));
H[p_] := (h / 2 + d / (2 * (pmax + 1)) + p * d / (qmax + 1));
(* define the magnitude of the field position vector *)
r[x_, y_, z_] := Sqrt[x^2 + y^2 + z^2];
(* define the magnetic field vector z component, Bz=(dAy/dx)-(dAx/dy)*)
Bz[p_, q_, x_, y_, z_] :=
  Module[{a, b, c}, {a, b, c} = {L[q], W[q], H[p]}; (* (dAy/dx) of the two coils *)
   -μ0 i / (4 π) ((x - a) / ((y - b + r[x - a, y - b, z - c]) r[x - a, y - b, z - c]) -
       (x - a) / ((y + b + r[x - a, y + b, z - c]) r[x - a, y + b, z - c]) +
       (x + a) / ((y + b + r[x + a, y + b, z - c]) r[x + a, y + b, z - c]) -
       (x + a) / ((y - b + r[x + a, y - b, z - c]) r[x + a, y - b, z - c]) +
       (x - a) / ((y - b + r[x - a, y - b, z + c]) r[x - a, y - b, z + c]) -
       (x - a) / ((y + b + r[x - a, y + b, z + c]) r[x - a, y + b, z + c]) +
       (x + a) / ((y + b + r[x + a, y + b, z + c]) r[x + a, y + b, z + c]) -
       (x + a) / ((y - b + r[x + a, y - b, z + c]) r[x + a, y - b, z + c])) +
    μ0 i / (4 π) ((y + b) / ((x - a + r[x - a, y + b, z - c]) r[x - a, y + b, z - c]) -
       (y + b) / ((x + a + r[x + a, y + b, z - c]) r[x + a, y + b, z - c]) +
       (y - b) / ((x + a + r[x + a, y - b, z - c]) r[x + a, y - b, z - c]) -
       (y - b) / ((x - a + r[x - a, y - b, z - c]) r[x - a, y - b, z - c]) +
       (y + b) / ((x - a + r[x - a, y + b, z + c]) r[x - a, y + b, z + c]) -
       (y + b) / ((x + a + r[x + a, y + b, z + c]) r[x + a, y + b, z + c]) +
       (y - b) / ((x + a + r[x + a, y - b, z + c]) r[x + a, y - b, z + c]) -
       (y - b) / ((x - a + r[x - a, y - b, z + c]) r[x - a, y - b, z + c]))];


MagBz[z_] := Sum_{p=1}^{pmax} Sum_{q=1}^{qmax} 10000 * Bz[p, q, 0, 0, z / 100];
Plot[MagBz[z], {z, -2, 2}, AxesLabel →
  {Row[{Style["z", Italic], " (cm)"}], "Bz (gauss)"}, PlotRange → Automatic]
Plot[D[MagBz[z], z] // Evaluate, {z, -0.1, 0.1}, Frame → True,
 PlotStyle -> {Thickness[0.005], RGBColor[0, 0, 1]}, Axes → False,
 FrameLabel -> {"Axial position [cm]", "Field gradient per unit current [G/cm]"},
 LabelStyle → {FontFamily → "Times", FontSize → 12, FontWeight → "Bold"}]
```

BIBLIOGRAPHY

[1] https://home.cern/about/experiments/isolde

[2] V. M. Schäfer, C. J. Ballance, K. Thirumalai, L. J. Stephenson, T. G. Ballance, A. M. Steane and D. M. Lucas, *arXiv:1709.06952v1* (2017).

[3] J. Zhang, G. Pagano, P. W. Hess, A. Kyprianidis, P. Becker, H. Kaplan, A. V. Gorshkov, Z.-X. Gong, and C. Monroe, *arXiv:1708.01044v2* (2017).

[4] M. F. Brandl *et. al*, *Review of Sci. Instrum.* **87** 113103 (2016).

[5] N. Fortson, *Phys. Rev. Lett.* **70** 2383 (1993).

[6] T. W. Koerber, M. Schacht, W. Nagourney and E. N. Fortson, *J. Phys. B* **36** 637 (2003).

[7] O. O. Versolato *et al.*, *Hyperfine Interactions*, **199** 9 (2011).

[8] M. G. Kokish, P. R. Stollenwerk, M. Kajita and B. C. Odom, *arXiv:1710.08589* (2017).

[9] N. Huntemann, C. Sanner, B. Lipphardt, Chr. Tamm, and E. Peik, *Phys. Rev. Lett.* **116** 063011 (2016).

[10] S. G. Turyshev, *From Quantum to Cosmos: Fundamental Physics Research in Space*, World Scientific, Singapore (2009).

[11] P. J. Morhr, D. B. Newell, and B. N. Taylor, *Rev. Mod. Phys.* **84** 035009 (2016).

[12] P. J. Morhr and B. N. Taylor, *Rev. Mod. Phys.* **72** 351 (2000).

[13] W. Cady, *(*Proceedings of the IRE) **10** 83 (1922).

[14] A. Hund, *Proceedings of the IRE* **14** 447 (1926).

[15] W. F. Snyder, *IEEE Transactions on Instrumentation and Measurement* **IM-22** 99 (1973).

[16] W. Itano and N. Ramsey, *Scientific American* **269** 56 (1993).

[17] S. Diddams, J. Bergquist, S. Jefferts, and C. Oates, *Science* **306** 1318 (2004).

[18] T. P. Heavner, E. A. Donley, F. Levi, G. Costanzo, T. E. Parker, J. H. Shirley, N. Ashby, S. Barlow and S. R. Jefferts, *Metrologia* **51** 174 (2014).

[19] J. Bergquist, S. Jefferts, D. Wineland, *Physics Today* **54** 37 (2001).

[20] L. Hollberg, C. Oates, G.Wilpers, C. Hoyt, Z. Barber, S. Diddams, W. Oskay, and J. Bergquist, *Journal of Physics B* **38** 469 (2005).

[21] H. Katori, M. Takamoto, V. G. Palchikov, V. D. Ovsiannikov, *Phys. Rev. Lett.* **91** 173005 (2003).

[22] M. Takamoto and H. Katori, *Phys. Rev. Lett.* **91** 223001 (2003).

[23] A. D. Ludlow, M. M. Boyd, T. Zelevinsky, S.M. Foreman, S. Blatt, M. Notcutt, T. Ido, and J. Ye, *Phys. Rev. Lett.* **96** 033003 (2006).

[24] X. Baillard, M. Fouché, R. Le Targat, P. G. Westergaard, A. Lecallier, Y. Le Coq, G. D. Rovera, S. Bize and P. Lemonde, *Opt. Lett.* **32** 1812 (2007).

[25] T. Akatsuka, M. Takamoto and H. Katori, *Nat. Phys.* **4** 954 (2008).

[26] A. D. Ludlow *et al.*, *Science* **319** 1805 (2008).

[27] A. Yamaguchi, M. Fujieda, M. Kumagai, H. Hachisu, S. Nagano, Y. Li, T. Ido, T. Takano, M. Takamoto and H. Katori, *Appl. Phys. Express* **4** 082203 (2011).

[28] S. Falke *et al.*, *Metrologia* **48** 399 (2011).

[29] F. L. Hong *et al.*, *Opt. Lett.* **34** 692 (2009).

[30] I. Ushijima, M. Takamoto, M. Das, T. Ohkubo and H. Katori, *Nature Photonics* **9** 185 (2015).

[31] C. Y. Park and T. H. Yoon, *Phys. Rev. A* **68** 055401 (2003).

[32] R. Maruyama, R. H. Wynar, M. V. Romalis, A. Andalkar, M. D. Swallow, C. E. Pearson and E. N. Fortson, *Phys. Rev. A* **68** 011403 (2003).

[33] C. W. Hoyt, Z. W. Barber, C. W. Oates, T. M. Fortier, S. A. Diddams and L. Hollberg, *Phys. Rev. Lett.* **95** 083003 (2005).

[34] T. Kohno, M. Yasuda, K. Hosaka, H. Inaba, Y. Nakajima and F. L. Hong, *Appl. Phys. Express* **2** 072501 (2009).

[35] A. Y. Nevsky *et al. Appl. Phys. B* **92** 501 (2008).

[36] M. Pizzocaro, G. Costanzo, A. Godone, F. Levi, A. Mura, M. Zoppi and D. Calonico, *IEEE Trans. Ultrason. Ferroelectr. Freq. Control.* **59** 426 (2012).

[37] K. P. Beloy *et al.*, *Phys. Rev. Lett.* **113** 260801 (2014).

[38] H. Hachisu, K. Miyagishi, S. Porsev, A. Derevianko, V. Ovsiannikov, V. Pal'chikov, M. Takamoto and H. Katori, *Phys. Rev. Lett.* **100** 053001 (2008).

[39] L. Yi, S. Mejri, J. J. McFerran, Y. Le Coq and S. Bize, *Phys. Rev. Lett.* **106** 073005 (2011).

[40] K. Yamanaka, N. Ohmae, I. Ushijima, M. Takamoto, and H. Katori, *Phys. Rev. Lett.* **114** 230801 (2015).

[41] T. W. Hänsch, and A. L. Schawlow, *Opt. Comm.* **13** 6869 (1975).

[42] D. J. Wineland, R. E. Drullinger, and F. L. Walls, *Phys. Rev. Lett.* **40** 1639 (1978).

[43] W. Neuhauser, M. Hohenstatt, P. Toschek and H. Dehmelt, *Phys. Rev. Lett.* **41** 233 (1978).

[44] W. Neuhauser, M. Hohenstatt, P. E. Toschek and H. Dehmelt, *Phys. Rev. A* **22** 1137 (1980).

[45] D. J. Wineland and W. M. Itano, *Phys. Lett. A* **82** 75 (1981).

[46] S. Stenholm, *Rev. of Mod. Phys.* **58** 699 (1986).

[47] W. Paul and M. Raether, *Z. Phys.* **140** 262 (1955).

[48] M. G. Raizen, J. M. Gilligan, J. C. Bergquist, W. M. Itano and D. J. Wineland, *Phys. Rev. A* **45** 6493 (1992).

[49] C. A. Schrama, E. Peik, W. W. Smith and H. Walther, *Opt. Comm.* **101** 32 (1993).

[50] A. Rastogi, N. Batra, A. Roy, J. Thangjam, V. P. S. Kalsi, S. Panja and S. De.,*Mapan: Journal of Metrology Society of India*, DOI 10.1007/s12647-015-0140-6, (2015).

[51] J. Friebe *et al.*, *New J. of Phys.* **13** 125010 (2011).

[52] A. P. Kulosa *et al.*, *Phys. Rev. Lett.* **115** 240801 (2015).

[53] C. Degenhardt, H. Stoehr, C. Lisdat, G. Wilpers, H. Schnatz, B. Lipphardt, *Phys. Rev. A* **72** 062111 (2005).

[54] G. Wilpers *et al.*, *Metrologia* **44** 146 (2007).

[55] G. K. Campbell *et al.*, *Metrologia* **45** 539 (2008).

[56] T. L. Nicholson *et al.*, *Nat. Comm.* **6** 6896 (2015).

[57] R. Le Targat *et al.*, *Nat. Comm.* **4** 2109 (2013).

[58] S. Falke *et al.*, *New J. of Phys.* **16** 073023 (2014).

[59] H. Hachisu *et al.*, *Opt. Lett.* **39** 4072 (2014).

[60] D. Akamatsu, H. Inaba, K. Hosaka, M. Yasuda, A. Onae, T. Suzuyama, M. Amemiya and F. Hong, *App. Phys. Express* **7** 012401 (2014).

[61] H. Katori *OSA Technical Digest of Conference on Lasers and Electro-Opttics (CLEO 2015), San Jose* (2015).

[62] C. W. Oates *et al.*, *Phys. Rev. Lett.* **103** 063001 (2009).

[63] N. Hinkley, J. A. Sherman, N. B. Phillips, M. Schioppo, N. D. Lemke, K. Beloy, M. Pizzocaro, C. W. Oates and A. D. Ludlow, *Science* **341** 6151 (2013).

[64] D. Akamatsu, M. Yasuda, H. Inaba, K. Hosaka, T. Tanabe, A. Onae, and F. Hong, *Opt. Express* **22** 7898 (2014).

[65] C. Y. Park *et al.*, *Metrologia* **50** 119 (2013).

[66] D. H. Yu *et al.*, in *Proceedings of Conference on Precision Electromagnetic Measurements (CPEM 2014), Rio de Janeiro* 668 (2014).

[67] J. J. McFerran, L. Yi, S. Mejri, S. Di Manno, W. Zhang, J. Guéna, Y. Le Coq, and S. Bize, *Phys. Rev. Lett.* **108** 183004 (2012).

[68] T. Rosenband *et al.*, *Science* **319** 1808 (2008).

[69] M. Chwalla *et al.*, *Phys. Rev. Lett.* **102** 023002 (2009).

[70] G. Huang *et al.*, *Chinese Phys. B* **24** 054213 (2015).

[71] K. Matsubara *et al.*, *Opt. Express* **20** 22034 (2012).

[72] J. Cao, P. Zhang, J. Shang, K. Cui, J. Yuan, S. Chao, S. Wang, H. Shu and X. Huang, *arXiv1607.03731* (2016).

[73] G. P. Barwood, G. Huang, H. A. Klein, L. A. M. Johnson, S. A. King, H. S. Margolis, K. Szymaniec and P. Gill, *Phys. Rev. A* **89** 050501 (2014).

[74] P. Dube, A. Madej, Z. Zhou and J. E. Bernard, *Phys. Rev. A* **87** 023806 (2013).

[75] Y. H. Wang *et al.*, *Laser Phys.* **17** 1017 (2007).

[76] N. Ohtsubo, Y. Li, K. Matsubara, T. Ido, and K. Hayasaka, *Optics Express* **25** 11725 (2017).

[77] C. Tamm, N. Huntemann, B. Lipphardt, V. Gerginov, N. Nemitz, M. Kazda, S. Weyers and E. Peik, *Phys. Rev. A* **89**, 023820 (2014).

[78] R. Godun *et al.*, *Phys. Rev. Lett.* **113** 210801 (2014).

[79] J. E. Stalnaker *et al.*, Appl. Phys. B **10** 89 (2007).

[80] L. V. Wense *et al.*, *Nature* **533** 47 (2016).

[81] H. G. Dehmelt and P. Toschek, *Bull. Am. Phys. Soc.* **20** 61 (1975).

[82] D. J. Wineland and H. Dehmelt, *Bull. Am. Phys. Soc.* **20** 637 (1975).

[83] T. Rosenband, P. O. Schmidt, D. B. Hume, W. M. Itano, T. M. Fortier, J. E. Stalnaker, K. Kim, S. A. Diddams, J. C. J. Koelemeij, J. C. Bergquist, and D. J. Wineland, *Phys. Rev. Lett.* **98** 220801 (2007).

[84] G. Tommaseo, T. Pfeil, G. Revalde, G. Werth, P. Indelicato and J. P. Desclaux, *Eur. Phys. J. D* **25** 113 (2003).

[85] G. P. Barwood, P. Gill, G. Huang and H. A. Klein *Conference on Precision Electromagnetic Measurements (CPEM 2012)*, 270 (2012).

[86] T. Becker, J. Zanthier, A. Nevsky, C. Schwedes, M. Skvortsov, H. Walther and E. Peik, *Phys. Rev. A* **63** 051802(R) (2001).

[87] W. F. Meggers, *J. Res. Natl. Bur. Stand.* **71A** 396 (1967).

[88] W. M. Itano, *J. Res. natl. Inst. Stand. Technol.* **105** 829 (2000).

[89] M. S. Safronova, M. G. Kozlov and C.W. Clark, *Phys. Rev. Lett.* **107** 143006 (2011).

[90] D. Jiang, B. Arora, M. S. Safronova and C.W. Clark, *Journal Phys. B: Atomic, Molecular and Optical Physics* **42** 154020 (2009).

[91] A. Roy, S. De, Bindiya Arora and B. K. Sahoo, *Journal Phys. B: Atomic, Molecular and Optical Physics* **50** 20 (2017).

[92] P. Dubé, A. A. Madej, M. Tibbo and J. E. Bernard, *Phys. Rev. Lett.* **112** 173002 (2014).

[93] N. Huntemann, M. Okhapkin, B. Lipphardt, S. Weyers, Chr. Tamm and E. Peik, *Phys. Rev. Lett.* **108** 090801 (2012).

[94] T. Schneider, E. Peik and C. Tamm, *Phys. Rev. Lett.* **94** 230801 (2005).

[95] N. Poli, C. W. Oates, P. Gill, and G. M. Tino, *Riv. Nuovo Cimento* **36** 555 (2013).

[96] C. F. Roos, M. Chwalla, K. Kim, M. Riebe and R. Blatt, *Nature* **443** 316 (2006).

[97] G. P. Barwood, H. S. Margolis, G. Huang, P. Gill, and H. A. Klein. *Phys. Rev. Lett.* **93** 133001 (2004).

[98] C. W. Chou, D. B. Hume, J. C. J. Koelemeij, D. J. Wineland, T. Rosenband, *Phys. Rev. Lett.* **104** 070802 (2010).

[99] D. J. Larson, J. C. Bergquist, J. J. Bollinger, W. M. Itano, and D. J. Wineland, *Phys. Rev. Lett.* **57** 70 (1986).

[100] J. B. Wübbena, S. Amairi, O. Mandel, and P. O. Schmidt, *Phys. Rev. A* **85** 043412 (2012).

[101] J. I. Cirac and P. Zoller, *Phys. Rev. Lett.* **74** 4091 (1995).

[102] P. Barton *et al.*, *Phys. Rev. A* **62** 032503 (2000).

[103] G. KeLin, *Chinese Sci. Bull.* **58** 853 (2013).

[104] Y. Huang, J. Cao, P. Liu, K. Liang, B. Ou, H. Guan, X. Huang, T. Li and K. Gao, *Phys. Rev. A* **85** 030503 (2012).

[105] K. Matsubara, K. Hayasaka, Y. Li, H. Ito, S. Nagano, M. Kajita and M. Hosokawa, *Appl. Phys. Express* **1** 067011 (2008).

[106] J. Benhelm, G. Kirchmair, U. Rapol, T. Körber, C. F. Roos and R. Blatt, *Phys. Rev. A* **75** 032506 (2007).

[107] C. Champenois, M. Houssin, C. Lisowski, M. Knoop, G. Hagel, M. Vedel and F. Vedel, *Phys. Lett. A* **331** 298 (2004).

[108] M. Kajita, Y. Li, K. Matsubara, K. Hayasaka and M. Hosokawa, *Phys. Rev. A* **72** 043404 (2005).

[109] M. S. Safranova and U. I. Safranova, *Phys. Rev. A* **83** 012503 (2011).

[110] Bindiya Arora, M. S. Safronova, and Charles W. Clark, *Phys. Rev. A* **76** 064501 (2007).

[111] M. G. Boshier, G. P. Barwood, G. Huang and H. A. Klein, *Appl. Phys. B* **71** 51 (2000).

[112] H. S. Margolis, G. P. Barwood, G. Huang, H. A. Klein, S. N. Lea, K. Szymaniec and P. Gill, *Science* **306** 1355 (2004).

[113] P. Dubé, A. A. Madej, J. E. Bernard, L. Marmet, J. S. Boulanger and S. Cundy, *Phys. Rev. Lett.* **95** 033001 (2005).

[114] P. Dubé *et al.*, *Metrologia* **54** 290 (2017).

[115] J. V. Zanthier, M. Eichenseer, A. Yu. Nevsky, M. Okhapkin, Ch. Schwedes and H. Walther, *Laser Phys.* **15** 7 (2005).

[116] E. Peik, G. Hollemann and H. Walther, *Phys. Rev. A* **49** 402 (1994).

[117] E. Peik, G. Hollemann and H. Walther, *Phys. Scr.* **403** (1995).

[118] T. Liu *et al.*, *2007 IEEE International Frequency Control Symposium Joint with the 21st European Frequency and Time Forum* 407 (2007).

[119] J. Sherman, W. Trimble, S. Metz, W. Nagourney and N. Fortson, *Digest of the LEOS Summer Topical Meetings* 99 (2005).

[120] K. Pyka, N. Herschbach, J. Keller, T. E. Mehlstaübler, *Appl. Phys. B* **114** 231 (2014).

[121] Y. Li, N. Ohtsubo, K. Matsubara, S. Nagano, and K. Hayasaka, *Conference on Precision Electromagnetic Measurements (CPEM 2014), Rio de Janeiro,* 60 (2014).

[122] N. F. Ramsey, *Molecular Beams*, Oxford Univ. Press, London, (1956).

[123] B. Appasamy, I. Siemers, Y. Stalgies, J. Eschner, R. Blatt, W. Neuhauser and P. E. Toschek, *Appl. Phys. B* **60** 473 (1995).

[124] W. Nagourney, N. Yu, and H. Dehmelt, *Opt. Comm.* **793** 176 (1990).

[125] N. Yu, X. Zhao, H. Dehmelt and W. Nagourney, *Phys. Rev. A* **50** 2738 (1994).

[126] A. Kleczewski, M. R. Hoffman, J. A. Sherman, E. Magnuson, B. B. Blinov and E. N. Fortson, *Phys. Rev. A* **85** 043418 (2012).

[127] T. W. Koerber, M. H. Schacht, K. R. G. Hendrickson, W. Nagourney and E. N. Fortson, *Phys. Rev. Lett.* **88** 143002 (2002).

[128] J. A. Sherman, T. W. Koerber, A. Markhotok, W. Nagourney and E. N. Fortson, *Phys. Rev. Lett.* **94** 243001 (2005).

[129] B. K. Sahoo, R. Chaudhuri, B. P. Das and D. Mukherjee, Phys. Rev. Lett. **96** 163003 (2006).

[130] B. K. Sahoo, R. G. E. Timmermans B. P. Das and D. Mukherjee, *Phys. Rev. A* **80** 062506 (2009).

[131] B. G. Whitford, K. J. Siemsen, A. Madej and J. D. Sankey, *Opt. Lett.* **19** 356 (1994).

[132] S. A. King *et al.*, *New J. Phys.* **14** 013045 (2012).

[133] K. Arnold, E. Hajiyev, E. Paez, C. H. Lee, M. D. Barret and J. Bollinger, *Phys. Rev. A* **92** 032108 (2015).

[134] M. D. Barrett, *New J. Phys.* **17** 053024 (2015).

[135] E. Paez, *et al.*,*Phys. Rev. A* 93 042112 (2016).

[136] Arifin, *B. S. Thesis*, National University of Singapore, (2014).

[137] Prof. M. D. Barrett (private communication).

[138] A. Kozlov, V. A. Dzuba, and V. V. Flambaum, *Phys. Rev. A* **90** 042505 (2014).

[139] K. J. Arnold, R. Kaewuam, A. Roy, E. Paez, S. Wang, and M. D. Barrett, *Phys. Rev. A* **94** 052512 (2016).

[140] W. Oskay, W. Itano, and J. Bergquist, *Phys. Rev. Lett.* **94** 163001 (2005).

[141] W. Oskay *et al.*, *Phys. Rev. Lett.* **97** 020801 (2006).

[142] D. J. Berkeland, J. D. Miller, J. C. Bergquist, W. M. Itano and D. J. Wineland, *J. Appl. Phys.* **83** 10 (1998).

[143] O. O. Versolato, L. W. Wansbeek, K. Jungmann, R. G. E. Timmermans, L. Willmann and H. W. Wilschut, *Phys. Rev. A* **83** 043829 (2011).

[144] O. O. Versolato *et al.*, *Phys. Lett. A* **375** 3130 (2011).

[145] O. O. Versolato *et al.*, *Phys. Rev. A* **82** 010501(R) (2010).

[146] G. S. Giri *et al.*, *Phys. Rev. A* **84** 020503(R) (2011).

[147] V. A. Dzuba and V. V. Flambaum, *Phys. Rev. A* **61** 034502 (2000).

[148] L. W. Wansbeek, B. K. Sahoo, R. G. E. Timmermans, K. Jungmann, B. P. Das and D. Mukherjee, *Phys. Rev. A* **78** 050501R (2008).

[149] M. N. Portela *et al.*, *Appl. Phys. B* **114** 173 (2014).

[150] I. I. Sobelman, *Atomic Spectra and Radiative Transitions* Springer-Verlag, Berlin, (1979).

[151] Recommendation 2 (CI-2015) 2015 Session II of the 104th Meeting of the CIPM (www.bipm.org/utils/en/pdf/CIPM/CIPM2015-II-EN.pdf)

[152] K. Sugiyama and J. Yoda, *Phys. Rev. A* **55** R10 (1997).

[153] V. A. Dzuba, V. V. Flambaum, M. S. Safronova, S. G. Porsev, T. Pruttivarasin, M. A. Hohensee and H. Häffner, *Nature Physics* **12** 465 (2016).

[154] T. Pruttivarasin *et al.*, *Nature* **517** 592 (2015).

[155] H. S. Margolis, *Contemporary Phys.* **51** 37 (2010).

[156] W. Paul, O. Osberghaus, and E. Fischer, *Forschungsbe. Wirtsch.-Verkehrminist.Nordrhein-Westfalen* **415** (1958).

[157] D. J. Griffiths, *Introduction to Electrodynamics*, Prentice Hall, 3rd edition, (1999).

[158] M. Abramowitz and I. A. Stegun, *Handbook of Mathematical Functions, NBS Applied Mathematics Series No.* **55** (1972).

[159] F. M. Arscott, *Periodic Differential Equations: An introduction to Mathieu, Lame and Allied Functions*, Pergamon press, New York, **66** (1964).

[160] N. W. McLachlan, (Theory and Applications of Mathieu Functions(Clarendon, Oxford)) (1947).

[161] R. E March, *J. of Mass Spectrometry* **32** 351 (1997)

[162] A. G. Sinclair, M. A. Wilson and P. Gill, *Optics Communications* **190** 190 (2001)

[163] B. Stein, *Ph.D. thesis*, Universitat Hannover, (2010)

[164] Y. Wang, *Rapid Comm. in Mass Spec.* **7** 920 (1993).

[165] P. Mandal, M. Mukherjee, (arXiv:1306.5582v1) (2013).

[166] F. H. Read and N. J. Bowring, *The CPO programs and the BEM for charged particle optics*, Nucl. Instrum. Meth. **A645** 273 (2011).

[167] E. C. Beaty, *J. App. Phys.* **61** 2118 (1987).

[168] E. C. Beaty *Phys. Rev. A* **33** 3645 (1986).

[169] A. R. Edmonds, *Angular Momentum in Quantum Mechanics*, Princeton Univ. Press, New Jersey, (1974).

[170] N. Batra, B. K. Sahoo, S. De, *Chinese Phys. B* **25** 113703 (2016).

[171] P. J. Blythe, S. A. Webster, K. Hosaka and P. Gill *J. Phys. B* **36** 981 (2003).

[172] W. M. Itano *Phys. Rev. A* **73** 022510 (2006).

[173] S. G. Porsev, M. S. Safronova and M. G. Kozlov *Phys. Rev. A* **86** 022504 (2012).

[174] K. V. P. Latha *et al. Phys. Rev. A* **76** 062508 (2007).

[175] D. K. Nandy and B. K. Sahoo *Phys. Rev. A* **90** 050503(R) (2014).

[176] R. H. Dicke, *Phys. Rev.* **89** 472 (1953).

[177] J. C. Bergquist, W. M. Itano, and D. J. Wineland, *Phys. Rev. A* **36** 428 (1987).

[178] G. Gabrielse *Phys. Rev. A* **29** 462 (1984).

[179] P. Gill. *Metrologia* **42** S125 (2005).

[180] J. R. P. Angel and P. G. H. Sandars, *Proc. Roy. Soc. A* **305** 125 (1967).

[181] J. R. P. Angel, P. G. H. Sandars, and G. K. Woodgate, J. Chem. Phys. **47** 1552 (1967).

[182] E. J. Angstmann, V. A. Dzuba, and V. V. Flambaum, *Phys. Rev. Lett.* **97** 040802 (2006).

[183] R. B. Warrington, Private communication.

[184] J. W. Farley and W. H. Wing, *Phys. Rev. A* **23** 2397 (1981).

[185] G. K. Woodgate, *Elementary Atomic Structure*, Oxford University Press, 2nd edition, (1983).

[186] *NIST atomic spectra database*, version 5, National Institute of Standards and Technology, USA.

[187] C. Liu, D. Ryding, R. W. Nielsen, T. L. Kruy and T. M. Kuzay *Rev. Sci. Instrum.* **67** 3378 (1996).

[188] D. A. Hite, Y. Colombe, A. C. Wilson, D. T. C. Allcock, D. Leibfried, D. J. Wineland and D. P. Pappas *MRS Bull.* **38** 826 (2013).

[189] M. Doležal *et al. Metrologia* **52** 842 (2015).

[190] W. W. Macalpine, R.O. Schildknecht, *Proc. IRE* **47** 2099 (1959).

[191] T. Nishikawa, S. Tamura, Y. Ishikawa, H. Matsumoto, *US patent* US 4398164 A (1983).

[192] A. I. Zverev, H. J. Blinchikoff *IEEE Trans. Component Parts* **8** 99 (1961).

[193] S. Panja, S. De, S. Yadav and A. Sen Gupta. *Rev. Sci. Instrm.* **86** 056104 (2015).

[194] J. D. Siverns, L. R. Simkins, S. Weidt, W. K. Hensinger *Appl. Phys. B* **107** 921 (2012).

[195] A. Roy, N. Batra, S. Majhi, S. Panja, A. Sen Gupta and S. De, *Mapan: Journal of Metrology Society of India*, DOI 10.1007/s12647-017-0241-5, (2017).

[196] A. Acharya, S. De, P. Arora and A. Sen Gupta, *Measurement* **61** (2014).

[197] NI 6353 PCI card manual, http://www.ni.com/pdf/manuals/374592d.pdf

[198] N. Batra, A. Roy, C. Samal, S. Majhi, S. Panja and S. De, *IEEE Conf. Proc of 2nd International conference on control, instrumentation, energy and communication* 78 (2016).

List of Publications

Articles in Refereed Journals

1. Design of the Ion Trap and Vacuum System for ^{171}Yb-ion Optical Frequency Standard, A. Rastogi, **N. Batra**, A. Roy, J. Thangjam, V. P. S. Kalsi, S. Panja and S. De, MAPAN-Journal of Metrology Society of India, DOI 10.1007/s12647-015-0140-6 (2015).

2. An optimized ion trap geometry to measure quadrupole shifts of $^{171}Yb^{+}$ clocks, **N. Batra**, B. K. Sahoo & S. De, Chin. Phys. B Vol 25, 11, 113703 (2016).

3. Singly charged ions for optical clocks, **N. Batra**, A. Roy, S. Majhi, S. Panja and S. De, Asian Journal of Physics, Vol 25, 9, 1069 (2016).

4. Design and Construction of a Helical Resonator for Delivering Radio Frequency to an Ion Trap, **N. Batra**, S. Panja, S. De, A. Roy, S. Majhi and A. Sen Gupta, MAPAN-Journal of Metrology Society of India, DOI 10.1007/s12647-017-0209-5, (2017).

5. Design of a Stable DC Voltage Source and Computer Controlling of It Using an Indigenously Developed All-Digital Addressing-Cum-Control Hardware, A. Roy, **N. Batra**, S. Majhi, S. Panja, A. Sen Gupta and S. De, MAPAN-Journal of Metrology Society of India, DOI 10.1007/s12647-017-0241-5, (2017).

Conference Proceedings

1. Trapped Ytterbium Ion for Optical Frequency Standards in India, S. De, A. Rastogi, **N. Batra**, S. Panja, and A. Sen Gupta, Kiran 25, 13 (2014).
2. **N. Batra**, A. Rastogi, S. De, S. Panja and A. Sen Gupta, Proceedings of fourth international conference on current developments in atomic, molecular, optical and nano-physics with applications (CDAMOP), India: University of Delhi, (2015).
3. Automation of an optical frequency standard experiment, **N. Batra**, A. Roy, C. Samal, S. Majhi, S. Panja and S. De, CIEC 2016 conference at Kolkata University, Kolkata, India, IEEE Conference proceeding, pp. 78 - 82 (2016).